

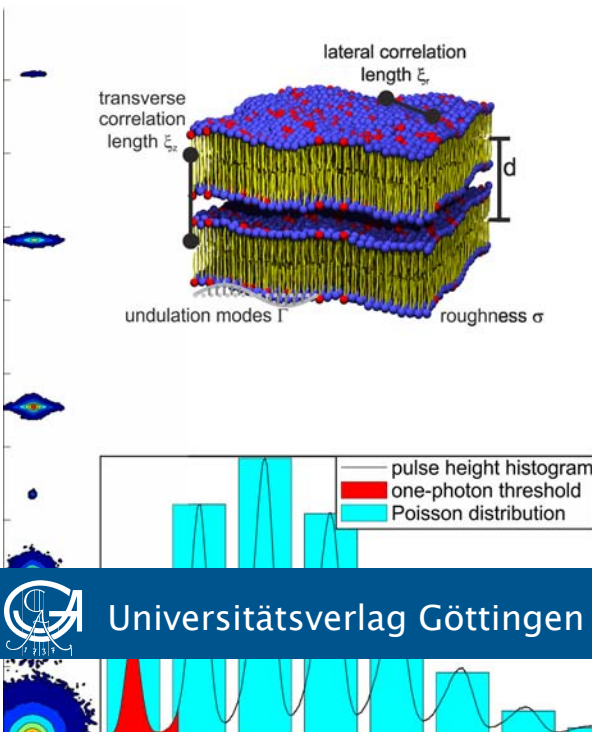
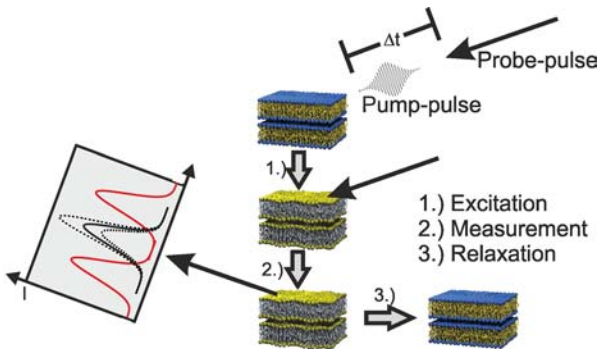
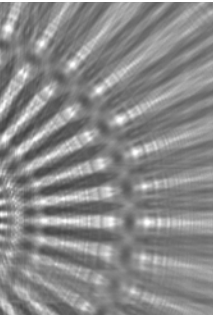


Göttingen Series in  
X-ray Physics

Tobias Reusch

## Non-equilibrium dynamics of lipid bilayers

Time resolved x-ray scattering at in-house  
and synchrotron sources



Universitätsverlag Göttingen



Tobias Reusch

Non-equilibrium dynamics of lipid bilayers

This work is licensed under the [Creative Commons](https://creativecommons.org/licenses/by-sa/3.0/) License 3.0 “by-sa”, allowing you to download, distribute and print the document in a few copies for private or educational use, given that the document stays unchanged and the creator is mentioned.



Published in 2013 by Universitätsverlag Göttingen  
as Volume 12 in the series „Göttingen series in x-ray physics“

---

Tobias Reusch

# Non-equilibrium dynamics of lipid bilayers

Time resolved x-ray scattering at  
in-house and synchrotron sources

Göttingen series in x-ray physics  
Volume 12



Universitätsverlag Göttingen  
2013

## Bibliographische Information der Deutschen Nationalbibliothek

Die Deutsche Nationalbibliothek verzeichnet diese Publikation in der Deutschen Nationalbibliographie; detaillierte bibliographische Daten sind im Internet über <http://dnb.ddb.de> abrufbar.

### *Address of the Author*

Dr. Tobias Reusch  
e-mail: [treusch@gwdg.de](mailto:treusch@gwdg.de)

Dissertation  
for the award of the degree  
“Doctor rerum naturalium”  
of the Georg-August-Universität Göttingen

Referent: Prof. Dr. Tim Salditt  
Koreferentin: Prof. Dr. Simone Techert

This work is protected by German Intellectual Property Right Law.  
It is also available as an Open Access version through the publisher's homepage and the Online Catalogue of the State and University Library of Goettingen (<http://www.sub.uni-goettingen.de>). Users of the free online version are invited to read, download and distribute it.

Layout: Tobias Reusch  
Cover: Jutta Pabst  
Cover image: Tobias Reusch

© 2013 Universitätsverlag Göttingen  
<http://univerlag.uni-goettingen.de>  
ISBN: 978-3-86395-127-6  
ISSN: 2191-9860

## **Preface of the series editor**

The Göttingen series in x-ray physics is intended as a collection of research monographs in x-ray science, carried out at the Institute for X-ray Physics at the Georg-August-Universität in Göttingen, and in the framework of its related research networks and collaborations.

It covers topics ranging from x-ray microscopy, nano-focusing, wave propagation, image reconstruction, tomography, short x-ray pulses to applications of nanoscale x-ray imaging and biomolecular structure analysis.

In most but not all cases, the contributions are based on Ph.D. dissertations. The individual monographs should be enhanced by putting them in the context of related work, often based on a common long term research strategy, and funded by the same research networks. We hope that the series will also help to enhance the visibility of the research carried out here and help others in the field to advance similar projects.

Prof. Dr. Tim Salditt, Editor  
Göttingen February 2011





# Contents

<b>Introduction</b>	<b>1</b>
<b>1 Time resolved x-ray scattering</b>	<b>5</b>
1.1 A typical pump-probe experiment . . . . .	5
1.2 In house femtosecond x-ray generation . . . . .	8
1.2.1 X-ray generation in laser induced plasmas . . . . .	9
1.2.2 In house setup for time resolved x-ray scattering at the PXS	11
1.2.3 Optical excitation mechanisms available at the PXS . . . . .	14
1.2.4 The timing system at the PXS . . . . .	16
1.3 Time resolved experiments at P08 / Petra III . . . . .	18
1.4 Time resolved diffraction at beamline ID09B, ESRF . . . . .	23
<b>2 Materials and Methods</b>	<b>25</b>
2.1 Surface Acoustic Wave generation . . . . .	25
2.2 Sample preparation and environments . . . . .	29
2.3 Specular and diffuse scattering from lipid multilayers . . . . .	31
2.3.1 Specular scattering from lipid multilayers . . . . .	33
2.3.2 Diffuse scattering from lipid multilayers . . . . .	34
<b>3 Ultrafast multi photon counting – Detector development</b>	<b>39</b>
3.1 Desired specifications / Ultrafast multi photon counting . . . . .	39
3.2 The analog signal chain . . . . .	42
3.2.1 Preamplifier . . . . .	43
3.2.2 Gated integrator (Boxcar averager) . . . . .	43
3.2.3 Commissioning of the analog signal chain – single photon counting capability . . . . .	47
3.3 High speed data acquisition and online analysis at 31MHz . . . . .	49
3.3.1 Commissioning of the digital signal chain – speed and effective dynamic range . . . . .	50
3.4 Power supply and user interface . . . . .	57
3.5 Conclusion and outlook . . . . .	59
<b>4 SAW induced dynamics in lipid multilayers</b>	<b>63</b>
4.1 The high resolution diffraction beamline P08 at Petra III, DESY, Hamburg . . . . .	63
4.2 Results – Pure $LiNbO_3$ substrates . . . . .	64
4.2.1 General remarks on x-ray scattering from a SAW distorted crystal lattice . . . . .	64
4.2.2 Time resolved measurements of the rocking curve at the first and fifth harmonic SAW frequency . . . . .	66
4.2.3 Measurements at the fifth harmonic SAW frequency . . . . .	68
4.2.4 The first harmonic SAW frequency . . . . .	69
4.2.5 Higher acoustic harmonic generation? . . . . .	70

4.2.6	Analytic calculation of the structure factor of a SAW distorted crystal lattice in kinematic approximation . . . . .	72
4.3	Results – Lipids excited by SAWs of Rayleigh type . . . . .	74
4.4	Conclusions . . . . .	79
<b>5</b>	<b>Laser induced structural dynamics</b>	<b>81</b>
5.1	Pure phospholipids on silicon substrates . . . . .	81
5.1.1	Preparatory experiments at the in-house femtosecond x-ray source . . . . .	81
5.1.2	X-ray scattering setup at the ID09B at the ESRF, Grenoble	88
5.1.3	Elimination of laser and x-ray induced drift – Sample environments and possible pitfalls . . . . .	88
5.1.4	Excitation of lipid multilayers on silicon substrates by nanosecond laser pulses – A molecular movie . . . . .	92
5.1.5	Conclusion . . . . .	99
5.2	Collective undulations in Texas-red labeled lipid multilayers . . . .	100
5.2.1	Conclusions . . . . .	107
<b>6</b>	<b>Summary and outlook</b>	<b>109</b>
<b>A</b>	<b>Appendix</b>	<b>111</b>
A.1	Excitation mechanisms for lipid bilayers . . . . .	111
A.1.1	Excitation of lipid membranes by pulsed laser radiation . .	111
A.1.2	Lipid bilayers excited by strong electric field pulses . . . . .	112
A.1.3	The high voltage pulser / The thin film diffraction chamber	116
A.2	Ionization chambers in the case of femtosecond x-ray pulses . . . .	119
A.3	Electronic schematics of the preamplifier circuit . . . . .	121
A.4	Electronic schematics of the gated integrator . . . . .	124
A.5	Electronic schematics of the power supply circuit . . . . .	127
	<b>References</b>	<b>131</b>
	<b>Danksagung</b>	<b>141</b>

## Introduction

The aim of the present thesis is to explore molecular and collective non equilibrium phenomena in lipid bilayers, as model systems for nature's most important interface - the biological membrane. Towards this goal, an adaption and extension of time resolved x-ray scattering experiments to soft matter sample systems was required. In the following a brief outline of the physiological situation as well as technologically interesting parameter ranges will be given.

Every active or living system is strictly far from thermodynamic equilibrium. The active cytoskeleton, protein activity, transport phenomena or phase transitions lead to local forces, driving a biological membrane out of equilibrium. Among the physiologically and technologically most interesting driving forces are the activity of embedded proteins, electric field effects and photo physical processes.

Under physiological conditions, biological membranes are exposed to electric fields on the order of  $E \approx 10^7 \text{V/m}$  due to an ion gradient across the lipid bilayer. This electric field strongly influences the elastic properties and interaction forces of the lipid bilayer. It affects the functional aspects, such as diffusion as well as parallel and perpendicular transport through the bilayer and a fast switching of this field is commonly believed to be a key parameter in the process of nerve pulse propagation [1, 2, 3, 4]. The instability of lipid bilayers at transverse electric fields of  $E \geq 10^8 \text{V/m}$ , as well as the effects below this threshold, are the basis for commonly used techniques such as electro- and opto-poration. Although these techniques are standard tools to introduce foreign material, i.e. drugs or plasmid DNA-vectors, into living cells, the molecular process of electroporation is still under discussion. It has long been proposed [5, 6, 7] and recently been demonstrated through molecular dynamics simulations that the permeabilization of lipid bilayers is dominated by the formation of transient, water filled, pores which evolve on the first approximately 5ns after exposure to an electric field [8, 9, 10].

Fluorescent chromophores are commonly used additives in a broad range of photo-physical microscopy experiments [11, 12, 13, 14, 15]. In the course of the conduction and interpretation of these experiments it is tacitly assumed that molecular interactions and structural properties remain unchanged during the excitation as well as the relaxation of the fluorophores. This assumption is in strict contradiction to the fact that collective modes and structural changes are easily excited by small local forces. In a more physiological case, a variety of photo-active proteins such as the highly studied bacteriorhodopsin (BR) molecule [16] is embedded in biological membranes. Although being a highly complex situation, changes of elementary membrane properties induced by protein activity are expected to be qualitatively comparable to changes induced by the localized deposition of thermal energy by for example fluorophores. The latter case of chromophore labeled lipid bilayers can therefore serve as a model system for the more complex situation of embedded active proteins.

As already touched earlier, structural and functional properties of actively driven membranes are expected to differ dramatically from the equilibrium situation. This has been predicted by numerous theoretical studies, focusing e.g. on the ac-

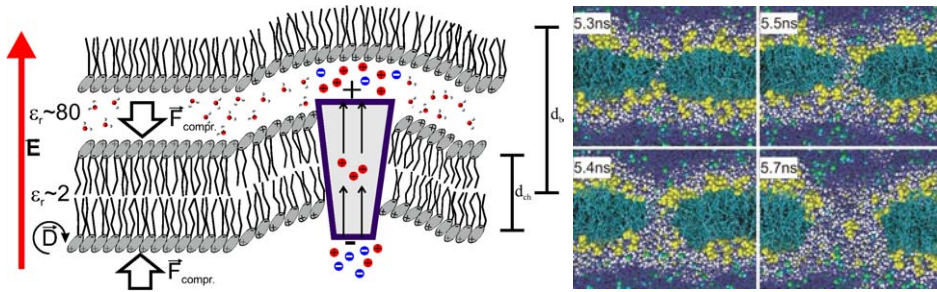


**Figure 1:** *Left:* Active proteins, the active cytoskeleton as well as external electric fields lead to a variety of compressive  $F_{\text{compr.}}$ , tensile, orientational and rotational forces on the lipid bilayer, making biological membranes strictly non-equilibrium systems. *Right:* The formation of transient water filled pores at transverse electric fields  $E \geq 10^8 \text{V/m}$  is the basis for electroporation. Simulations by P. Tieleman [8] (among others) give access to typical underlying time scales, pore formation can be observed within the first 5ns after the application of a transverse electric field of  $E \approx 10^8 \text{V/m}$ .

tivity of especially photo active membrane proteins [17, 18, 19, 20, 21, 22, 23, 24] or external electric fields [25].

The equilibrium dynamics of lipid membranes have extensively been studied with e.g. inelastic neutron scattering and revealed a rich spectrum of dynamics from the 0.1ps to the  $\mu\text{s}$  time scale [26, 27, 28, 29]. Structural properties of lipid bilayers under varying ambient conditions can well be resolved by specular and diffuse x-ray scattering experiments [30, 31, 32, 3, 33]. However, an experimental technique capable of probing fast, especially field and light induced, transient non-equilibrium structural dynamics is necessarily accompanied by two major experimental challenges: (i) Ultrafast temporal resolution on the order of picoseconds is needed in order to probe non equilibrium effects (ii) The outlined effects involve structural changes in the sub-nm length scale. Hence, ultrafast temporal resolution has to be combined with 'molecular' spatial resolution. Out of a narrow pool of experimental techniques capable of combining both requirements we will put our focus on time resolved x-ray diffraction (TRXD) experiments [34, 35, 36, 37]. The basic concept of time resolved diffraction experiments will be sketched in *chapter 2*. For the course of this introduction it should suffice to note that any TXRD experiment follows the well known *pump-probe* scheme and is therefore in the need for excitation mechanisms matching parameters occurring in the physiological or technical situation of experimental interest. Short laser pulses of varying pulse lengths  $\tau$  and central wavelengths  $\lambda$  are the most commonly applied driving force (or pump mechanism), mainly because of the comparatively easy experimental realization. Depending on the question under discussion, more advanced, dedicated excitation mechanisms may be preferable to a mere laser excitation.

Among other techniques especially Surface Acoustic Waves (SAWs) have been

shown to induce a number of phenomenal dynamic effects in soft matter thin films and samples deposited on top of the piezoelectric substrate [38, 39]. Radio frequency (RF) alternating voltages applied to the metallic inter digital transducers (IDTs) of the SAW device induce standing waves or propagating pulses at the surface of a piezoelectric substrate accompanied by strong electric fields, an enabling technology for electromechanical frequency filters, micro-fluidic devices [40, 41] as well as sensor applications [42]. With respect to the rich phenomenology of SAW induced effects on lipid membranes, questions regarding the nature of the coupling (i.e. electric versus mechanical interactions), the effect on phase transitions, as well as possible effects of micro phase separation and raft formation arise. In order to unravel the underlying molecular mechanisms of SAW induced excitation, both in view of understanding fundamental soft matter dynamic effects as well as in view of sensor and device operation, a time resolved structural probe is needed. Central questions that arose in the context of this thesis are: (i) How, and on which time scales, do lipid membranes react on a short pulse excitation? (ii) What are the underlying mechanisms on the molecular level? (iii) Can lipid phase transitions and raft formation be induced by electro- acoustic waves?

**Goals and structure of this thesis** Within the outlined context, the primary goal of the present thesis was to design and perform time resolved x-ray scattering experiments on lipid multilayers, investigating the molecular and collective non-equilibrium answer of lipid bilayers to various excitation mechanisms. This task included close collaborations during the design phase as well as the commissioning of an in house femtosecond x-ray source and the conduction of time resolved as well as time integrating x-ray scattering experiments at synchrotron [43], Free Electron Laser [44] and in house x-ray sources. To achieve these goals the work was divided into three major branches of activity.

In the first branch the optimal experimental setup and necessary infrastructure for the successful conduction of in house time resolved x-ray scattering experiments had to be identified, built and commissioned. The hereby acquired know-how on time resolved x-ray scattering, timing mechanisms as well as a basic expertise on short pulse laser systems had to be transferred to synchrotron and Free Electron Laser x-ray sources, where higher resolution studies complementing preliminary in house experiments were to be conducted.

Time resolved scattering experiments from soft matter sample systems are strongly complicated by thermal drift and sample degradation associated with the respective pumping mechanisms. The focus of the second branch of activities hence lay on the screening for, design and application of advanced excitation mechanisms resembling the complex physiological situation, whilst minimizing unwanted side effects. Most notably, surface acoustic waves had to be used to drive lipid bilayers out of equilibrium. Additionally, laser parameter regimes, sample environments and lipid compositions allowing for the reproducible and reversible excitation of multilamellar lipid bilayers by intense light pulses had to be identified.

In addition to fundamental questions associated with non-equilibrium dynamics of soft matter films (driven membrane undulations), our experiments will address

technological challenges of time resolved x-ray diffraction and imaging. Importantly, conceptually new x-ray detection schemes, well exceeding the performance of present detector concepts, had to be developed in the third branch of the thesis. These developments were driven by the lack of dedicated detection mechanisms for especially time resolved experiments as well as the experience gained in earlier parts of the thesis.

Two additional experiments related to

- (i) a characterization of x-ray induced radiation damage by means of a combination of high resolution diffuse x-ray scattering with a scanning Kelvin-probe [43]
- (ii) the characterization of the single shot coherence properties of the 'Freie-Elektronen-Laser in Hamburg' (FLASH) third harmonic [44] have been carried out in the context of this thesis. We refer to the original publications for further details.

**The thesis is structured as follows.** After this introduction, basic concepts of time resolved x-ray scattering experiments along with basic experimental and technical considerations are reviewed in *chapter 2*. The purpose is to provide, in combination with the literature [45, 37, 34, 46], the information necessary to understand and set up time resolved experiments in line with the experiments performed within the context of this thesis.

*Chapter 2* provides details on the generation of Surface Acoustic Waves 2.1, the sample preparation protocols 2.2 as well as details on specular and diffuse x-ray scattering from lipid multilayers 2.3. Fundamentals of x-ray scattering will not be described in this thesis, only advanced details necessary for the understanding of the data analysis routines will be discussed. We refer to the literature [47, 32] for a more detailed introduction to the scattering phenomena under discussion.

*Chapter 3* presents a conceptually new detection mechanism for time resolved x-ray scattering experiments and further applications requiring framing rates of up to 31MHz. A first fully functional prototype based on a quadrant avalanche photodiode is presented and extensive commissioning experiments at the synchrotron Petra III, Desy, Hamburg are described.

The knowledge provided in *chapter 2* is then used in *chapter 4* in the context of ultrafast dynamics in lipid bilayers as stimulated by the acousto-electric field of standing SAWs. Synchrotron experiments characterizing SAWs of Rayleigh type on piezoelectric  $LiNbO_3$  substrates are described in section 4.2, before experimental details along with the analysis of the structural response of lipid bilayers to SAW excitation are presented in section 4.3.

*Chapter 5* focuses on experiments at the in house femtosecond x-ray source (section 4.4) and two experiments at the beamline ID09B at the European Synchrotron Radiation Facility (ESRF) in Grenoble, France (sections 4.4 and 5.1.5) using pulsed laser excitation. These experiments can be further subdivided into two groups, depending on the sample character (chromophore labeled 5.1.5 vs. unlabeled lipids 4.4) and the substrate material used (quartz glass 5.1.5 vs. silicon substrates 4.4). Finally, *chapter 6* summarizes the main results presented in this dissertation.

# 1 Time resolved x-ray scattering - Experimental requirements, instrumentation and timing

*An experimental technique capable of probing ultrafast, especially electric field or light induced, molecular dynamics is necessarily accompanied by two major experimental challenges: i) Temporal resolution on the picosecond time scale is needed in order to probe non equilibrium effects ii) The outlined effects involve structural changes on the sub-nm length scale. Therefore, ultrafast temporal resolution has to be combined with sub-Å ('molecular') spatial resolution. Time resolved x-ray diffraction (TRXD) [34] combines both requirements and has therefore been used for a broad range of experiments focusing on the structural evolution of solid state [48, 35] and organic (including biological) systems [37, 46] after short pulse excitation.*

*Basic concepts of time resolved x-ray scattering experiments are introduced in this chapter (section 1.1), experimental details related to the generation and timing of short x-ray pulses (section 1.1) as well as the setup at the beamlines P08 (section 1.3) (Petra III, Hamburg) and ID09B (section 1.4) (ESRF, Grenoble) are reviewed. Concepts presented in this chapter are not limited to elastic diffraction experiments but are also applicable to inelastic scattering techniques (e.g. nuclear resonant scattering and x-ray spectroscopy [EXAFS, NEXAFS [49]]).*

## 1.1 A typical pump-probe experiment

The basic principle of a time resolved scattering, or 'optical pump – x-ray probe', experiment focusing on the light driven out of equilibrium dynamics of lipid multilayers is sketched in figure 1.1.

1. Membrane dynamics are excited (or pumped) by a short (fs to ns) laser pulse.
2. The instantaneous sample structure is probed by a short x-ray pulse at a well defined time delay  $\Delta t$  after the excitation.
3. The pump-probe scheme is repeated in a stroboscopic fashion at a fixed time delay  $\Delta t$  until a suitable signal to noise ratio is achieved.

In the special case of very high x-ray intensities (e.g. at a Free Electron Laser source) a single x-ray pulse may be sufficient to collect structural information for a given time delay with high resolution. A variation of  $\Delta t := t$  now allows to follow the structural evolution after short pulse excitation.

The observable quantities are in the case of a diffraction experiment the position  $\vec{q}(n, t)$ , integrated intensity  $II(\vec{q}(n, t), t)$  and lineshape of individual reflections  $n$  as a function of temporal delay  $t$ . Let us shortly discuss how processes on the atomistic scale translate to changes in the scattering pattern based on four basic examples in order to facilitate an intuitive understanding of the experiment, see figure 1.2. The entire information content of the more complicated specular- and

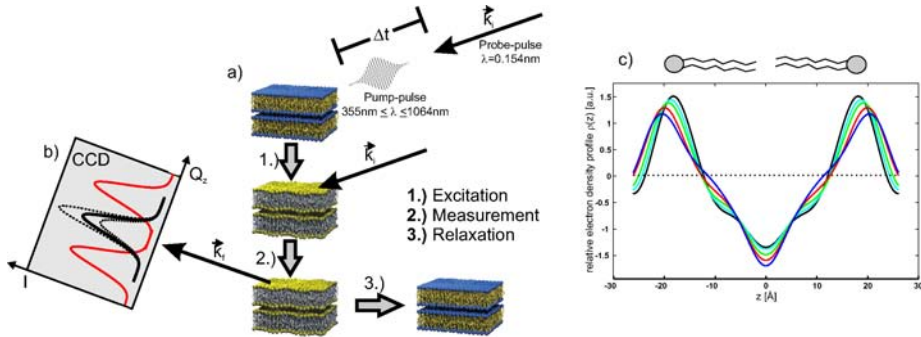


**Figure 1.1:** a) Schematic of a laser pump / x-ray probe measurement on a multi lamellar lipid stack. The temporal evolution of the specular and diffuse scattering b) is observed to deduce information about the lamellar periodicity, the bilayer structure c) on a molecular scale as well as the undulations in response to the non-equilibrium excitation.

diffuse scattering patterns of a multi lamellar lipid bilayer will be discussed in section 2.3.

- Figure 1.2 a) Heat effects lead to an increased mean square displacement  $\sigma$  of the crystal lattice. The reflected intensity  $II(\vec{q}(n, t), t)$  decreases according to the *Debye-Waller factor*  $\exp(-q^2(n, t)\sigma^2(t))$ .
- Figure 1.2 b) Homogeneous deformations  $d(t)$  of the lattice planes (e.g. thermal expansion) lead to positional variations of the reflections  $\Delta q(n, t)$ .
- Figure 1.2 c) Acoustic phonons lead to sidebands next to the reflection of the undistorted crystal lattice. The wavelength of the excited phonon can be inferred from the positions of the satellite peaks.
- Figure 1.2 d) The lineshape of a reflection is determined by the *structure factor*  $S(\vec{q}, t)$  of the crystal lattice. Lineshape variations therefore reflect changes in the lattice sum or in the correlation functions.

Due to limitations related to synchrotron beamtime, sample degradation and the typically low flux of pulsed x-ray sources (at low repetition rates of approximately 1kHz) it is generally desirable to limit experimental degrees of freedom to a minimum. Time resolved diffraction experiments are hence more than often performed with a convergent or divergent x-ray beam, fully illuminating the intrinsic angular width  $\Delta\theta$  of the reflection under observation without angular scanning. This situation is sketched in 1.3 for the situation of a scattering experiment from a multilayer system at a point like x-ray source, e.g. the plasma x-ray source (PXS) described in section 1.1. The angular width (acceptance angle)  $\Delta\theta$  of the reflection is over



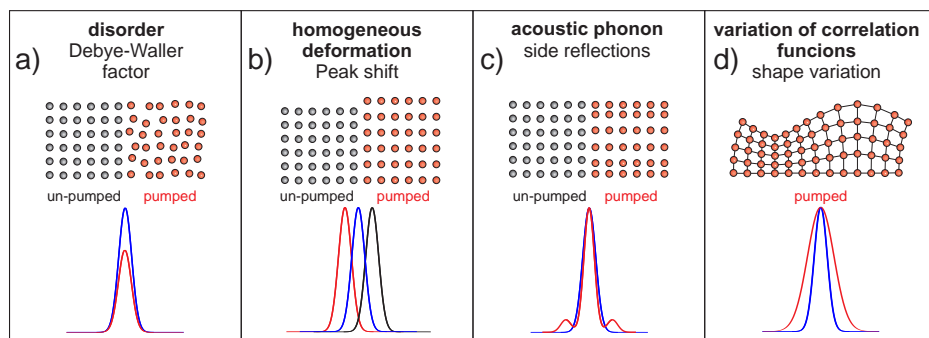


**Figure 1.2:** Structural variations on the atomic scale translate to characteristic variations of the lineshape, intensity and position of individual reflections as sketched for an arbitrary regular lattice. Pure heat effects (a) can well be distinguished from homogeneous deformations (b), acoustic phonons (c) or modified correlation functions (d) as detailed in the main text. Adapted from [36].

illuminated by the effective divergence  $\Delta\alpha_i$  of the x-ray beam, positional changes as well lineshape variations of the reflection can hence be observed without angular scanning. Numbers given in 1.3 are valid for a typical scattering geometry at the PXS and a multi lamellar lipid bilayer, see section 1.1 for details. The requirement for a convergent x-ray beam is an import design consideration for choosing the optimal x-ray optics for time resolved experiments [50].

Another approach to relax the need for angular scanning is to use the polychromatic (‘white’) beam of an undulator [51]. X-ray induced radiation damage is however a major concern when following this approach, especially in the case of soft matter sample systems.

Lipid multilayers under conditions of nearly full hydration are especially well suited for time resolved diffraction experiments as they exhibit a pronounced diffuse scattering signal which contains a rich spectrum of informations on both molecular structure [30, 31, 52, 53] and interactions [32, 54, 55] as addressed in section 2.3. The diffuse scattering signal is accessible at a fixed angle of incidence.

Given a source delivering short x-ray pulses (see sections 1.1, 1.3 and 1.4), a suitable timing mechanism (see sections 1.3 and 1.2.4) and a sophisticated x-ray scattering setup (see sections 3.3, 4.4 and 5.1.2) one major hurdle remains: An excitation mechanism resembling the physiologically relevant or otherwise interesting situation has to be found. Additional constraints on the excitation mechanism are:

1. It has to be non destructive (except for the special case of single shot experiments).
2. It has to provide a homogeneous excitation of the probed sample volume (‘spatial overlap’).

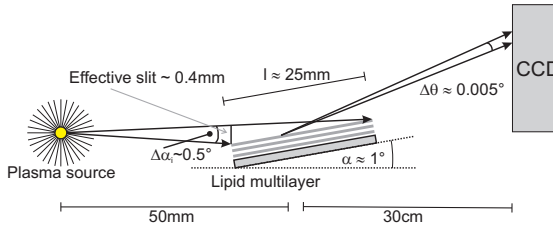


**Figure 1.3:** Sketch of a basic x-ray reflectivity experiment from a multilayer system at a point like x-ray source. When the effective angular divergence  $\Delta\alpha_i$  of the incident x-ray beam exceeds the angular width  $\Delta\theta$  of the observed reflection, positional as well as lineshape variations can be detected without changing  $\alpha_i$ . Numbers are valid for a typical scattering geometry at the in house plasma x-ray source and a multi lamellar lipid bilayer, see section 1.1 for details.

3. Temporal jitter has to be minimized, the time-zero has to be well definable ('temporal overlap').

The second constraint is a special concern in the case of laser excitation of powder like or highly absorbing samples [45] since the absorption / extinction length of laser light and x-ray radiation differ generally by orders of magnitude. These issues will be addressed in sections A.1.1, 2.1 and A.1.2. Further experimental challenges related to thermal drift and denaturing of the sample system due to the high peak powers of the pumping laser will be discussed in the chapters 3.3, 5.1.2 and 4.4.

## 1.2 In house femtosecond x-ray generation: The plasma x-ray source (PXS)

With the advent of commercial high intensity pico- to femtosecond laser systems the generation of ultra short x-ray pulses at in house sources became possible, a broad range of sources has evolved ranging from the soft- to the hard x-ray regime. Among the most prominent techniques are higher harmonic generation [56, 57], gas based laser plasma sources [58] and laser plasma sources using solid state targets [59, 60, 61, 62, 63], all being based on high intensity short pulse laser systems. As the outlined biophysical questions require spatial resolution in the sub-angstrom range we will focus on the latter one, producing femtosecond pulsed hard x-ray radiation. For the following discussion we will refer to 'plasma x-ray source, PXS' as the name of the actual in house instrument in the central laboratory of the Courant Research Center 'Nano spectroscopy and x-ray imaging', Göttingen. Where given, product names and exact values do refer to the setup of the PXS.

The basic operating principle of a plasma x-ray source applying solid state targets is to tightly focus a high intensity laser beam onto the target material ( $d = 20\mu\text{m}$  copper foil in the case of the PXS) where a hot plasma is generated. The

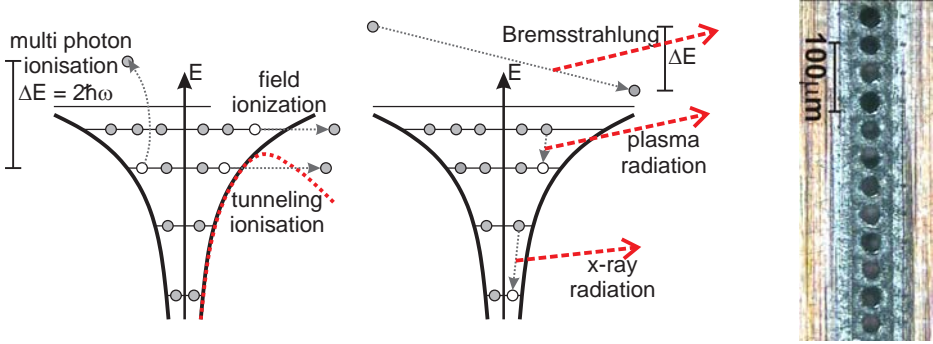


**Figure 1.4:** *Left:* A hot plasma can be generated by intense femtosecond laser pulses, the primary laser–target interaction is strongly dependent on the laser intensity. Adapted from [64]. **Right:** A rough estimation of the source size of a laser plasma source can be made from the hole diameter on the target material. In the case of the in house PXS the diameter is approximately  $33\mu\text{m}$ .

free electrons in the hot plasma are heated by the intense laser light, producing Bremsstrahlung as well as characteristic x-ray radiation just like in a conventional x-ray tube. In the case of solid state targets, laser peak intensities  $P_p \geq 10^{18}\text{W}/\text{cm}^2$  are needed in order to generate a significant amount of characteristic x-ray radiation. These peak intensities are commercially only available with femtosecond laser systems.

### 1.2.1 X-ray generation in laser induced plasmas

Depending on the peak intensity  $P_p$  and hence associated electric field  $E_l = \sqrt{\frac{2P_p}{c\epsilon_0}} \approx 27.4\sqrt{P_p}$  ( $P_p$  in  $[\text{W}/\text{m}^2]$ ,  $E$  in  $[\text{V}/\text{m}]$ ) of the femtosecond laser pulses, the primary laser target interaction is mediated by different pathways, see figure 1.4 left. X-ray generation is in all cases either based on inelastic scattering of free electrons ('Bremsstrahlung') or characteristic radiation due to the ionization of atoms. In order for characteristic inner shell radiation to be generated the kinetic energy of the electrons has to exceed the inner shell ionization energy of the target material ( $E \approx 8.8\text{keV}$  for copper). Given a photon energy of  $E \approx 1.55\text{eV}$  in case of a  $\lambda = 800\text{nm}$  Ti:Sa femtosecond laser system, x-ray generation is necessarily a three step process, independent on the exact reaction pathway:

1. The target material is ionized (outer shell ionization).
2. Free electrons are then further heated by the high intensity laser pulses.
3. Inner shell ionization occurs due to impact ionization.

Basic comments on the most important mechanisms governing the intensity regimes  $P_p \geq 10^{10} \text{W/cm}^2$  are meant to facilitate the understanding of the working principle of a plasma x-ray source, see additionally figure 1.4 a). We refer to the literature (e.g. [64, 65]) for a detailed description.

**$P_p \approx 10^{10} \text{W/cm}^2$**  Single- and multi photon ionization dominates for peak intensities  $P_p \approx 10^{10} \text{W/cm}^2$ . The probability for a  $n > 2$  photon ionization is negligible, low energy free electrons are however heated by inelastic scattering with optical photons ('inverse-Bremsstrahlung') leading to electron temperatures  $\geq 2 \cdot \hbar\omega$ . As the work function of copper is approximately 4.4eV, ( $\gg 2 \cdot 1.55\text{eV}$  for  $\lambda = 800\text{nm}$ ) a significant degree of ionization and characteristic radiation are not expected in this intensity regime.

**$P_p \geq 10^{12} \text{W/cm}^2$**  For  $P_p \geq 10^{12} \text{W/cm}^2$  the strong electric field associated with the laser pulses leads to an asymmetric distortion of the potential barrier of the target atoms (see figure 1.4 a)) leading to field ionization as well as tunneling ionization.

Free electrons can be regarded as an oscillator in the high frequency AC electric field of the incident laser light, their kinetic energy ('ponderomotive energy') is accordingly given by  $E_{kin.} = \frac{e^2 E_l^2}{4m\omega^2}$ .  $\omega$  and  $E_l$  denote the frequency and amplitude of the electric field,  $e$  and  $m$  are the elementary charge and relativistic mass of the free electrons. The kinetic energy is  $E_{kin.} = 5\text{eV}$  for  $P_p = 10^{14} \text{W/cm}^2$  and  $E_{kin.} = 5\text{keV}$  for  $P_p = 10^{17} \text{W/cm}^2$ , significant inner shell ionization is therefore not expected for  $P_p \ll 10^{17} \text{W/cm}^2$ .

**$P_p \approx 10^{16} \text{W/cm}^2$**  At intensities  $P_p \approx 10^{16} \text{W/cm}^2$  collective resonant absorption phenomena start to become prominent. Coulomb repulsion between free electrons counteracts electromagnetic forces due to the electric field of the laser, leading to plasma waves at a resonant frequency of  $\omega_p = \sqrt{\frac{n_e e^2}{m\epsilon_0}}$ .  $\omega_p$  is, apart from prefactors, singularly given by the plasma density  $n_e$  which for a tightly focused laser beam decays exponentially as a function of distance from the focal spot. At some distance from the focal spot  $\omega_p$  matches the frequency of the laser light ( $\omega = 3.7 \cdot 10^{14} \text{Hz}$  for  $\lambda = 800\text{nm}$ ), leading to resonant absorption processes and hence a strong increase of electron energy.

**$P_p \geq 10^{18} \text{W/cm}^2$**  Relativistic electron acceleration occurs for  $P_p \geq 10^{18} \text{W/cm}^2$ . The oscillation energy of an electron nearly reaches it's rest energy for  $P_p \approx 3 \cdot 10^{18} \text{W/cm}^2$ , the velocity of the electron is now  $v \approx c$  resulting in strong Lorenz- and ponderomotive forces perpendicular to the electric field. The high energy free electrons are accelerated towards the target, hard x-ray radiation is generated as inner shell radiation and Bremsstrahlung.

Pulse energies of  $E_p \leq 8\text{mJ}$  at pulse widths of  $\tau \approx 50\text{fs}$  are regularly achieved in commercially available femtosecond laser systems at 1kHz repetition rate. When focused to a  $\varnothing 10\mu\text{m}$  spot, peak intensities of  $P_p = \frac{8\text{mJ}}{50\text{fs} \cdot \pi \cdot (5\mu\text{m})^2} = 2 \cdot 10^{17} \text{W}/\text{cm}^2$  are achieved. Resonant and relativistic absorption processes are therefore expected.

### 1.2.2 In house setup for time resolved x-ray scattering at the PXS

The heart piece of the setup for time resolved hard x-ray diffraction in the central laboratory of the Courant Research Center is the high energy Ti:Sa femtosecond laser system (Legend Elite Duo, Coherent, Santa Clara, USA). It generates pulses with a pulse duration of  $\tau \leq 50\text{fs}$  at a repetition rate of 1kHz, each pulse has an energy of  $E_p \leq 8\text{mJ}$ . The general setup including the laser, the PXS and additional optical elements related to the control of the pump- and probe pulses is sketched in figure 1.5.

The high energy laser beam is expanded to a diameter of approximately 2cm directly behind the high energy laser system in order to reduce the peak intensity  $P_p$  to a minimum and hence prevent optical damage of subsequent optical elements. Furthermore non-linear optical effects (e.g. self-focusing) strongly compromise the beam quality of high intensity laser pulses, see e.g. [66]. The first optical element after the high energy laser system is a beam splitter, guiding 80% of the laser pulse energy to the PXS. 20% of the pulse energy is used for optical pumping, the 'pump part' of the setup will be described in section 1.2.3.

The laser pulses are ultimately focused onto the copper target by an off axis parabolic mirror (gold coated, Edmund Optics) with a focal length of 12cm, see figure 1.5. Directly in front of the PXS the beam is expanded to a diameter of  $d \approx 5\text{cm}$  in order to increase the numerical aperture of the off axis parabolic mirror (.). Furthermore, in order to allow for a tight focusing of the high intensity laser directly onto the target surface a vacuum chamber is needed, plasma formation in air would otherwise occur far in front of the beam waist. The laser beam enters the vacuum chamber through a 1mm thin  $\varnothing 5\text{cm}$  anti reflective coated quartz glass window. A rough estimation of the minimal achievable focal size  $w_0$  in this configuration yields  $w_0 = \frac{1.22\lambda f}{nd} \approx 2.5\mu\text{m}$  where  $n = 1$  is the index of refraction in air or vacuum.

As each laser pulse destroys the target in a localized region near the focal spot (see figure 1.4) the target material has to be constantly refed. Different approaches have been proposed in order to solve this issue, including wire based solutions [67, 61] and the use of liquid metal jets [63, 68]. In the case of the PXS a  $20\mu\text{m}$  thin and 2cm wide copper tape is used. The copper tape is constantly refed at a speed of approximately 5cm/s by a pair of spools, allowing each laser pulse to hit a fresh spot on the copper surface at a 1kHz repetition rate, see figure 1.6. In order to prevent the entrance and exit windows of the vacuum chamber from contamination with molten copper ('debris') two  $30\mu\text{m}$  thin Mylar foils are guided parallel to the target tape and serve as debris protection. See figure 1.6 (left) for a photo of the interior of the PXS. More than the capacity of the copper spools, the significant amount of debris is the limiting factor for the maximum continuous operation of

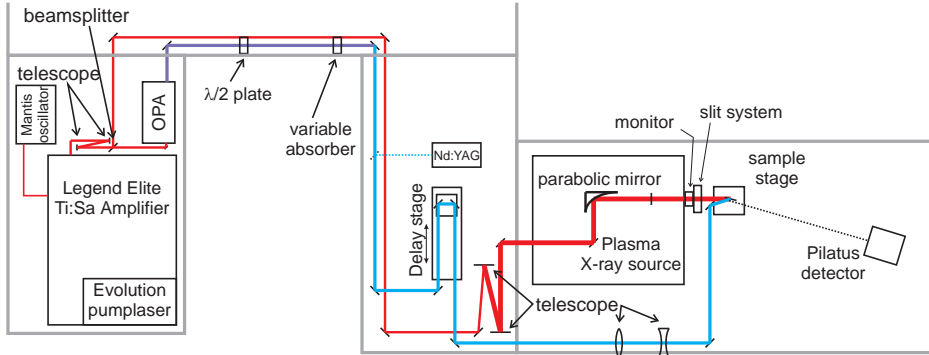


**Figure 1.5:** Rough sketch of the time resolved hard x-ray scattering setup at the PXS. Femtosecond laser pulses are generated and amplified in the Mantis laser oscillator and the Legend Elite Duo laser amplifier. The laser beam is split directly behind the laser amplifier. 80% of the pulse energy is used for x-ray generation (red), 20% are available for optical pumping (blue). An Optical parametric amplifier (OPA) provides a frequency conversion of the pump pulses. Wavelength adjustable half wave plates, variable attenuators and telescopes can be used for beam steering and polarization control. An external Nd:YAG laser can be used in order to study slowly relaxing dynamics on the nanosecond to microsecond timescale.

the PXS. After a maximum of approximately 6h the contamination of debris tapes and ball bearing does hamper a stable operation. Two photos of the PXS are presented in figure 1.6.

The alignment procedure aims for a tight focusing of the high energy laser pulses and hence a maximization of the laser intensity at the surface of the copper tape. A valuable indicator for the quality of the alignment is the extension and shape of the laser focus parallel to the optical axis as obtained by scanning the laser focus parallel to the direction of propagation through the copper tape, see 1.7 (b). The x-ray intensity is in this case monitored with an ionization chamber (JJXray, see appendix A.1.3) at a distance of 5cm behind the laser focus, a misalignment would manifest itself in a distorted shape of the focus, e.g. distinct side maxima in case of an astigmatism. The (polychromatic) primary x-ray flux as detected by the ionization chamber is approximately  $10^{10}$  cps/ $4\pi$ , see section A.1.3 for details. This value is consistent with estimations made at the hand of x-ray scattering experiments, see section 4.4.

The Bremsstrahlung of laser plasma generated x-ray radiation differs significantly from the spectrum of a conventional x-ray tube. An exponential decay of the spectral intensity as a function of photon energy  $E$  is observed [69] rather than a well defined cutoff as for a conventional x-ray tube. Although not a concern for the actual scattering experiment, the high energy Bremsstrahlung background up to photon energies of  $E \geq 150$ keV has to be taken into account for the design process

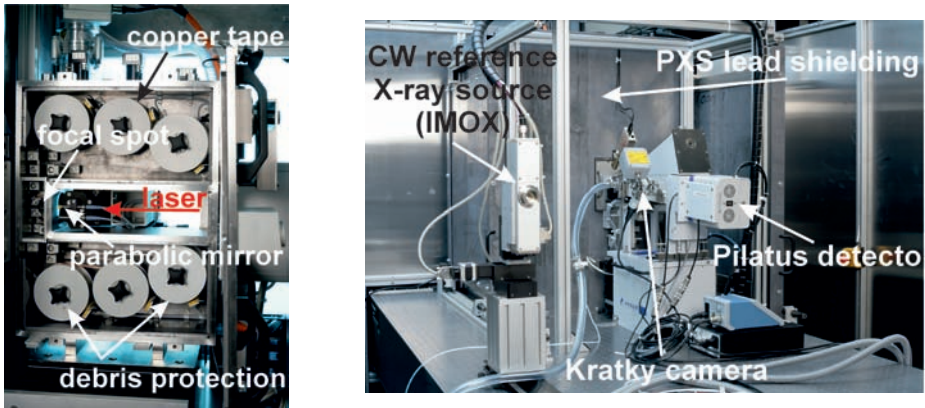


**Figure 1.6:** *Left:* Photo of the vacuum chamber of the in house laser plasma source (PXS). High intensity laser pulses enter the chamber from the right, the off axis parabolic mirror provides a tight focus on the surface of the copper tape. Additional debris protection prevents the optical elements from getting contaminated. *Right:* A dedicated small angle scattering (SAXS) setup ('Kratky-camera') can be used in conjunction with a Pilatus detector at the PXS to record low noise high resolution SAXS data. A standard micro focus x-ray tube is available for reference experiments in combination with the Kratky camera.

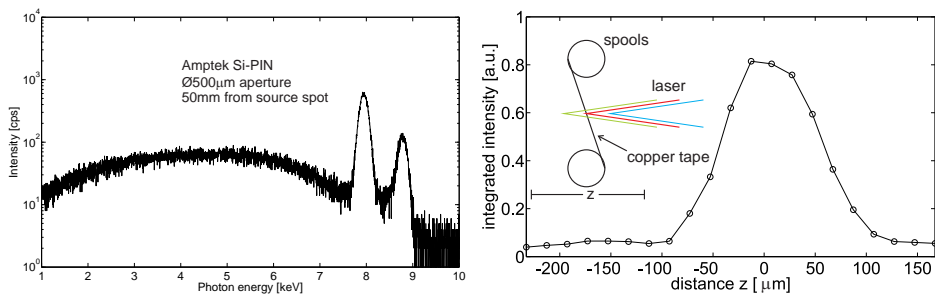


**Figure 1.7:** *Left:* The x-ray spectrum of the PXS as measured with a Amptek X-123 silicon drift detector at a distance of approximately 10cm from the source spot. The maximal intensity of the characteristic  $\text{Cu-K}_\alpha$  and  $\text{Cu-K}_\beta$  lines is a factor of approximately 50 higher than the Bremsstrahlung background. *Right:* Integrated x-ray intensity as a function of focal position in the direction parallel to the laser beam. Maximal intensity corresponds to a perfect overlap between copper tape and laser focus.

laser energy	$E_p \leq 8\text{mJ}$
laser pulse duration	$\tau \approx 50\text{fs}$
laser intensity	$P_p \approx 2 \cdot 10^{17}\text{W}/\text{cm}^2$
laser wavelength	$\lambda = 800\text{nm}$
polychromatic x-ray flux	$10^{10}\text{cps}/4\pi$
x-ray source size	$\approx 30\mu\text{m}$
x-ray pulse duration [59]	$100\text{fs} \leq \tau \leq 500\text{fs}$

**Table 1.1:** Typical specifications and main operating parameters of the PXS.  
The x-ray source size has been estimated based on figure 1.4 (right).

of the radiation safety lead shielding.

A direct measurement of the pulse duration of laser plasma generated x-ray pulses is not possible until now. Standard optical auto-correlation methods [66] can not be transferred to x-ray science in a straight forward manner as a splitting of the x-ray beam is non-trivial and non-linear effects are too small at the achievable intensities, conventional streak camera techniques are limited to pulse widths  $\geq 100\text{fs}$  [70] and ultrafast beam characterization techniques evolving due to the advent of Free Electron Lasers usually require highly brilliant x-ray beams [71, 72] or a highly complex experimental infrastructure (e.g. THz-generation [73]). It has however been shown indirectly by pump probe experiments on solid state sample systems, that the pulse duration obtained for the described setup lies within the range of  $100\text{fs} - 500\text{fs}$  [36, 59].

Basic operating parameters and benchmark specifications as obtained for the PXS are summarized in table 1.1.

### 1.2.3 Optical excitation mechanisms available at the PXS

A basic optical-pump x-ray-probe scheme can be realized by splitting the high intensity femtosecond laser beam, see figure 1.5. Depending on the required pump intensity, a percentage of approximately 80% of the pulse energy is used to generate x-ray radiation (red in figure 1.5), 20% of the pulse energy is used to optically excite the sample system (blue in 1.5). The temporal delay  $t$  between both pulses is set by introducing a geometric path length difference. At the PXS a motorized delay stage (IMS600PP, Newport) with a travel range of approximately 60cm delays the beam by a maximum of  $\Delta t = 1.20m/c \approx 4ns$ , the mechanical step width of  $1\mu\text{m}$  corresponds to a temporal step width of  $\Delta t \approx 3\text{fs}$ . Temporal accuracy is therefore only limited by the precision of the temporal overlap since electronic jitter is fully eliminated in this operating mode.

In a straight forward implementation the optical wavelength  $\lambda = 800\text{nm}$  of the pump pulses is fixed by the wavelength of the femtosecond laser system. However, it is in some cases highly desirable to match the pump wavelength  $\lambda$  to specific absorption properties of e.g. active proteins or chromophores. In the case of the PXS, wavelength conversion is achieved by an Optical Parametric Amplifier



	Ti:Sa	OPA (Topas)	Nd:YAG
wavelength	$\lambda = 800\text{nm}$	$530\text{nm} \leq \lambda \leq 1600\text{nm}$	$\lambda \in [355\text{nm}, 532\text{nm}, 1064\text{nm}]$
pulse duration	$\tau \approx 50\text{fs}$	$\tau \approx 50\text{fs}$	$\tau \approx 1\text{ns}$
pulse energy	$E_p \leq 1.5\text{mJ}$	$E_p \leq 350\mu\text{J}$	$E_p \in [50\mu\text{J}, 50\mu\text{J}, 220\mu\text{J}]$
delay range	$50\text{fs} \leq t \leq 4\text{ns}$	$50\text{fs} \leq t \leq 4\text{ns}$	$1\text{ns} \leq t \leq 1\text{ms}$

**Table 1.2:** Optical excitation mechanisms available at the PXS. Timescales from the 100fs range up to the 1ms scale, corresponding to on ten orders of magnitude, are accessible without any gaps.

(OPA, TOPAS, Light conversion, San Francisco, USA) which effectively provides a frequency conversion from the  $\lambda = 800\text{nm}$  fundamental wavelength of the Ti:Sa femtosecond laser to a continuously variable output wavelength  $530\text{nm} \leq \lambda \leq 1600\text{nm}$ . The tuning curve of the OPA is highly complex, a maximum of 25% of the incident pulse energy is converted to the desired output wavelength. The pulse duration is not affected by the frequency conversion process, we refer to the TOPAS manual for further details.

An external Nd:YAG laser with a pulse duration of  $\tau \approx 1\text{ns}$  (Pulseas HP, Alphalabs, Göttingen) can be used in combination with a dedicated timing system (see figure 1.2.4) in order to study slowly relaxing dynamics in between  $1\text{ns} \leq t \leq 1\text{ms}$ . The fundamental wavelength of a Nd:YAG laser is  $\lambda = 1064\text{nm}$ , the Pulseas laser at the PXS can be frequency doubled as well as frequency tripled allowing for laser excitation at  $\lambda_2 = 532\text{nm}$  and  $\lambda_3 = 355\text{nm}$ . Depending on the wavelength, the achievable pulse energy is  $E_p \geq 220\mu\text{J}$  for  $\lambda = 1064\text{nm}$ ,  $E_p \geq 50\mu\text{J}$  for  $\lambda = 532\text{nm}$  and  $E_p \geq 50\mu\text{J}$  for  $\lambda = 355\text{nm}$ .

The broad wavelength range  $355\text{nm} \leq \lambda \leq 1600\text{nm}$  available for optical pumping in combination with high intensity laser beams has to be considered when choosing optical elements for the pump beam path. In contrast to optical elements in the probe beam path where the wavelength is fixed to  $\lambda = 800\text{nm}$ , it is generally advantageous to use optical elements without special anti reflective coating in the probe beam path.

The temporal overlap between pump- and probe pulses is in each case confirmed by a fast photodiode with a rise time of approximately 30ps (Alphalabs, Göttingen) in combination with a high bandwidth oscilloscope (Tektronix DPO4104B, bw  $\geq 1\text{GHz}$ ). The copper tape can in this case easily be removed in order to detect the attenuated (usually x-ray generating) laser pulses on the photodiode. No significant delays due to the x-ray generation process are expected.

The experimental setup at the PXS leads to a huge parameter range achievable in time resolved diffraction experiments. Ultrafast dynamics can be studied on ten temporal orders of magnitude ( $100\text{fs} \leq t \leq 1\text{ms}$ ), a broad range of laser parameters (different wavelengths  $\lambda$ , pulse lengths  $\tau$  and intensity regimes) is achievable with only minimal adjustments. The various possibilities for optical excitation are summarized in table 1.2.

### 1.2.4 The timing system at the PXS

**Generation and amplification of femtosecond laser pulses** An understanding of the timing scheme at the PXS requires a basic knowledge of the operating principle of the Legend Elite Duo laser system. A detailed explanation is however beyond the scope of this thesis, only a rough sketch of the working principle of a regenerative laser amplifier at the example of the Legend Elite Duo laser system will be given in this context. We refer to the Coherent manual and the literature (e.g. [66]) for details.

Low energy femtosecond laser pulses are generated in a mode locked Ti:Sa laser oscillator (Mantis, Coherent) at a repetition rate of approximately 80MHz. The repetition rate is given by the optical path length ( $l \approx 3.75\text{m}$ ) of the laser resonator and hence subject to thermal fluctuations. Mode locking is furthermore initiated as a spontaneous process, the relative timing of the laser oscillator can in this case not be controlled externally<sup>1</sup>. The timing systems of the femtosecond laser system as well as reference signals for various pump mechanisms at the PXS have to correspondingly be synchronized with a photodiode inside the Mantis laser-oscillator. The laser oscillator is the 'master-clock' of the setup at the PXS.

Low energy femtosecond pulses are amplified in a regenerative laser amplifier (RGA, Legend Elite Duo, Coherent). The layout of the amplifier can be roughly divided into four parts, see figure 1.8: (i) Femtosecond pulses are temporally elongated in a *pulse-stretcher* in order to lower the pulse intensities and hence prevent subsequent optical elements from permanent damage. (ii) Individual pulses are amplified in a regenerative laser cavity. The active medium (Ti:Sa) is pumped at a repetition rate of 1kHz by a high energy Nd:YLF laser system ( $\tau \approx 160\text{ns}$ , cw output power  $P_{cw} \approx 40\text{W}$ , Evolution HE, Coherent). Amplification at higher frequencies is limited by thermal load as well as, up to a reasonable scale, the pulse energy of the pump laser pulses. The inlet and outlet of the laser cavity and therefore the number of amplifying round trips of each laser pulse is controlled by two Pockels cells (see figure 1.8), operating basically as a high speed optical switch. (iii) The pulses exiting the RGA are further amplified in a single pass laser cavity before they are temporally compressed in a laser compressor (iv). It becomes obvious that the exact timing of the Pockels cells and the Evolution pump laser to the pulse train of the laser oscillator is critical for stable operation of the system. Further details on this issue can be found in the Legend Elite manual as well as the PXS manual.

### Timing of external pump lasers and advanced excitation mechanisms

Let us return to the laser pump / x-ray probe experiment. As explained earlier it is straight forward to split and delay the output of the femtosecond laser system in order to perform time resolved experiments using parts of individual pulses for pump and probe. Applying an additional external pump laser (a Nd:YAG laser in the present case) is slightly more complicated as a pretrigger has to be generated

---

<sup>1</sup> A successful approach to control the timing of a mode locked laser oscillator is e.g. based on a variation of the resonator length using piezoelectric actuators [74, 75].

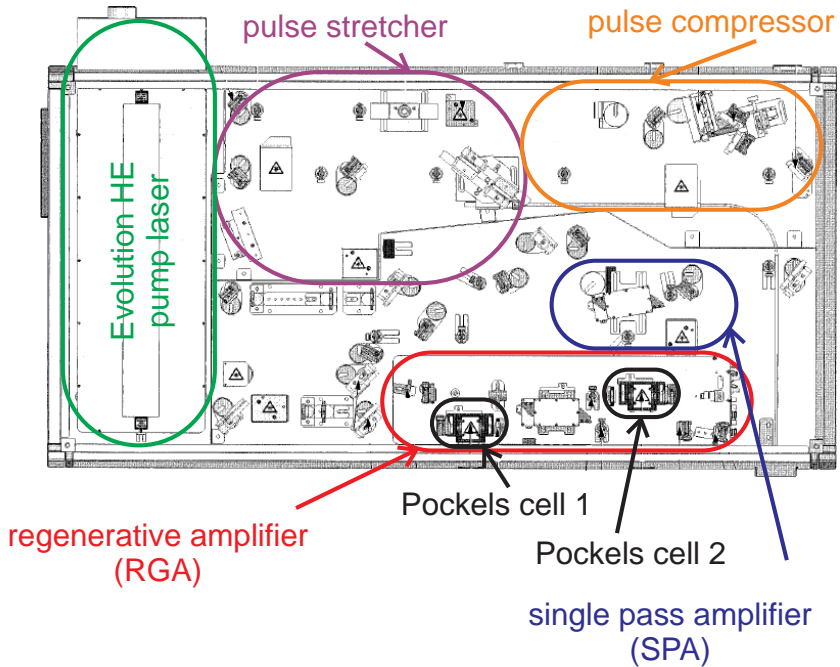


**Figure 1.8:** Schematic setup of the Coherent Legend Elite Duo laser amplifier. Low energy femtosecond laser pulses are stretched, and amplified in a two step process before they are re compressed and emitted at a kHz repetition rate. Pulse energies  $E \geq 8\text{mJ}$  at pulse durations  $\tau \leq 50\text{fs}$  are achieved on a routine basis. Based on the Coherent manual.

– the external laser has to be triggered prior to the laser amplifier in order for the pump- pulses to arrive prior to the probe pulses. It is not possible to directly reference the external pump laser to the amplified laser pulses as the pulse to pulse jitter of the Coherent timing system (Synchronization and Delay Generator, SDG in 1.9) is as large as  $\pm 36\text{ns}$  in the standard operation mode (corresponding to up to three round trips at the oscillator frequency of 80MHz). The timing scheme of the femtosecond laser system had hence to be modified with a home build synchronization unit (HSU), '80MHz laser Sync.' in figure 1.9. The HSU reduces the 80MHz signal of the Mantis oscillator to a 1kHz signal by an integral divider, see figure 1.9 and 1.9. It furthermore produces a 80MHz output signal ('80MHz out' in 1.9) as well as two 1kHz signals which are delayed by  $\Delta t = 10\mu\text{s}$  relative to each other. The 'first' 1kHz signal ('SYNC out' in 1.9) has to have an opening time of exactly  $5\mu\text{s}$  and is used to synchronize the Evolution pump laser, which in turn enables the Pockels cells in the Legend Elite Duo. The delayed 1kHz signal ('Verz. out' in 1.9) is used to trigger a Stanford DG535 delay generator. The DG535 now operates the external Nd:YAG laser (channel 'A' and 'B' in 1.9 for the laser head as well as the pump laser inside the Nd:YAG laser). The delay of the DG535 is adjusted to  $t \approx 990\mu\text{s}$ , so that the pump laser hits the sample *before* ( $t \leq 990\mu\text{s}$ ) or *shortly after* ( $t \geq 990\mu\text{s}$ ) the next Ti:Sa pulse arrives. This way, the Nd:YAG pump laser is effectively pre-triggered in order to allow for pump-probe experiments. The jitter of this setup is below the pulse width of the Nd:YAG pump laser ( $\leq 1\text{ns}$ ).

Additionally a reference signal of approximately 10MHz is provided by the HSU. It is generated from the  $\approx 80\text{MHz}$  repetition rate of the laser oscillator by an integral divider of 8, it is hence phase stable with respect to the oscillator frequency but the exact value is slightly different from an exact 10MHz reference signal. As high precision phase locked loops (PLLs) in high end frequency generators generally require more accurate reference signals (relative precision  $\leq 10^{-6}$ ) in order to synchronize to an external reference, the signal has to be slightly detuned by an 'undemanding' frequency generator (e.g. a Thurlby Thandar TG5001) before it is accepted by standard radio frequency (RF) equipment. See section 1.3 for details on phase locked excitation mechanisms.

### 1.3 Time resolved experiments at P08 / Petra III

As explained earlier, the basic principle of a stroboscopic time resolved experiment is to match the frequency of a cyclic excitation (pump) with the repetition rate of short probe pulses. A precise variation of the time delay  $t$  between pump- and probe pulse allows to sample the dynamics induced by the pump pulse at a high number of time points. The temporal resolution is limited by probe pulse length and the overall jitter of the experimental setup.

The revolution frequency  $f_{rev.}$  of a synchrotron is approximately given by the circumference and the speed of light. More precisely, it depends on the energy  $E$  of the relativistic electrons (or positrons) in the storage ring, which in turn is set by the microwave frequency  $f_{acc.}$  in the accelerating cavities. Furthermore the fill-

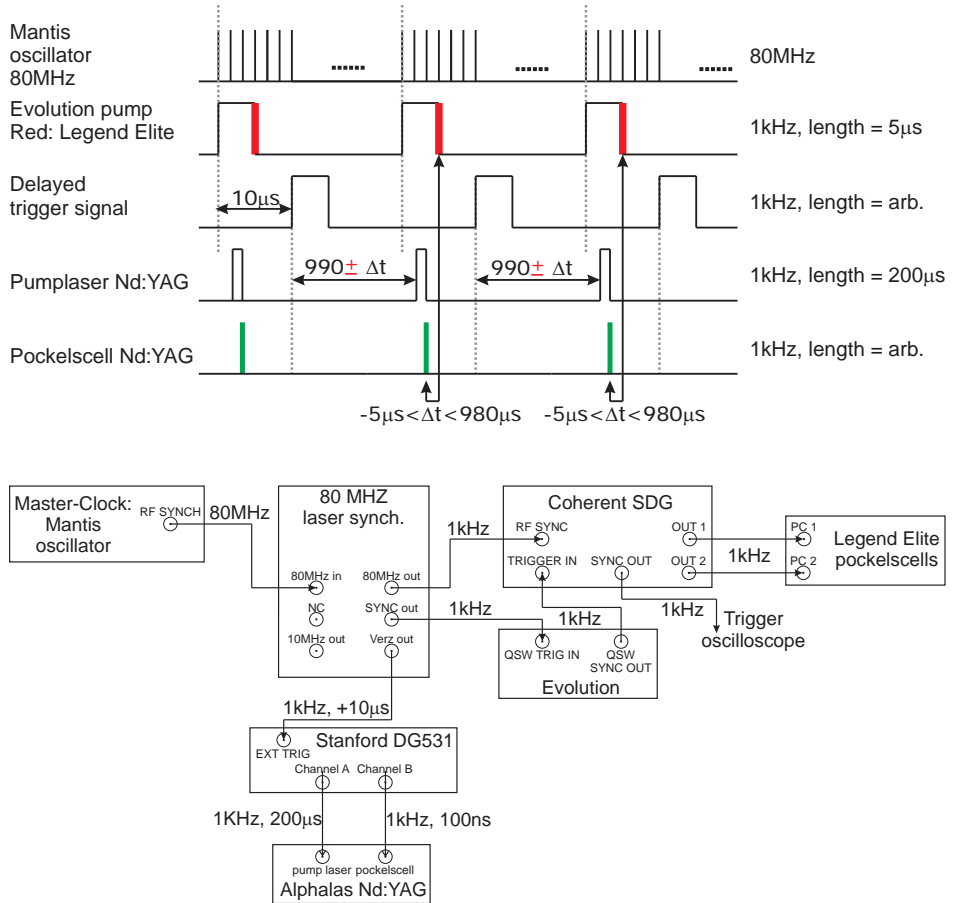


**Figure 1.9: Top:** Timing scheme at the PXS. The Mantis oscillator serves as a master clock operating at a frequency of  $f \approx 80\text{MHz}$ . A  $f \approx 1\text{kHz}$  trigger signal is generated from the master clock by an integral divider in order to synchronize subsequent laser systems as detailed in the text. **Bottom:** Schematic of the actual cabling for time resolved experiments using external pump lasers or advanced excitation mechanisms at the PXS. The 80MHz laser synchronization provides stable trigger signals exactly matched to the requirements of the Coherent Legend Elite Duo laser amplifier.

ing mode of the storage ring determines the repetition rate  $f_b$  of the synchrotron bunches in an actual experiment. For Petra III the circumference of approximately 2304m leads to a revolution frequency of  $f_{rev.} \approx 130.1\text{kHz}$  (microwave frequency  $f_{acc.} \approx 499.564\text{MHz}$ , positron energy  $E \approx 6\text{GeV}$ ) and hence a bunch frequency of  $f_b \approx 5.2\text{MHz}$  in the 40-bunch mode and  $f_b \approx 31\text{MHz}$  in the 240-bunch mode. Note that  $f_{acc.}$  and therefore  $f_b$  are known and stable during each experimental run but may vary by some Hz between succeeding runs (machine alignment / tuning). The temporal structure of Petra III is highly favorable for time resolved experiments since the individual bunches are equally spaced in the the storage ring. No global phase factor or a distinction between individual x-ray pulses is necessary when synchronizing to the synchrotron frequency. Moreover, the temporal spacing of  $\frac{1}{f_b} \approx 192\text{ns}$  between individual x-ray pulses in the 40-bunch mode is long enough for fast gating of modern pixel detectors, such as the Pilatus pixel detector (DeCTRIS) [76], see e.g. 1.11. The pulse duration of individual x-ray pulses is roughly  $44\text{ps}^2$ .

The following discussion will focus on the application of Surface Acoustic Waves (SAWs) as an advanced excitation mechanism for time resolved experiments. Briefly, a SAW is an electro-acoustic wave propagating along the surface of a piezoelectric substrate. It is excited by metallic finger structures (Inter Digital Transducers, IDTs) on top of the surface, standing waves or propagating pulses can be produced. The electric field accompanying the SAW can be used to drive soft matter thin films on top of the piezoelectric substrate out of thermal equilibrium, a detailed description follows in section 2.1.

In order to synchronize a SAW to the synchrotron frequency a modified version of the Petra III bunchclock is used. The bunchclock provides two independent and basically arbitrary integral dividers of the microwave frequency which can be used to synchronize pulsed excitation mechanisms (e.g. pulsed lasers) or to gate modern pixel detectors [76, 77] relative to the bunch frequency  $f_b$  with phase stability. The exact frequency values and operating conditions of the storage ring are distributed to the bunchclock via a frequency modulated 40MHz signal, see figure 1.10 a). Furthermore, a highly stable 10MHz reference signal is distributed to every beamline which can be used to phase lock any external frequency- or delay generator to the synchrotron. This reference signal is generated from the microwave frequency by a rational divider.

These timing capabilities lead to two modes of SAW excitation:

In the first mode, standing SAWs at an integral multiple frequency  $f_{SAW} = n \cdot f_b$  of the bunch frequency are generated by phase locking a frequency generator (SG384, Stanford Research Systems) to the 10MHz reference. This allows for time resolved scattering experiments without the need for a reduction of the effective x-ray frequency and hence flux by gated detectors [76] or high speed choppers [78]. The effective time delay between SAW pump- and x-ray probe pulses is set as a phase  $\phi$  between the synchrotron pulses and the SAW signal directly on the frequency generator. This phase  $\phi$  is constantly monitored by a fast oscilloscope and im-

<sup>2</sup> [https://photon-science.desy.de/facilities/petra\\_iii/machine/parameters/index\\_eng.html](https://photon-science.desy.de/facilities/petra_iii/machine/parameters/index_eng.html)

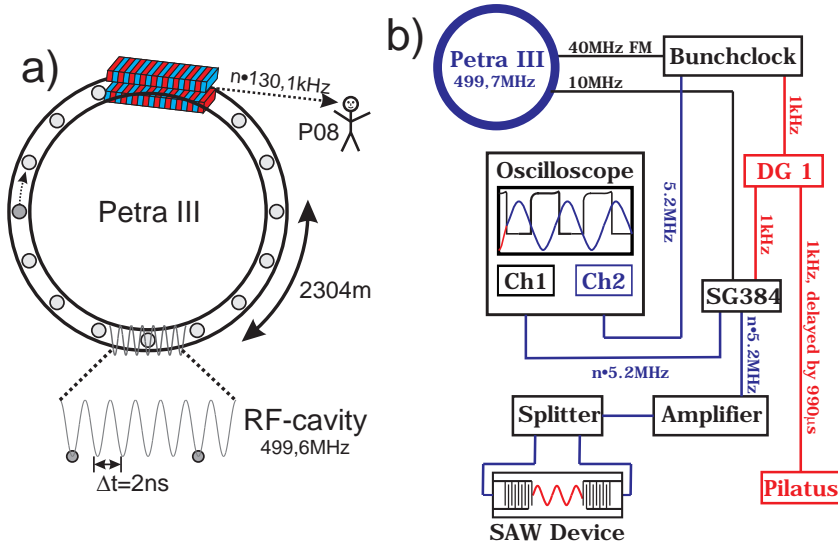


**Figure 1.10:** a) The synchrotron bunch frequency  $f_b$  is determined by the radio frequency  $f_{acc.}$  on the accelerating cavities, the circumference of the storage ring and the filling mode. In the case of Petra III the circumference of 2304 m leads to a revolution frequency of  $f_{rev.} \approx 130.1\text{kHz}$ . b) Schematic of the timing system used for phase matched time resolved x-ray scattering. The Petra III bunchclock provides a signal corresponding to the respective bunch frequency (5.2 MHz in the 40-bunch mode) as well as a variety of preinstalled integral dividers. An accurate 10 MHz signal is used in order to lock a frequency generator (SG384) to the synchrotron frequency. The output from the frequency generator can be pulse modulated by a delay generator (DG1) in order to produce RF pulses, amplified and split in order to generate standing SAWs. Individual x-ray pulses can be selected by gating the Pilatus detector with a second channel on DG1.

plemented as a virtual counter in the measurement and beamline control software (SPEC, Certified Scientific Software). Temporal drift can hence be corrected for during data analysis.

In the second mode, short SAW pulses at any integral divider  $f_{pp} = \frac{f_{acc.}}{499584} \approx 1\text{kHz}$  of the microwave frequency are applied by pulse modulation of the RF source. In order to retain time resolution it is necessary to reduce the effective x-ray pulse frequency to match the pump frequency so that only these x-ray pulses probing the structure at a well defined time delay with respect to the pump pulse are recorded. The advances of modern pixel detectors allow for an ultrafast gating of 2-D detectors at the pump frequency  $f_{pp}$  (in the 40-bunch mode), without the need for high speed choppers. In order to warrant phase stability between the synchrotron frequency  $f_b$  and the pump-probe frequency  $f_{pp}$  a divider of  $\frac{f_{acc.}}{f_{pp}} = 499584$  was chosen as an integral multiple of  $\frac{f_{acc.}}{f_b} = 96$  for the 40-bunch mode, phase stability is thus also provided for the 60-, 240- and 960 bunch modes. It could be demonstrated, that the time window of  $\frac{1}{5.2\text{MHz}} = 192\text{ns}$  between two subsequent x-ray pulses is long enough to select and measure an individual x-ray pulse in the 5.2MHz pulse train by gating a Pilatus 300k 2-d detector with nominally 50ns short TTL pulses at a rate of  $\approx 1\text{kHz}$ , see figures 1.11 and 1.10 (b). In the present case these gate ('probe') pulses have been produced by a Stanford Research Systems, DG535 delay generator (DG1 in figure 1.10 (b)). In addition it was demonstrated that the Pilatus detector can be directly gated by a modified version of the Petra III bunchclock (version 3.07), the duration of the gate pulse is in this case limited to 20ns at TTL level (+5V).

The temporal delay between the gated synchrotron pulse and the modulated SAW pulse, as well as the width of the SAW pulse, are as well controlled by DG1. Note that the effective length of the gate pulse provided by the Stanford Research Systems DG535 as observed by a fast oscilloscope is significantly shorter than 50ns for a  $50\Omega$  output load.

Both pump and gate pulses are referenced to a common trigger signal. In order to allow the pump pulse to be temporally ahead of the gate pulse, a pretrigger has to be generated similar to the situation in section 1.2.4. The gate pulse has therefore been delayed by approximately  $990\mu\text{s}$  on channel one of DG1 and fine tuned so that the gated intensity on the Pilatus detector is maximal, see figure 1.11 (b). For a desired time delay of  $t$  the pump pulse is now delayed by  $990\mu\text{s} - t$  on channel two of DG1 so that the excitation pulse arrives effectively ahead of the gate pulse.

With respect to earlier stroboscopic x-ray scattering experiments on SAWs [79, 80], the accurate control of phase, the extended flexibility of the timing scheme and the seamless integration into the beamline setup and control software significantly enhances the experimental possibilities. The presented timing scheme is not limited to experiments using SAW excitation. It can be applied to a broader range of stroboscopic experiments, using e.g. laser, high voltage or microwave based excitation mechanisms.



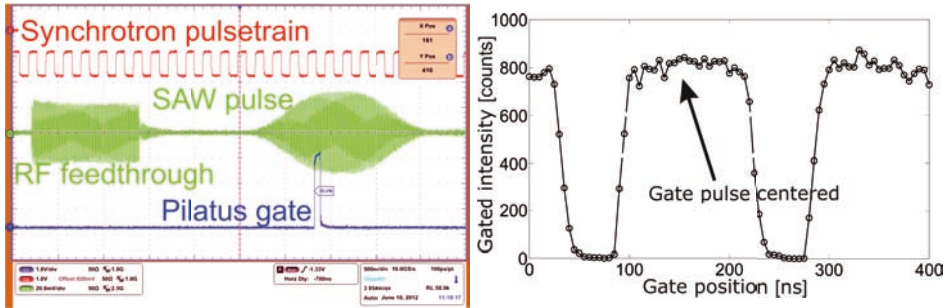


**Figure 1.11:** *Left: Oscilloscope trace taken during a time resolved scattering experiment using pulsed SAW excitation: The RF (SAW)-signal (purple,  $n \cdot 5.2\text{MHz}$ ) is phase stable to both the x-ray pulse train (cyan,  $5.2\text{MHz}$ ) as well as the gate pulses (yellow,  $1\text{kHz}$ ). The two RF pulses can be attributed to RF pickup (left pulse) and the propagating SAW pulse, broadened by the response function of the IDTs (right pulse) **Right:** For  $f_b \leq 6\text{MHz}$  (i.e. in the 40-bunch mode of Petra III) individual x-ray pulses can be selected by gating the Pilatus pixel detector. Any integral divider of  $f_{pp}$  can be used as gate / pump-probe frequency  $f_{pp}$ .*

## 1.4 Time resolved diffraction at beamline ID09B, ESRF

A detailed description of the beamline setup at the ID09B at the ESRF can be found in [78], we will just stick to an informal and brief description of the main experimental requirements.

As in section 1.3 the pulsed nature of synchrotron radiation is used in order to perform precise timing experiments. Depending on the exact operating conditions each electron / x-ray bunch has a pulse duration of  $\tau \leq 48\text{ps}$ <sup>3</sup> which mainly determines the achievable temporal resolution, the synchrotron bunch frequency is  $f_b \approx 5.7\text{MHz}$  in the ESRF 16-bunch mode.

Different from the gating approach outlined in section 1.3 the pulse frequency is reduced to  $f \approx 1\text{kHz}$  by a high speed rotating chopper which is synchronized to the bunchclock of the storage ring, see figure 1.12. Synchronization of pulsed lasers to the opening of this high speed chopper at a variable time delay  $t$  allows for time resolved scattering experiments. This approach has two major advantages over the gating technique outlined in section 1.3: (i) The x-ray flux at the sample position is reduced by a factor of  $\frac{f_{pp}}{f_p} \approx 5700$  depending on the filling mode, the effective flux at the detector equals the flux in the gating approach. X-ray induced beam damage is hence strongly reduced. (ii) Any kind of standard x-ray detector can be used at the ID09B. The requirement for (gateable) single photon counting pixel detectors limits the effective dynamic range to 1 photon/(pixel-pulse) in case of the gating approach. The mechanical and electrical infrastructure of the high speed chopper is however highly complex, it can only be set up at selected

<sup>3</sup> <http://www.esrf.eu/Accelerators/Performance/Performance>

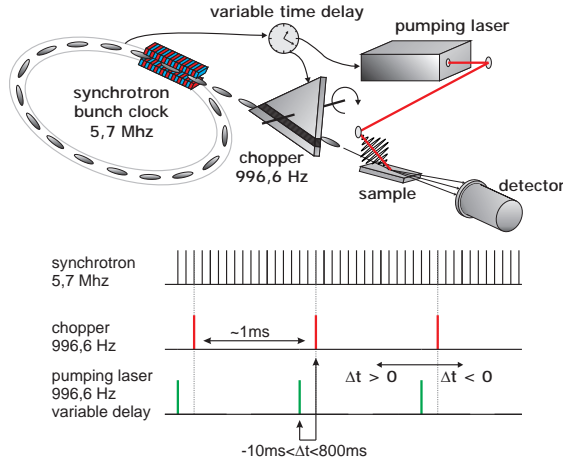


**Figure 1.12:** Simplified schematic of the laser pump x-ray probe setup at the beamline ID09B at the ESRF. A rotating mechanical chopper ( $f = 996.6\text{Hz}$ ) is synchronized to the bunch clock of the ESRF, reducing the  $\approx 5.7\text{MHz}$  synchrotron repetition rate to a frequency suitable for pump probe experiments. It is straight forward to synchronize pulsed lasers to the high speed chopper and to allow for a precise and stable control of the time delay  $t$ . Note that this sketch is a keen simplification, see [78] for a more detailed description.

dedicated beamlines. As the Pilatus detector is widely available at synchrotron sources, setting up the gating approach only involves minimal interference with a standard beamline setup.

A Ti:Sa picosecond laser system ( $\tau \approx 1\text{ps}$ ,  $\lambda = 800\text{nm}$ ,  $E_p \leq 4\text{mJ}$ , (*Legend Elite*, Coherent) is available for optical pumping. Similar to the setup at the PXS (section 1.1) an optical parametric amplifier (*TOPAS*, Light conversion, USA) can be used in order to tune the pumping wavelength. The Nd:YLF *Evolution* pump laser inside the *Legend Elite* can be used as an alternative pump source. It operates at the second harmonic wavelength  $\lambda = 527\text{nm}$ , the pulse duration of  $\tau \approx 160\text{ns}$  leads to mild peak intensities, minimizing laser induced damage (also see section 5.1.2).

The optical pump path can be adapted to meet the requirements of most experiments, the exact optical setup during the respective beamtimes reported on in this thesis will be reviewed in sections 4.4 and 5.1.5. Temporal overlap of laser pump and x-ray probe pulses is confirmed with a fast photodiode using a piece of white synthetic foam at the sample position in order to scatter parts of the x-ray as well as the laser beam. The stray light is then used for synchronization. Spatial overlap is confirmed with a small pinhole mounted in the center of rotation of the goniometer head. In a first step the pinhole is positioned directly in the center of the x-ray beam before the pump laser is adjusted to the fixed pinhole position.

## 2 Materials and Methods

*This chapter provides details on the sample preparation protocols 2.2, the generation of Surface Acoustic Waves 2.1 as well as specular and diffuse x-ray scattering from lipid multilayers 2.3. Basic fundamentals of x-ray scattering are omitted, the focus of section 2.3 lies on the analysis of the in-plane and out-of-plane correlation functions in a multi lamellar lipid stack from the pronounced diffuse scattering patterns. We refer to the literature [47, 32] for a more detailed introduction to the scattering phenomena under discussion.*

*Dedicated SAW devices suitable for the excitation of lipid multilayers and experiments at synchrotron sources have been designed in collaboration with the group of Prof. Dr. Achim Wixforth at the institute for experimental physics I at the university of Augsburg, Germany.*

### 2.1 Surface Acoustic Wave generation

Piezoelectric materials offer the possibility to excite SAWs electrically [81, 82]: A metallic comb-like finger structure is processed onto the surface by optical lithography and a RF voltage is applied to this so-called interdigital transducer (IDT), see 2.1. As the RF signal matches the design frequency  $f_{SAW}^1 = v_{SAW}/L_{SAW}^1$ , which is given by the SAW velocity  $v_{SAW}$  and the finger periodicity  $L_{SAW}^1$  of the IDT, a SAW is excited and propagates along the sound path. In the present experiment this acoustically active region was 1mm wide and was limited by a second IDT at a distance of 8mm, see figure 2.1. This configuration of two opposing IDTs is called 'delay line', as a generated signal at one IDT is received by the other one with a acoustic delay due to the wave propagation. The basic parameters for SAW devices are given by (i) the piezoelectric substrate material and (ii) its crystallographic surface orientation (cut angle) in addition to the propagation direction on this surface. In the experiments presented in section 3.3, we use the very common so called '128° rot. Y cut' of  $LiNbO_3$  as the X direction of this specific cut exhibits one of the highest coupling factors for electrical SAW excitation. However, we used the direction perpendicular to X due to frequency constraints by the timing setup as discussed in section 1.3. The fundamental periodicity of the corresponding IDTs is designed to  $L_{SAW}^1 = 100\mu\text{m}$  and, with  $v_{SAW} \approx 3670\text{m/s}$ , the fundamental frequency to  $f_{SAW} = 36.7\text{MHz}$ . The finite frequency response of the device enables a SAW excitation at the synchrotron-locked frequency  $f_{SAW}^1 = 7 \cdot f_b = 36.4\text{MHz}$ . Due to the layout of the IDTs, odd harmonics of the fundamental frequency can also be excited. In particular, we used the (locked) 5th harmonic  $f_{SAW}^5 = 182\text{MHz}$ , which corresponds to a wavelength of  $L_{SAW}^5 = 20\mu\text{m}$ .

The RF signal driving the IDTs is produced by a SG384 (Stanford Research Systems) RF generator, see figure 2.2. As detailed in section 1.3 standing waves or propagating pulses can be excited by pulse modulation of the RF generator. The RF signal is amplified by a ZHL-42W (Minicircuits) amplifier, standing waves can be generated by splitting the RF signal and simultaneous excitation of two

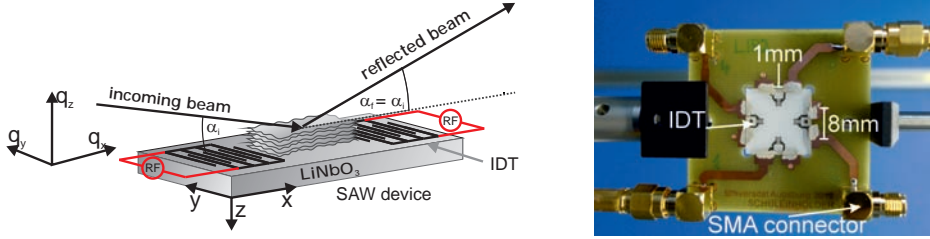


**Figure 2.1:** **Left:** By applying an RF-signal to the interdigital transducers (IDTs) standing waves or propagating SAW pulses can be induced on the piezoelectric  $LiNbO_3$  substrate. **Right:** Photo of a SAW device used in time resolved diffraction experiments. Two pairs of opposing inter digital transducers (IDTs) allow for the excitation of two different modes on a single  $LiNbO_3$  substrate. The dimensions of the sound path are determined by the width of 1mm and the distance of 8mm of the IDTs.

opposing IDTs.

The SAW excited on  $128^\circ$  rot. Y  $LiNbO_3$  in the direction perpendicular to X is a Rayleigh mode, so surface atoms follow an elliptical motion polarized in the sagittal plane (defined by SAW propagation direction and the surface normal, see figure 2.3). The piezoelectricity of the substrate material induces an electric potential  $\Phi$  which is linked to the deformation of the crystal. Both the deformation and  $\Phi$  decay exponentially into the substrate, but notably the electric potential also decays exponentially into the vacuum above the surface, see figure 2.3. As long as the distance from the surface is small compared to the wavelength  $L_{SAW}$ , the electric potential  $\Phi$  and thus the electric field  $E_z = -\partial\Phi/\partial z$  will effect e.g. thin films on the surface. The surface of  $128^\circ$  rot. Y cut  $LiNbO_3$  is parallel to the  $(1,0,4)$  crystal plane (space group  $R3c$ ), leading to a  $d$ -spacing of  $d = 2.737\text{\AA}$  for the first reflection along the  $q_z$  axis (unit cell constants  $a = b = 5.1483\text{\AA}$ ,  $c = 13.863\text{\AA}$ , see e.g.[83, 84]).

Within the framework of linear elasticity, the solution for the atomic displacements  $u_{1,2,3}$  and the electric potential  $\Phi$  of a surface wave propagating in  $x_1 \equiv x$  direction can be written as a superposition of  $m \leq 4$  partial waves [82] with the index  $j \in \{1, 2, 3\}$ :

$$u_j = \sum_m C_m \alpha_j^{(m)} \exp(i(kx_1 - \omega t)) \exp(ikb_m x_3) \quad \text{for } : z \leq 0 \quad (2.1)$$

$$\Phi = \sum_m C_m \alpha_4^{(m)} \exp(i(kx_1 - \omega t)) \exp(ikb_m x_3) \quad \text{for } : z \leq 0 \quad (2.2)$$

$$\Phi = \sum_m C_m \alpha_4^{(m)} \exp(i(kx_1 - \omega t)) \exp(-kx_3) \quad \text{for } : z \geq 0. \quad (2.3)$$

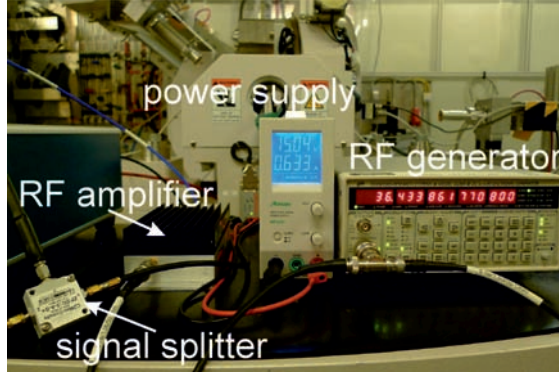


**Figure 2.2:** Photo of the most important parts of the electronic setup used for SAW generation. The RF signal is provided by a SRS SG384 RF generator and amplified by a Minicircuits ZHL-42W RF amplifier. Standing waves can be generated by splitting the RF signal and simultaneous excitation of two opposing IDTs.

These expressions solve the coupled wave equations of a piezoelectric solid [82]

$$\rho \frac{\partial^2 u_j}{\partial t^2} = c_{ijkl} \frac{\partial^2 u_k}{\partial x_i \partial x_l} + e_{kij} \frac{\partial^2 \Phi}{\partial x_i \partial x_k} \quad (2.4)$$

$$\epsilon_{ij} \frac{\partial^2 \Phi}{\partial x_i \partial x_j} = e_{ijk} \frac{\partial^2 u_j}{\partial x_i \partial x_k} \quad (2.5)$$

with  $\rho$  being the mass density of the substrate. The amplitudes  $\alpha_j^{(m)}$  and the values  $b_m$  depend on the elastic  $c$ , piezoelectric  $e$  and permittivity tensors  $\epsilon$  of the substrate, the weighting factors  $C_m$  are chosen to satisfy boundary conditions for surface waves. This typically works only for one specific velocity  $v$  which is the Surface Acoustic Wave velocity  $v_{\text{SAW}}$ . By calculating  $\alpha$ ,  $C$  and  $b$  the electric field  $E_z = -\frac{\partial \Phi}{\partial z}$  can be computed (see figure 2.3). Assuming a vertical displacement of 1nm at  $f_{\text{SAW}} = 37\text{MHz}$  (as justified by the analysis in section 4.2.5), the electric field at the surface is approximately calculated to  $E_z = 2 \cdot 10^5 \text{V/m}$ .

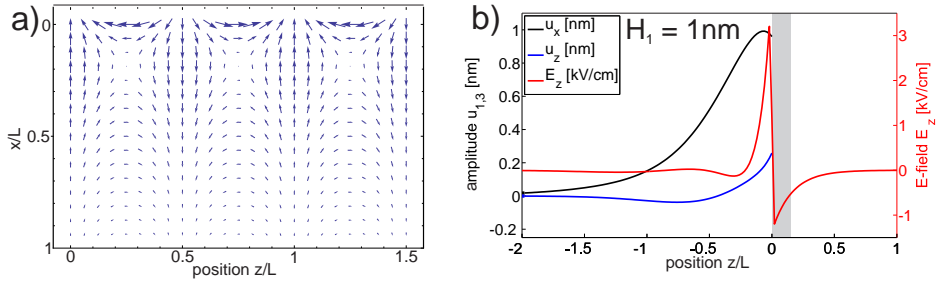


**Figure 2.3:** a) Vector representation of the wave field  $[u_1(x, z), u_3(x, z)]$  of a Rayleigh type Surface Acoustic Wave for  $L = 100\mu\text{m}$ ,  $v_{SAW} = 3670\text{m/s}$ . The coefficients  $C_m$ ,  $\alpha_j$  and  $b_j$  have been taken from the literature [82]. b) Vertical  $u_3(z)$  and longitudinal  $u_1(z)$  SAW amplitudes as well as the electric field  $E_z = -\frac{\partial\varphi}{\partial z}$  as a function of depth ( $z$ ) in the  $128^\circ$  rot. Y LiNbO<sub>3</sub> substrate for an amplitude of  $H_1 = 1\text{nm}$  and a frequency of 36.4MHz. The SAW penetration depth is approximately given by the wavelength  $L$ , the evanescent electric field penetrates a distance of approximately  $0.12 \cdot L$  ( $1/e$  length) into the free space above the substrate well including the multilamellar lipid stack as sketched in shaded gray.

In a more general description, higher order terms have to be included in the linear mechanical and electrical coefficients, leading to a broad range of non-linear acoustic phenomena [85]. Most important for the current discussion is the generation of second and third order acoustic harmonics. A basic theoretical treatment of higher order elasticity effects [85] predict second and third order acoustic harmonics of amplitude  $H_{2,3}$

$$\frac{H_2}{H_1} = 2\pi n \lambda_2 \frac{\omega H_1}{v_R} \quad (2.6)$$

$$\frac{H_3}{H_1} = 4\pi^2 n^2 \lambda_3 \left( \frac{\omega H_1}{v_R} \right)^2, \quad (2.7)$$

where  $n$  is the number of wavelengths in the SAW resonator and  $\lambda_{2,3}$  are complex constants taking into account the crystal orientation and the second and third order elasticity constants of the substrate. For  $H_1 = 1\text{nm}$ ,  $\omega = 2\pi f_{SAW}^1 = 229\text{MHz}$  and  $v_R = 3670\text{m/s}$  the leading term is on the order of  $\frac{\omega H_1}{v_R} \approx 6 \cdot 10^{-5}$ , quasi monochromatic waves are hence assumed from now on.

In order to confirm this assumption experimentally, electric measurements of the SAW spectrum have been performed with a Hameg HMS1000 spectrum analyzer. One IDT of the SAW device has been stimulated by the RF-electric field provided by a SRS SG384 signal generator in combination with a Minicircuits ZHL42W RF-amplifier, the second identical IDT has been used as receiver for the propagated SAW. It can be confirmed that the generation of second and third order harmonics is strongly intensified with increasing  $P_{SAW}$ , their relative amplitudes however are found being three orders of magnitude below the amplitude of the first har-

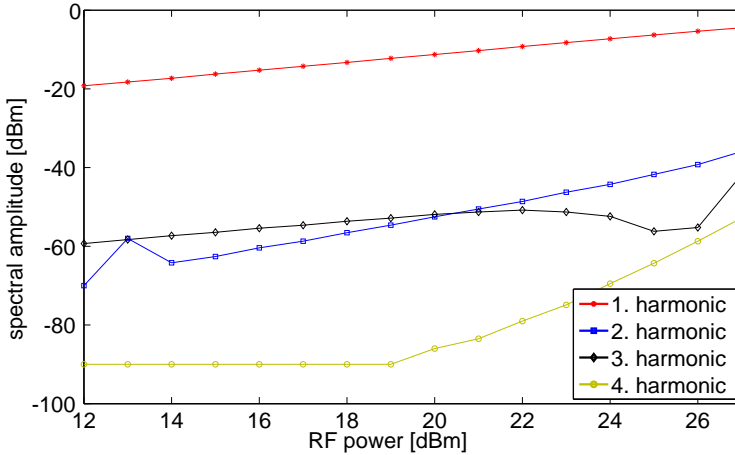


**Figure 2.4:** The frequency response of the SAW device as measured with a Hameg HMS1000 spectrum analyzer does not show any noticeable preferred generation of higher harmonic frequencies.

monic frequency. Note that the generation and detection at even harmonic SAW frequencies is suppressed by the *Split4* geometry of the IDTs.

## 2.2 Sample preparation and environments

The general sample preparation protocol is nearly the same for all presented experiments, only minor adjustments had to be made to meet the requirements of time resolved x-ray scattering experiments using pulsed laser- or SAW excitation mechanisms.

Highly oriented multilamellar lipid stacks deposited on solid substrates were prepared following the procedure described by Seul and Sammon [86]. Pure *1,2-Dioleoyl-sn-glycero-3-phosphatidylcholine* (DOPC) and *1,2-Diphytanoylsn-glycero-3-phosphatidylcholine* (DPhPC) was purchased from Avanti Polar Lipids (Alabaster, AL, USA) and used without further purification. Texas-red labeled *1,2-Dihexadecanoyl-sn-Glycero-3-Phosphoethanolamine* (DHPE) was purchased from Invitrogen Life Technologies Ltd (Paisley, UK). Lipids were dissolved in a 1:1 mixture of 2-2-2-trifluoroethanol (TFE) and chloroform at a concentration of 10mg/ml, mixed at the desired concentrations and carefully spread onto the well leveled substrates. After slow evaporation under a laminar flux hood at room temperature remaining traces of solvent have been eliminated in a vacuum chamber ( $p \approx 1\text{mbar}$ ,  $T \approx 20^\circ\text{C}$ ). Prior to the experiments samples were stored in a fridge ( $T \approx 6^\circ\text{C}$ ) in order to prevent sample degradation.

**Lipid multilayers on  $\text{LiNbO}_3$  SAW devices** The  $\text{LiNbO}_3$  SAW devices were repeatedly rinsed with methanol followed by ultra pure water (specific resistivity

$\geq 18\text{M}\Omega$ , Millipore, Bedford, MA) and drying under nitrogen flow. The amount of spread solution was  $100\mu\text{l}$ , well covering the  $15 \times 15\text{mm}^2$  substrate surface.

In preparatory in-house x-ray experiments we consistently observed that the width of the rocking curve (see e.g. figure 4.11) of the multilamellar samples was significantly larger than for an identical preparation protocol using silicon or quartz glass substrates. This finding may be attributed to tension and curvature of the  $500\mu\text{m}$  thin  $\text{LiNbO}_3$  substrate, induced by mounting the substrate into the SAW device and the metallic structures (IDTs, marker) on the sample surface. Also, a larger footprint of the x-ray beam might partly illuminate the lipid covered IDT area. Furthermore ultrasonic cleaning of the substrates surface could not be performed due to a possible damaging of the IDT structures.

Samples were kept at room temperature ( $T \approx 20^\circ\text{C}$ ) in a dedicated sample environment during the experiment. The relative humidity (RH) was fixed to  $RH \approx 100\%$  by adding ultra pure water to a small reservoir next to the sample surface. Samples hydrated by water vapor are generally very convenient to handle and provide a strong specular scattering signal due to the effective suppression of membrane undulations. Absorption and refraction of the pump beam in the surrounding media are also avoided. Two  $10\mu\text{m}$  thin Mylar foils (Goodfellow, Oakdale, USA) have been used as x-ray entrance and exit windows.

**Pure and Texas-red labeled lipid multilayers on solid support** In order to study / exclude thermal effects induced by heating the substrate with the pumping laser two different types of substrates have been used. Polished Si-wafers ((100) orientation, thickness  $d = 600\mu\text{m}$ ,  $15 \times 25\text{mm}^2$  and  $10 \times 15\text{mm}^2$ ) were purchased from Silchem (Freiberg, Germany), polished quartz glass wafers ( $d = 600\mu\text{m}$ ,  $10 \times 15\text{mm}^2$ ) were purchased from Hellma, Jena. All substrates were carefully cleaned by two 15 min. cycles of ultrasonic cleaning in methanol, followed by two 15 min. cycles in ultra pure water (specific resistivity  $\geq 18\text{M}\Omega$ , Millipore, Bedford, USA) and drying under nitrogen flow. The substrate surface has been rendered hydrophilic in a plasma cleaner (Harric PDC-002). The amount of spread solution has been  $220\mu\text{l}$  in case of the  $15 \times 25\text{mm}^2$  wafers and  $100\mu\text{l}$  in case of the  $10 \times 10\text{mm}^2$  wafers.

Unlabeled lipid mixtures have been deposited on Si and quartz glass substrates. Texas-red labeled lipids have been mixed at Texas-red mole fractions ( $\%TR$ ) of 5, 3 and 1. In order to exclude thermal effects induced by a heating of the substrate due to the pumping laser quartz glass has been used as a solid support.

In the case of silicon substrates strong thermal effects for pumping laser wavelengths  $\lambda \leq 1300\text{nm}$  are expected, silicon is nearly transparent for  $\lambda \geq 1300\text{nm}$  [87]. Glass substrates are transparent throughout the achievable wavelength range. See figure 2.5 for photos of both sample types.

**Sample environments for the observation of laser excited structural dynamics** Two conceptional different sample environments have been used throughout the optical-pump x-ray probe experiments.

Figure 2.6 a) shows a sample cell used for time resolved scattering experiments





**Figure 2.5:** Photos of the samples used in the time resolved diffraction experiments using pulsed laser excitation. **Left:** Unlabeled DOPC multilayers on polished Si wafers. **Right:** Texas-red labeled DOPC multilayers at a Texas-red-DHPE mole fraction (%TR) of 5.

on lipid multilayers hydrated by water vapor. Laser pump- as well as x-ray probe beam enter the chamber through three  $10\mu\text{m}$  thin Mylar windows (Goodfellow, Oakdale, USA). A quasi collinear as well as a perpendicular excitation geometry can be achieved. Relative ambient humidity (RH) can be adjusted by adding saturated salt solutions to a small reservoir next to the sample surface [53]. Samples hydrated by water vapor are generally very convenient to handle and provide a strong specular scattering signal due to the effective suppression of membrane undulations. Absorption and refraction of the pump beam in the surrounding media is generally not an issue.

On order to reduce possible remaining hydration related artifacts to an absolute minimum, samples have been kept in direct contact with liquid water during the experiments presented in sections 5.1.2 and 5.1.5, see figure 2.6 b). The sample chamber is made of Teflon throughout, entrance and exit windows for optical pump and x-ray probe beam are made from  $10\mu\text{m}$  thin Mylar foils. In addition to drift related advantages, this chamber allows for a controlled variation of osmotic stress and salt concentration. Osmotic stress can be applied by adding a solution of Polyethylene glycol (PEG, molar weight 20000u) and water at a defined w:w ratio. PEG(20000) is a clear, white synthetic material and fully soluble up to concentration of approximately 54% wt.. Due to the comparatively big size of this molecule, it is not able to penetrate the lipid bilayer. It therefore acts as an osmotic stressor and efficiently suppresses membrane fluctuations [88].

As detailed in appendix A.1.3 a thin film diffraction chamber inspired by [89] has been used for preliminary experiments on lipid multilayers in direct contact with liquid water using Cu- $K_\alpha$  radiation at the PXS. These experiments are otherwise hindered by strong x-ray absorption in liquid water.

## 2.3 Specular and diffuse scattering from lipid multilayers

For lipid multilayers on solid support, the individual bilayers are highly aligned with respect to the substrate surface (periodicity  $d$ , typical mosaicity  $\leq 0.01^\circ$ ). In the physiological most relevant lamellar phase no long ranged in-plane order can be observed, lipid multilayers are regarded as two dimensional liquid crystals

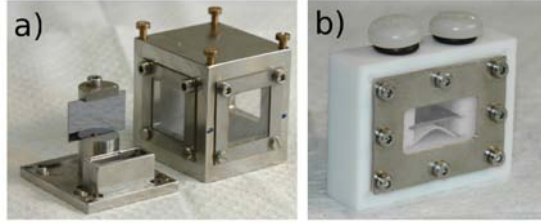


**Figure 2.6:** *a)* Sample cell used for time resolved scattering experiments on ('dry') lipid multilayers hydrated by water vapor. Relative ambient humidity can be adjusted by saturated salt solutions, x-ray as well as laser radiation enters through  $10\mu\text{m}$  thin Mylar windows. *b)* A precise variation of osmotic stress and salt concentration can be achieved in a dedicated ('wet') sample cell. The reservoir can be filled through inlets above the sample, absorption of laser radiation in liquid water is negligible at (near) visible laser wavelengths.

(fluid bilayers) [90]. Because of this 2d ordered nature a precise distinction between momentum transfer parallel ( $q_r = \sqrt{q_x^2 + q_y^2}$ ) and perpendicular ( $q_z$ ) to the bilayer surface can be made in a general x-ray scattering experiment, see figure 2.7. The high order perpendicular to the sample surface as well as the macroscopic flatness leads to sharp Bragg reflections at  $q_z = n \frac{2\pi}{d}$  along the  $q_z$  axis in a specular scattering geometry. Here  $d$  is the bilayer periodicity and  $n$  denotes the order of reflection. Additionally the presence of undulation- and peristaltic modes on the microscopic length scale leads to a prominent diffuse scattering signal as discussed in section 2.3.2.

The scattered intensity distribution  $I(q_r, q_z)$  of a multilamellar lipid sample is expressed in terms of the one dimensional (in case of lamellar phases) form factor  $F(q_z) = \mathcal{F}(\rho(z))$  as the Fourier transform  $\mathcal{F}$  of the vertical single bilayer electron density profile  $\rho(z)$ , the structure factor  $S(q_r, q_z)$  describing the multilamellar order and the Debye-Waller factor  $\exp(-q_z^2 \sigma^2)$  for a given mean-square fluctuation amplitude  $\sigma$ . Note that the Debye-Waller factor is included in  $S(q_r, q_z)$  in most notations, it will however be instructive in sections 3.3 and 5.1.2 to separate the term  $\exp(-q_z^2 \sigma^2)$  from  $S(q_r, q_z)$ .

It can be seen [92, 93] that for a set of multiple rough interfaces the structure factor  $S(q_r, q_z)$  can be separated into a specular  $S_{\text{spec.}}(q_z)$  as well as diffuse part  $S_{\text{diff.}}(q_r, q_z)$ .

$$I(q_r, q_z) \propto \exp(-q_z^2 \sigma^2) \cdot F(q_z) \cdot S(q_r, q_z) \quad (2.8)$$

$$= \exp(-q_z^2 \sigma^2) \cdot F(q_r, q_z) \cdot (S_{\text{spec.}}(q_z) + S_{\text{diff.}}(q_r, q_z)). \quad (2.9)$$

The specular structure factor  $S(q_z)$  in 2.8 is given by the lattice sum reflecting the macroscopic flatness of the individual surfaces and the well defined lattice

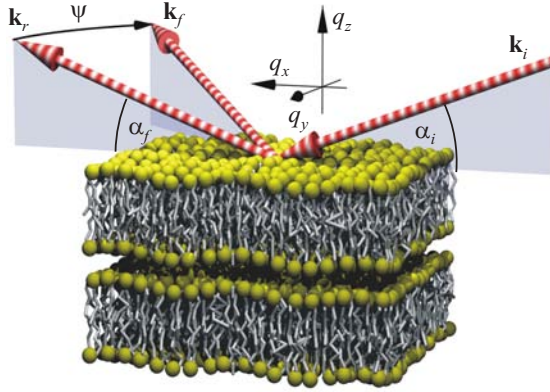


**Figure 2.7:** General geometry of a x-ray scattering experiment from lipid-multilayers. The wave vectors of the incident and exit waves have been labeled with  $\vec{k}_i$ ,  $\vec{k}_r$  and  $\vec{k}_f$ . From [91].

constant, see section 2.3.1. The rich information content contained in the diffuse structure factor  $S_{\text{diff}}(q_r, q_z)$  is addressed in section 2.3.2.

Specular and diffuse contributions to the scattering pattern can be separated experimentally by adjusting the angle of incidence  $\alpha_i$  such that the specular reflected x-ray beam falls in between successive diffraction orders, see figure 2.8. By this way (typically strong) specular scattering is effectively suppressed and the (typically weak) diffuse scattering component can be observed.

### 2.3.1 Specular scattering from lipid multilayers

For a multilamellar lipid stack the relative vertical electron density profile  $\Delta\rho(z)$  can be reconstructed from the integrated Bragg peak intensities  $I(0, q_z(n))$  and the corresponding positions  $q_z(n)$  as obtained from a standard reflectivity measurement by the well known Fourier synthesis approach [94, 95].

$$\Delta\rho(z) = \sum_n \nu_n \sqrt{I_{\text{corr.}}(q_z(n))} \cos(q_z(n) \cdot z). \quad (2.10)$$

Here  $I_{\text{corr.}}(q_z(n))$  denotes the Lorentz-, polarization- and illumination corrected integrated intensity (see e.g. [95]) of the n'th order Bragg reflection. The initially unknown relative phase factors  $\nu_n \in [-1, +1]$  can be reconstructed by e.g. the swelling method [96], reference data for a broad range of lipid model systems is readily available [30, 31]. Details on the Fourier synthesis approach as well as the application of the swelling method to lamellar and non-lamellar lipid phases are extensively reviewed in [53, 52, 97].

It has been shown by Huang and coworkers [98, 99] that the integral of the modulus squared of the continuous bilayer form factor  $F|(q_z)|^2$  equals the sum over

all observable form factor amplitudes squared  $F(q_z(n))^2 = I_{corr.}(q_z(n))$  and is furthermore inversely proportional to the bilayer periodicity  $d$

$$\int |F(q_z)|^2 dq_z = \frac{2\pi}{d} \sum_n F(q_z(n))^2. \quad (2.11)$$

For small changes of  $\Delta\rho(z) = \mathcal{F}^{-1}(F(q_z))$  the left side of 2.11 is approximately constant. Equation 2.11 is therefore used in sections 4.3 and 5.1.2 to normalize e.g. time resolved diffraction data.

Because the higher order specular scattering intensity is strongly reduced by membrane fluctuations a reflectivity experiment aiming for maximum spatial resolution is best done on slightly dehydrated and therefore 'rigid' samples. Membrane fluctuations can efficiently be suppressed by applying osmotic stress onto the lipid bilayer, either by decreasing the relative ambient humidity to  $RH \leq 100\%$  or by adding an osmotic stressor (e.g. PEG) to an aqueous environment.

### 2.3.2 Diffuse scattering from lipid multilayers

A multilamellar stack of lipid bilayers can be regarded as a system of smectic-A liquid crystalline symmetry, it's free energy describable by the well known linearized smectic free energy functional  $H$  (Hamiltonian) [100, 101]. The compressional and bending modes of the smectic liquid crystal are mainly influenced by the elastic coefficients  $K = \kappa/d$  and  $B$ .

The geometrical shape of the  $i$ 'th fluctuating bilayer in the membrane stack can be characterized in terms of the vertical displacement  $u_i(\vec{r})$  with respect to a flat surface at  $z = i \cdot d$ ,  $\vec{r}$  being the vector in the x-y plane of the  $i$ 'th bilayer. The characteristic height-height displacement correlation functions

$$g_{ij}(\vec{r}) = \langle [u_i(\vec{r}) - u_j(\vec{r} + \vec{r})]^2 \rangle \quad (2.12)$$

fulfilling the boundary conditions of the lipid stack can be calculated from  $H$ , external forces can be included in  $H$  by suitable model assumptions [102, 17]. It is convenient to define the height-height pair correlation function  $c_{ij}(r)$  as

$$c_{ij}(r) = \langle u_i(\vec{r})^2 \rangle + \langle u_j(\vec{r})^2 \rangle - g_{ij}(\vec{r}) = \langle u_i(\vec{r})^2 u_j(\vec{r} + \vec{r})^2 \rangle. \quad (2.13)$$

$c_{ij}(\vec{r})$  is usually split into self  $c_{ii}(\vec{r})$  and cross-correlation terms  $c_{i=j}(\vec{r}) = c_z(z)$ , for radial symmetric distributions is is then reasonable to set  $\vec{r} = r$ . In the case of 'thick' ( $N \approx 1000$ ) multilamellar films it is furthermore reasonable to omit the well characterized  $i$  dependence [54] of  $c_{ii}(r) \equiv c_r(r)$ , effectively neglecting the boundary regions of the stack. This yields

$$c_r(r) = \langle u(\vec{r})^2 \rangle + \langle u(\vec{r})^2 \rangle - g_r(r) = 2\sigma^2 - g_r(r). \quad (2.14)$$

A mere exponential damping  $c_z(z) \propto \exp(-q_r^2 \Lambda z)$  on a typical length scale of  $\xi_z = \frac{1}{q_r^2 \Lambda}$  depending on the radial wave number  $q_r$  of the undulation as well as the smectic penetration length  $\Lambda$  is assumed for the cross correlation terms.

Smectic elasticity theory predicts a logarithmic correlation function  $c_r(r)$  for infinite bulk systems [100], the shape being characterized by a lineshape parameter  $\nu = \frac{\pi k_B T}{2d^2 KB}$ . Finite size effects and the boundary conditions of a flat substrate modify the logarithmic divergence by a cut-off, resulting in a finite lateral correlation length of undulations  $\xi_r$  [54].

Regardless of the exact functional form of  $c_r(r)$  and  $c_z(z)$  the in-plane and out of plane correlations can be described by  $\nu$  in case of  $c_r(r)$  as well as four fundamental length scales, see also figure 2.8.

1. The smectic penetration length  $\Lambda = \sqrt{K/B}$  determines the vertical length scale over which a localized corrugation decays as a function of depth in the bilayer stack.
2.  $\xi_z \propto \frac{1}{\Lambda q_r}$  denotes the vertical correlation length of a  $q_r$  distorting Fourier mode. We will refer to the unscaled length scale  $\xi_z \propto \frac{1}{\Lambda}$  for the following discussion.
3. The in-plane correlation length  $\xi_r$ .
4. The rms fluctuation amplitude  $\sigma = \langle_i \langle u_i(\vec{r})^2 \rangle \rangle$  of the bilayer / water interfaces.

In the case of strong fluctuation amplitudes (small bending rigidity  $\kappa \lesssim 10k_B T$ , typically under conditions of full hydration) and oriented bilayers these length scales and basic scaling parameters can be inferred from diffuse x-ray scattering patterns by a full lineshape analysis [93, 55].

As already shortly touched, the diffuse intensity distribution can be described by a structure factor  $S(q_r, q_z)$  measured as a function of parallel  $q_r = \sqrt{q_x^2 + q_y^2}$  and vertical  $q_z$  momentum transfer with respect to the plane of incidence. A detailed derivation of the diffuse structure factor of a softly correlated rough multilayer system can be found in [92, 93] yielding

$$S_{\text{diff.}}(q_z, q_r) \propto \frac{1}{q_z^2} \sum_{i,j}^N e^{-q_z^2 \sigma_i \sigma_j} e^{-iq_z(i-j)d} \epsilon_{i,j}(q_z, q_r) \quad (2.15)$$

$$\epsilon_{i,j}(q_z, q_r) = \int dr r (e^{q_z^2 c_{ij}(r)} - 1) J_0(q_r r), \quad (2.16)$$

where  $J_0(q_r r)$  is the zeroth order Bessel function of the first kind. Data analysis routines aiming for the detailed characterization of the in-plane and out of plane correlations are based on a two step process.

**In plane correlations** In a first step a  $q_z$  integration of  $S(q_r, q_z)$  covering the first Brillouin zone  $q_z(n) \pm \frac{\pi}{d}$  around the  $n$ 'th order diffuse reflection leads to a bilayer averaged structure factor  $S(n, q_r)$  [103], see 2.9. For  $q_r$  greater than a characteristic cutoff  $q_r^*(n) = \frac{2\pi}{\xi_r}$  and  $q_z \sigma \leq 1$ ,  $S(n, q_r)$  can be understood as the Fourier

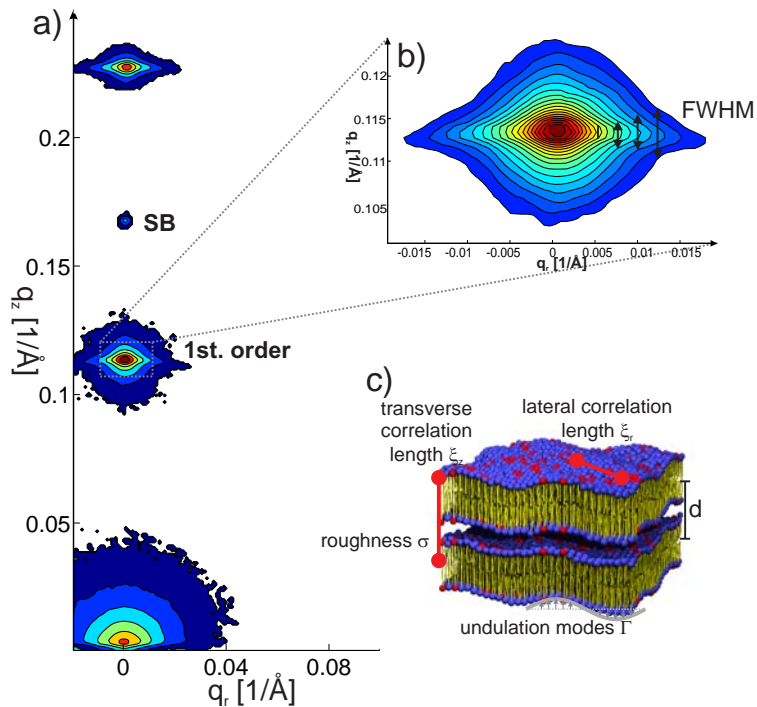


**Figure 2.8:** a) The diffuse scattering pattern of a multilamellar lipid stack is dominated by pronounced diffuse reflections 'Bragg-sheets' (BS) centered around  $q_z(n) = \frac{2\pi}{d}$ , the specular beam (SB) is centered between the first and second order. b) A full lineshape analysis of the individual reflections provides details on structural properties as well as lateral  $\xi_r$  and transverse  $\xi_z$  correlation lengths as sketched in c).

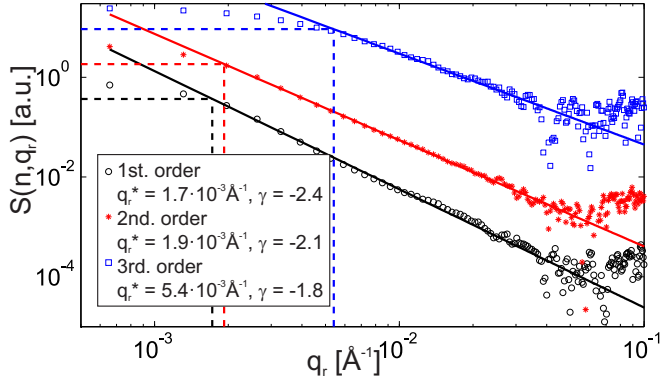


**Figure 2.9:** The  $q_z$  integrated structure factor  $S(n, q_r)$  of the  $n = 1$ ,  $n = 2$ ,  $n = 3$  order Bragg-sheet. A plateau at  $q_r \leq q_r^*$  is followed by a clear power-law decay  $S(n, q_r) = a \cdot q_r^\gamma$ . For  $q_z \sigma \leq 1$  a typical in plane correlation length  $\xi_r = \frac{2\pi}{q_r^*}$  can be inferred from the crossover  $q_r^*$  as quantified by the HWHM of  $S(n, q_r)$ . For the current example a systematic shift in  $\gamma$  as well as  $q_r^*$  with  $n$  indicated that this identification can only be made for  $n = 1$ . Curves have been shifted for clarity.

transform of the in plane correlation function  $c(r)$  [103, 104]. A logarithmic correlation function  $c(r)$  leads to a power-law decay  $S(n, q_r) \propto a \cdot q_r^\gamma$  [100] with  $\gamma \leq 0$ . The scaling behavior of  $S(n, q_r)$  does however only softly depend on the exact representation of  $c(r)$  [105] and hence the lineshape parameter  $\nu = 2 - \gamma$  as well as estimates for typical in plane correlation lengths can be extracted from  $S(n, q_r)$  even in the case of slightly fraud model assumptions (e.g. not a mere logarithmic divergence). After normalization to  $S(n, q_r = 0)$  and background subtraction  $\gamma$  as well as the HWHM of the power-law decay can be extracted from a non-linear least squares batch fit.

For  $q_z \sigma \leq 1$  the HWHM of  $S(n, q_r)$  provides an estimate for the in plane correlation length  $\xi_r = \frac{2\pi}{HWHM}$ . An exemplary data set obtained for DOPC multilayers can be found in figure 2.9 (experimental details will be given in section 5.1.5). The  $q_z$  integrated structure factor  $S(n, q_r)$  is characterized by a plateau for  $q_r \leq q_r^*$  followed by the predicted power-law decay for  $q_r \geq q_r^*$ . In the dataset shown in figure 2.9 the crossover  $q_r^*$  increases with  $n$ , reflecting the fact that  $S(n, q_r)$  is not a mere Fourier transform of the fluctuation spectrum for  $q_z \sigma \geq 1$  [106, 93, 92] and membrane undulations are probed at different depths in the multilamellar stack.

**Out of plane correlations** In a second step the smectic penetration length  $\Lambda$  is extracted from the broadening of the diffuse reflections along  $q_z$  that is seen while  $q_r$  increases, see 2.10. Each of the vertical lines,  $S(q_z, q_r = \text{const.})$ , is fitted to a Lorentz function, corresponding to an exponentially decreasing cross-correlation function. The FWHM of the non-linear least squares fits as plotted in 2.10 show

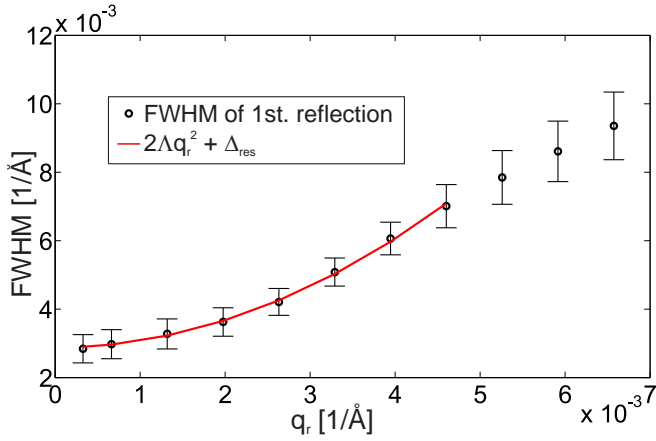


**Figure 2.10:** The smectic length  $\Lambda$  as extracted from the increase of  $FWHM$  of the first Bragg sheet as a function of  $q_r$ . Smectic elasticity predicts a quadratic dependence of the  $FWHM$  on  $q_r$ ,  $FWHM(q_r) = 2\Lambda q_r^2 + \Delta_{res}$ . The quadratic fit has been restricted to the region of clear lorentzian line profiles, the offset  $\Delta_{res}$  has been introduced to account for the finite instrumental resolution.

a parabolic increase with  $q_r$ . This observation follows the prediction of smectic elasticity theory, and the parabolic fits of the  $FWHM(q_r)$  curve can therefore give access to  $\Lambda$  using  $FWHM(q_r) = 2\Lambda q_r^2 + \Delta_{res}$ . Here  $\Delta_{res}$  accounts for the finite instrumental resolution.

In summary, we obtain estimates for  $\nu = \frac{\pi k_B T}{2d^2 KB}$  and  $\Lambda = \sqrt{\frac{K}{B}}$  by two independent procedures. The elastic coefficients  $B = \frac{\pi}{2d^2 \nu \Lambda}$  and  $K = \frac{\pi \Lambda}{2d^2 \nu}$  can therefore in principle be obtained directly from the diffuse scattering signals. As observed before [32], values for  $K$  and  $B$  tend to differ systematically from reference values computed from literature data [107]. However, as one is in the context of time resolved scattering experiments mainly interested in relative variations, the outlined data analysis procedure provides reliable mechanical parameters characterizing the out of equilibrium behavior of lipid multilayers.



### 3 Ultrafast multi photon counting – Detector development for time resolved x-ray diffraction experiments

*This experimental section is devoted to the development and commissioning of an ultrafast x-ray detector based on a quadrant avalanche photodiode.*

*The speed, by means of exposure time and hence sample throughput, of x-ray experiments at synchrotron or Free Electron Laser (FEL) sources is in many cases limited by the dynamic range and readout time of current detector technologies rather than the peak brilliance of the x-ray source. This is especially true for time resolved stroboscopic scattering experiments, where an ultrafast selection of individual pulses by means of a gating of modern pixel detectors or the application of high speed choppers (see sections 1.3 and 1.4) is necessary to obtain high temporal resolution in the picosecond range. Single pulse selection at a frequency of more than often  $f_{pp} = 1\text{kHz}$  (matched to the stroboscopic experiment) is necessarily accompanied by a tremendous decrease of effective x-ray intensity for high frequency  $f_b$  x-ray sources, i.e. a factor of  $\frac{f_b}{f_{pp}} \approx 31000$  in the 240-bunch mode of Petra III ( $f_b \approx 31\text{MHz}$ ). This intensity loss poses significant restrictions on possible sample systems and leads to typically long exposure times. Furthermore individual x-ray pulses can only be selected for  $f_b \leq 6\text{MHz}$  due to technological limitations, limiting stroboscopic time resolved x-ray experiments to low frequency filling modes.*

*The need for an increased effective intensity due to typically low scattering intensities (especially in the case of diffuse scattering signals, see section 5.1.5 and 3.3) lead to the development of an advanced high resolution pulse resolved detection mechanism as a part of this thesis. As the detection scheme is based on a quadrant avalanche photodiode the detector is named 'QAPD' in the following.*

*As the results presented in this chapter are based on extensive teamwork, technological contributions from collaborating scientists (in particular J. Agricola, Dr. M. Osterhoff and M. Könnemann) are generously acknowledged. Results are being published at the moment of writing.*

#### 3.1 Desired specifications / Ultrafast multi photon counting

Let us start with a short review of the operating principles of commonly applied detector technologies in order to further illustrate the motivation for advanced x-ray detection schemes, especially in the context of time resolved x-ray scattering experiments. See additionally figure 3.1 for a sketch of the operating principle of a single photon counting x-ray detector.

Current detector technologies are either *single photon counting* or *integrating*. Single-photon counting devices are based on highly sensitive detector front ends (e.g. scintillator crystals, photo multiplier tubes, multichannel plates or avalanche photodiodes) and a single channel analyzer (SCA). The front-end electronics provide strongly amplified signals corresponding to individual hit-events. When the

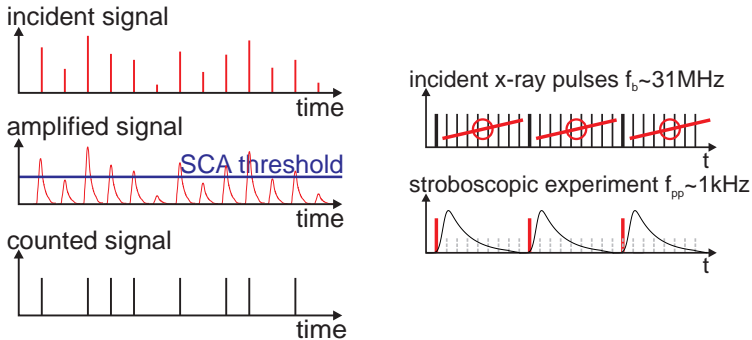


**Figure 3.1:** *Left:* Schematic of the operating principle of current single photon counting detectors. A single channel analyzer (SCA) discriminates events from background noise, individual events are counted. No discrimination between single- and multi photon events can be made. **Right:** Stroboscopic experiments at a repetition rate  $f_{pp}$  smaller than the synchrotron pulse frequency  $f_b$  require ultrafast individual pulse selection. This approach is necessarily accompanied by a tremendous loss of effective primary x-ray intensity.

pulse height of the amplified signal exceeds a selectable threshold in the SCA a digital counter is increased and an event is detected. Due to the typically strong electronic amplification even individual photons can clearly be discriminated from electronic noise. The dynamic range, by means of the maximal number of processible events per second, of this technique is limited by the maximal operating frequency of the SCA and the digital counter, the bit depth of the digital counter and the response time of the front end electronics. The biggest constraint is however related to the binary nature of a SCA, no distinction between events corresponding to individual photons and events corresponding to multiple photons impinging within the dead-time of the detector can be made.

Time-integrating detectors such as e.g. charge coupled devices (CCDs) or photo films do not suffer from the limitation to single photon events. However, the intensity is in these cases not intrinsically calibrated by the detection mechanism, the signal acquired for each pixel is only proportional to the number of detected photons. Thermal- and readout noise do furthermore limit the performance at the very low intensity scale, a detection of a individual photon is in generally not possible.

Both techniques do not provide temporal information ('a time stamp') for each individual event, only intensity signals integrated over the exposure time are measurable. It is in principle possible to limit the effective exposure time to  $\leq 200\text{ns}$  by gating modern single photon counting Pixel detectors (see section 1.3), continuous framing rates at  $f_b \approx 31\text{MHz}$  are not yet achieved. Although modern ultrafast adaptable gain detector technologies (e.g. the AGIPD [108] or the CSPAD [109]) developed at various FEL sources can be operated at framing rates of up

to  $\leq 5\text{MHz}$ , a continuous operation of these devices is limited to the detection of several hundred subsequent pulses.

In order to overcome these limitations, and to further promote time resolved x-ray scattering experiments, an improved detection mechanism should fulfill the following specifications:

1. It should be able to detect single photon events, noise is therefore a critical issue.
2. Multi-photon events should be detectable, a dynamic range of  $\geq 8\text{bit}$  (10bit desirable) is required *within each x-ray pulse*. This corresponds to the simultaneous detection of  $N \leq 256$  ( $N \leq 1000$  desirable) photons per pulse.
3. The detector is to be position and intensity sensitive, as these are generally the most important observables in e.g. time resolved x-ray scattering experiment.
4. Each event has to be *time-stamped* in order to enable sorting relative to a pump-probe experiment. The signal corresponding to each individual x-ray pulse is to be stored in a mass storage device along with the respective time stamp.
5. Pulse to pulse online data analysis (i.e. position and correlation analysis, temporal binning, waveform averaging) is required, see e.g. figure 3.7.
6. The detector should be usable in the 240-bunch mode of Petra III ( $f_b \approx 31\text{MHz}$ , standard operating mode). Pulse processing including online data analysis is hence to be completed in  $t \leq 30\text{ns}$ .

In order to fulfill these requirements, especially (2) and (3), our approach is based on a quadrant avalanche photodiode operating in the linear mode. A silicon based sensor is chosen because of comparatively low electronic noise, especially when compared to GaAs based diodes. Optical spectral response properties of different semiconductor materials is of secondary importance in the case of x-ray detection.

**Single x-ray photon detection using Si photodiodes?** Let us shortly estimate the current signal corresponding to the detection of an individual x-ray photon at an energy of  $8\text{keV}$  in a silicon diode. The ionization energy of un-doped silicon is  $3.6\text{eV}$  [110], one fully absorbed  $8\text{keV}$  x-ray photon will therefore create  $N \approx 2200$  free charges. With an estimated width of  $\tau = 20\text{ns}$  of the electric response of a fast silicon diode this leads to an electric current of  $I_p = \frac{2200e^-}{20\text{ns}} \approx 17\text{nA}$ , already precisely measurable in the case of a hypothetical DC signal<sup>4</sup>. In order to further amplify the signal and therefor relax the requirements on the subsequent amplification and pulse processing electronics, an Avalanche photodiode (APD) is used. When operated in the linear regime, the avalanche effect of an APD provides a current amplification of  $\times 100 - \times 500$  [111], a single photon signal of  $I_p = 100 \cdot 17\text{nA} = 1.7\mu\text{A}$  is therefore assumed as a starting point for the design of the subsequent pulse amplification and processing electronics. In addition to

<sup>4</sup> <http://www.keithley.de/data?asset=10756>

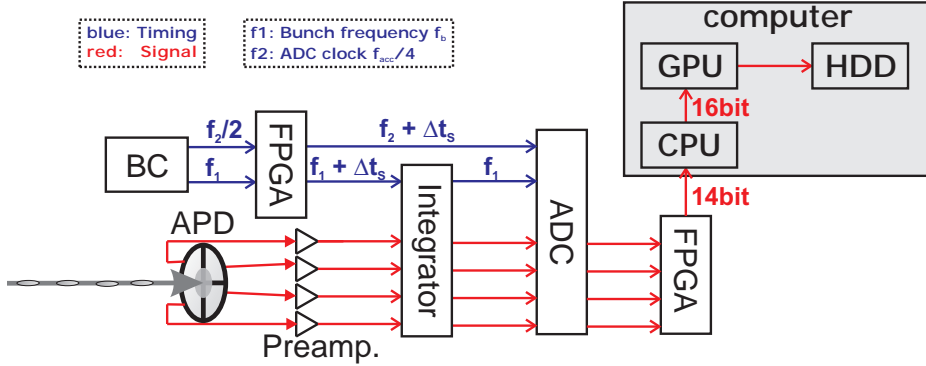


**Figure 3.2:** Sketch of the data acquisition scheme of the quadrant avalanche photodiode x-ray detector (QAPD). Individual x-ray pulses are detected and amplified by an internal gain of approximately 100 in the linear mode of the APD. A fast preamplifier based on the high speed operational amplifier LMH6629 converts individual charge pulses into voltage signals to be integrated by the actively gated voltage integrator. Readout by a high speed analog to digital converter (ADC) is followed by data encoding and transfer by a Xilinx Virtex 6 FPGA. Online data analysis can be performed by the graphics processing unit (GPU) of a standard personal computer.

advantages related to the internal gain of an APD, faster rise times and shorter pulse widths compared to standard photodiodes can be achieved.

### 3.2 Linear amplification, integration and digitalization of individual x-ray pulses

The basic concept of the APD based detection scheme is sketched in figure 3.2. Each channel of a quadrant avalanche photo-diode (QA4000-10, First Sensor AG, Berlin) is routed to a fast preamplifier circuit, integrated by a gated integrator and digitized by a high bandwidth analog to digital converter (ADC, FMC-104, 4DSP, USA). By synchronizing the sampling rate and phase to external trigger and clock sources the signal corresponding to individual x-ray pulses can be digitized and further analyzed in a FPGA (Virtex 6, Xilinx). The exact timing of the integration and digitalization cycle is the most crucial prerequisite for a successful operation, see e.g. figure 3.9. In the following sections a rough description of the individual components will be given, we refer to the extensive literature, especially [112] as well as the respective data sheets, for a detailed explanation of the complex electronic circuits involved. The outlined operating principle will be named *multi photon counting* in the following.

**Detector front end** As already mentioned, the current detector front end is a silicon based quadrant APD with an active area of  $\varnothing 4\text{mm}$ , individual elements

are separated by a gap of  $110\mu\text{m}$ . The silicon layer has a thickness of  $240\mu\text{m}$ , leading to a detection efficiency of approximately 30% for 20keV x-ray photons, higher detection efficiencies can be achieved for thicker depletion layers at the expense of slightly increased pulse widths (longer drift times). A linear gain of  $\times 100$  is reached for a bias voltage of  $U \approx 200\text{V}$ . The detector front end is highly exchangeable, smaller gaps, different materials or higher detection efficiencies can be introduced without interference with subsequent elements.

### 3.2.1 Preamplifier

As already shortly discussed the absorption of x-ray photons leads to short current pulses. Subsequent measurement electronics, especially analog to digital converters, generally process voltage signals, an operational amplifier (OPA) based low noise high bandwidth current-to-voltage converter (trans impedance amplifier) had to be designed. The circuit is based on the Texas Instruments LMH6629 OPA (specified  $-3\text{dB}$  bandwidth  $\lesssim 900\text{MHz}$ ). The most elementary part of this circuit has been sketched in figure 3.3. An incoming current signal  $I_p$  is converted to a voltage signal  $U_p = R1 \cdot I_p$  by the central operational amplifier. The optimal value of  $R1$  depends on the x-ray energy as well as the bunch frequency, a value of  $R1 = 10\text{k}\Omega$  fits the needs of most experimental situations. Higher values are desirable in the case of low x-ray energies at the expense of slightly elongated pulse lengths. Additional elements  $C2$ ,  $C3$  and  $R3$  in figure 3.3 are necessary for a correct electric compensation of the circuit, see [112] for details. Optimal values for  $C2$ ,  $C3$  and  $R3$  are determined according to the data sheet of the OPA, exact values are given in appendix A.3.

An estimated current signal of  $I_p = 1.7\mu\text{A}$  (see section 3.1) leads to a voltage pulse of  $U_p = R1 \cdot I_p \approx 17\text{mV}$  for  $R1 = 10\text{k}\Omega$ , a value of  $U_p \approx 2.7\text{mV}$  has been determined experimentally for the absorption of a single 8keV x-ray photon, see figure 3.6. The preamplifier is fully DC coupled, no offset voltage exceeding the minimal offset voltage of the OPA is present in the output signal.

Additional features such as micro controller ( $\mu\text{C}$ ) based test charge injection and automatic identification are implemented via an Atmel ATtiny44  $\mu\text{C}$  on the printed circuit board (PCB) of the preamplifier, a dedicated firmware for the ATtiny is being developed at the time of writing. Photos of the fully assembled preamplifier including the quadrant APD are shown in figure 3.4.

### 3.2.2 Gated integrator (Boxcar averager)

As it is in general however the integrated charge  $Q = \int Idt$  and not the current  $I_p$  that is directly proportional to the number of incident photons<sup>5</sup>, a high speed gated integrator circuit had to be designed. No commercial product at the required specifications is available. A gated integrator furthermore strongly

<sup>5</sup> In case of an effectively unlimited bandwidth of the trans impedance amplifier. Note that a passive low pass filter would also lead to a partial integration of the analog signal.

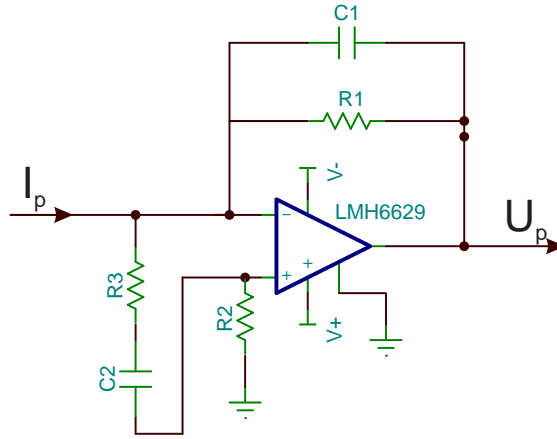


**Figure 3.3:** Schematics of the preamplifier PCB. A basic trans impedance amplifier is implemented basing on the Texas Instruments LMH6629 operational amplifier. Optimal values of the electronic components have been determined experimentally in an iterative procedure. See appendix A.3 for detailed schematics including optimal component values.



**Figure 3.4:** Photos of the printed circuit board (PCB) of the high bandwidth preamplifier. **Left:** Front view. The quadrant APD is located in the center of the PCB. It is covered by a approximately  $30\mu\text{m}$  thin Al-foil in order to prevent an exposure to ambient light, dust contamination and humidity uptake. **Right:** Back view. Amplified signals are routed to four SMA connectors. Communication with the on-board micro controller, high voltage biasing of the APD and supply voltages are provided via a Conec mixed Sub-D connector.

increases the signal quality by filtering high frequency white noise and slightly relaxes the requirements on the timing of the ADC. Each channel of the quadrant APD is integrated separately.

A basic sketch of the gated integrator is depicted in figure 3.5, let us focus on integrator (A) in figure 3.5 (top) for a short explanation of the operating principle. The central part of the active integrator consists of two high speed switches  $SW1$  and  $SW2$  (specified rise time  $t_{on} \approx 0.8\text{ns}$ , SST211, Calogic), an integrating capacitor  $C1$  and a Texas Instruments OPA355 operational amplifier. See figure 3.5 (bottom) for a sketch of the voltage signals involved. An integration cycle is initiated by closing  $SW1$  while  $SW2$  remains in the open position (the gate signal (black) in figure 3.5 (bottom) is high). Incoming voltage signals  $U_p$  (blue in figure 3.5 (bottom)) are hence integrated in the capacitor  $C1$ , the output voltage  $U_I$  (red in figure 3.5 (bottom)) at  $C1$  is given by  $U_I = \frac{1}{R_1 C_1} \int U_p dt$ , where  $R_1$  is the input resistance of the integrator circuit. The OPA355 operates at unity gain, a  $-3\text{dB}$  bandwidth of  $450\text{MHz}$  is specified. The output voltage  $U_I$  is hold constant as long as  $SW2$  remains in the open position and the input is decoupled by opening  $SW1$ . As soon as the subsequent data acquisition is accomplished the integrator is reset by closing  $SW2$ . The capacitor  $C1$  is hereby discharged, the associated time constant is  $\tau = R2 \cdot C1$ , where  $R2 = 50\Omega$  denotes the on-resistance of  $SW2$ . Extensive simulations using the Texas Instruments simulation tool TINA<sup>6</sup> provide an educated guess for optimal component values, in particular  $C1 \approx 100\text{pF}$ . This leads to an ideal decay constant of  $\tau \geq 50\Omega \cdot 100\text{pF} = 5\text{ns}$ , not taking into account the finite slew rate and settling time of the OPA. The voltage at  $C1$  is therefore decayed to  $0.001 \cdot \max(U_I)$  ( $\hat{=}$  10bit resolution) within  $t \geq \log_e(0.001) \cdot 5\text{ns} \approx 35\text{ns}$  (i.e. subsequent pulses do not influence each other). This illustrates the need for two alternating integrator circuits (integrator (A) and (B) in figure 3.5) for the detector to be fully functional in the Petra III 240-bunch mode, where subsequent x-ray pulses are separated by  $\Delta t = 30\text{ns}$ . Both integrator circuits are operating in parallel to each other, two low voltage differential signal (LVDS) drivers (DS90LV027A, Texas Instruments) distribute the incoming signal variantly to both integrators by complementary switching  $SW1/2/5$  and  $SW3/4/6$ . Only one gate signal is used for both circuits, one integrator is in the integration phase while the other integrator is resetting.

The DC operation of the preamplifier facilitates the construction of the integrator circuit compared to AC coupled electronic devices, where the integration of offset voltages poses a significant problems. Charge injection by stray capacitances of  $SW1$  and  $SW2$  is suppressed by arranging  $SW1$  and  $SW2$  such that the capacity of  $SW1$  is exactly compensated by  $SW2$ .

As it is in cases desirable to digitize the unintegrated signal of the preamplifier (e.g. for high repetition rate experiments, where a complete re-biasing is not possible), two high bandwidth signal relays ( $RL1$  and  $RL2$ , G6Z-1F-A-DC5, Omron Electronics) allow for a direct routing of the preamplified signal to the ADC.

The last element in the analog signal chain is the active offset adjustment. The

<sup>6</sup> <http://www.ti.com/tool/tina-ti>

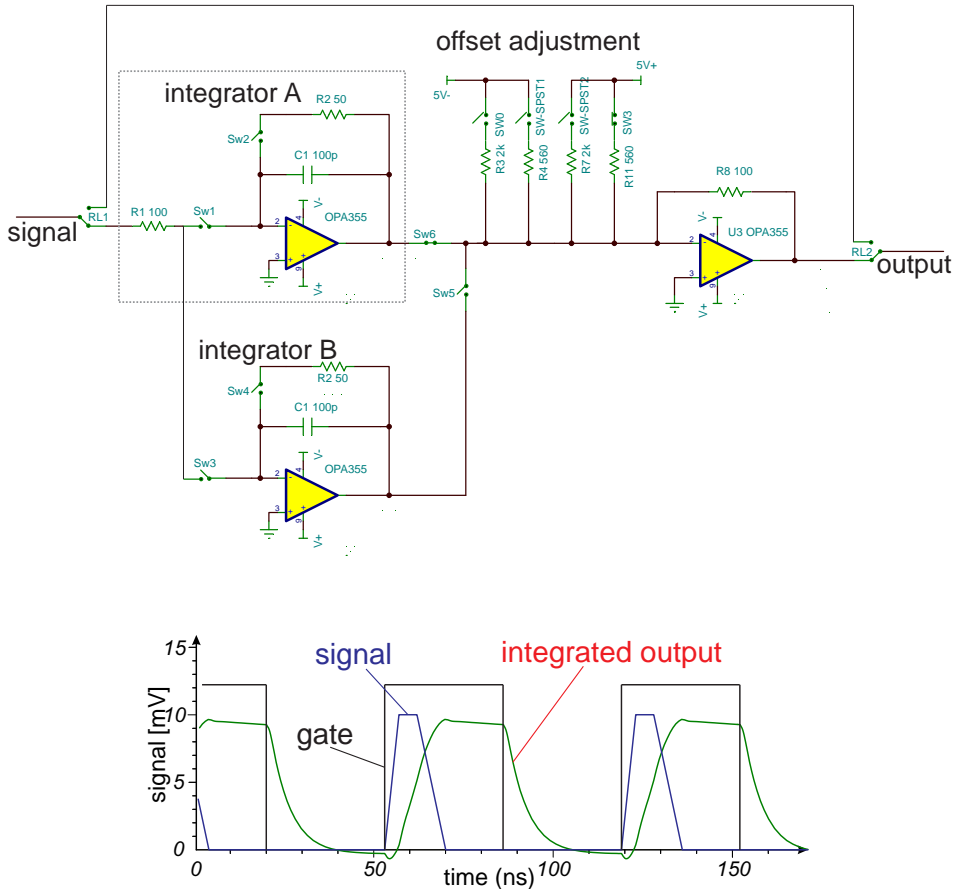


**Figure 3.5:** *Top:* Simplified schematic of the fast gated integrator circuit. Two integrators A and B operate in parallel to each other, the DC operating point can be set by a basic summing OPA (offset adjustment). **Bottom:** Schematic of the most important signals involved in the integration cycles as simulated by TINA (Texas Instruments). The incoming voltage signal (blue) is integrated on the capacitor  $C1$  while the gate signal (black) is high, the height of the output signal (red) can be optimized by adjusting  $R1$ . The integrator is reset as long as the gate signal is low.



input range of the ADC is fixed to 1Vpp while the output from the integrator / preamplifier is centered around 0V. Furthermore only unipolar signals are expected due to the nature of the APD, the sign of the voltage pulse depends on the detector front end and the direction of the bias voltage. In order to utilize the full dynamic range of the ADC it is desirable to shift the DC value of the integrator / preamplifier, a basic summing OPA circuit based on a Texas Instruments OPA355 is therefore located at the output of the integrator. Four different offset voltages determined by the resistors  $R4$ ,  $R5$ ,  $R6$  and  $R7$  in figure 3.5 are user selectable.

### 3.2.3 Commissioning of the analog signal chain – single photon counting capability

Generous beamtime allocation at the beamlines P08 and P10 at Petra III allowed for extensive commissioning of the analog signal chain. Three main test runs have been carried out at a photon energy of 24keV in the Petra III 240-bunch mode (P08,  $f_b \approx 31\text{MHz}$ ), a photon energy of 18keV in the Petra III 40-bunch mode (P08,  $f_b \approx 5.2\text{MHz}$ ) as well as a photon energy of 13.6keV in the Petra III 40-bunch mode at P10. High bandwidth oscilloscopes (LeCroy WaveRunner 640Zi, Tektronix DPO4104B, Tektronix DPO7254C) have been used to analyze the analog signal.

**Commissioning of the preamplifier circuit** Optimal values for the electric components of the preamplifier circuit (especially  $R1$ ) have been determined in the first commissioning experiment (240-bunch mode, photon energy  $E = 24\text{keV}$ ), detailed electronic schematics including optimal component values can be found in appendix A.3. Two typical signals recorded after several iterative optimization cycles are depicted in figure 3.6 for a primary x-ray intensity of  $I_0 \approx 1 \cdot 10^7\text{ph/s}$  (3.6 left) and  $I_0 \approx 6 \cdot 10^7\text{ph/s}$  (3.6 right).  $R1$  has been  $R1 = 10\text{k}\Omega$  in both cases. The signal rise time of  $\tau \leq 8\text{ns}$  is roughly independent on the respective pulse height, the integral pulse length of  $\tau \leq 30\text{ns}$  allowing for experiments in the Petra III 240-bunch mode. However at intensities  $I_0 \geq 5 \cdot 10^8$  detected photons/second a complete re-biasing of the APD is not possible, an offset voltage of  $\leq 10\text{mV}$  at a pulse height of 3V remains. This offset is subtracted in the subsequent digital signal chain, see section 3.3.

The average pulse height corresponding to the detection of an individual 24keV x-ray photon is determined by means of pulse height histograms, plotted brown in figure 3.6. The peak pulse height, marked by a vertical brown dash-dotted line in figure 3.6 right, of each displayed event is therefore recorded, a clean Poisson statistic in the resulting histograms indicates that multi photon events can clearly be distinguished. An individual 24keV x-ray photon leads to a pulse height of approximately 8mV, the signal corresponding to a single x-ray photon can clearly be distinguished from electronic noise.

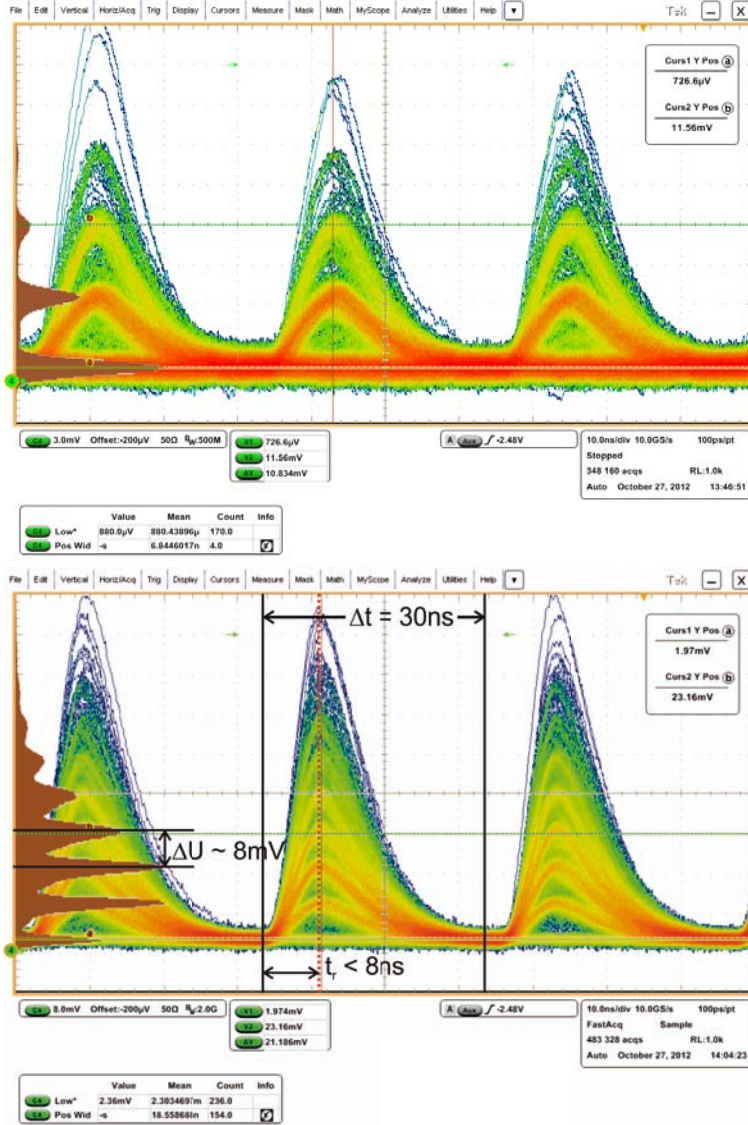


**Figure 3.6:** The (pre-)amplified signal of an individual channel of the quadrant APD for a primary intensity of  $I_0 \approx 1 \cdot 10^7$  ph/s (top) and  $I_0 \approx 6 \cdot 10^7$  ph/s (bottom) along with a histogram of the peak intensities (plotted in brown). Experiments have been performed at the beamline P08, the photon energy was  $E = 24$ keV (240-bunch mode). The clean Poisson statistic of the histogram clearly indicates that individual x-ray photons can be detected and that multi-photon events can be measured. Pulse widths are  $\tau \leq 30$ ns in all cases, allowing for experiments in the Petra III 240-bunch mode. The value of the amplifying resistor was  $R_1 = 10$ k $\Omega$ .

**Commissioning of the gated integrator** An extensive commissioning of the gated integrator circuit is in progress at the moment of writing. The performance is tested and verified using a standard, all electronic laboratory setup at the institute for x-ray physics in Göttingen. A high bandwidth arbitrary waveform generator (specified bandwidth 400MHz, Aglient) is programmed to resemble the signal corresponding to single and multi photon events as measured in the preceding paragraph, the electronic answer of the circuit is recorded with a high speed oscilloscope. The gate signals are as well provided by the arbitrary waveform generator, pulse height histograms of the resulting integrated signals are recorded in order to quantify electronic noise.

### 3.3 High speed data acquisition and online analysis at 31MHz

The integrated analog signal is digitized by a four channel 14bit high speed high bandwidth ADC (sampling rate  $\leq 250$ Msp, analog bandwidth 320MHz, FMC-104, 4DSP, USA), digital data is directly streamed to a Xilinx Virtex 6 FPGA on a MI605 FPGA evaluation board. The most crucial experimental tasks are connected to a low noise signal routing and an exact timing of the analog to digital conversion process.

The FMC-104 ADC provides four DC coupled signal inputs, an external clock source can be provided in order to synchronize the sampling process to an external reference oscillator. The ADC records one sample at each rising edge of the external clock, individual samples are transferred to the FPGA. An additional trigger signal can be provided to the FPGA, individual signals are in this case only digitally processed if the trigger signal is high at the moment of sampling.

In order to synchronize the ADC to the operating frequency of Petra III an external clock frequency of  $f_{clock} = \frac{f_{acc.}}{2} \approx 250$ MHz is chosen, see section 1.3 for details on the timing scheme of Petra III. The trigger frequency is given by the bunch frequency of the respective filling mode. Both frequencies are ultimately provided by the Petra III bunchclock, a precise delay (resolution 71ps) can be introduced to the clock as well as the trigger pulses by the Virtex 6 FPGA in order to exactly time the sampling process.

In the case of unintegrated high repetition rate operation (direct routing of the preamplified signal to the ADC using relays *RL1* and *RL2* in figure 3.5), remaining offset due to incomplete re-biasing of the APD can be subtracted in the FPGA. Two trigger pulses separated by  $\Delta t = 8$ ns are in this case generated by the Virtex 6 FPGA, subsequent samples are subtracted from each other to eliminate remaining offset components. Note that  $\Delta t$  is restricted to integral clock cycles  $\Delta t = n \cdot \frac{1}{f_{sampling}} \approx n \cdot 4$ ns.

In resume, four 14bit digital signals, corresponding to four quadrants on the photodiode, are transiently recorded by the Virtex 6 FPGA at a sampling rate of up to 31MHz. This corresponds to a data rate of  $4\text{channels} \cdot 2\text{byte} \cdot 31 \cdot 10^6 \cdot \frac{14}{16} = 217\text{Mb/s}$ <sup>7</sup>.

<sup>7</sup> one 16bit integer is encoded by 2bytes

As the maximum data rate of wide spread external interfaces (e.g USB or 1 GigE) does not allow for a real time streaming to mass storage devices at these data rates, data is directly transferred to the CPU via a PCI-e connection (PCI-e FPGA implementation using Xillybus, Xillybus Ltd., Haifa, Israel). The CPU decodes the 14bit signals to 16bit data streams (unsigned integer), the full data stream can be either stored in a fast solid state disk (SSD) or a RAID 0 compound of several common magnetic hard disks, the only limit being the capacity of the mass storage devices.

**Online data analysis at up to 31MHz** Depending on the mode of operation it is usually desirable to perform an online data analysis of the acquired waveforms in order to limit the amount of data and facilitate further data processing. Easy examples are e.g. a temporal binning of individual data points (setting a ‘macroscopic’ exposure time) or a position- and or intensity correlation analysis (‘x-ray photon correlation spectroscopy’). In the context of time resolved x-ray diffraction especially an exact temporal sorting of events relative to the stroboscopic experiment is necessary, see figure 3.7. The sample system is stroboscopically excited at a frequency of more than often  $f_{pp} = 1\text{kHz}$ , structural changes by means of intensity- and positional variations of the diffracted x-ray beam are recorded by subsequent x-ray pulses. Individual pulses are added to registers depending on their relative delay with respect to the excitation, the temporal sampling is in this case given by the bunch frequency of the synchrotron. These registers are read out after a user selectable exposure time, providing an averaged ‘pump-probe waveform’. This analysis technique will therefore be named ‘waveform averaging’. In the case of a time resolved experiment in the Petra III 240-bunch mode the pump-probe signal (i.e. an intensity trace  $II(n, t)$  as in section 5.1.5) is hence simultaneously sampled with a temporal resolution of  $\Delta t \approx 30\text{ns}$  on the full achievable temporal scale of  $0 \leq t \leq 1\text{ms}$ . Finer sampling is achieved by combining multiple experiments for temporally slightly shifted excitations.

Real time data signal processing is performed in a medium scale graphics processing unit (GPU, Nvidia), the rate and complexity of the analysis is (by far) not yet limited by the performance of the GPU. In the case of waveform averaging an online analysis strongly limits the effective data rate. A hypothetical exposure of 30 seconds during the 240-bunch mode of Petra III produces a total amount of 7.2Gb. The stroboscopic nature of a time resolved diffraction experiment at  $f_{pp} = 1\text{kHz}$  limits this amount to 240kb, independent on the exposure time.

### 3.3.1 Commissioning of the digital signal chain – speed and effective dynamic range

A fully functional version of the QAPD including the complete analog and digital data chain has been tested at the beamlines P08 and P10 during the 40-bunch mode of Petra III, photon energies of 18keV (P08) and 13.6keV (P10) have been used. A basic sketch of the most important beamline components in case of the

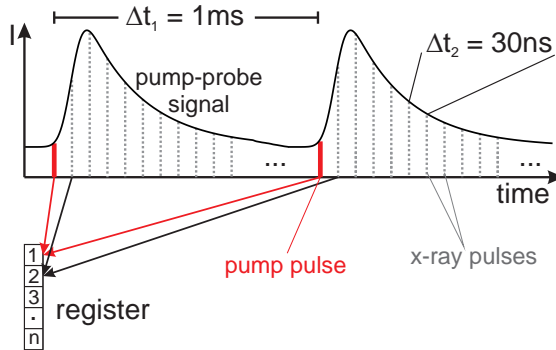


**Figure 3.7:** Acquired waveforms can be on-line averaged at a user selectable rate of  $f_{pp}$  ( $f_{pp} = 1\text{kHz}$  in this example). Individual x-ray pulses are stored in a register of the GPU depending on the time of arrival, ultrafast dynamics as induced by e.g. pulsed lasers (as sketched in red) can therefore be probed in a stroboscopic manner without the need for ultrafast pulse selection.

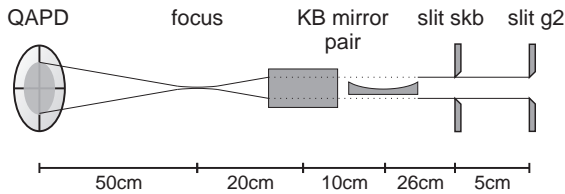


**Figure 3.8:** Sketch of the most important components of the experimental setup for the detector commissioning experiments conducted at beamline P10, Petra III.

detector commissioning experiments at P10 can be found in figure 3.8. The x-ray beam is focused to  $\leq 500\text{nm}$  (both directions) by a KB mirror pair, slit systems in front of the KB optics allow for a collimation of the beam and the adjustment of the coherence properties. In the case of the experiments presented here the exact positions of the slit systems were  $g2hg = 0.38\text{mm}$ ,  $g2vg = 0.38\text{mm}$ ,  $skbhg = 0.45\text{mm}$  and  $skbvg = 0.45\text{mm}$ . The QAPD is placed in the center of the optical axis at a distance of  $\approx 50\text{cm}$  from the focus position. An expected beam divergence of  $\approx 1.5\text{mrad}$ . (both directions) leads to a x-ray spot size of  $\approx 1.5\text{mm}$  diameter at the surface of the QAPD, all four quadrants are hence illuminated. A more detailed description of the layout of the Göttingen Instrument for Nano Imaging with coherent X-rays (GINIX) can e.g. be found in [113].

In the first step the exact timing between the synchrotron pulses and the analog to digital conversion process has been optimized for the unintegrated, preamplified signals. The temporal delay (adjusted by the Virtex 6 FPGA) between the signal provided by the Petra III bunchclock and the ADC clock has been scanned via

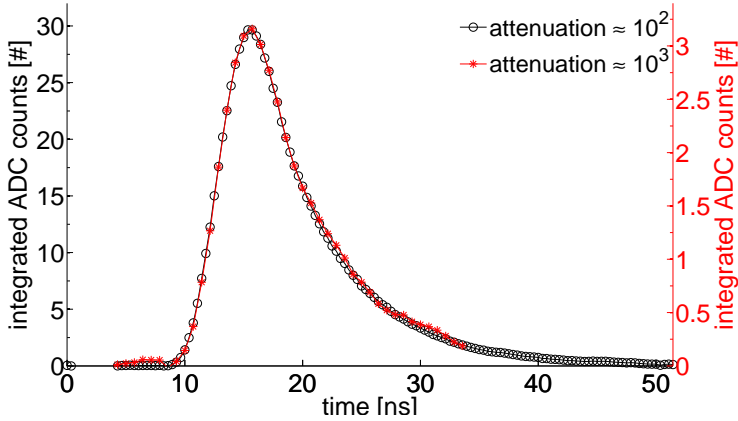


**Figure 3.9:** By scanning the delay between the signal provided by the Petra III bunchclock and the sampling instant, the QAPD can be used for equivalent time sampling of the preamplified signal. The temporally averaged preamplified signal is measured to determine the optimal sampling instant, i.e. the maximum pulse height. It was observed that, contrary to the initial expectations, the pulse width does not depend on the number of simultaneously detected photons (the pulse height). Measurements have been performed at the beamline P08 at a photon energy of  $E = 18\text{keV}$ .

the measurement control software SPEC (Certified Scientific Software<sup>8</sup>), the sum of the temporally integrated signal is plotted versus delay time in figure 3.9. The detector can in this case be thought of as a high speed oscilloscope (more accurate: *equivalent time sampling data acquisition*), the scans depicted in figure 3.9 correspond to the signal of a preamplified pulse averaged over  $N \approx 520000$  iterations (exposure time 0.1seconds, temporal resolution  $\leq 71\text{ps}$  given by the step width of the FPGA). The signals corresponding to two different primary x-ray intensities have been plotted in figure 3.9 in order to check for possible variations (i.e. a broadening) of the pulse shape with increasing x-ray intensity. It is observed that, in contrast to the expectations, the averaged pulse shape does not depend on the primary intensity of the x-ray beam.

The intrinsic linearity as well as the single photon counting capability are demonstrated by means of a pulse height histogram of the recorded ADC counts (proportional to the measured voltage), see figure 3.10. The sampling instant is in this case set to match the respective maximum in figure 3.9, pulse height histograms have been recorded for varying primary x-ray intensities at an exposure time of one second (corresponding to  $\approx 5200000$  samples) each.

A Poisson distribution observed in the histograms depicted in figure 3.10 clearly demonstrates the multi photon counting capability of the QAPD. The Poisson

<sup>8</sup> <http://www.certif.com/>

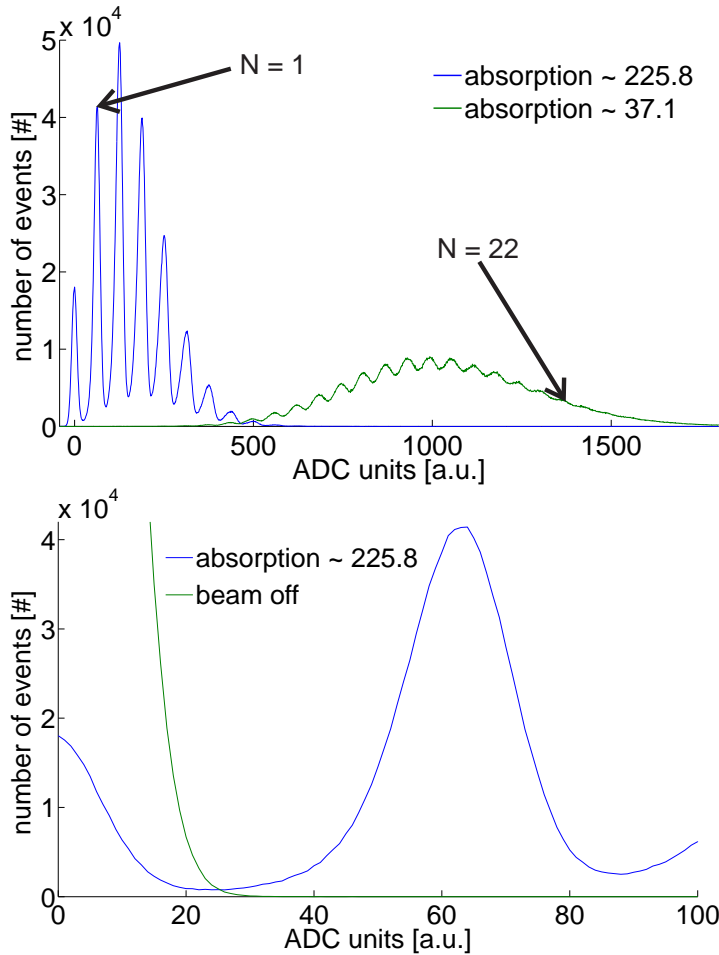


**Figure 3.10:** Pulse height histograms for the digitized data points of the un-integrated preamplified signal as measured in the direct synchrotron beam at P10, Petra III, photon energy was  $E = 13.6\text{keV}$ . A Poisson distribution (see additionally figure 3.11) indicates the single- and multi photon counting capability of the QAPD. **Top:** Pulse height histograms corresponding to two different primary x-ray intensities. Individual photon numbers can clearly be distinguished up to  $N = 22$  photons/pulse, the integral of the respective histograms is proportional to the incident x-ray flux up to  $N \approx 250$  photons/pulse (limited by the full scale deflection of the ADC). **Bottom:** A zoom into the overlap region between the zero- and the one photon event reveals a strong separation and hence clearly confirms the single photon counting capability.

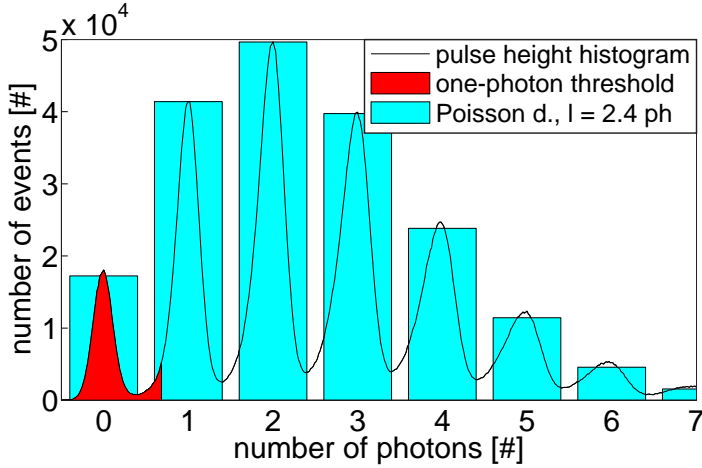


**Figure 3.11:** A conversion from ADC units to exact photon numbers is made by binning the ADC units according to the distribution observed in a pulse height histogram. Dead counts are effectively suppressed to  $\leq 0.1\text{ph/s}$  by adjusting a user selectable threshold, the solid red region of the pulse height histogram is set to zero during the conversion process. The Poisson character of the acquired histograms is emphasized by an exemplary Poisson fit, plotted in light blue. An average number of  $\lambda = 2.4$  photons per pulse is determined.

nature of the measured histograms is further emphasized in figure 3.11, where a Poisson distribution ( $P_\lambda(N) = \frac{\lambda^k}{N!}e^{-\lambda}$ ,  $\lambda$  being the expected value and  $N$  is the number of photons) has been fitted to an exemplary histogram by means of a non-linear least squares fit. An average number of  $\lambda = 2.4$  photons per pulse is determined from the Poisson fit. Individual photon numbers can clearly be distinguished up to  $N = 22$  photons/pulse, an individual photon corresponds to roughly 65 ADC units at a photon energy of 13.6 keV. The full scale deflection of the ADC of 16384 ADC units (corresponding to 14-bits) hence limits the dynamic range to  $\leq 250$  photons/pulse.

A first basic conversion from ADC units to photon numbers is made by binning the ADC units according to the distribution observed in a pulse height histogram, see figure 3.11. Care has to be taken to suppress any dark counts by introducing a user selectable threshold, represented by the red shaded area in figure 3.11. Note that this procedure induces a slight non-linearity for the one photon event because the effective bins are not equally broad and the number of 'cropped' (the red area of the one photon event in figure 3.11) photons depends on the intensity of the x-ray pulses. This slight error will have to be corrected for in a later version of the GPU based online data analysis.

The basically noise free single photon counting capability is demonstrated by a pulse height histogram obtained for a very low intensity ( $I \leq 100\text{ph/s}$ ) x-ray



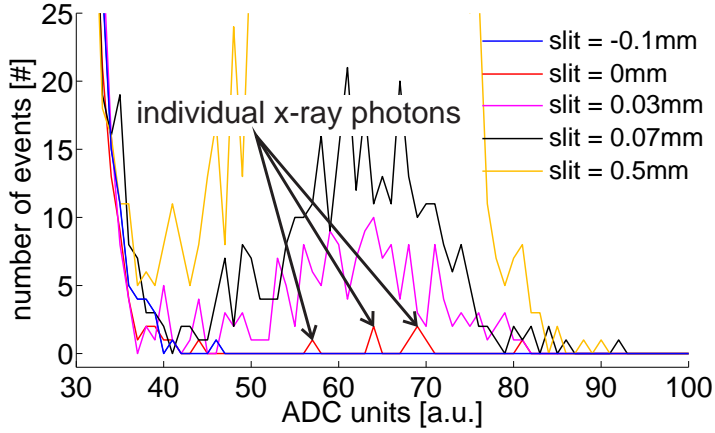


**Figure 3.12:** Zoom into the overlap region between the zero- and the one photon event for low ( $I_0 \leq 1000\text{ph/s}$ ) x-ray intensities, photon energy was  $E = 13.6\text{keV}$ . The intensity is in this case varied by changing the width of a x-ray slit system (beamline motor *g2hg*). Individual x-ray photons can clearly be identified.

beam, see figure 3.12. Events in the range between 40 ADC units and 88 ADC units strictly correspond to the detection of individual x-ray photons.

A simultaneous detection of up to  $N = 250$  photons in combination with a clear separation of individual photons from electronic noise leads to a cw dynamic range of  $5.2 \cdot 10^6 \text{Hz} \cdot 250 \frac{\text{photons}}{\text{pixel}} \approx 1.3 \cdot 10^9 \frac{\text{photons}}{\text{pixel} \cdot \text{second}}$  in case of the Petra III 40-bunch mode and a cw dynamic range of  $31 \cdot 10^6 \text{Hz} \cdot 250 \frac{\text{photons}}{\text{pixel}} \approx 7.7 \cdot 10^9 \frac{\text{photons}}{\text{pixel} \cdot \text{second}}$  in case of the Petra III 240-bunch mode.

This tremendous dynamic range is easily demonstrated by means of a knife edge (i.e. a slit system) scan, see figure 3.13. As the resulting intensity traces may be influenced by beam inhomogeneities, measurements have been repeated for various primary x-ray intensities, see figure 3.13 left. A perfect overlap of the resulting curves is a proof of the intrinsic linearity of the QAPD and the multi photon counting detection scheme. Taking into account the respective absorber values, a primary x-ray intensity of  $I_0 = 1.13 \cdot 10^{11} \text{ph/s}$  is determined in all cases, not taking into account the detection efficiency of the QAPD. The tremendous dynamic range becomes evident in a semi logarithmic representation of the resulting intensity traces, see figure 3.13 right. In conclusion, a x-ray flux of  $\leq 1 \approx 10^9 \text{ph/s}$  can be detected by the QAPD while still resolving individual photons in the low intensity regions of any measurement.

The intrinsic gain of the APD can be tuned to match the requirements imposed by different x-ray energies or expected x-ray intensities, see figure 3.14. In this case a trade-off between a) a clear separation of the one-photon event from electronic noise (3.14 left) and b) the economic utilization of the dynamic range of the

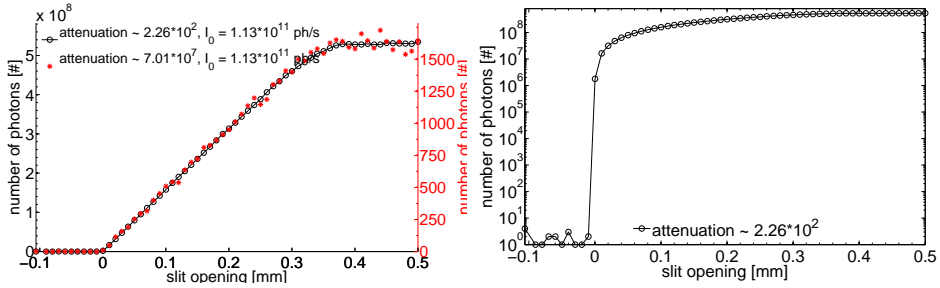


**Figure 3.13:** *Left:* Integrated number of photons as a function of the knife edge position (opening of g2hg, see fig. 3.8) at a photon energy of  $E = 13.6\text{keV}$  (40-bunch mode) for two different primary x-ray intensities. The intrinsic linearity of the QAPD manifests itself in the perfect reproduction of the resulting intensity curve over a large range of primary x-ray intensities. The acquisition time has been one second per point, the unattenuated intensity is determined to  $I_0 \approx 1.13 \cdot 10^{11}\text{ph/s}$  in both cases. *Right:* The tremendous dynamic range of the QAPD becomes evident in a semi logarithmic representation of the resulting intensity traces.

ADC has to be made. The pulse height corresponding to the absorption of a single x-ray photon is linearly dependent on the photon energy, noise hence becomes a challenging issue for low x-ray intensities ( $E \leq 8\text{keV}$ ). As the internal gain of the APD increases with increasing bias voltage, the pulse height corresponding to the detection of a single x-ray photon can however be adjusted to compensate for the reduced signal strength. It was furthermore observed, that the Poisson character of the photon distribution becomes increasingly diffuse with increasing bias voltage in the case of photon numbers  $N \geq 20$ . A good general purpose setting for APD bias voltage is  $U = 190\text{V}$ .

During a very recent beamtime at beamline P10 (photon energy  $E = 13.6\text{keV}$ , 40-bunch mode  $f_b \approx 5.2\text{MHz}$ ) the temporal resolution of the QAPD has been exploited in first preliminary beam characterization experiments. One quadrant of the QAPD has been illuminated by the KB focused x-ray beam at a distance of  $\approx 50\text{cm}$  from the focal position, see figure 3.8 for details. An intensity waveform  $I(t)$  of a duration of one second has been sampled by the QAPD at a primary x-ray intensity of  $\approx 1.3 \cdot 10^7\text{photons/s}$  (corresponding to the histogram depicted in figure 3.11), the  $f_b \approx 5.2\text{MHz}$  synchrotron bunch frequency leads to equally spaced sampling points at integral multiples of  $t \approx \frac{1}{5.3 \cdot 10^6}\text{s} \approx 192\text{ns}$ . The resulting  $I(t)$  waveform (corrected for the mean of  $I(t)$ ) has been analyzed in terms of the auto-correlation  $ACF(t) = \frac{1}{N-t} \sum_n^{N-t} I(n) \cdot I(n-t)$  (matlab function `xcorr`, option `'unbiased'`, see figure 3.15 top), as well as the power spectral density  $PSD(f) = |\mathcal{F}[I(t)]|$ , figure 3.15. Two characteristic frequencies  $f_1 \approx 35\text{Hz}$  and  $f_2 \approx 250\text{Hz}$  are detected by both approaches. Although data analysis and interpretation (in close collaboration with the Petra III beamline and machine

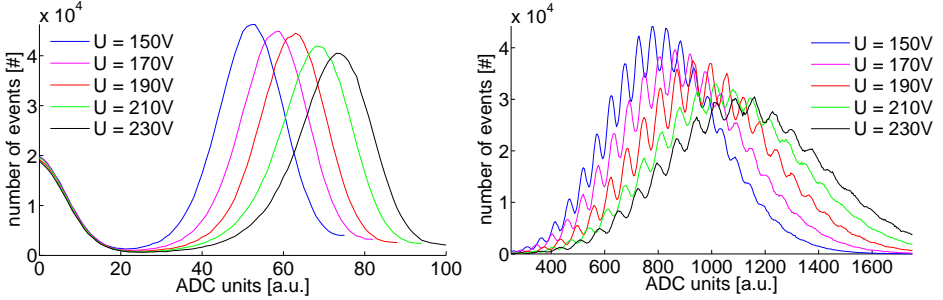


**Figure 3.14:** Pulse height histograms for the digitized data points of the unintegrated preamplified signal as a function of the APD bias voltage, photon energy was  $E = 13.6\text{keV}$  (40-bunch mode). **Left:** Zoom into the overlap region between the zero- and the one photon event. As the internal gain of the APD increases with increasing bias voltage the separation of the one-photon event from electronic noise increases with increasing bias voltage. **Right:** In the case of a simultaneous detection of  $N \geq 20$  photons/pulse the Poisson character of the photon distribution becomes increasingly diffuse with increasing bias voltage. The clearest distinction between subsequent photon numbers can be made for  $U = 190\text{V}$ .

staff) is in progress at the moment of writing and hence the observed characteristic frequencies can not yet be assigned to exact beamline components or beam undulation modes, it can be stated that the observed characteristic frequencies are not induced by the measurement electronic. All electronic reference experiments do not exhibit characteristic features in both, the auto-correlation or the PSD. Let us just shortly point out, that in principle characteristic frequencies up to  $f \leq \frac{1}{2} \cdot 5.2\text{MHz}$  (the Nyquist limit) can be detected by the outlined approach.

### 3.4 Flexible power supply and dedicated software interfaces facilitate user operation

The electronic infrastructure necessary to operate the QAPD is highly complex, various stable low voltage (LV) supplies as well as a tunable low noise high voltage biasing of the APD are needed. The situation is further complicated by the demand for a highly flexible detector front end, exact values of the the LV supplies as well as the direction and value of the HV bias have to be user selectable.

To allow for a straight forward operation of the QAPD by untrained users, a flexible power supply circuit has been designed, see appendix A.5. The basis of this fully automatic circuit is the ATtiny44  $\mu\text{C}$  on the PCB of the preamplifier. Informations on the exact type of the front end as well as optimal settings for supply and bias voltages are stored in the EEPROM of this chip and are automatically set when the QAPD is connected to the power supply. The value of the HV APD bias, the signal routing (integration, direct measurement of preamplified signals)

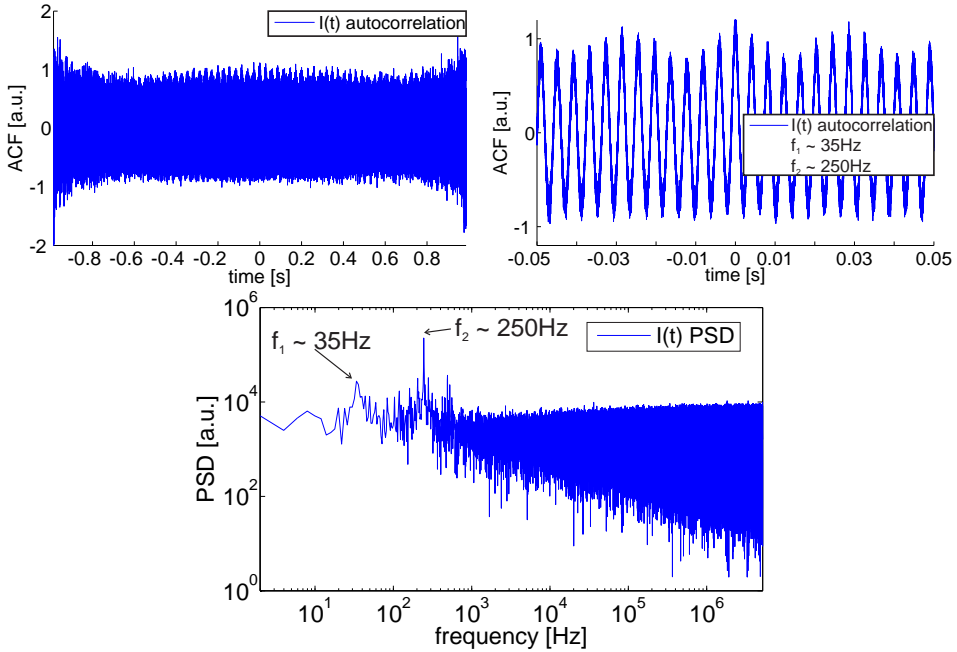


**Figure 3.15:** *Top:* Autocorrelation of the intensity waveform  $I(t)$  plotted over the exposure time of one second (left). The Dirac peak at  $t = 0$  (corresponding to the autocorrelation of white noise) has been omitted, two characteristic fluctuation modes at frequencies of  $f_1 \approx 35\text{Hz}$  and  $f_2 \approx 246\text{Hz}$  become prominent by plotting the autocorrelation over a timescale of  $\approx \pm 0.05$  seconds (right). *Bottom:* Power spectral density (PSD) of the acquired intensity waveform. Frequency components up to the MHz range are accessible via an on-line analysis, two characteristic intensity fluctuation modes at  $f_1 \approx 35\text{Hz}$  and  $f_2 \approx 250\text{Hz}$  are observed in line with the autocorrelation analysis.

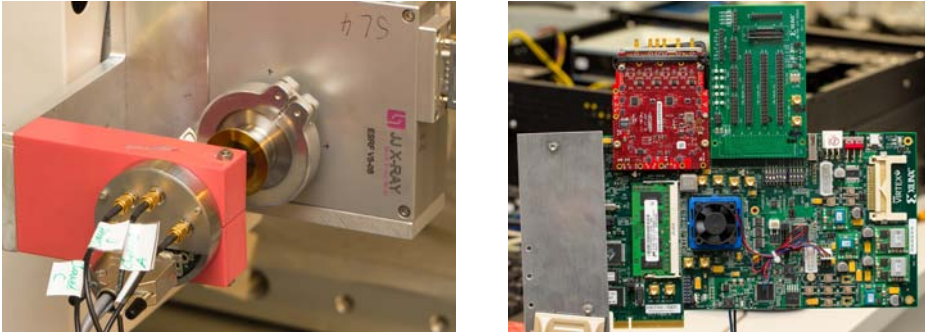


**Figure 3.16:** *Left:* Photo of the detector head containing the quadrant APD as well as the preamplifier PCB as mounted at the beamline P08 at Petra III. *Right:* Photo of the ML605 Virtex 6 evaluation board. The FMC-104 high speed ADC (left) as well as an additional connector board (right) are attached via FMC connectors.

and the offset adjustment are user selectable via a basic terminal application. The details of the operating principle shall not be discussed in this context, the electronic schematics can be found in appendix A.5.

All electronic components (data acquisition PC, FPGA, integrators, power supply as well as the Petra III bunchclock) can be accommodated in a single easily transportable 10HE 19" rack, the only external connections are the 40MHz carrier timing signal (see section 1.3) and a single Ethernet connection to the beamline measurement and control system. A photo of the fully assembled preamplifier module can be found in figure 3.16 left, a photo of the interior of the data acquisition PC including the analog to digital converter as well as the Virtex 6 FPGA is found in figure 3.16.

### 3.5 Conclusion and outlook – Future and current applications of pulse resolved detection schemes

To the very best of our knowledge the work presented here is the first successful approach to continuously measure the intensity and position of individual x-ray pulses at repetition rates of up to 31MHz. The detection and read-out scheme has been verified and commissioned during two experiments carried out beamlines P08 and P10 at Petra III, x-ray energies between 13.6keV and 24keV have been applied. A tremendous dynamic range of  $\leq 250 \frac{\text{photons}}{\text{pulse}}$  at a photon energy of 13.6keV has been demonstrated in the Petra III 40-bunch mode while clearly distinguishing individual photons. Each event is time stamped, allowing for a pulse to pulse characterization of ultrafast changes of molecular structure and interactions in the

number of pixels	$4 \Rightarrow$ position and intensity sensitivity
framing rate	$\leq 31\text{MHz}$
dynamic range @5MHz	$\leq 250 \frac{\text{photons}}{\text{pulse} \cdot \text{pixel}}$
dynamic range @31MHz	$\leq 250 \frac{\text{photons}}{\text{pulse} \cdot \text{pixel}}$
cw dynamic range @5MHz	$1 \cdot 10^9 \frac{\text{photons}}{\text{pixel} \cdot \text{second}}$
cw dynamic range @31MHz	$6 \cdot 10^9 \frac{\text{photons}}{\text{pixel} \cdot \text{second}}$
cw data rate @31MHz	248Mb/s @16bit

**Figure 3.17:** Specifications of the QAPD. Extensive online data analysis can be performed in a medium scale GPU at full data rate.

context of time resolved x-ray diffraction experiments. Online data analysis at a rate of  $\geq 31\text{MHz}$  is performed in a medium scale GPU. Let us summarize the specifications of the QAPD before we turn to a discussion of the tremendously increased experimental possibilities, see table 3.17.

The most straight forward application of the QAPD is connected to the huge cw dynamic range, outranging values obtained for current detector technologies by orders of magnitude due to the inherent linearity of the pulse by pulse readout scheme. This dynamic range leads to a relaxation of the need for x-ray attenuators and simultaneously increases the achievable signal to noise ratio. A temporal binning of the data points is implemented in the GPU, allowing to set basically arbitrary short exposure times down to a single x-ray pulse.

Our primary goal is however to use the QAPD in order to measure fast dynamics of membranes in diffraction (see sections 3.3 and 4.4) and imaging mode, both in equilibrium and driven systems. As illustrated earlier the operating principle of the QAPD allows in these cases for a tremendous reduction in measurement time, extending the range of possible sample systems, scattering experiments and ultimately physiological questions. Furthermore experimental constraints for time resolved experiments are greatly relaxed. Contrary to experiments using high speed choppers or gated pixel detectors, which are limited to dedicated 'low frequency' filling modes, the presented detection scheme is applicable in a much broader parameter range. The QAPD is highly portable and easy to implement into any beamline layout, the only requirement being a reference timing signal. Time resolved experiments are hence no longer limited to specialized end stations. In addition to the significant benefit for time resolved scattering applications, pulse-by-pulse readout will greatly extend existing and open up new experimental techniques. Pulse resolved beam characterization, high speed x-ray photon correlation spectroscopy (XPCS) and x-ray imaging experiments will profit from the greatly enhanced dynamic range, effectively unlimited readout speed and novel normalization procedures.

When compared to concurring approaches (e.g. the AGIPD [108] or the CSPAD [109]) the easy integration into any beamline setup at synchrotron or FEL sources, the high flexibility of the quadrant approach and the comparatively low production cost of  $\leq 10\text{k€}$  make the QAPD an outstanding instrument. Future improvements

include the implementation of fully differential analog signaling, extensive testing of alternative detector front ends (including CVD diamond based, GaAs based and Si based materials) as well as the development of a 1-D line detector based on the presented data acquisition scheme. High resolution time-to-digital converters are already foreseen in the design of the integrator PCB.

Last but not least, let us point out that although the focus of this section lay on experiments carried out at synchrotron sources, the most significant benefit of the described detection scheme will possibly be obtained at Free Electron Lasers (FELs), where ultrafast high dynamic range detectors are needed in order to cope with these highly brilliant x-ray sources.





## 4 Ultrafast dynamics in lipid multilayers excited by Surface Acoustic Waves

*This experimental chapter is devoted to time resolved stroboscopic diffraction experiments on model lipid multilayers excited by Surface Acoustic Waves (SAWs) as well as on pure SAW excited  $LiNbO_3$  substrates. The advanced, dedicated timing system at Petra III (see section 1.3) is commissioned, allowing for phase locked stroboscopic scattering experiments applicable to a broad range of timescales and experimental conditions. After a short introduction to the scattering setup at the P08 we discuss time resolved scattering experiments from pure  $LiNbO_3$  substrates in view of dynamical scattering effects as well as higher harmonic acoustic generation. We then turn to the experiments analyzing SAW induced membrane undulations, presenting the first molecular movie of non-equilibrium shape fluctuations driven by SAWs.*

*The majority of this experimental section is being published at the moment of writing. Contributions from co-authoring scientists are cordially acknowledged.*

### 4.1 The high resolution diffraction beamline P08 at Petra III, DESY, Hamburg

Time resolved scattering experiments from SAW excited lipid bilayers have been performed at an x-ray energy of 18keV at the high resolution diffraction beamline P08, Petra III, DESY [114]. The sample was mounted on a multi-circle diffractometer (Khozu NZD-3) in a horizontal scattering geometry, the x-ray beam being directed along the sound path of the SAW device. To ensure a perfect overlap of the x-ray beam with the acoustically excited area of the SAW device (see section 2.1), the beam was collimated to  $55\mu\text{m} \times 290\mu\text{m}$  (h,v) using a slit system at a distance of approximately 1m as well as a set of collimating compound refractive lenses (CRLs) at a distance of 30m in front of the sample. The x-ray attenuation length of  $28\mu\text{m}$  in  $LiNbO_3$  for the  $(1,0,4)$  Bragg reflection ( $\theta = 7.2306^\circ$  at  $E = 18\text{keV}$ ) is well below the penetration length of the SAW, which is on the order of the acoustic wavelength (see e.g. figure 2.3). The horizontal beam size of  $55\mu\text{m}$  leads to a footprint of  $411\mu\text{m}$  along the sample surface for the  $1,0,4$  reflection, therefore only the acoustically stimulated substrate volume is probed by the x-ray beam. The energy bandwidth after the Si(111) high heat-load monochromator and the Si(311) large offset monochromator was  $\frac{\Delta E}{E} \approx 1 \cdot 10^{-5}$ . Time resolved reflectivity and rocking measurements on standing SAWs were performed using a NaI scintillation counter (Cyberstar, Oxford), the angular step size of  $\frac{1}{10000}^\circ$  for the rocking measurements (figure 4.2) was limited by the mechanical resolution of the Khozu Diffractometer. The nominal horizontal beam divergence in the P08 collimation mode is  $\Delta\alpha_i \approx 8\mu\text{rad} = \frac{5}{10000}^\circ$  (FWHM). The actual horizontal beam divergence as the minimal angular spacing between distinguishable diffrac-

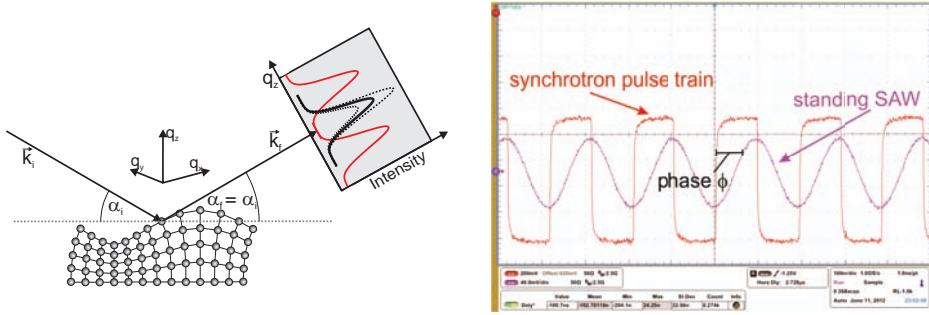


**Figure 4.1:** *Left:* Schematic of a phase locked time resolved scattering experiment on a SAW distorted crystal lattice. The temporal evolution of shape and intensity of a single (i.e. the  $(1,0,4)$ ) Bragg reflection is observed as a function of phase  $\phi$  between the synchrotron pulses and a standing SAW. *Right:* Oscilloscope trace as taken during phase locked SAW generation. Successive synchrotron pulses (red) probe the standing SAW (blue) at a constant phase  $\phi$ .

tion satellites has however been measured to be  $\Delta\alpha_i \approx 28\mu\text{rad}$  (FWHM) during the experiment, see section 4.2.

## 4.2 Results – Pure $\text{LiNbO}_3$ substrates

Time resolved experiments on standing SAWs have been performed by recording the intensity  $I(U, \phi)$  of the  $\text{LiNbO}_3$   $(1,0,4)$  Bragg reflection as a function of phase shift  $\phi$  between the standing wave and the synchrotron bunches, for a given (SAW) radio frequency (RF)-amplitude  $U$ . See figure 4.1 (left) for a sketch of a phase locked stroboscopic scattering experiment using SAW excitation. We will refer to the nominal RF-power  $P_{\text{SAW}} \propto U^2$  after the RF amplifier (see figure 2.2 and 1.10 b)) rather than the RF-amplitude  $U$  when giving experimental numbers. A typical oscilloscope trace as taken during phase locked experiments is depicted in figure 4.1 (right).

### 4.2.1 General remarks on x-ray scattering from a SAW distorted crystal lattice

In order to facilitate the understanding of the complex interplay between scattering related and sample related effects, four main remarks on x-ray scattering from a SAW distorted crystal lattice will be given. We will turn to an extensive discussion of the experimental data in section 4.2 ff.

**1: Kinematic approximation – The instantaneous Debye Waller factor**  
For standing waves,  $I(U, \phi)$  can in strictly kinematic approximation be easily understood in terms of the instantaneous Debye Waller factor  $I(U, \phi) \propto e^{-q_z^2 \sigma(U, \phi)^2}$ , with the effective mean square displacement  $\sigma(U, \phi)$  being proportional to the am-

plitude  $H_1$  of the standing wave (in good approximation also proportional to the amplitude  $\propto U$  of the SAW exciting RF signal) and varying harmonically with the phase  $\phi$  (see 4.3 a)). At an instant  $\phi_0$  the x-ray pulses probe the node of the standing wave, the apparent  $\sigma(U, \phi)$  is hence that of an undistorted substrate and the integrated Bragg-intensity is at its maximum level. At a phase of  $\phi_0 + 90^\circ$  the x-ray pulses probe the crest of the standing wave, leading to a minimum of the diffracted intensity.

**2: Kinematic approximation – Satellite reflections corresponding to a harmonically distorted crystal lattice** Depending on the acoustic wavelength of the SAW, diffraction satellites arising from the SAW modulated substrate [115] (also see section 4.2.5) contribute to the resulting phase and amplitude dependent intensity traces  $I(U, \phi)$ . In case of the fifth harmonic SAW frequency ( $f_{SAW}^5 = 182\text{MHz}$ ,  $L_{SAW}^5 = 20\mu\text{m}$ ) the angular spacing of  $\Delta\theta \approx 0.0016^\circ = 28\mu\text{rad}$  between adjacent diffraction satellites can just be resolved in the time resolved rocking measurements (see section 4.2) and has thus been used as an estimate for the beam divergence  $\Delta\alpha_i$  in the horizontal scattering plane. In case of the first harmonic SAW frequency ( $f_{SAW}^1 = 36.4\text{MHz}$ ,  $L_{SAW}^1 = 100\mu\text{m}$ ) a beam divergence of  $\Delta\alpha_i \approx 28\mu\text{rad}$  leads to an integration over approximately  $N = 5$  diffraction satellites.

**3: Kinematic approximation – The phase problem. Higher acoustic harmonic generation?** It is important to note that in line with the well known phase problem of x-ray scattering only the modulus squared of the instantaneous displacement can be measured as  $I(U, \phi) \propto e^{-q_z^2 \sigma(U, \phi)^2}$  (in the case of purely kinematic diffraction). The measurement of  $I(U, \phi)$  can therefore only provide information on the relative weight of the temporal Fourier components in  $\sigma(U, \phi)^2$ . An analysis of the underlying wave components

$$\sigma(U, \phi)^2 = (a_1(U) \sin(\phi + b_1(U)) + a_2(U) \sin(2(\phi + b_2(U))) + \dots)^2 \quad (4.17)$$

can be carried out by modeling  $I(U, \phi)$  by a superposition of a minimal set of basis functions  $I(U, \phi) = \sum_i a_i(U) \sin(i \cdot (\phi + b_i(U)))$ . The generation of higher order acoustic harmonics has been discussed as one possible approach of understanding the data presented in section 4.2.4. Although the observed effects can now be clearly attributed to dynamical scattering phenomena as detailed in the following, the discussion on higher acoustic harmonics will be shortly summarized in section 4.2.5 to avoid possible future pitfalls.

**4: Dynamic scattering** Dynamical scattering effects have to be taken into account for diffraction experiments on highly oriented  $LiNbO_3$  single crystals [116, 117]. Extinction effects strongly influence the shape and intensity of individual Bragg reflections since the linear attenuation length  $1/\mu_x \approx 27.3\mu\text{m}$ <sup>9</sup> is

<sup>9</sup> [http://henke.lbl.gov/optical\\_constants/atten2.html](http://henke.lbl.gov/optical_constants/atten2.html)

more than one order of magnitude larger than the extinction length  $\chi \approx 1.2\mu\text{m}$  for the undistorted  $\text{LiNbO}_3$   $(1,0,4)$  reflection. The Darwin width  $\Delta\theta_D$  of the  $(1,0,4)$  Bragg reflection is  $\Delta\theta_D = 18.6\mu\text{rad}$ <sup>10</sup>. Given a horizontal beam divergence of  $\Delta\alpha_i \approx 28\mu\text{rad}$  (as estimated in section 4.2) during the experiment an angular integration exceeding the intrinsic width of the  $(1,0,4)$  Bragg reflection is performed even without sample rotation. It is then straightforward to show that a small distortion, or an increase in mosaicity, leads to an increase of the integrated intensity (see 4.3) rather than a decrease with respect to a perfectly ordered crystal lattice. In other words, the increase in extinction length in the dynamical theory of x-ray diffraction [47] over-compensates the intensity decrease due to the Debye Waller factor in the kinematic approximation.

It is in general extremely challenging to disentangle these counter acting effects in a time resolved diffraction experiment. Phase dependent rocking measurements complementing intensity traces  $I(U, \phi)$  have been performed in order to shed light on this issue.

#### 4.2.2 Time resolved measurements of the rocking curve at the first and fifth harmonic SAW frequency

The two characteristic length scales of the SAW, namely its wavelength  $L$  and its amplitude  $H_1$  can be extracted from time (i.e. phase) resolved rocking curves around the  $(1,0,4)$  Bragg reflection, see figure 4.2. As shown in [118], the transverse acoustic amplitude  $H_1 = \frac{Nd}{2\pi}$  can be expressed in terms of the inter planar spacing  $d = 2.5741\text{\AA}$  of the  $1,0,4$ -reflection and the number of observable satellite reflections  $N$ . For the first harmonic SAW frequency  $f_{SAW}^1 = 36.4\text{MHz}$ , the instrumental resolution is however not sufficient to distinguish between individual satellite reflections since  $q_x = \frac{2\pi}{\lambda}(\cos(\alpha_i) - \cos(\alpha_f)) = \frac{2\pi}{L}$  becomes too small for large  $L$ . Assuming however a linear relation between  $\dot{U}$  and  $H_1$  and given the results of section 4.2.5 the amplitude of the SAW in case of the first harmonic can be estimated to be  $H_1 = 16 \cdot 0.6334\text{\AA} \approx 10\text{\AA}$  for  $P_{SAW} = 27\text{dBm}$  (an amplitude of  $0.6334\text{\AA}$  has been measured for  $P_{SAW} = 15\text{dBm}$ ), corresponding to a broadening of the rocking curve by a number of  $N = H_1 2\pi/d \approx 23$  experimentally unresolved satellite reflections. In case of the fifth harmonic frequency  $f_{SAW}^5 = 182\text{MHz}$  the amplitude is determined to be  $H_1 = 3.51\text{\AA}$  for  $P_{SAW} = 27\text{dBm}$ , deviating slightly from the results ( $H_1 = 1.97\text{\AA}$ ) obtained in section 4.2.5 by comparing experimentally determined modulation amplitudes in  $I(U, \phi)$  to basic prediction of kinematic scattering theory, i.e. equation 4.19. The angular spacing of  $\Delta\theta = 0.0016^\circ$  is in perfect agreement with the expectation for the SAW wavelength ( $L_{SAW}^5 = 20\mu\text{m}$  for  $f_{SAW}^5 = 182\text{MHz}$ ).

Let us briefly discuss the rocking curve measurements in terms of dynamical and kinematic scattering effects. Without SAW or at nodes of the standing waves the  $\text{LiNbO}_3$  single crystal is perfect enough to be described by dynamical scattering.

<sup>10</sup><http://sergey.gmca.aps.anl.gov/x0h.html>

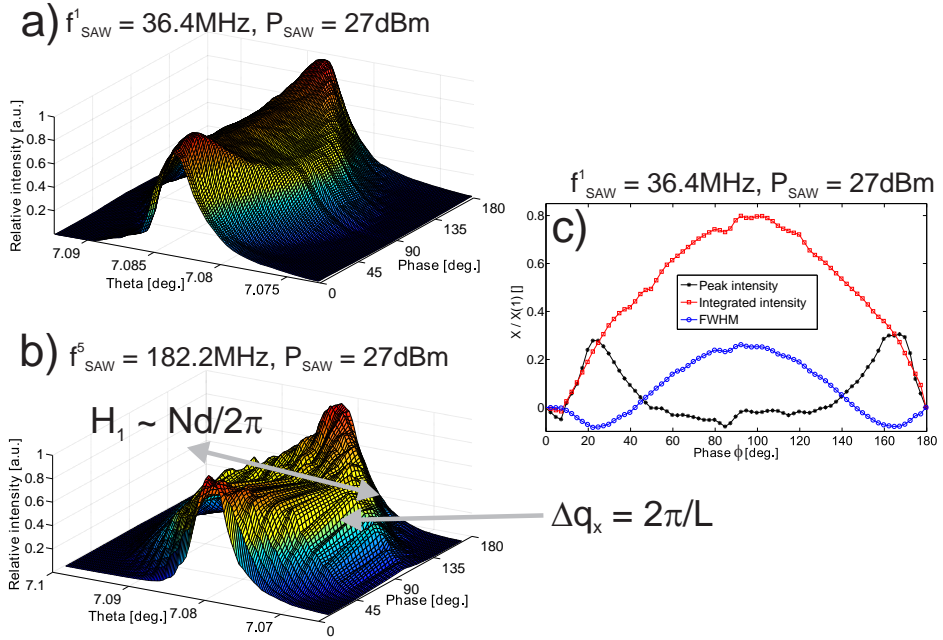


**Figure 4.2:** Rocking curves of the  $LiNbO_3$   $(1,0,4)$  reflection as a function of phase (i.e. delay time). The peak intensity and width oscillate with the standing wave excitation in a characteristic manner, reflecting the length scales of the SAW (amplitude, wavelength). **a)** The broadening originates from side reflections (satellite peaks) induced by the SAW, which can not be resolved for the 1st harmonic. **b)** Contrarily, for smaller wavelengths, i.e. the 5th SAW harmonic distinct satellite reflections appear for  $\phi \neq \phi_0$ . The angular spacing  $\Delta\theta = 0.0016^\circ$  of these side reflections is in perfect agreement with the expectation ( $L_{SAW}^5 = 20\mu\text{m}$  for  $f_{SAW}^5 = 182\text{MHz}$ ). From the number of observable diffraction satellites, the SAW amplitude can be determined [117, 118]. **c)** Relative changes in peak intensity (stars, black), integrated peak intensity (squares, red), and full width at half maximum (FWHM, circles, blue) of the rocking curves shown in (a), as a function of phase  $\phi$ . A sharpening of the reflection for  $\phi \approx 25^\circ$  and  $\phi \approx 165^\circ$  is observed accompanied by a steep increase of the intensity at the ridge of the rocking curve. This effect can be attributed to an increased extinction length  $\chi$  induced by the SAW at small amplitudes. A transition from dynamical to kinematic scattering regimes occurs as soon as  $\chi$  becomes equal to the linear attenuation length  $1/\mu_x$ . As soon as the kinematic regime is reached, the peak intensity is reduced by the Debye-Waller factor, while the integrated intensity increases due to the satellites (i.e. the broadening). Analysis of these three observables thus allows for the disentanglement of dynamical and kinematic scattering effects of the  $LiNbO_3$  crystal distorted by the SAW.

When the amplitude of the SAW increases, the extinction length  $\chi$  of the reflection extends by the lattice distortion of the SAW accompanied by a sharpening of the rocking curve. A transition from dynamical to kinematic scattering regime occurs as soon as  $\chi$  becomes equal to the linear attenuation length  $1/\mu_x$ . Since the SAW amplitude oscillates as a standing wave, this transition occurs at  $4f_{SAW}$  (for increasing / decreasing amplitudes as well as positive and negative displacements) and can be identified from the phase dependent plots of the three rocking curve parameters: peak intensity, integrated intensity as well as the width (FWHM), see figure 4.2.

Let us first identify the node of the standing wave denoted as  $\phi_0$  below. Due to uncertainties related to cable lengths and the electro-mechanical interaction at the IDTs,  $\phi_0$  is not known a priori. However, it can be extracted from figure 4.2 because nodes of the standing wave strictly occur at a phase difference of  $\Delta\phi = 180^\circ$ . Therefore the minimal of the FWHM curve cannot correspond to nodes of the standing wave. Instead,  $\phi_0$  can be identified with the minimum of the integrated intensity at  $\phi \approx 5^\circ$  in figure 4.2. The further interpretation of the intensity traces  $I(U, \phi)$  below is based on this identification of  $\phi_0$  and the assumption that a *mild* increase of SAW amplitude  $0\text{\AA} \leq H_1 \leq 3\text{\AA}$  leads to an increase of the peak intensity due to a reduction of extinction effects (dynamical scattering theory) whereas high SAW amplitudes  $H_1 \geq 3\text{\AA}$  lead to a decrease of diffraction intensity due to the Debye-Waller factor in kinematic scattering theory. This view is further supported by the  $U$  dependence of  $I(U, \phi)$  as discussed below in 4.2.3 and 4.2.4. As further justification we note that in contrast to the peak intensity, the integrated peak intensity in figure 4.2 follows the SAW excitation with a sinusoidal response, which is expected since it corresponds to the sum over  $N \approx 23$  side reflections (satellites) which increase with  $\sigma^2$  and can be described in kinematic approximation.

### 4.2.3 Measurements at the fifth harmonic SAW frequency

The first example of a  $I(U, \phi)$  data set, displayed as a function of phase and RF-power is shown in figure 4.3 a), recorded at the fifth harmonic  $f_{SAW}^5 = 182\text{MHz} = 35 \cdot f_b = 5 \cdot f_{SAW}^1$ . At small  $P_{SAW}$  only thermal heating and a corresponding average decrease of scattering intensity is observed, independent of phase  $\phi$ . For  $P_{SAW} \geq 20\text{dBm}$  the intensity of the  $(1,0,4)$  Bragg reflection starts to follow the harmonic signal of the exciting RF-field. More precisely, the signal variation  $\Delta I(U, \phi)$  is in good approximation proportional to the square of the amplitude. Changes in the peak intensity can be expected to be proportional to the squared instantaneous real space amplitude  $\Delta I(U, \phi) \propto \pm \sigma^2(U, \phi) = a_1(U) \sin^2(\phi + b_1)$  for  $q_z \sigma \leq 1$ , as soon as the functional dependence on the SAW can be linearized for small amplitudes  $\sigma$ . The sign of  $\pm \sigma^2(U, \phi)$  depends on the process under investigation. It will be positive if the SAW changes the acceptance and/or extinction length  $\chi$  and thereby the Bragg peak reflectivity, or it will be negative if the dependence is described by a Debye-Waller factor. Note that in both cases  $\sigma$  is an effective amplitude. Since the SAW amplitude decreases exponentially with depth in the substrate it must be distinguished from the SAW amplitude  $H_1$  directly at the sample surface. In

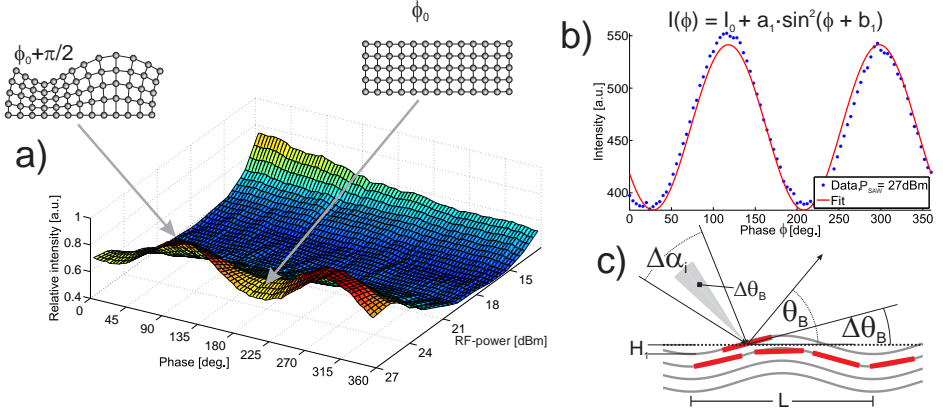


**Figure 4.3:** **a)** The intensity of the  $LiNbO_3$  1,0,4-Bragg reflection measured as a function of phase  $\phi$  and RF-power, as recorded for the 5th harmonic ( $f_{SAW}^5 \approx 182$  MHz). The average slope of the intensity trace can be attributed to thermal heating for  $P_{SAW} \leq 21$  dBm, before the coherent motion of the substrate atoms becomes observable for  $P_{SAW} \geq 21$  dBm. The stroboscopic nature of the time resolved experiment provides snapshots of the instantaneous atomic displacements induced by the standing acoustic wave. **b)** For  $P_{SAW} \geq 21$  dBm  $I(U, \phi)$  could well be modeled by the distortion  $\Delta I(U, \phi) = a_1(U) \sin^2(\phi + b_1)$  corresponding to a single component wave. **c)** The distortion of the crystal lattice due to a SAW leads to an increased acceptance angle  $\Delta\theta_b$  of a given reflection. For an acceptance angle  $\Delta\theta_b \leq \Delta\alpha_i$  smaller than the divergence  $\Delta\alpha_i$  of the primary beam this will lead to an increased reflected intensity. A rough estimation for  $L = 100 \mu\text{m}$  and  $H_1 = 3 \text{ \AA}$  yields an increase of the acceptance angle by approximately  $12 \mu\text{rad}$ .

light of the results displayed in figure 4.2 and the discussion above, we attribute the observed behavior to the changed properties of the dynamically scattering reflection.

#### 4.2.4 The first harmonic SAW frequency

Let us now turn to the  $I(U, \phi)$  dataset of the 1st harmonic frequency ( $f_{SAW}^1 = 36.4 \text{ MHz} = 7 \cdot f_b$ , figure 4.4). Since the coupling of the RF field to the SAW is higher than for the 5th harmonic, larger amplitudes  $\sigma$  and a transition from dynamical to kinematic scattering can be expected. For  $P_{SAW} \leq 17$  dBm  $I(U, \phi)$ , the signal is well described by the  $\Delta I \propto \sin^2(f_{SAW})$  behavior, which we already observed in the case of the 5th. harmonic. It essentially corresponds to a single standing wave of frequency  $f_{SAW}^1$ . For  $P_{SAW} \geq 17$  dBm, a splitting of the intensity maxima in  $I(U = \text{const.}, \phi)$  is observed, indicating a transition from dynamical to kinematic scattering regimes. We therefore put forward the interpretation based on an interplay between kinematic and dynamical scattering effects, in line with the argumentation presented in section 4.2.3. For low RF-powers  $P_{SAW} \leq 17$  dBm

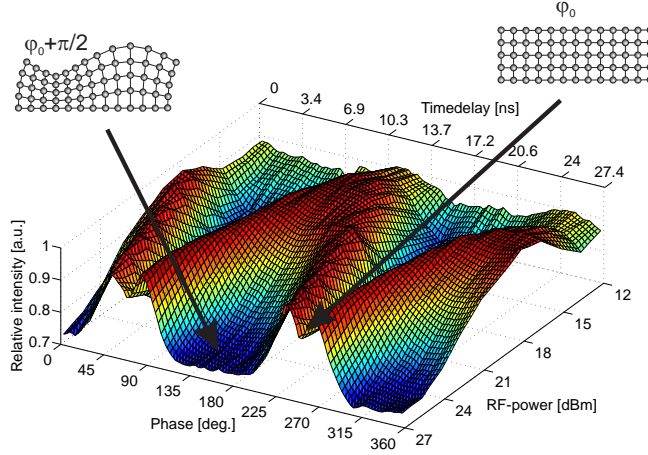


**Figure 4.4:** The intensity of the  $\text{LiNbO}_3$  1,0,4-Bragg reflection measured as a function of phase  $\phi$ , and RF power, as recorded for the fundamental, i.e. the 1st harmonic frequency. A harmonic intensity trace directly reproducing the SAW frequency can only be observed for  $P_{SAW} \leq 17\text{dBm}$ . For  $P_{SAW} \geq 17\text{dBm}$ , a splitting of the intensity maxima is observed. In the main text, this pattern is interpreted based on a transition from dynamical to kinematic scattering regimes.

crests of the standing wave lead to an increase in scattering intensity due to dynamical effects, as discussed for the 5th harmonic. For  $P_{SAW} \geq 17\text{dBm}$ , linear absorption of x-ray radiation dominates over extinction effects, i.e. a transition from dynamical to kinematic scattering regimes takes place. Now the peak amplitude of the standing wave leads to a decrease of diffraction intensity due to the Debye-Waller factor.

An exact description in terms of detailed dynamical scattering equations is beyond the scope of this thesis. But it becomes evident that the accurate control of phase between the standing acoustic wave and the synchrotron bunches as implemented in this thesis has proven to be absolutely indispensable for the data interpretation. Measurement artifacts evoked by any electronic or mechanical effects in the IDTs can be excluded.

#### 4.2.5 Higher acoustic harmonic generation?

As already discussed, for  $P_{SAW} \geq 17\text{dBm}$  a splitting of the intensity maxima in  $I(U = \text{const.}, \phi)$  is observed (see figure 4.4), resulting in a curve which appears to be effectively frequency doubled. Increasing the RF-power beyond 22dBm strongly attenuates the frequency doubling effect in  $I(U = \text{const.}, \phi)$ , corresponding again to a single standing wave of frequency  $f_{SAW}^1$ , phase shifted by  $\frac{\pi}{2}$ .



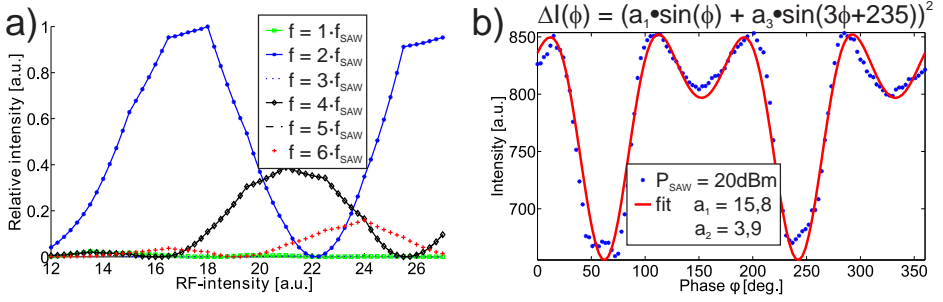


**Figure 4.5:** **a)** The frequency components dominating  $I(\phi)$  can be quantified in terms of the power spectral density (PSD)  $\mathcal{P}SD(U, f) = |\mathcal{F}(I(\phi))|^2$ . The most prominent spectral components are  $\mathcal{P}SD(2f_{SAW})$ ,  $\mathcal{P}SD(4f_{SAW})$ ,  $\mathcal{P}SD(6f_{SAW})$ . **b)**  $\Delta I(U, \phi)$  can be modeled by the instantaneous displacement  $\sigma(U, \phi)$  corresponding to a standing wave of frequency  $f_{SAW}^1$  along with a wave component  $a_3$  corresponding to the third acoustic harmonic  $\sigma(U, \phi) = a_1(U) \sin(\phi) + a_3(U) \sin(3 \cdot \phi + 235)$ . The relative weight of both components  $a_{1,3}$  can be fitted to  $\frac{a_1}{a_3} = \frac{1}{0.25}$  for the displayed case of  $P_{SAW} = 12\text{dBm}$ .

An empirical quantification of the observed effects can be made in terms of the power spectral density (PSD)  $\mathcal{P}SD(U, f) = |\mathcal{F}(I(U, \phi))|^2$ , see figure 4.5 (left). The RF-amplitude dependent PSD is dominated by an alternating behavior of the second, fourth and sixth Fourier component.

Since not amplitudes but intensity signals are recorded, a decomposition of the frequency components must be based on the trigonometric relation  $\sin(x) \sin(y) = \frac{1}{2}(\cos(x-y) - \cos(x+y))$ . Let us assume a superposition of three harmonic SAW frequencies by modeling the SAW as  $\sigma(\phi) = a_1 \sin(\phi) + a_2 \sin(2\phi) + a_3 \sin(3\phi)$ . Applying  $\sin(x) \sin(y) = \frac{1}{2}(\cos(x-y) - \cos(x+y))$  and comparing the arguments of the resulting cos functions (see equation 4.18) allows for a rough description of the Fourier components  $\mathcal{P}SD(n \cdot f_{SAW})$  of  $I(U, \phi)$  in terms of the coefficients  $a_{1,2,3}(U)$ .

$$\begin{aligned}
 I(\phi) &\propto (a_1 \sin(\phi) + a_2 \sin(2\phi) + a_3 \sin(3\phi))^2 & (4.18) \\
 &= a_1^2 \sin^2(\phi) + 2a_1a_2 \sin(\phi) \sin(2\phi) + a_2^2 \sin^2(2\phi) + 2a_1a_3 \sin(\phi) \sin(3\phi) \\
 &\quad + 2a_2a_3 \sin(2\phi) \sin(3\phi) + a_3^2 \sin^2(3\phi) \\
 &= \frac{1}{2}(a_1^2 + a_2^2 + a_3^2) + \underbrace{a_1a_2 \cos(\phi) + a_2a_3 \cos(\phi)}_{\mathcal{P}SD(1 \cdot f_{SAW})} - \underbrace{\frac{1}{2}a_1^2 \cos(2\phi) + a_1a_3 \cos(2\phi)}_{\mathcal{P}SD(2 \cdot f_{SAW})} \\
 &\quad - \underbrace{a_1a_2 \cos(3\phi)}_{\mathcal{P}SD(3 \cdot f_{SAW})} - \underbrace{\frac{1}{2}a_2^2 \cos(4\phi) - a_1a_3 \cos(4\phi)}_{\mathcal{P}SD(4 \cdot f_{SAW})} - \underbrace{a_2a_3 \cos(5\phi)}_{\mathcal{P}SD(5 \cdot f_{SAW})} - \underbrace{\frac{1}{2}a_3^2 \cos(6\phi)}_{\mathcal{P}SD(6 \cdot f_{SAW})}
 \end{aligned}$$

Given that the first as well as the the third harmonic components of  $I(U, \phi)$  do

Fourier component	SAW coefficients
$PSD(1 \cdot f_{SAW})$	$a_1 a_2 + a_2 a_3$
$PSD(2 \cdot f_{SAW})$	$a_1^2 + a_1 a_3$
$PSD(3 \cdot f_{SAW})$	$a_1 a_2$
$PSD(4 \cdot f_{SAW})$	$a_2^2 + a_1 a_3$
$PSD(5 \cdot f_{SAW})$	$a_2 a_3$
$PSD(6 \cdot f_{SAW})$	$a_3^2$

**Figure 4.6:** By comparing the coefficients of the cosine functions in 4.18, the amplitudes of the underlying wave components  $a_{1,2,3}(U)$  contributing to the  $n$ 'th harmonic component  $PSD(n \cdot f_{SAW})$  of the power spectral density can be obtained.

not enter the power spectral density at a significant magnitude (see figure 4.5 left) we can exclude a significant contribution of the second harmonic frequency. This assumption is further supported by modeling  $I(U, \phi)$  over a broad parameter range as well as a broad range of basis functions. The quantitative functional form of  $I(U, \phi)$  could only be modeled for  $I(U, \phi) \propto +q_z^2 \sigma^2(U, \phi)$  and  $\sigma(U, \phi)$  written as a superposition of the first and third harmonic, see e.g. figure 4.5 (right).

It becomes clear that the 'frequency doubling effect' observed for  $I(U, \phi)$  could only be attributed to a preferential generation of the third acoustic harmonic, while second harmonic generation is negligible. Given the theoretical predictions for the generation of higher acoustic harmonics (equations 2.6) as well as the results obtained in section 2.1 the preferred generation of the third acoustic harmonic over the second harmonic is however very unlikely.

#### 4.2.6 Analytic calculation of the structure factor of a SAW distorted crystal lattice in kinematic approximation

It has been shown [115] that the intensity of the  $m$ th order diffraction satellite for SAW excited substrates is in kinematic approximation proportional to

$$I_m \propto \int_0^z dz e^{-\mu_x z} J_m(H_1 q_z e^{-\mu_{ac} z}), \quad (4.19)$$

with  $H_1$  the amplitude of the SAW.  $\mu_x$  and  $\mu_{ac}$  are the penetration depth of the x-ray beam and the acoustic wave. For time (phase) resolved experiments on standing SAWs, a pure sinusoidal variation  $H_1(\phi) = H_1 \sin(\phi)$  of the wave amplitude can be assumed for the vertical wave component. Longitudinal variations of the lattice constant do not lead to an intensity change in this scattering geometry. The zeroth order satellite intensity  $I_0(H_1, \phi)$  is plotted in figure 4.7 as a function of  $H_1$  and  $\phi$  for the first and fifth harmonic SAW frequency. For  $\phi = 90^\circ$  the intensity  $I(H_1, 90)$  is maximally affected by the Debye-Waller factor  $I(H_1, 90) \propto e^{-q_z^2 H_1^2}$ . Cuts of  $I(H_1, \phi)$  for small (constant)  $H_1$  match the experimental results.

The SAW amplitude can be determined by modeling the experimental data  $I(U, \phi)$  with the predicted shape 4.19 as a function of  $H_1$ . Due to the complexity

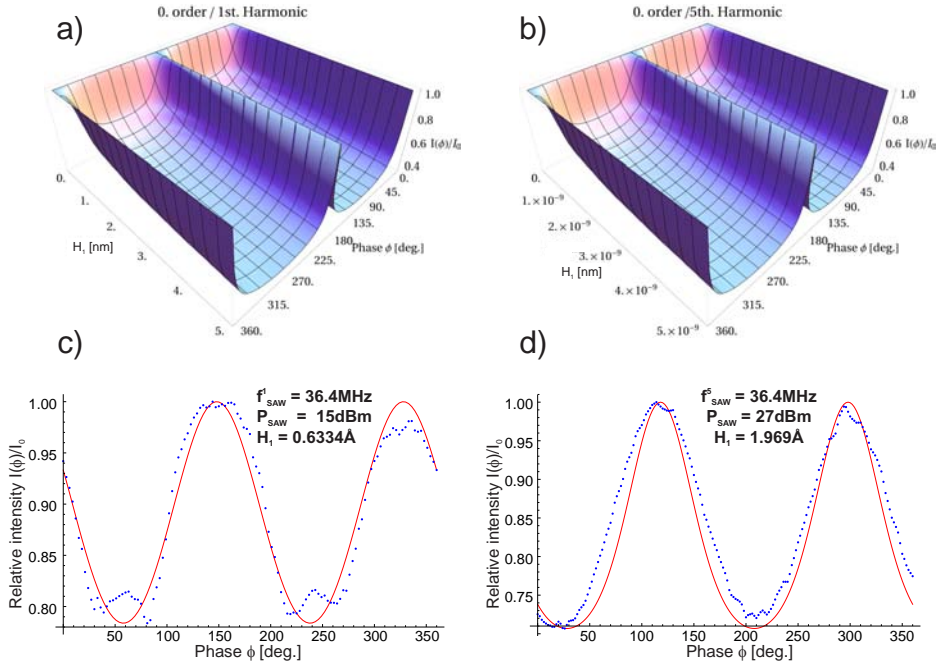


**Figure 4.7:** The intensity  $I(H_1, \phi)$  of the zeroth order diffraction satellite follows the  $\propto \exp(\sigma^2 \sin(\phi)^2)$  behavior expected for a periodic modulation of the crystal lattice. No qualitative differences are observed for excitations by the first (a) and fifth (b) harmonic SAW frequency. No (apparent) higher harmonic generation appears in this strictly kinematic framework. The SAW amplitude was determined from equation 4.19 to  $H_1 = 0.6334\text{\AA}$  (first SAW harmonic, c) and  $H_1 = 1.969\text{\AA}$  (fifth SAW harmonic, d). These values correspond to the small amplitude regime before the onset of more complicated scattering effects change the functional form of the  $I(U, \phi)$  curves, leading to an apparently an-harmonic pattern.

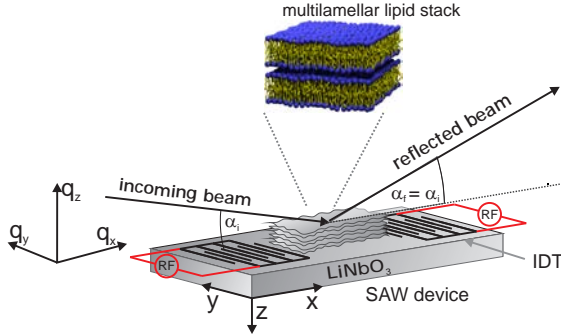


**Figure 4.8:** Schematic of a phase locked time resolved x-ray reflectivity experiment on a SAW excited multilamellar lipid stack. Standing waves are generated by applying an RF signal to the metallic IDTs.

of the observed effects only datasets displaying a clear harmonic / monochromatic intensity trace  $I(U, \phi)$  have been taken into account (mostly recorded for low RF-amplitudes  $U$ ), the experimental shape is in these cases well reproduced by the model, see figure 4.7. The SAW amplitude  $H_1$  was determined to  $H_1^5 = 1.97 \text{ \AA}$  for  $P_{SAW} = 27 \text{ dBm}$  in case of the fifth harmonic SAW frequency and  $H_1^1 = 0.63 \text{ \AA}$  at  $P_{SAW} = 15 \text{ dBm}$  for  $f_{SAW}^1 = 36.4 \text{ MHz}$ . Although equation 4.19 is strictly limited to kinematic scattering and can therefore not describe the observed dynamical effects (section 4.2) in full detail, these estimations are valid even for phenomenologically different processes as soon as the functional dependence on the SAW can be linearized for small amplitudes  $\sigma$  since  $\Delta I = \pm q^2 \sigma^2 \propto \exp(\pm q^2 \sigma^2)$  for  $q_z \sigma \leq 1$ . Let us now turn to the most important part of this chapter: the SAW induced effects in lipid membranes deposited on the SAW devices.

### 4.3 Results – Lipids excited by SAWs of Rayleigh type

With a detailed analysis of the pure  $LiNbO_3$  substrate at hand, the same SAW device was used to excite lipid membranes (1,2-dioleoyl-sn-glycero-3-phosphocholine, DOPC) deposited on the device as multi-bilayers with the first harmonic SAW frequency  $f_{SAW} = 36.4 \text{ MHz}$ , see figure 4.8 for a sketch of the experimental situation.

In line with section 4.2.3 and section 4.2.4 the integrated intensity  $I(h, U, \phi)$  of the first six Bragg reflections ( $1 \leq h \leq 6$ ) of the multilamellar lipid stack was measured as a function of phase  $\phi$  for  $P_{SAW} = 27 \text{ dBm}$  and  $P_{SAW} = 21 \text{ dBm}$ . Three successive identical measurements have been performed in each case, individual intensity traces were perfectly reproduced. The averaged  $I(h, U, \phi)$  have been modeled by an eighth order Fourier series ( $I(h, U, \phi) = a_0(h, U) \cdot \sum_{i=1}^8 a_i(h, U) \cdot \cos(\phi) + b_i(h, U) \cdot \sin(\phi)$ , see figure 4.9) in order to analyze the leading spectral components and obtain a set of parameters  $a_i, b_i$  well describing the experimental data in the following analysis.

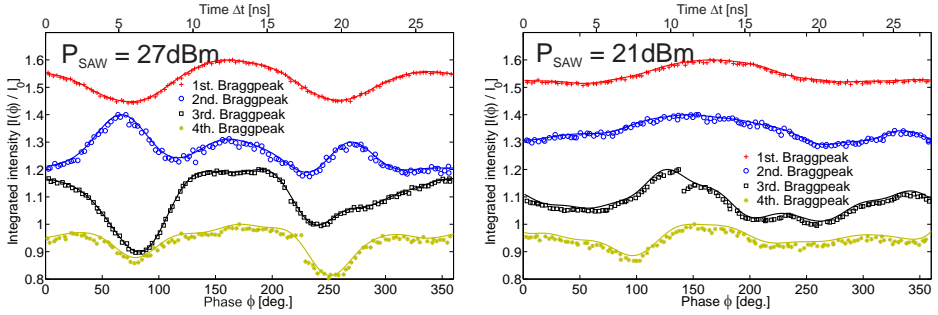


**Figure 4.9:** The integrated intensities  $I(h, U, \phi)$  of the first four diffraction orders  $h$  of the multilamellar lipid stack, averaged over three identical successive measurements in each case, plotted as a function of relative phase  $\phi$  for (left)  $P_{SAW} = 27\text{dBm}$  and (right)  $P_{SAW} = 21\text{dBm}$ . The individual intensity traces  $I(h, U, \phi)$  are strictly out of phase, pointing to a complex interaction between the SAW and the lipid multilayer. It is further noteworthy that the  $I(\phi)$  are strictly periodic for phase shifts of  $\Delta\phi = 360^\circ$  but not for phase shifts of  $\Delta\phi = 180^\circ$ . The plots have been shifted for clarity.

The measured  $I(h, U, \phi)$  exhibit three particularly striking features which cannot be explained by a single fingerprint of a SAW induced Debye-Waller factor:

1. The intensity traces corresponding to different reflection orders  $h$  are out of phase as it is most obvious for  $P_{SAW} = 27\text{dBm}$ , figure 4.9 left.
2. The functional form of  $I(h, U, \phi)$  does not match the sinusoidal of the exciting SAW for each order of reflection. Most eye-catching is the course of the second reflection for  $P_{SAW} = 27\text{dBm}$  which exhibits three intensity maxima for one period of the SAW.
3.  $I(h, U, \phi)$  is in general not (completely) symmetric for phase shifts of  $\Delta\phi = 180^\circ$  but symmetric for phase shifts of  $\Delta\phi = 360^\circ$ .

These observations have been confirmed by various complementary measurements including time resolved experiments on different lipid model systems during a following beamtime. Data screening and analysis is in progress at the moment of writing, details on these measurements will be given in a later publication.

Given observation (1) we do not include a SAW induced Debye-Waller factor in the data interpretation. Time resolved rocking and reflectivity measurements have been performed in order to disentangle possible form-factor effects corresponding to changes of individual bilayers from structure-factor effects corresponding to changes of the inter- and intra bilayer correlation functions, see figure 4.10 and 4.11. A slight variation of the peak positions in the reflectivity measurements, as observed e.g. in 4.10 and 4.11 for the first Bragg reflection, can clearly be attributed to thermal heat effects as observed changes are dependent on the acquisition number (i.e. the integral exposure time) rather than  $\phi$ .

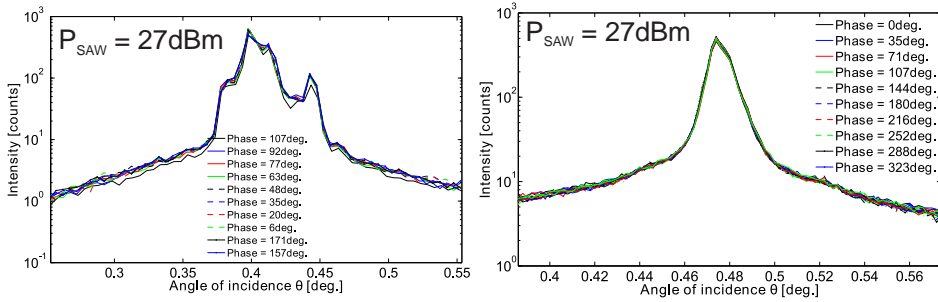


**Figure 4.11:** **Left:** No changes of the rocking curve apart from small intensity effects are detected for a variation of phase  $\phi$  in the case of pure DOPC samples. In particular the broad diffuse plateau is not affected by the Surface Acoustic Wave. The unusual high mosaicity / disorder of lipid multilayers prepared on  $LiNbO_3$  substrates leads to the broad and distorted shape of the rocking curve. **Right:** A qualitatively identical diagnosis is made in the case of Texas Red labeled DOPC multilayers. The improved overall sample quality is attributed to the fresh and hence uncontaminated substrate of the SAW device used in this case.

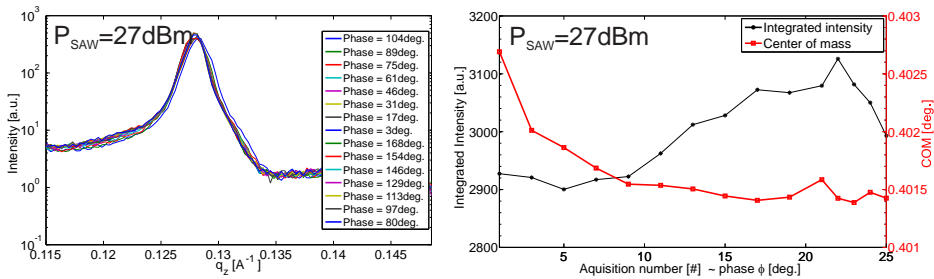


**Figure 4.10:** **Left:** Time resolved reflectivity measurements show a slight shift of the Bragg peak positions towards lower  $q_z$ . This variation can be attributed to pure thermal heat effects due to the Surface Acoustic Wave, the corresponding center of mass (COM, **right**) displays a saturating behavior as a function of acquisition number rather than an ultrafast effect which would vary as a function of phase.

Rocking measurements on lipid multilayers prepared on  $LiNbO_3$  SAW devices display a broad / distorted shape which can be attributed to a high degree of disorder / mosaicity of the bilayer stack, see 4.11. The broad plateau of diffuse scattering does not vary as a function of  $\phi$ , it can therefore be concluded that the structure factor  $S(q_r, q_z)$  and hence the inter- and intra- bilayer correlations are not affected by the standing Surface Acoustic Wave, at least not in ways which affect the present conclusions.

As the shape and position of the reflections (as quantified by the FWHM in

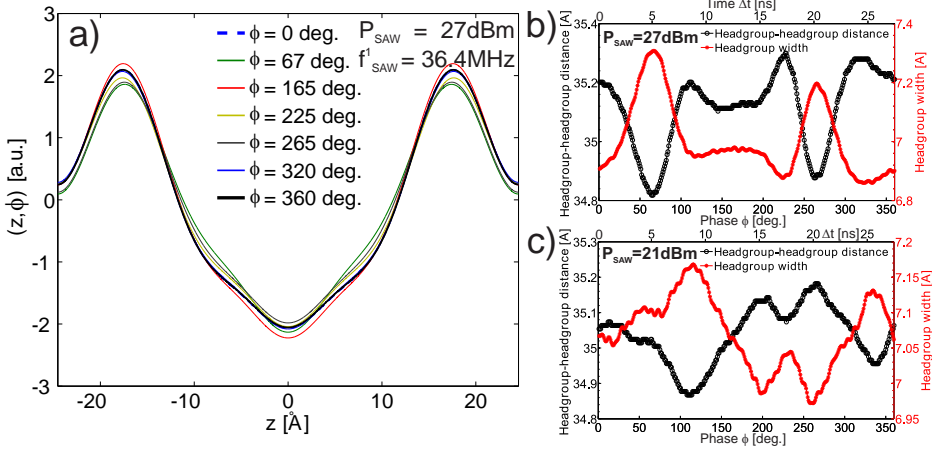


**Figure 4.12:** **a)** A molecular movie of lipid bilayer fluctuations could be reconstructed from the phase dependent intensity traces  $I(h, U, \phi)$  by the well known Fourier synthesis method. Pronounced variations of the resulting relative electron density  $\Delta\rho(z, \phi)$  in the headgroup region accompanied by a variation of membrane thickness can clearly be observed. Characteristic bilayer parameters (headgroup-headgroup distance and headgroup width) have been extracted from the time dependent electron density profiles for  $P_{SAW} = 27\text{dBm}$  (**a**) and  $P_{SAW} = 21\text{dBm}$  (**b**). The qualitative influence of the standing SAW on the bilayer structure agrees for both RF-powers apart from a phase retardation of  $\Delta\phi \approx 50^\circ \hat{=} \Delta t = 3.8\text{ns}$ .

both  $q_r$  or  $q_z$  and the center of mass) do not change as a function of  $\phi$ , the observed  $I(h, U, \phi)$  variations must be attributed to form-factor changes and hence structural changes on the level of single bilayers. Therefore, the next step is to reconstruct the relative electron density profile  $\Delta\rho(z)$  from the measured  $I(h, U, \phi)$  by means of the standard Fourier synthesis method, see section 2.3. The initially unknown phase factors  $\nu_h \in [-1, +1]$  have been taken from the literature [30]. The  $\nu_h$  have been assumed to be constant over the whole time range as changes of  $\nu_h$  would be connected to an unobserved zero crossing of the corresponding Bragg intensity for continuous structural changes. Furthermore absolute values of  $F(q_z(h))$  have been calculated by scaling the integrated peak intensities  $I(q_z(h))$  obtained in reference reflectivity experiments under matching ambient conditions by relative variations of  $I(h, U, \phi)$  measured in the current time resolved experiments. By this procedure, the comparatively poor sample quality of lipid multilayers on  $LiNbO_3$  substrates did not affect the data analysis.

The resulting  $\Delta\rho(z)$  are depicted in figure 4.12. Pronounced variations of the resulting relative electron density  $\Delta\rho(z, \phi)$  in the headgroup region ( $z \approx \pm 17\text{\AA}$ ) as well the hydrophobic core ( $z \approx 0\text{\AA}$ ) accompanied by a variation of membrane thickness can clearly be observed. Characteristic bilayer parameters (headgroup-headgroup distance and headgroup width) have been extracted from the time

dependent electron density profiles for figure 4.12 a)  $P_{SAW} = 27\text{dBm}$  and figure 4.12 b)  $P_{SAW} = 21\text{dBm}$ . The qualitative influence of the standing SAW on the bilayer structure matches for both RF-powers apart from a phase retardation of  $\Delta\phi \approx 50^\circ$ .

The structural changes can be qualitatively attributed to the interaction between the electric field accompanying the SAW (see section 2.1) and the strongly dipolar lipid headgroups. At crests of the standing SAW, corresponding to maxima of the associated electric field, a membrane thinning as well as a broadening of the headgroup region can be expected. We thus attributed the observed maxima of the headgroup width at  $\phi \approx 70^\circ$  in figure 4.12 a) and figure 4.12 b)  $\phi \approx 115^\circ$  in to the maxima of the standing SAW field. The polarized nature of the lipid headgroups leads to a strong dipole moment, i.e.  $D \approx 16\text{Debye} = 5.34 \cdot 10^{-29}\text{Cm}$  for the PC-headgroup. Due to the tendency of the lipid headgroup to shield the hydrophobic interior and due dipole-dipole interactions the headgroup orientation in zero field is tilted by  $\alpha \approx 60^\circ$  with respect to the surface normal [10]. The broadening of the headgroups observed in figure 4.12 can now qualitatively be explained by an alignment along the field vector of the acousto-electric wave. The maximal amplitude  $E$  of the electric field accompanying the SAW can be estimated from the gradient of the potential  $\Psi$  (see section 2.1 and [82]) to  $E = 2 \cdot 10^5\text{V/m}$ . By switching on the field, the potential energy change  $W_{pot.}$  of each headgroup is calculated to (see additionally appendix A.1.2)

$$W_{pot.} = -\vec{D} \cdot \vec{E} \approx 1.1 \cdot 10^{-23}\text{J} \approx 2.7 \cdot 10^{-3}\text{k}_B\text{T}. \quad (4.20)$$

A potential energy of  $W_{pot.} \approx 2.7 \cdot 10^{-3}\text{k}_B\text{T} \ll 1\text{k}_B\text{T}$  will have a negligible effect on the orientation of a single lipid molecule compared to thermal fluctuations (magnitude  $\approx 1\text{k}_B\text{T}$ ). In an oriented lipid bilayer consisting of several thousand molecules, however, even energy differences  $\ll 1\text{k}_B\text{T}$  can outweigh thermal fluctuations because of collective effects.

Although the observed structural changes can well be explained as driven by strong electric fields, it has to be noted that the results of a recent beamtime strongly suggest that the observed dynamics are excited by the acoustic (mechanic) component of the piezoelectric wave rather than the associated electric field. This suggestion is backed up by two observations:

1): Two identical parallel sound paths (Rayleigh waves, SAW frequency  $f_{SAW}^1 = 80\text{MHz}$ ) have been prepared on the same SAW device, see figure 4.13. One path is covered by a 50nm thin Au layer, effectively shielding the electric field whilst minimizing interference with the acoustic component of the SAW. Time resolved experiments on DOPC lipid multilayers have been carried out on both sound paths, the results / observations are identical within the experimental uncertainty.

2): Ultrafast dynamics could not be induced in reference experiments applying SAW excitation by pure shear- (in contrast to Rayleigh-) waves. Shear waves are characterized by pure in plane displacements, no acoustic components perpendicular to the substrate surface are excited. The magnitude of electric field components  $E_z$  perpendicular to the sample surface is however comparable to the case of Rayleigh waves [82].



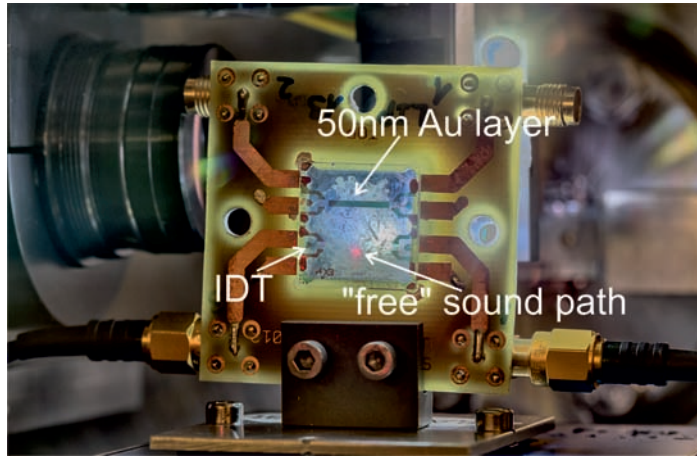


**Figure 4.13:** Two identical parallel sound paths have been prepared on the same SAW device. For one sound path the electric field accompanying the SAW is shielded by a 50nm thin Au layer.

Detailed data screening, analysis and interpretation for these very recent experiments is in progress at the moment of writing.

#### 4.4 Conclusions

We conclude that time resolved x-ray scattering experiments on SAW excited multilamellar lipid membranes as presented in section 4.3 allow for the reconstruction of a bilayer structural movie at molecular resolution perpendicular to the membrane, i.e. a molecular movie of collective bilayer oscillations on nanosecond time scales. The observed changes in the relative electron density profile  $\Delta\rho(z)$  can be attributed to orientational effects of the acousto-electric field. Future studies covering a broader range of experimental conditions (lipid composition, SAW frequency and amplitude, ambient conditions) will allow for a quantitative characterization of the influence of strong electric fields on membrane structure on ultrafast timescales, playing a key role in technological (e.g. electroporation) and physiological processes (such as switching of ion channels and nerve pulse propagation).

Preparatory phase locked time resolved diffraction experiments from pure  $LiNbO_3$  substrates allowed for the observation of a seamless transition between kinematic and dynamical scattering regimes, clearly demonstrating the tremendous potential of phase locked x-ray scattering experiments in the field of solid state physics. Last but not least, the timing scheme of Petra III, which has been developed in the context of this thesis, has been proven to be highly accurate and stable, its great flexibility will be highly beneficial for a broad range of time resolved x-ray experiments at Petra III.



## 5 Laser induced structural dynamics in pure and Texas-red labeled lipid multilayers

A characterization of non-equilibrium structural dynamics in lipid multilayers as induced by short laser pulses was the primary goal and central topic of this thesis. Time resolved x-ray scattering experiments have hence been carried out on a broad parameter space. Major experimental difficulties related to (i) thermal drift and denaturing of the lipid membranes due to the pumping laser as well as the x-ray beam, and even more challenging (ii) finding the laser parameters which efficiently drive the membrane out of equilibrium whilst minimizing sample damage, had to be solved. An initial idea is to use the high frequency electric field  $E_l$  associated to a high intensity laser pulse to drive the membrane out of thermal equilibrium, before more elaborated approaches using fluorescently labeled molecules (e.g. Texas-red) are applied.

This chapter is divided in three experimental parts, discriminated by the parameters of the applied pumping laser, the substrate material, the sample environment and the presence of fluorophore labeled lipids.

(i) Preliminary experiments at the PXS using femtosecond and nanosecond laser excitation (section 4.4) of mainly pure lipid bilayers on silicon substrates in a 'dry' sample chamber.

(ii) Synchrotron experiments at the beamline ID09B, ESRF, using picosecond and nanosecond laser excitation of unlabeled lipid multilayers on silicon substrates (section 4.4). This experiment includes the elaborate elimination of laser- and x-ray induced drift (section 5.1.2).

(iii) Time resolved diffraction from Texas-red [119] labeled lipid multilayers on quartz glass substrates using nanosecond laser pulses (section 5.1.5) at the beamline ID09B, ESRF.

In case of (i) the first order specular reflection of the multilamellar lipid stack has been observed as a function of laser excitation, in case of (ii) and (iii) the focus was on the diffuse scattering pattern as described in section 2.3.

The majority of this experimental section is being published at the moment of writing. Contributions from co-authoring scientists are cordially acknowledged.

### 5.1 Ultrafast laser induced structural dynamics in pure phospholipids on silicon substrates

#### 5.1.1 Preparatory experiments at the in-house femtosecond x-ray source

In order to narrow the initially broad parameter space (i.e. different lipid compositions, sample environments and excitation mechanisms) especially during the starting period of this project, preparatory experiments at the in-house plasma x-ray source (PXS, see 1.1) were an indispensable step towards the realization of

more advanced experiments at synchrotron and FEL sources. The focus of these experiments lay on possible ultrafast effects associated to the electric field  $E_l$  of the high intensity  $P_p$  (pump) laser beam  $E_l = \sqrt{\frac{2P_p}{c\epsilon_0}} \approx 27.4\sqrt{P_p}$ . As detailed in section A.1.2 especially a compression on the order of  $1\text{\AA}$  of the individual bilayers is expected to take place on a  $t \leq 5\text{ns}$  time scale for a transverse field strength of  $E_l \approx 10^7\text{V/m}$  ( $\hat{=} P_p = 2 \cdot 10^9\text{W/cm}^2$ ). This parameter regime can be probed by using the  $\lambda = 800\text{nm}$ ,  $\tau \approx 50\text{fs}$  (Ti:Sa laser system) pump beam in combination with the motorized delay stage available at the PXS (see section 1.1).

The limited primary x-ray flux of  $I_0 \leq 10^{10} \frac{\text{ph}}{\text{s} \cdot 4\text{pi}}$  (Cu- $K_\alpha$  radiation) at the PXS implies a specular scattering geometry. Strong Bragg reflections at a reflectivity of up to 10% are expected for highly ordered lipid multilayers [30], specular Bragg reflections can hence be observed at high resolution with reasonable exposure times of approximately 10 seconds even at rather weak sources as the PXS. The x-ray scattering setup at the PXS is sketched in figure 5.1. As a horizontal scattering geometry is chosen, the sample surface is aligned vertically with respect to the optical table. To facilitate the alignment procedure, being strongly complicated by the need for a regular realignment of the PXS, no optical elements except for a 2-D slit system (JJXray) are introduced between the x-ray source spot and the sample. The primary intensity is monitored by an ionization chamber (JJXray, air or argon filled, optimal voltage  $U \approx 250\text{V}$ , see appendix A.1.3). A photo of the sample setup at the PXS can be found in figure 5.2.

The maximal opening of the slit system is limited to 6mm in each direction, a Pilatus 100k 2-D pixel detector (active area  $83.8 \times 33.5\text{mm}^2$   $h \times v$ ) is hence placed at a distance of  $d_{sd} \approx 50\text{cm}$  relative to the source spot, allowing to just capture the whole vertical extension of the divergent x-ray beam.

For multilamellar samples vertical 'Bragg-streaks' are observed on the 2-D detector, see figure 5.3 for an exemplary data set. Since no monochromator (except for the multilamellar sample itself) is introduced in the beam path, two Bragg-streaks corresponding to the Cu- $K_\alpha$  and Cu- $K_\beta$  spectral components of the primary x-ray beam appear.

Let us shortly estimate the effective reflectivity of a multilamellar lipid stack and the expected intensity of the first multilamellar reflection for the described setup. Given an acceptance angle of  $\Delta\theta = 0.005^\circ$  for the first multilamellar reflection, a sample to source distance of  $d_{ss} = 5\text{cm}$  and a sample area of  $1.5 \times 2.5\text{cm}^2$  (vertical  $\times$  horizontal), the first order Bragg reflection covers a solid angle of  $\Omega = \frac{1.5\text{cm} \cdot \sin(0.005^\circ)}{4/3\pi d_{ss}} \approx 1.25 \cdot 10^{-5}$ . For a primary (Cu- $K_\alpha$ ) x-ray flux of  $I_0 \approx 10^{10}\text{ph/s}$ , as determined in [59] and verified during the experiment, a total number of approximately 10000ph/s can be expected for the first order Bragg reflection. A sample reflectivity of  $R \approx 10\%$  is assumed. This estimation has been verified and in cases even slightly exceeded experimentally.

In the following the data acquisition and analysis pathway will be explained for the example of a time resolved dataset obtained for DOPC lipid multilayers hydrated by water vapor (relative humidity  $\lesssim 100\%$ , see section 2.2). The system has been excited with  $\lambda = 800\text{nm}$ ,  $\tau \approx 50\text{fs}$  laser pulses at intensities

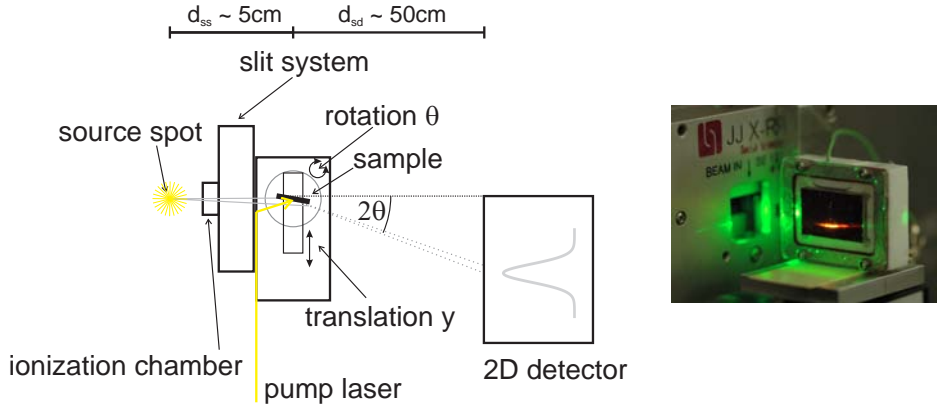


**Figure 5.1:** *Left:* Schematic (top view) of the x-ray scattering setup at the PXS. The divergent (basically in  $4\pi$ ) x-ray beam is collimated by a 2-D slit system, the primary intensity is monitored by an ionization chamber. The sample can be adjusted by a rotation around  $\theta$  (corresponding to the angle of incidence) and a translation along  $y$  above the rotation. *Right:* Photo of a frequency doubled Nd:YAG laser ( $\lambda = 532\text{nm}$ ) impinging on a multilamellar lipid stack in a dedicated thin-film wet sample environment (see appendix A.1.3).

$5 \cdot 10^{11} \text{W/cm}^2 \leq P_p \leq 1 \cdot 10^{12} \text{W/cm}^2$ . A quasi collinear excitation geometry was chosen in order to (i) maximize the horizontal spatial overlap of pump and probe beam (see figure 5.1) and to (ii) achieve p-polarized laser light corresponding to an electric field vector perpendicular to the multilamellar stack. A wavelength adjustable half-wave plate (Alphas, Göttingen) is introduced in the pump beam path in order to control the polarization direction.

As detailed in appendix A.1.3, the primary intensity of the PXS is considered to be rather unstable compared to standard x-ray tubes or synchrotron sources [120]. While pulse to pulse fluctuations can in principle be eliminated by averaging over many ( $N \approx 10000$ ) pulses at a laser repetition rate of 1kHz, long time scale intensity fluctuations arising from mechanical instabilities of the copper tape, increasing debris contamination and uncertainties in the positioning of the laser focus can only be eliminated from the data by a suitable monitor signal. It turned out that the scattering pattern itself is the best available monitor signal, as changes in the position of the source spot, intensity fluctuations and even variations of the primary x-ray spectrum directly translate into changes of the Bragg peak intensity. Therefore pumped- and drift (reference) scattering patterns have been measured simultaneously by only partially illuminating the sample surface contributing to the scattering process, see figure 5.3 left and 5.1 right for an exaggerated example. The laser footprint is therefore restricted to a vertical extension of  $\leq 2\text{mm}$  while homogeneously illuminating the full horizontal width of the



**Figure 5.2:** Photo of the setup sketched in figure 5.1. The spectrum of the plasma radiation can be constantly monitored with an Amptek Si-drift detector mounted above the sample.

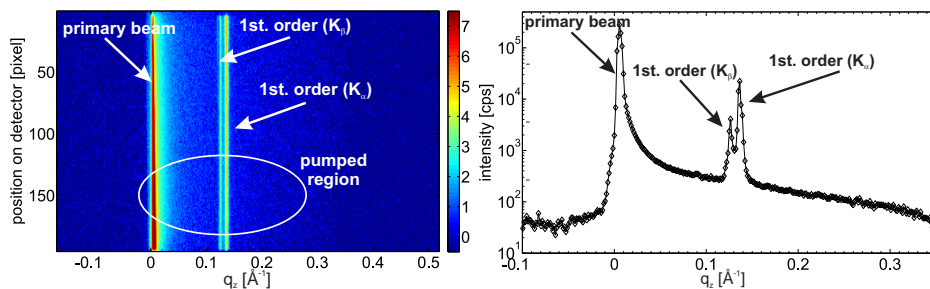


**Figure 5.3:** **Left:** Raw detector image (Pilatus 100k pixel detector) as recorded during a specular x-ray reflectivity experiment from a multilamellar lipid sample at the PXS. The sample horizon clips the primary beam at the far left of the image, the first order Bragg reflection has been excited by a careful adjustment of incidence angle  $\theta$ . Due to the polychromatic x-ray beam (no optics apart from a slit system has been used) the first order reflection is simultaneously excited by  $\text{Cu-K}_\alpha$  and  $\text{Cu-K}_\beta$  radiation. **Right:** The vertically integrated scattering pattern provides high resolution data on the multilamellar diffraction peaks.

sample, the exact position of the pumped region on the detector is (temporally) marked with a thin needle. An integration along the vertical direction in figure 5.3 left, extending over the pumped and reference regions respectively, provides one dimensional quasi-reflectivity<sup>11</sup> profiles  $I_{\text{pumped}}(q_z, t)$  and  $I_{\text{reference}}(q_z, t)$ . No information is lost due to the integration because of the 2-D liquid crystal character of the multilamellar sample as well as the vertically divergent x-ray beam. Data analysis focuses on three generic observables: The integrated intensity  $II(t) = \sum I(q_z, t)$  and the position in  $q_z$  direction of the first order reflection as determined by the shape independent center of mass  $\text{com}(t)$

$$\text{com}(t) = \frac{\sum_{q_z} (q_z \cdot I(q_z, t))}{II(t)}, \quad (5.21)$$

as well as the width (FWHM) in  $q_z$  direction as determined by the second moment of the Bragg reflection  $R(t)$

$$R(t) = \sqrt{8 \ln 2} \cdot \sqrt{\frac{\sum_{q_z} ((q_z - \text{com}(t))^2 \cdot I(q_z, t))}{II(t)}}. \quad (5.22)$$

The prefactor  $\sqrt{8 \ln 2}$  in equation 5.22 takes into account the difference between rms- and fwhm values. No distinction is made between the  $\text{Cu-}K_\alpha$  and  $\text{Cu-}K_\beta$  reflections since relative variations between both are not expected for a fixed spectrum of the primary x-ray beam. The  $K_\beta$  spectral component therefore just adds to an improved signal to noise ratio.

We further refer to reference corrected observables ( $II(t)$ ,  $\text{com}(t)$ ,  $R(t)$ ) as determined by

$$\text{observable}(t) = \langle (\text{reference}(t))_t \rangle \cdot \frac{\text{signal}(t)}{\text{reference}(t)}, \quad (5.23)$$

where  $\text{signal}(t)$  and  $\text{reference}(t)$  denote the observables determined in the pumped-  $I_{\text{pumped}}(q_z, t)$  or un-pumped  $I_{\text{reference}}(q_z, t)$  regions on the 2-D detector. This procedure is especially important and noteworthy in the case of the integrated intensity  $II(t)$ , where a relative rms deviation  $\frac{\Delta II}{II(t)}$  of

$$\frac{\Delta II}{\langle II(t) \rangle} = 2.1 \cdot 10^{-3} \quad (5.24)$$

is achieved by the outlined procedure for reasonable exposure times on the order of 20s in the case of a effectively un-pumped reference measurement. Let us note that a rms deviation of  $2.1 \cdot 10^{-3}$  for an integrated intensity of  $\langle II(t) \rangle \approx 200000$  is basically Poisson noise  $\propto \frac{1}{\sqrt{II(t)}}$ . When compared to rms deviations obtained for the un-normalized data from the same dataset ( $\frac{\Delta II}{II(t)} = 7.6 \cdot 10^{-2}$ ), it becomes clear that fluctuations associated to the instability of the primary x-ray flux can

<sup>11</sup>Specular reflections in an angular range of  $\Delta\theta = \arcsin\left(\frac{25\text{mm} \cdot \sin(\alpha_i)}{50\text{mm}}\right) \approx 0.5^\circ$  are excited at a fixed angle of incidence  $\alpha_i = 1^\circ$

well be eliminated by the reference normalization. The datasets obtained for a pump intensity of  $P_p = 5 \cdot 10^{11} \text{W/cm}^2$  displayed in figure 5.4 (bottom left, blue) have been used for this reference.

Let us review the actual course of the presented pump-probe experiment:

- Figure 5.4 (blue): The system has been equilibrated at a laser intensity of  $P_p = 5 \cdot 10^{11} \text{W/cm}^2$  for a duration of roughly 10 minutes prior to the first experimental run. This equilibration was followed by two successive time resolved experiments, covering a delay range of  $-0.5 \text{ns} \leq t \leq 3 \text{ns}$ . No significant variations in either observables is detected within the instrumental resolution.
- Figure 5.4 (red): Next, two un-pumped reference measurements directly following the first experimental run have been carried out. An equilibration on the minute time scale (i.e. on the time scale of the exposure time) can be observed, the system is fully equilibrated after the first measurement. The increase in bilayer periodicity (top) is attributed to an increased hydration in case of the un-pumped (hence 'cold') bilayer stack.
- Figure 5.4 (black): The laser intensity has been increased to  $P_p = 1 \cdot 10^{12} \text{W/cm}^2$  for the next run. As for the preceding runs a relaxation to the new thermodynamic equilibrium is observed on the minute time scale. No effects are observed for the fully equilibrated system.

In conclusion, no ultrafast effects are induced in the current experiment, only thermal equilibration on the one minute time scale can clearly be observed. The data hence serves as a benchmark for the instrumentally achievable resolution.

As mentioned earlier the rms fluctuation amplitude of the integrated intensity is determined to  $\frac{\Delta I I}{I I(t)} = 2.1 \cdot 10^{-3}$  in a series of  $N = 36$  twenty second exposures.

The bilayer periodicity  $d(t)$  is measured with an uncertainty of  $\Delta d = 1.6 \cdot 10^{-4} \text{\AA}$ , the second moment of the Bragg reflection  $R(t)$  is measured with an uncertainty of  $\Delta R = 2.3 \cdot 10^{-3} \text{mrad}$ . (both rms) as determined from the un-pumped dataset.

Given numerous qualitatively similar experimental results obtained at the PXS, as well as various complementary synchrotron experiments 4.4, it can be concluded that ultrafast dynamics in lipid bilayers can not be induced in the parameter range applied so far. Different lipid species (varying headgroups, charged vs. neutral lipids, saturated vs. unsaturated lipid chains) as well as a broad laser parameter range (wavelengths  $400 \text{nm} \leq \lambda \leq 1340 \text{nm}$ , intensities  $10^5 \text{W/cm}^2 \leq P_p \leq 10^{12} \text{W/cm}^2$ , pulse lengths  $50 \text{fs} \leq \tau \leq 1 \text{ns}$ ) have been applied.

A straight forward extension of the just presented in house measurements using dedicated ('wet') sample environments as successfully applied in sections 4.4 and 5.1.5, is hindered by the strong absorption of  $\text{Cu-K}\alpha$  radiation in liquid water. The development of advanced sample environments (in particular a 'thin-film' wet chamber, allowing for experiments under conditions of full hydration using  $\text{Cu-K}\alpha$  radiation, see appendix A.1.3) and the use of high  $Z$  target materials (e.g. molyb-



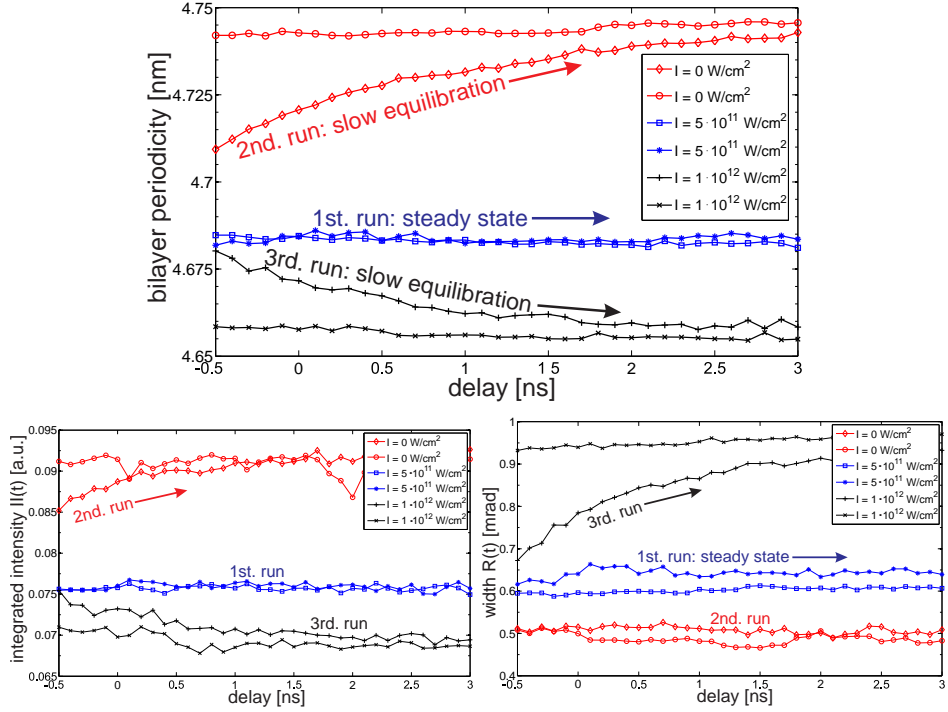


**Figure 5.4:** **Top:** No fast timescale effects on the bilayer periodicity are observed for laser excitation using femtosecond pulses. The experiment was carried out in the following order: **1: blue** The thermally well equilibrated sample has been pumped with  $P_p = 5 \cdot 10^{11} \text{ W/cm}^2$ ,  $\lambda = 800 \text{ nm}$  laser pulses and probed in a delay range  $-0.5 \text{ ns} \leq t \leq 3 \text{ ns}$ . Two successive runs have been carried out in order to ensure thermal equilibrium, no changes significantly exceeding the rms fluctuation amplitude of  $\Delta d = 1.6 \cdot 10^{-4} \text{ \AA}$  are observed. **2: red** The laser has been switched off, the sample relaxes to room temperature on a timescale of minutes as apparent by a rehydration (water uptake). No variations are observed in a succeeding experiment. **3: black** The sample has been pumped by a laser intensity of  $P_p = 2 \cdot 10^{12} \text{ W/cm}^2$ . Thermal equilibration on a timescale of minutes is followed by a steady state experiment. **Bottom left:** An  $P_p$  dependent intensity decrease (Debye-Waller factor) as well as an increase in width of the reflection (**bottom right**) on the minute timescale can well be attributed to temperature effects.

denum) is ongoing and upcoming research.

Let us now turn to time resolved x-ray scattering experiments on pure and fluorescently labeled lipid multilayers performed at the beamline ID09B at the ESRF in Grenoble.

### 5.1.2 X-ray scattering setup at the ID09B at the ESRF, Grenoble

Samples were mounted on a goniometer head (Huber) above the  $h\phi i$  (angle of incidence) rotation and illuminated under conditions suitable for grazing incidence small angle x-ray diffraction (GISAXS). The configuration of this basic sample stage implied a vertical scattering plane. The substrate surface was placed in the center of rotation by using the quasi- on axis microscope available at the ID09B. A photodiode just behind the sample was used to adjust the angle of incidence as well as the vertical position of the sample, the vertical translation is hereby technically below the  $h\phi i$  rotation. Monochromatic undulator radiation (U17) at  $E = 17\text{keV}$  (energy resolution approximately  $3\text{eV}$ ) was used in order to minimize x-ray absorption in liquid water, the x-ray beam size on the sample was  $\approx 0.3 \cdot 0.15\text{mm}^2$  ( $h \times v$ ). Diffuse scattering signals were recorded by a Frelon detector<sup>12</sup> 726.5mm behind the sample. Care has to be taken to suppress specular ('Bragg') scattering by adjusting the angle of incidence such that the specular reflected beam (SB) falls in between the first and the second diffraction order, see figure 5.5.

### 5.1.3 Elimination of laser and x-ray induced drift – Sample environments and possible pitfalls

In the first part of the experiment the Ti:Sa picosecond laser system ( $\tau = 1\text{ps}$ ,  $\lambda = 800\text{nm}$ ,  $E_p \leq 4\text{mJ}$ , *Legend Elite*, Coherent) available at the ID09B has been used for optical pumping, see section 1.4. Various pump intensities  $P_p \leq 1 \cdot 10^{11}\text{W}/\text{cm}^2$  corresponding to associated electric fields of  $E_l \leq 1 \cdot 10^9\text{V}/\text{m}$  have been applied. Due to the small angle of incidence in the GISAXS geometry the synchrotron beam has a strongly elongated shape on the sample surface. Therefore in line with section 4.4 a quasi collinear excitation geometry ( $\alpha_{i,\text{laser}} \approx 10^\circ$ ) has been chosen in order to fully illuminate the part of the sample contributing to the scattering process (spatial overlap). The sample was placed in the defocus of a planoconvex lens, resulting in laser beam sizes between  $1 \cdot 1\text{mm}^2$  and  $0.5 \cdot 0.5\text{mm}^2$  (measured perpendicular to the laser propagation direction) at the sample position. Laser polarization could be controlled with a tunable  $\frac{\lambda}{2}$  plate in front of the focusing lens. P-polarized laser light has been chosen to maximize possible electric field effects.

Diffuse scattering patterns obtained from DOPC multilayers  $I(q_r, q_z, t)$  have been

<sup>12</sup><http://www.esrf.eu/UsersAndScience/Experiments/Imaging/ID22/BeamlineManual/Detectors/Ccd/Frelon>

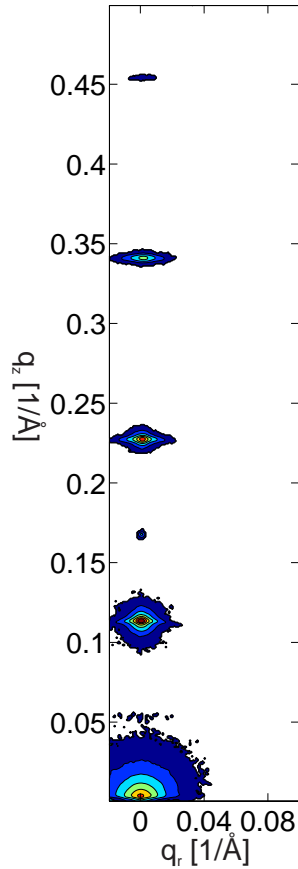


**Figure 5.5:** Exemplary diffuse scattering pattern  $I(q_r, q_z)$  as obtained for unpumped DOPC multilayers in direct contact with a 30% wt. PEG solution. Four diffuse reflections 'Braggsheets' (BS) can clearly be observed, the specular reflected beam (SB) is centered between the first- and second order reflection. The effective exposure time was 700 seconds at a synchrotron pulse frequency of  $f_b \approx 1\text{kHz}$  after the high speed chopper (see section 1.4).

dark corrected and normalized to the storage ring current prior to data analysis. A  $3 \times 3$  pixel 2-D median filter has been used to eliminate hot- or dead pixels. In line with the procedure described in section 4.4 the integrated intensity  $II(n, t)$ , center of mass ( $\text{com}_{q_x}(n, t)$ ,  $\text{com}_{q_z}(n, t)$ ) and second moment ( $R_{q_x}(n, t)$ ,  $R_{q_z}(n, t)$ ) of the individual diffuse orders  $n$  are the first generic observables of the pump-probe experiment. In extension to the results presented in section 4.4 the two-dimensionally collimated x-ray beam allows for a clear separation of in plane ( $q_x$ ) scattering components.

As in section 4.4, drift induced by x-ray as well as laser radiation is found to be the dominant effect for samples hydrated by water vapor, see e.g. figure 5.6 and section 2.2. No effects on the timescale of the laser pulse duration  $\tau$  are observed. The drift is characterized by a shrinking of the bilayer periodicity  $d(t) = 2\pi / \left[ \frac{1}{n_{max.}} \cdot \sum_n^{n_{max.}} \text{com}_z(n, t)/n \right]$  in response to laser as well as x-ray exposure. This effect is attributed to heat induced changes in local relative humidity which will generally decrease the water layer thickness separating two lipid bilayers [31, 88]. The decrease of bilayer periodicity continues seamlessly for repetitive measurements (see figure 5.7 b) and saturates in thermal equilibrium.

X-ray induced drift effects are minimized by keeping the samples in direct contact with liquid water in a dedicated sample chamber, see figure 5.6 and section 2.2. Laser induced drift is in this case characterized by a slight swelling of the lipid membrane, which is consistent with the previously observed temperature dependence of the water layer thickness  $d_w$  [121]. Laser induced heating of the sample will lead to an increased fluctuation repulsion between adjacent bilayers whereas attractive Van-der-Waals forces are roughly temperature independent.

In conclusion, thermal drift and sample degradation are minimized by using the 'wet chamber' described in section 2.2, destabilization of the multilayers is in this case prevented by using a solution containing 30% wt. Polyethylene Glycol (PEG) (corresponding to an osmotic stress of 1.54MPa<sup>13</sup>).

**Possible pitfall – Non-equidistant temporal sampling** An important note has to be made on 'ghost effects' which have mistakenly been taken for ultrafast effects on the picosecond timescale during one experimental shift, see figure 5.7.

It is generally good practice to choose a non-equidistant temporal sampling for time resolved x-ray scattering experiments. Tightly spaced delay values (e.g.  $t = 100\text{ps}$ ) are chosen around the time zero in order to resolve possible fast time scale effects, the sampling frequency is then reduced in order to observe relatively slow relaxation processes on the  $\mu\text{s}$  time scale. As obvious from e.g. figure 5.7 this non-equidistant sampling can easily lead to a misunderstanding of the observed effects. When plotted as a function of time delay (figure 5.7 a)) even linear drift effects seem to occur on a timescale of picoseconds. However, when plotted as a function of acquisition number (or integral exposure time, figure 5.7 b)) the true nature of the effects becomes obvious.

<sup>13</sup><http://lpsb.nichd.nih.gov/peg20000.htm>

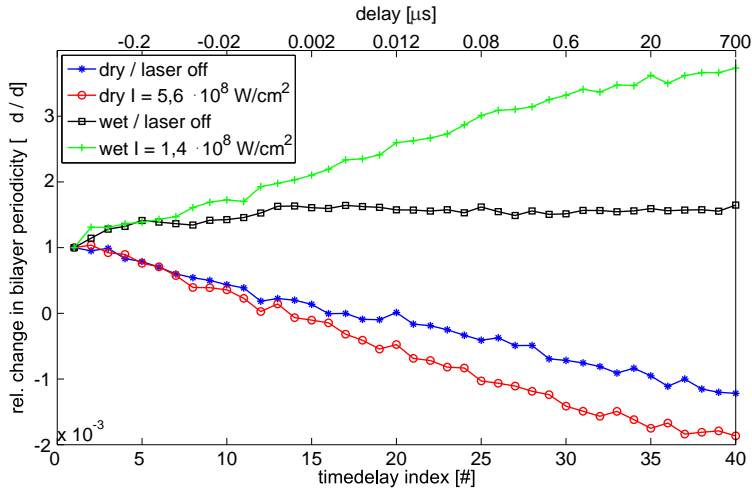


**Figure 5.6:** X-ray induced drift is minimized by keeping the sample in contact with liquid water during the experiment. Relative changes of the bilayer periodicity have been plotted against acquisition number rather than time delay in order to emphasize drift effects. Time zero corresponds to acquisition number 14.

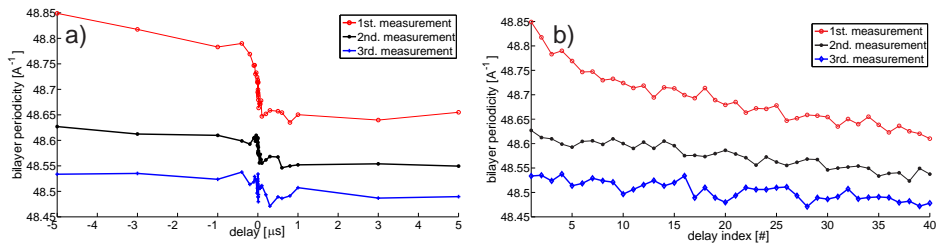


**Figure 5.7:** a) Samples hydrated by water vapor are subject to strong drift induced by the laser as well as the x-ray beam. Because the temporal sampling has been chosen to be non-equidistant, one could easily interpret laser as well as x-ray induced drift as a non reversible fast timescale effect. Note that such an irreversible effect can generally not be observed due to the nature of a stroboscopic pump-probe experiment. b) The bilayer periodicity has been plotted as a function of acquisition number for three consecutive time resolved measurements, clearly identifying the dependence of thermal drift effects on the acquisition number (or integrated exposure time) rather than the time delay  $t$ . Pump intensity was  $4 \cdot 10^9 \text{ W/cm}^2$  ( $@ \tau = 1\text{ps}$ ).

### 5.1.4 Excitation of lipid multilayers on silicon substrates by nanosecond laser pulses – A molecular movie

Although experiments using femtosecond and picosecond laser excitation helped tremendously to gain experience in time resolved experiments and to reduce thermal drift to an absolute minimum (section 5.1.2), fast timescale effects are so far not induced by femtosecond and picosecond laser pulses.

In order to overcome this 'quenched' nature of the sample system on fast timescales a nanosecond laser system (*Evolution*, Coherent,  $\tau = 180\text{ns}$ ,  $\lambda = 527\text{nm}$ ) has been used in the next experimental step. Applying know-how obtained in earlier parts of this project, the sample has been kept in direct contact with a water based solution containing 30% wt. PEG in order to minimize thermal drift as well as hydration related artifacts. Beam steering and optical alignment were identical to the setup described in section 5.1.2, the  $10^5$  increase in pulse duration however leads to dramatically decreased peak intensities  $P_p$  and therefore electric fields  $E_l$ . One major advantage of this large pulse length approach is, that comparatively large pulse energies can be applied without reaching the – mainly intensity dependent – damage threshold of the lipid sample. As the experiments performed in sections 4.4 and 5.1.2 clearly indicate that ultrafast effects are not triggered by comparatively strong peak intensities  $P_p$  or electric fields  $E_l \propto \sqrt{P_p}$  of (ultra-) short pulse laser systems, we will refer to the integrated pulse energy  $E_p$  rather than the peak intensity  $P_p$  for the following discussion. Pulse energies up to  $E_p \leq 3\text{mJ}$  corresponding to peak intensities of  $P_{\text{peak}} \leq 2 \cdot 10^6\text{W/cm}^2$  have been applied. Increasing the pulse energy above 3mJ resulted in an irreversible damage of the sample system, possibly due to the integrated amount of deposited energy ( $\approx 300\text{W/cm}^2$  cw averaged laser intensity).

Signal- (pumped) and reference ('drift') diffraction patterns at a constant delay of  $t_{\text{drift}} = -10\mu\text{s}$  were recorded in an alternating manner. Due to this protocol, remaining drift effects could be monitored and eliminated from the measurements. We will therefore refer to drift normalized observables in all cases.

Let us focus on two exemplary experiments, both performed at a pulse energy of  $E_p = 1500\mu\text{J}$ . Two complementary polarization states have been chosen. A sharp increase of the total amount of diffuse scattering by approximately 40% (horizontal polarization) and approximately 80% (vertical polarization) is observed in both cases, as plotted in figure 5.8 for the first and second order diffuse reflection ( $II(1, t)$  top and  $II(2, t)$  bottom left) in case of horizontally (p-) polarized laser light and in figure 5.9 (top and bottom left) in case of vertically (s-) polarized laser light. This transient intensity increase takes place within  $3\mu\text{s}$  after optical excitation, relaxation to thermal equilibrium takes place on a  $10\mu\text{s}$  timescale. The system has fully relaxed within  $t \leq 100\mu\text{s}$ . Remarkably, structural parameters as characterized by the in plane correlation length  $\xi_r$ , the lineshape parameter  $\gamma$ , the smectic penetration length  $\Lambda$  and the bilayer periodicity  $d$  remain unchanged within the experimental resolution. Details on the analysis and the batch fitting procedures involved in the analysis of the latter parameters will be given in section 5.1.5, where in contrast to the experiments presented here the temporal evolution

of the bilayer correlations is found to be the dominant effect.

As expected for energy  $E_p$  rather than electric field  $E_l$  driven effects, no quantitative differences between experiments applying horizontally and vertically polarized laser light are observed. A mere scaling between the intensity traces  $II(n, t)$  depicted in figures 5.8 and 5.9 can well be explained by sample inhomogeneities. Furthermore, in strict contradiction to hypothetical direct electric field effects, the observed intensity variations were not reproduced in reference experiments using pure lipid molecules on quartz glass rather than silicon substrates, even up to the maximum laser pulse energy of  $E_p = 6\text{mJ}$ . We will therefore focus on the dataset obtained for vertically polarized laser light, showing more intense but qualitatively identical effects to the case of horizontal polarization.

Further data analysis and interpretation is performed in line with section 4.3. Note however that we are in this case dealing with diffuse scattering patterns in contrast to section 4.3, where the focus lay on the specular reflectivity of the bilayer stack. However, similar to section 4.3, a mere increase of the diffuse intensity at constant structural and mechanical parameters  $d, \gamma, \Lambda, \xi_r$  can be attributed to three different scenarios (compare section 2.3).

(i) A variation of the time dependent bilayer form factor  $F(q_z, t)$  and hence the individual molecular structure as represented by the electron density profile  $\rho(z, t) = \mathcal{F}^{-1}(F(q_z, t))$ .

(ii) An increase of the average mean square displacement  $\sigma(t)$ , or

(iii) a modulation of the correlation functions  $c_r(r)$  or  $c_z(z)$ .

The latter would necessarily be accompanied by a variation of the functional form / the shape of the diffuse reflections, whereas changes of  $F(q_z, t)$  and  $\sigma$  manifest themselves in pure intensity variations. The following discussion will focus on the disentanglement of effects associated to an increased fluctuation amplitude and structural modifications on the molecular scale.

Let us shortly review how changes of  $\sigma(t)$  translate to the integrated intensity  $II(n, t)$  of a diffuse reflection order  $n$ . As already mentioned in section 2.3 the diffuse structure factor can be written as a unique transform of the in plane correlation function  $c_r(r)$ , see equation 2.15. By definition  $c_r(r)$  is always proportional to  $\sigma^2(t)$ , no matter which exact functional form is assumed for  $c_r(r)$  [92, 93, 104]. Inserting  $c_r(r) = \sigma^2(t) \cdot b_r(r)$  in 2.15 and performing a Taylor expansion for  $q_z^2 \sigma^2(t) \ll 1$  yields

$$\begin{aligned} S(q_r, q_z) &= \frac{1}{q_z^2} (1 - q_z^2 \sigma^2(t)) \cdot q_z^2 \sigma^2(t) \sum_{i,j} e^{-iq_z(i-j)d} \int_r dr r b^2(r) J_0(q_r r) \\ &\approx \frac{q_z^2 \sigma^2(t)}{q_z^2} \sum_{i,j} e^{-iq_z(i-j)d} \mathcal{F}(b^2(r))(q_r). \end{aligned} \quad (5.25)$$

Here  $\mathcal{F}(b^2(r))(q_r)$  denotes the Fourier transform of  $b^2(r)$ . The assumption  $q_z^2 \sigma^2(t) \leq 1$  especially holds for the  $n = 1$  reflection ( $q_z(n = 1) \approx 0.11 \text{\AA}^{-1}$ ) and slightly dehydrated samples, as in the present case of an applied osmotic stress on the order of 1.54MPa. For these parameters an educated guess is  $\sigma_{\text{mean}} \approx 2.5 \text{\AA}$  as observed

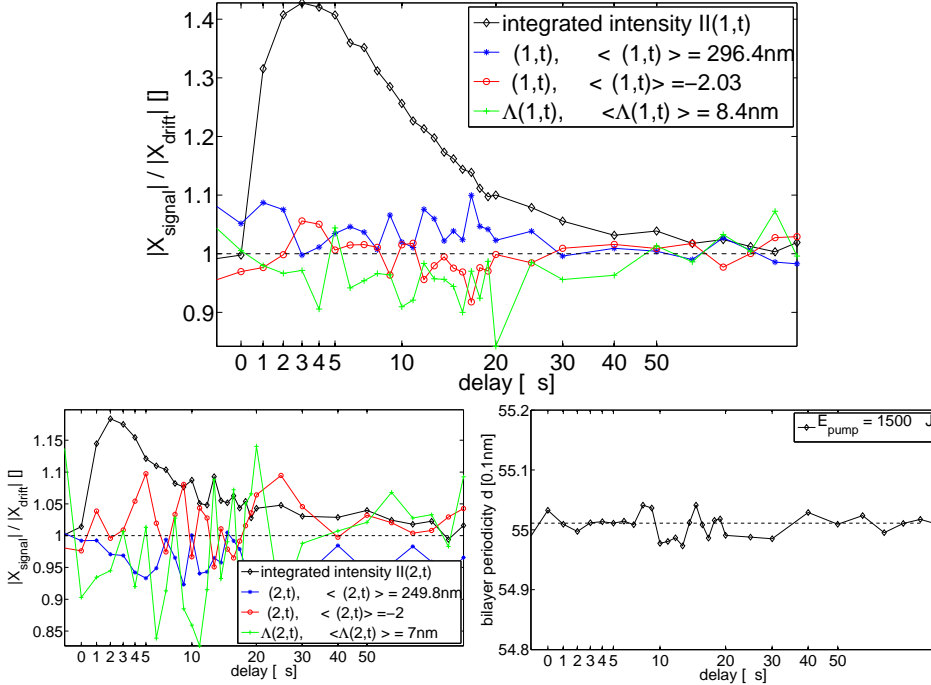


**Figure 5.8:** Drift normalized time dependent observables as obtained for pure DOPC multilayers on a silicon substrate excited by  $E_p = 1500\mu\text{J}$  laser pulses of horizontal (p-) polarization. **Top:** A steep increase of the integrated diffuse intensity  $I(1,t)$  of the  $n = 1$  first order reflection by approximately 40% is observed within  $3\mu\text{s}$  after optical excitation. Relaxation to thermal equilibrium takes place on a  $10\mu\text{s}$  time scale, structural parameters remain unchanged. **Bottom left:** A steep intensity increase by approximately 15% is observed for the second order diffuse reflection. **Bottom right:** The bilayer periodicity remains unchanged within the experimental resolution.



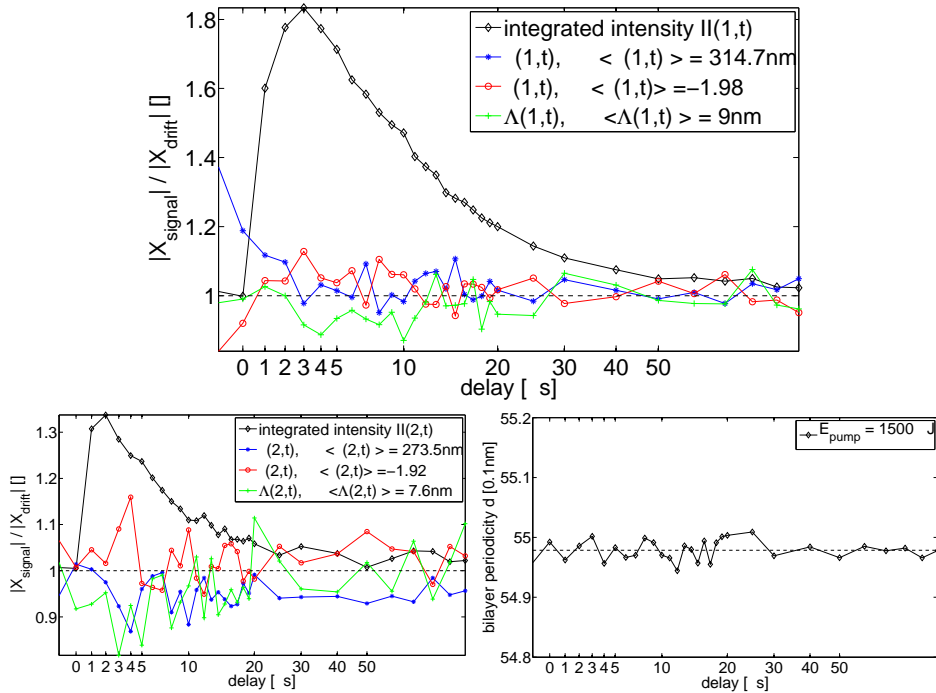


**Figure 5.9:** Drift normalized time dependent observables as obtained for pure DOPC multilayers on a silicon substrate excited by  $E_p = 1500\mu\text{J}$  laser pulses of vertical ( $s$ -) polarization. The composition of the plots is identical to 5.8. **Top:** Relative changes for the first order diffuse reflection. **Bottom left:** Relative changes for the second order diffuse reflection. **Bottom right:** The evolution of the bilayer periodicity shows no characteristic traits.

in [88] for DMPC lipid multilayers. The  $q_z$  and  $q_r$  integrated diffuse intensity  $II(n, t) \propto \sigma^2(t)$  of an order  $n$  diffuse reflection is therefore always proportional to the instantaneous rms surface roughness. Since no shape variations of the individual reflections are observed, the integrated intensity  $II(n, t) \propto \sigma^2(t) \cdot F(n, t)$  is also proportional to the bilayer form factor squared  $F(n, t)^2$ . For a number of  $n_{max}$  observable diffuse reflections this imposes a linear system of equations with  $n_{max} + 1$  unknown parameters  $F(n, t)$  and  $\sigma(t)$  but only  $n_{max}$  observables  $II(n, t)$ . In line with the argumentation in 2.3 and [52, 53, 98] it is additionally assumed that the integral over the continuous form factor squared  $F(q_z, t)^2$  is approximately constant, the sum over  $F(n, t)^2$  is hence proportional to the instantaneous bilayer periodicity  $\sum_n F(n, t)^2 \propto d(t)$ . Structural changes on the molecular scale can therefore be disentangled from an increased surface roughness by

$$\sigma(t) \propto \sqrt{\frac{\sum_n II(n, t)}{d(t)}} \quad (5.26)$$

$$F(n, t) \propto \frac{\sqrt{II(n, t)}}{\sigma(t)}. \quad (5.27)$$

The temporal evolution of  $\sigma(t)$  has been plotted in figure 5.10 for the case of horizontally (black, circles) and vertically (red, squares) polarized pump pulses. As expected from the observed intensity traces  $II(n, t)$  a sharp increase by 15% (horizontal) and 30% (vertical) of the rms-roughness is observed within the first  $3\mu s$  after optical excitation, relaxation to thermal equilibrium takes place on a  $10\mu s$  time scale. As for the intensity traces  $II(n, t)$  relative variations are more intense for the case of vertically polarized laser light, presumable due to sample inhomogeneities.

As only relative variations of the  $F(n, t) \equiv F_{pp}(n, t)$  are determined by the approach presented above, based on a time resolved scattering experiment, reference x-ray reflectivity measurements providing absolute values for  $|F(n, 0)|$  have been performed at an in house diffractometer (D8 Advanced, Bruker AXS), see figure 5.10. Experimental conditions were identical to those of the time resolved measurements, Mo- $K_\alpha$  radiation at a wavelength of  $\lambda = 0.7107\text{\AA}$  has been used to suppress x-ray absorption in liquid water. After corrections for illumination, polarization and absorption, background subtracted peak intensities have been determined by trapezoidal integration. Multiplication with the usual Lorentz factor  $L(n) = \frac{1}{q_z(n)}$  for oriented samples yields integrated peak intensities proportional to the modulus squared of the bilayer form factor  $I_{corr.}(n) \cdot L(n) = |F_{ref.}(q_z(n))|^2$ . A more detailed description of the standardized data analysis routines is e.g. found in [52, 53]. Absolute values of  $F(n, t) = \nu_n \cdot |F_{ref.}(n)| \cdot \frac{F_{pp}(n, t)}{F_{pp}(n, 0)}$  are now determined by scaling the reference values  $|F_{ref.}(n)|$  with relative changes  $\frac{F_{pp}(n, t)}{F_{pp}(n, 0)}$  obtained in the time resolved experiment, phase factors  $\nu_n \in \pm 1$  are readily available for a broad range of lipid systems [52, 53, 31, 30]. Relative electron density profiles  $\Delta\rho(z, t)$  are reconstructed by the standard Fourier synthesis approach, see section 2.3 and figure 5.11. In conclusion, relative electron density profiles  $\Delta\rho(z, t)$  are

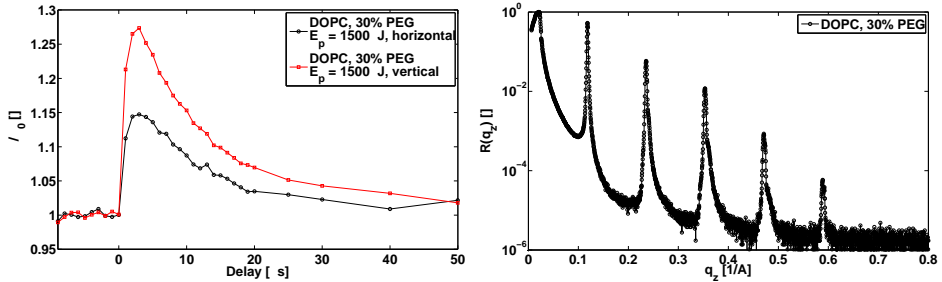


**Figure 5.10: Left:** Relative variations of the rms roughness  $\sigma(t)$  after excitation with horizontally (black, circles) and vertically (red, squares) polarized laser pulses at a pulse energy of  $E_p = 1500\mu\text{J}$ . A sharp increase of 15% (h) and 30% (v) is observed within  $3\mu\text{s}$  after optical excitation. **Right:** Reference x-ray reflectivity experiment from DOPC multilayers in direct contact with a watery solution containing 30% wt. PEG.

obtained at each time point  $t$  after the optical excitation. Structural variations on the molecular scale are visualized as a 'molecular movie'. A slight expansion of the membrane along with a slightly increased headgroup width is observed.

A detailed analysis of the observed changes in the relative electron density profiles  $\Delta\rho(z, t)$  of an individual lipid bilayer is made in terms of typical length scales characterizing the structure of the lipid bilayer, in particular the width and distance of the two headgroups. The analysis is based on a Gaussian fit in case of the headgroup-headgroup distance (corresponding to the membrane thickness) and the FWHM of a shape preserving interpolation in case of the headgroup width. Results are plotted in figure 5.12. An expansion by approximately  $0.5\text{\AA}$  of the membrane is observed, the expansion of the headgroup width amounts to approximately  $0.25\text{\AA}$ .

Let us shortly summarize our experimental findings.

- (i) Non-equilibrium effects are induced by  $\lambda = 527\text{nm}$ ,  $\tau = 180\text{ns}$  laser pulses of  $E_p = 1500\mu\text{J}$ .
- (ii) The observed variations are clearly triggered by the integrated pulse energy  $E_p$  rather than the peak intensity  $P_p$ .
- (iii) Individual bilayers react by an expansion of the membrane thickness as well as an increase of the headgroup width.
- (iv) The interaction between laser light and the lipid bilayers is clearly mediated by the silicon substrate. Furthermore the observed changes can not be attributed to mere heat effects, as a slight thinning of the lipid bilayer accompanied by an expansion of the water layer thickness for DOPC is reported for a temperature increase from  $15^\circ\text{C}$  to  $45^\circ\text{C}$  [121].

A detailed interpretation, by means of an interaction mechanism on the molecular scale, can not be performed on the basis of the current data. However, we suppose that an interaction mechanism is likely to be based on electric field effects arising

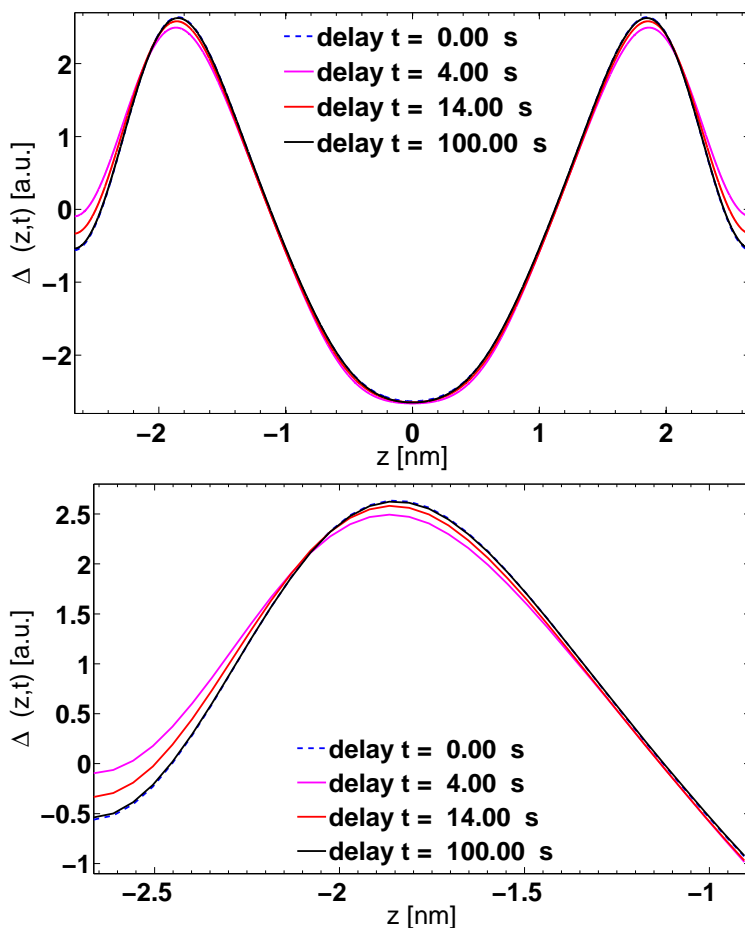


**Figure 5.11: Top:** Relative electron density profile  $\Delta\rho(z,t)$  for four different time delays  $t$  after optical excitation. Most prominent changes are located in the headgroup regions of the lipid bilayer. **Bottom:** Zoom into the headgroup region of the electron density profiles of the lipid bilayers. The reduction of the electron density in the headgroup region upon optical excitation is accompanied by an increased density in the region of the water layers. A slight expansion of the membrane along with a slightly increased headgroup width is observed.

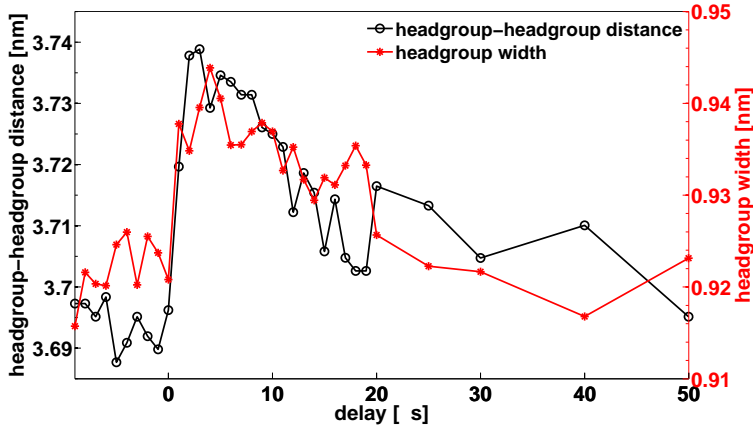


**Figure 5.12:** A sharp decrease by  $\Delta d_{hw} \approx 0.4\text{\AA}$  of the headgroup width  $d_{hw}$  as well as an increase of the headgroup-headgroup spacing by  $\Delta d_{hh} \approx 0.3\text{\AA}$  is observed upon laser excitation.

from the interaction of high energy laser light with the silicon substrate (band gap 1.11eV, work function 4.6eV). Future experiments should include the direct measurement of electric properties of the lipid stack on various substrate materials. In the slightly different context of a detailed characterization of x-ray induced beam damage in lipid multilayers, in particular a Kelvin probe experiment has already successfully been combined with a high resolution x-ray scattering experiment [43]. Although these Kelvin probe experiments are in a close relation to the work presented in this thesis we have to refer to the actual publication for further details.

### 5.1.5 Conclusion

As a first essential step towards a more wide spread application of time resolved x-ray diffraction using laser excitation of soft matter sample systems, thermal drift and sample degradation originating from both, laser pump- as well as x-ray probe pulses, could be minimized in a multitude of complementary experiments, see section 5.1.2.

Reference experiments at the in-house femtosecond laser plasma x-ray source (PXS) served to reduce the initially broad parameter space (section 4.4), the setup at the PXS is proven to be compatible with high resolution time resolved x-ray scattering experiments. Dedicated online data correction and analysis routines are readily available.

Finally, time resolved x-ray scattering experiments have convinced us that  $\tau = 180\text{ns}$ ,  $\lambda = 527\text{nm}$  laser pulses at pulse energies  $E_p \geq 500\mu\text{J}$  induce reproducible and reversible structural dynamics in lipid bilayers on Si substrates at the molecular scale, while the dynamic seems to be 'quenched' if the pump pulse is too short.

The 'quenched' character is attributed to the fact, that a significant amount of energy  $E_p$  can not be transferred into the sample system by femto- and picosecond laser pulses without reaching the, mainly intensity  $P_p$  dependent, damage threshold.

Importantly, we were able to record the diffuse scattering pattern of multilamellar lipid stacks at a signal level compatible with a full lineshape analysis and to attribute laser induced intensity variations  $II(n, t)$  to an increased bilayer fluctuation amplitude  $\sigma(t)$  as well as changes of the bilayer structure on the molecular level. To the very best of our knowledge the presented data reduction and analysis approach combining high resolution diffuse x-ray scattering and reference x-ray reflectivity experiments have not been presented before. These advanced data analysis routines led to the reconstruction of the first molecular movie of laser driven non-equilibrium membrane fluctuations.

## 5.2 Out-of-equilibrium correlations in Texas-red labeled lipid multilayers

In this section we report on time resolved x-ray scattering experiments on fluorophore labeled DOPC multilayers, focusing again on the temporal evolution of the diffuse scattering pattern after short pulse excitation (see section 2.3). As a first step towards the insertion of active centers in the membrane, Texas-red [119] has been used as an exemplary localized force center, driving the membrane out of equilibrium upon optical stimulation. Chromophore labeled lipid multilayers furthermore serve as a model system for a broad range of soft matter sample systems in the context of fluorescence microscopy and related photo physical experiments. A Texas-red mole fraction of 5% has been chosen. The sample preparation protocol is described in section 2.2. As already successfully applied in section 5.1.2, samples have been kept in direct contact with a water based solution containing 30% wt. PEG throughout the experiment in order to prevent excessive sample degradation and thermal drift. Experiments have been carried out at beamline ID09B at the ESRF, Grenoble. The main experimental setup (laser setup as well as x-ray diffraction setup) applied in this experimental part is identical to the setup described in sections 5.1.2 and 5.1.2. The laser wavelength  $\lambda = 527\text{nm}$  of the  $\tau = 180\text{ns}$  laser system (*Evolution*, Coherent) matches well to the edge of the absorption spectrum of Texas-red [119], allowing for a homogeneous excitation of the multilamellar stack. In addition to the experiments reported on in section 4.4, a Pockels cell has been used during parts of the experiment to slice the laser pump beam in the temporal domain. The temporal resolution is in this case increased to 5ns, the pulse energy  $E_p$  is however limited to  $E_p \leq 200\mu\text{J}$ .

The first generic observable of this time resolved diffraction experiment is again the time dependent integrated intensity  $II(n, t)$  of the individual BS orders, see 5.13. A sharp intensity increase within the first  $\approx 1\mu\text{s}$  after optical excitation is observed in all cases, the functional form of  $II(n, t)$  as well as the relative amplitude being both dependent on pump energy  $E_p$  as well as  $n$ . The rise time of the initial intensity increase decreases from  $t \approx 1\mu\text{s}$  for  $E_p \approx 100\mu\text{J}$  to  $t \approx 100\text{ns}$  for

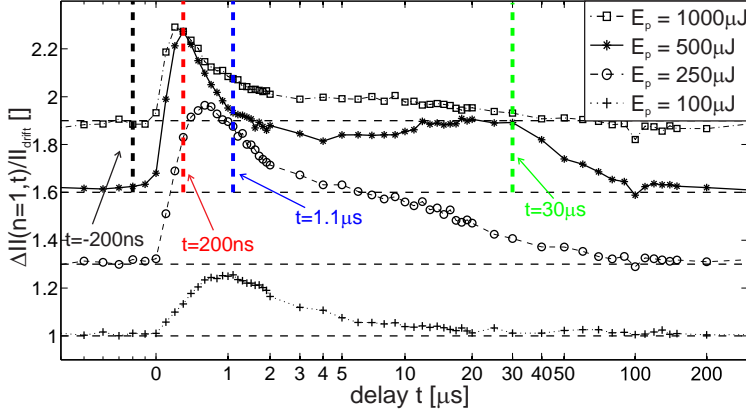


**Figure 5.13:** The drift normalized integrated intensity  $II(n = 1, t)$  of the first diffuse reflection on a logarithmic temporal axis for laser energies of  $E_p = 100\mu\text{J}$  (cross, dotted),  $E_p = 250\mu\text{J}$  (circle, dashed),  $E_p = 500\mu\text{J}$  (asterisk, solid) and  $E_p = 1000\mu\text{J}$  (square, dash-dotted). A steep increase on the 100ns timescale is followed by a relaxation on the  $10\mu\text{s}$  timescale. Rise time and functional form of  $II(n, t)$  are strongly related to  $E_p$ . Curves have been shifted for clarity.

$E_p \approx 1000\mu\text{J}$ . Relaxation to thermal equilibrium happens on a  $10\mu\text{s}$  time scale, the system has fully relaxed after  $t = 100\mu\text{s}$  in all cases. Remarkably a distinct second intensity maximum at  $t \approx 40\mu\text{s}$  is observed for the second diffuse order as plotted in figure 5.16 (bottom). As  $II(n, t) \propto q_z^2 \sigma^2$  for  $q_z \sigma \leq 1$  the fast intensity increase can be linked to an increased rms-roughness of the lipid water interface upon laser excitation. The broad plateau following the initial intensity increase can be attributed to the subsequent energy dissipation via collective modes, possibly a collective undulation amplitude. The bilayer periodicity  $d(t) = \frac{n \cdot 2\pi}{q_z(n)} = 53.6\text{\AA}$  as determined by the shape independent center of mass of the individual reflections remains unchanged in all cases.

Next, lineshape changes were investigated in addition to the diffuse scattering intensity, see figures 5.14 and 5.15.

In figure 5.14 the  $q_z$  integrated structure factor  $S(n, q_r, t)$  is exemplary plotted for the case of  $E_p = 500\mu\text{J}$  corresponding to a peak intensity of  $P_p \approx 5 \cdot 10^4 \text{W}/\text{cm}^2$  for four delays  $t$ . The  $t$  values have been chosen in view of characteristic traits in 5.13. Although especially the determination of  $\gamma(t)$  and hereby  $\nu(t) \propto \gamma(t)$  suffers from slight uncertainties associated to the fitting procedure, a steepening of  $\frac{\Delta\gamma(t)}{\gamma_{\text{drift}}(t)} \approx +20\%$  within  $t \approx 1\mu\text{s}$  is clearly observed for the first BS, see figure 5.16. The steepening is accompanied by a lateral broadening of the diffuse reflections and consequently a strong reduction of the in plane correlation length  $\frac{\Delta\xi_r}{\xi_{r, \text{drift}}} \approx -40\%$ .

Let us now turn to an analysis of the vertical (cross-bilayer-)correlations in the

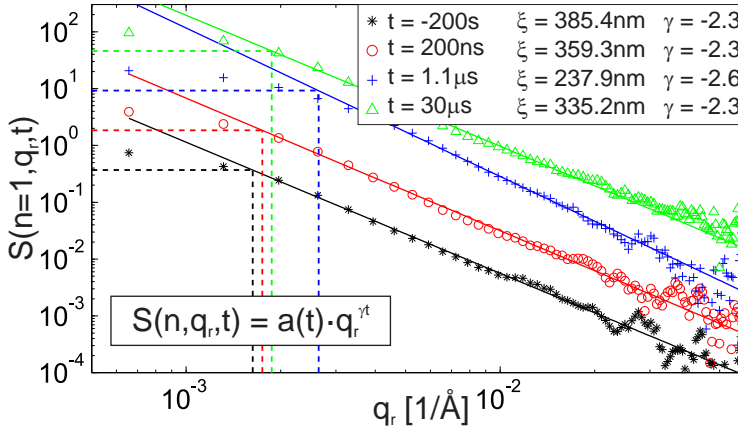


**Figure 5.14:** The  $q_z$  integrated structure factor  $S(n, q_r, t)$  of the first order BS along with a power-law fit  $S(n, q_r, t) = a(t) \cdot q_r^{\gamma(t)}$  for the four delays ( $t = -200\text{ns}$ , asterisk, black,  $t = 200\text{ns}$ , circle, red,  $t = 1.1\mu\text{s}$ , cross, blue,  $t = 30\mu\text{s}$ , triangle, green) indicated in 5.13. A clear broadening / steepening of the reflections is most obvious for  $t = 1.1\mu\text{s}$ .

multilamellar membrane stack as quantified by the smectic length scale  $\Lambda$  and the associated vertical correlation length  $\xi_z = 1/\Lambda q_r^2$  (see figure 5.15). The observed sharpening of the diffuse reflections in the vertical ( $q_z$ ) direction translates to a flattening of the FWHM curves 5.15 and hence a reduced smectic length scale  $\Lambda$  after laser excitation. As  $\xi_z \propto \frac{1}{\Lambda}$  this corresponds to transiently significantly ( $\frac{\Delta \xi_z}{\xi_{z, \text{drift}}} \approx 50\%$ ) increased out of plane correlations  $\xi_z$ .

Although all lineshape effects as quantified by  $\gamma(t)$ ,  $\xi_r(t)$  and  $\Lambda(t)$  decay on the same  $10\mu\text{s}$  time scale as the observed intensity changes  $II(n, t)$ , the rise time of these collective effects is significantly larger, i.e. by a factor of five. This is most obvious in 5.17, where all drift normalized observables extracted from the first BS have been plotted for the case of an excitation with  $\tau = 5\text{ns}$  laser pulses and therefore strongly increased temporal resolution.

As we obtain estimates for  $\gamma \propto \nu(t) = \frac{\pi k_B T}{2d^2 \sqrt{K(t)B(t)}}$  and  $\Lambda(t) = \sqrt{\frac{K(t)}{B(t)}}$  at each time point  $t$  by two independent procedures, the temporal evolution of the elastic coefficients  $B(t) = \frac{\pi}{2d^2 \nu(t) \Lambda(t)}$  and  $K(t) = \frac{\pi \Lambda(t)}{2d^2 \nu(t)}$  can in principle be obtained directly from the diffuse scattering signals [106, 54]. Following this straight forward approach would imply a transient decrease of characteristic bending energy  $K \propto \Lambda$  and an increase of the bilayer compressibility  $B \propto \frac{1}{\Lambda}$ . However, a clear definition of  $K(t)$  and  $B(t)$  can only be made in thermal equilibrium. A closer analysis of the integrated structure factors presented in 5.14 will clarify, that apparent changes of  $K(t)$  and  $B(t)$  are linked to the excitation of collective undulation modes rather than modified mechanical properties of the lipid bilayers.



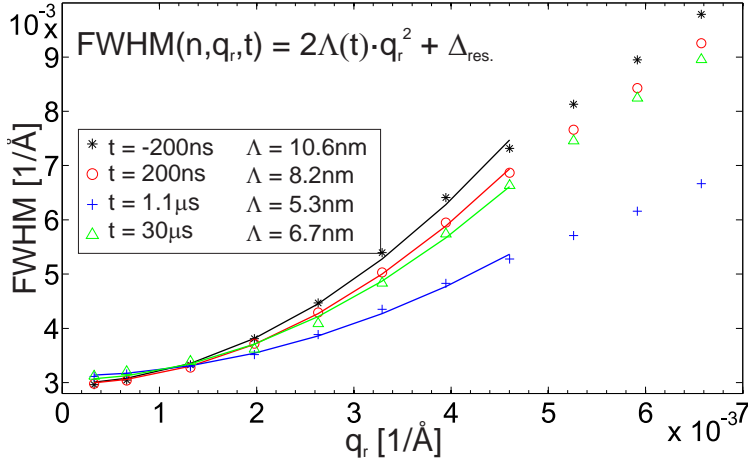


**Figure 5.15:** The smectic penetration length  $\Lambda(t)$  as extracted from the increase of FWHM of the first Bragg sheet as a function of  $q_r$ ,  $FWHM(q_r, t) = 2\Lambda(t)q_r^2 + \Delta_{res}$ . A flattening in response to laser excitation is strictly connected to a transiently increased out of plane correlations length  $\xi_z(t)$ .

Let us turn to a closer analysis of the  $q_z$  integrated structure factors  $S(n, q_r, t)$ , see figure 5.14. Difference spectra of possibly collectively excited undulation modes have been determined by means of relative changes  $\frac{S(1, q_r, t)}{S(1, q_r, 0)}$ , see figure 5.18. Individual difference spectra could well be modeled by an exponentially modified Gaussian distribution (EMG), taking into account a Gaussian distribution of undulation wavelengths around  $\Lambda$  as well as an exponential suppression of energetically expensive short wavelength modes. A general form of the exponentially modified Gaussian distribution  $emg(x)$  is given by

$$emg(x) = 1 + \frac{A}{t_0} \exp\left(\frac{1}{2} \left(\frac{w}{t_0}\right)^2 - \frac{x - x_0}{t_0}\right) \cdot \left(\frac{1}{2} + \frac{1}{2} \operatorname{erf}\left(\frac{1}{\sqrt{2}} \left(\frac{x - x_0}{w} - \frac{w}{t_0}\right)\right)\right), \quad (5.28)$$

where  $A$  is proportional to the amplitude,  $t_0$  is the skewness,  $w$  and  $x_0$  are the approximate width and position of the maximum. The central wavelength  $\Gamma = 138\text{nm}$  and bandwidth  $\Delta\Gamma = 63\text{nm}$  are determined from non-linear least squares EMG fits by means of the center of mass and FWHM. Both parameters do not dependent on  $t$  (see figure 5.18). Only a transient excitation of undulations in a well defined wavelength band is observed on the  $1\mu\text{s}$  time scale.

This observation can be interpreted in terms of a buckling instability as predicted and observed [122, 123, 124] for tensile forces perpendicular to the bilayer normal, acting on a mechanically quenched system. In the present case in plane fluctuation repulsion due to increased positional disorder on the nanosecond time scale leads to internal stress as a hypothetical homogeneous variation of the film thickness  $L$

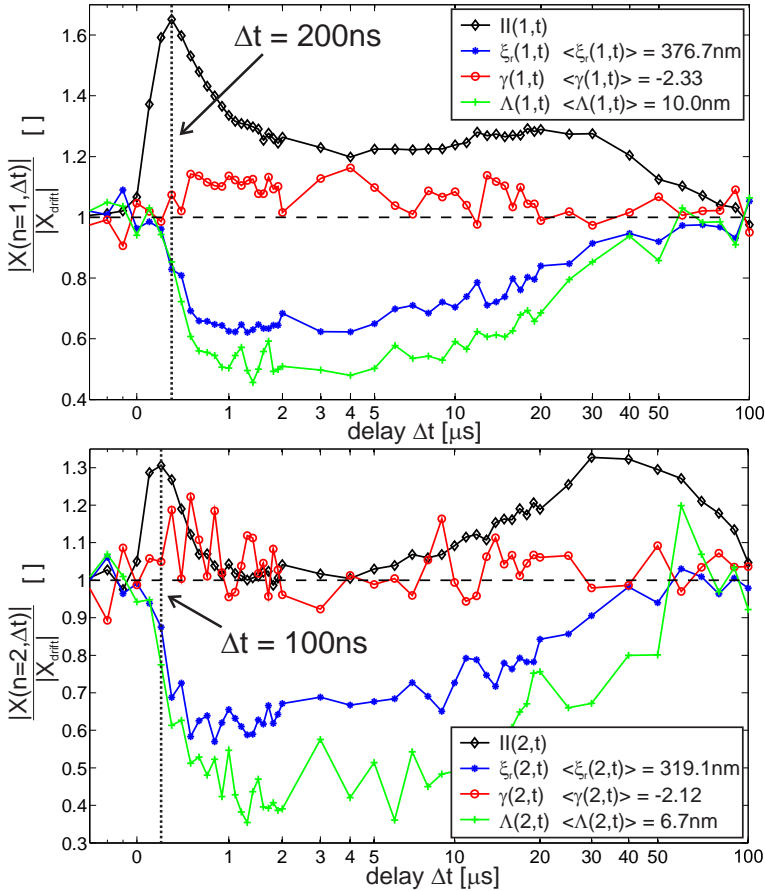


**Figure 5.16:** Temporal evolution of the integrated intensity  $II(n, t)$  (diamond, black), lateral correlation length  $\xi_r(t)$  (asterisk, blue), lineshape parameter  $\gamma(t)$  (circle, red) and smectic length scale  $\Lambda(t)$  (cross, green) for the first ( $n = 1$ ) (top) and second ( $n = 2$ ) (bottom) order diffuse reflection for  $E_p = 500 \mu\text{J}$ . The functional form of  $II(n, t)$  depends strictly on  $n$ . In both cases the smectic length  $\Lambda(t)$  as well as the lateral correlation length  $\xi_r(t)$  are reduced by approximately 50% within the first 600ns after the optical stimulation.

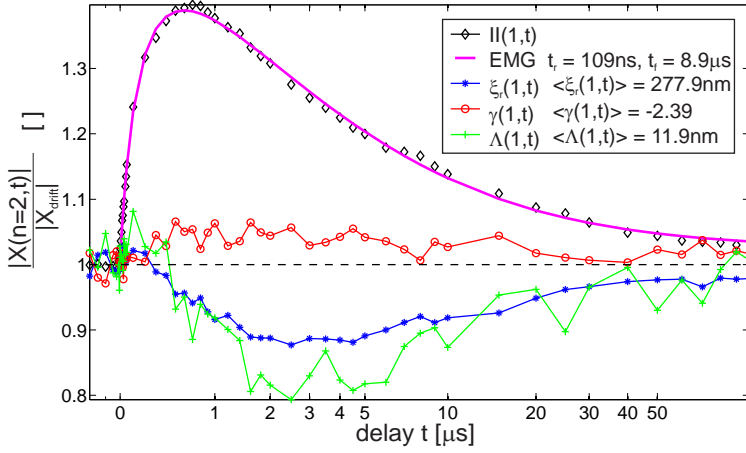


**Figure 5.17:** Temporal evolution of the integrated intensity  $II(n,t)$  (diamond, black), lateral correlation length  $\xi_r(t)$  (asterisk, blue), lineshape parameter  $\gamma(t)$  (circle, red) and smectic length scale  $\Lambda(t)$  (cross, green) for laser excitation by  $\tau \approx 5\text{ns}$  pulses at  $E_p = 200\mu\text{J}$ . No qualitative changes are observed compared to the observation made in figure 5.16. Temporal resolution is hence not limited by  $\tau$ .  $II(n,t)$  could well be modeled by an exponentially modified Gaussian distribution (EMG), allowing for a clear determination of rise  $t_r$  and decay  $t_f$  constants  $t_r = 109\text{ns}$ ,  $t_f = 8.9\mu\text{s}$  (as  $\frac{II(t)}{II(0)} = 1/e$ ).

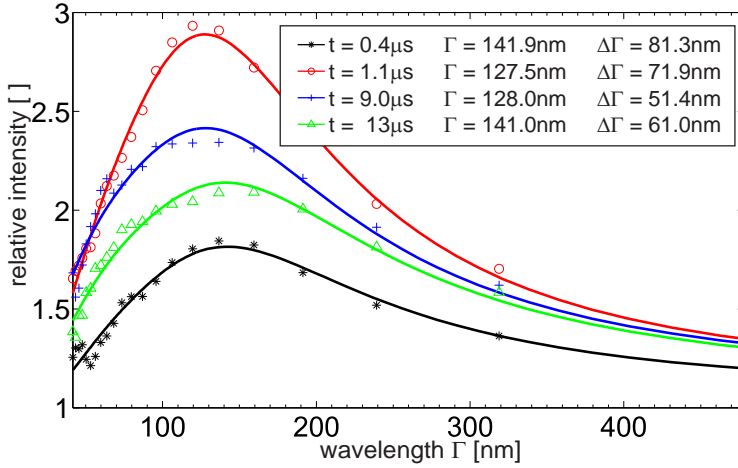


**Figure 5.18:** Difference spectra of collectively excited undulation modes as determined by relative changes  $\frac{S(1,q_r,t)}{S(1,q_r,0)}$ . Individual spectra have been modeled by an exponentially modified Gaussian distribution (EMG), the central undulation wavelength  $\Gamma$  and bandwidth  $\Delta\Gamma$  do not change as a function of  $t$ . Four representative delays  $t$  have been selected, illustrating the build up and decay of collective undulations on the  $\mu\text{s}$  time scale.

would be linked to naturally slow diffusive material transport. A rough estimation of the associated time scales can be done as follows. The velocity of lateral diffusion is limited by the speed of sound in the sample medium ( $v_{\text{sound}} \approx 2000\text{m/s}$  in our case). Hence an individual water molecule directly in the center of the laser spot will need a minimum of  $t \approx \frac{0.5\text{mm}}{2000\text{m/s}} \approx 250\text{ns}$  to move out of the pumped sample volume and to allow for a thinning of the water layer. The system is mechanically quenched during this time window. Experimentally this situation is reflected by the constant bilayer periodicity  $d(t)$ . We therefore assume that in line with [122, 123, 124] free energy is minimized by the evolution of buckling modes at a characteristic wavelength  $\Gamma_b = 2\sqrt{\pi\Lambda L}$ , where  $L = Nd$  is the thickness of the multilamellar film. For  $L \approx 1300 \cdot 53.6\text{\AA} \approx 7\mu\text{m}$  and  $\Lambda = 6\text{nm}$  (see figure 5.16) a rough estimation yields  $\Gamma_b \approx 726\text{nm}$ , being on the same order of magnitude as the experimental result.

For multilamellar stacks, typical time scales to build up an undulation mode with a central wavelength of  $\Gamma$  scale according to  $\tau(\Gamma) = \frac{\eta d}{\kappa} \left(\frac{\Gamma}{2\pi}\right)^2$ , in contrast to fluctuations of a free bilayer which are characterized  $\tau \propto \Gamma^3$  [125, 126]. With a measured inter-membrane sliding viscosity of  $\eta_3 = 0.016\text{ Pas}$  for a similar lipid sample [127], a typical bilayer bending rigidity of  $\kappa \simeq 14K_B T$  and a lamellar periodicity  $d = 53.6\text{\AA}$ , we obtain relaxation times of  $\tau \simeq 1\mu\text{s}$  for  $\Gamma = 138\text{nm}$ . This is in good agreement with the observations in figures 5.17 and 5.16. Of course, the superposition of many modes and dissipation channels is a more complicated issue,

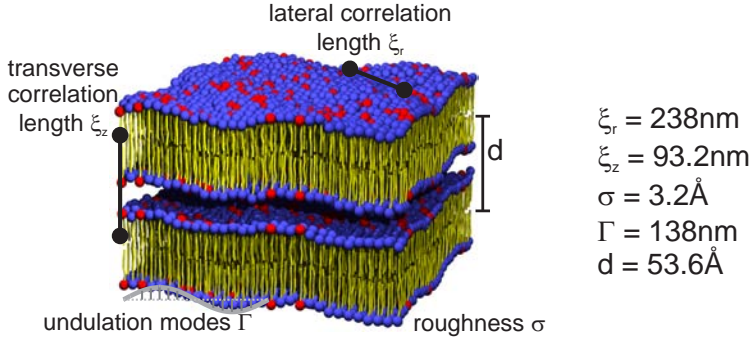


**Figure 5.19:** Schematic of the most important structural observables of a diffuse x-ray scattering experiment from a multilamellar lipid stack. Transient collective undulations at a well defined central wavelength of  $\Gamma$  are induced by nanosecond laser excitation and can clearly be detected by time resolved x-ray scattering.

and in particular the further relaxation pathway can certainly not be accounted for by a simple (single) mode picture.

Furthermore figures 5.16 and 5.17 provide another handle to answer the question whether the integrated laser pulse energy  $E_p$  or the peak intensity  $P_p$  trigger the observed dynamics. Since the temporal intensity profile of the  $\tau = 180\text{ns}$  laser pulses is rather flat,  $P_p$  is not affected by the  $\tau = 5\text{ns}$  pulse slicing. Even more, in order to reach  $E_p = 200\mu\text{J}$  in case of  $\tau = 5\text{ns}$ ,  $P_p$  had to be increased by a factor of  $\frac{P_p^{5\text{ns}}}{P_p^{180\text{ns}}} \approx 14$ . Relative changes of the observables plotted in figures 5.16 and 5.17 clearly depend on pulse energy  $E_p$  rather than  $P_p$ .

Last but not least, we have to point out that the excitation can not be described by a mere effective temperature increase, since, apart from the relatively slow time scales on the  $\mu\text{s}$  scale in the present case, the functional form of the changes would be different: An increase in  $T$  would result in an increase in  $\eta$  and hence the changes would mainly be observed in the exponent  $\gamma$ , and not in  $\Lambda$  in contrast to the experiment. This is further supported by a rough estimation of the laser induced temperature increase  $\Delta T = \frac{100 \cdot 10^{-6} \text{J}}{7 \cdot 10^{-5} \text{g} \cdot 4.182 \frac{\text{J}}{\text{g}\cdot\text{K}}} \leq 0.35\text{K}$  of the pumped sample volume (for  $E_p = 1000\mu\text{J}$ , an estimated absorbance of 10% and a specific heat capacity of  $c = 4.18 \frac{\text{J}}{\text{g}\cdot\text{K}}$ ). We therefore conclude that models based on an effective temperature and/or time dependent elastic moduli after excitation do not capture the experimental phenomena observed here.

### 5.2.1 Conclusions

Relative variations of  $II(n, t)$ ,  $\nu(t)$ ,  $\xi_r(t)$  and  $\Lambda(t)$  as well as the well defined wavelength  $\Gamma$  of transient collective undulations draw a consistent and conclusive picture of the non-equilibrium situation, see additionally figure 5.19: The observed

intensity changes, which are brought about by creating rms-roughness and structural changes of the membranes at molecular scales, occur within the first  $\approx 100$ ns after excitation. The mesoscopic dynamical pathway is characterized by the formation of collective modes in response to the increased in-plane fluctuation repulsion. Observed time scales of  $\tau \approx 1\mu\text{s}$  perfectly agree with theoretical predictions [125]. A characteristic length scale of  $\Gamma = 138 \pm 63\text{nm}$  roughly coincides with predictions for an undulation instability [122, 123, 124]. The evolution of collective modes is reflected by apparent changes of the mechanical parameters  $K$  and  $B$ . Collective modes lead to an apparently decreased bending rigidity  $K$  and therefore an apparently decreased in plane correlation length  $\xi_r$ . Vertical correlations are in this case seemingly increased, leading to an apparently increased compressional modulus  $B$ . Subsequent relaxation back to thermal equilibrium happens on the  $10\mu\text{s}$  timescale, possibly through a wide range of dissipation channels. Experimentally, this fluctuation dissipation can be observed as e.g. a distinct second maximum of  $II(2, t)$ , see figure 5.16.

**Impact on photo physical experiments?** Let us close with a short discussion on the impact of these findings on photo physical experimental techniques. The laser intensities  $P_p \leq 10^5\text{W}/\text{cm}^2$  applied in these experiments are relatively mild when compared to confocal microscopy ( $P_p \approx 10^6\text{W}/\text{cm}^2$  [12]), two-photon-microscopy ( $P_p \leq 10^{11}\text{W}/\text{cm}^2$  [13, 14]) or super resolution techniques ( $P_p \leq 10^9\text{W}/\text{cm}^2$  [15]). Although pulse energies applied in microscopy experiments are typically one order of magnitude smaller compared to the present experiment, it seems likely that high peak intensities in combination with cumulative effects due to typically high repetitions rates of  $100\text{MHz}$  ( $t \approx 10\mu\text{s}$ ) alter the dynamical properties of photo labeled soft matter sample systems dramatically, effectively driving the structure under observation away from thermal equilibrium. Although these effects may not change elementary properties on the molecular scale, collective effects on the mesoscopic scale are certainly expected. An extension of the presented experiments to a broader range of sample systems and ambient conditions is strongly proposed.

## 6 Summary and outlook

The main goal of the present thesis was to extend and apply time resolved x-ray scattering experiments at in-house, synchrotron and Free Electron Laser sources to soft matter sample systems, in particular aligned lipid multilayers on solid support. A special emphasis was placed on a characterization of the non-equilibrium fast time response of the multilamellar stack to shortly pulsed optical excitation (section 4.4) as well as the acousto-electric field accompanying a Surface Acoustic Wave (SAW), section 3.3.

As a first step towards this goal, a flexible in-house diffraction setup based on a femtosecond Cu- $K_\alpha$  laser plasma x-ray source (PXS) has successfully been constructed and commissioned at the University of Göttingen. First experiments at the PXS (section 4.4) clearly demonstrate the high flexibility, the great accessible parameter range and the high (only Poisson limited) instrumental resolution.

This knowledge on time resolved x-ray scattering as well as instrumentation and timing schemes has directly been transferred to synchrotron sources (ESRF, Grenoble and Petra III, Hamburg) where higher resolution experiments complementing first in-house experiments have been performed. These experiments are divided into three subgroups.

In a first experiment at the beamline ID09B (ESRF, Grenoble) the optical pump x-ray probe experiments performed at the PXS have been improved and extended, eventually minimizing thermal drift induced by the pumping laser as well as by x-ray radiation (section 5.1.2). Reproducible and reversible structural dynamics in (pure) lipid multilayers on Si substrates were induced by nanosecond laser pulses ( $\tau = 180\text{ns}$ ,  $\lambda = 527\text{nm}$ ,  $E_p \geq 500\mu\text{J}$ ), see section 5.1.2. Relative variations of the high resolution diffuse scattering patterns could clearly be attributed to an increased rms surface roughness  $\sigma$  as well as variations of the relative electron density profile  $\Delta\rho(z, t)$  on the molecular scale. A conceptually new data analysis approach based on a combination of high resolution diffuse- and reference reflectivity experiments allowed for (i) the disentanglement of roughness variations and form factor changes and (ii) the reconstruction of the relative electron density profile  $\Delta\rho(z, t)$  for each time point after the optical excitation.

A direct extension of these experiments was achieved by the introduction of fluorescent markers (Texas-red), serving as localized force centers as well as a model system for more complex active proteins. By the analysis of high resolution diffuse scattering patterns (section 5.1.5) it could be shown that collective in-plane undulation modes at a well defined wavelength  $\Gamma = 140\text{nm}$  are induced upon laser stimulation ( $\tau = 180\text{ns}$ ,  $\lambda = 527\text{nm}$ ,  $E_p \geq 100\mu\text{J}$ ). Corresponding time scales of approximately  $1\mu\text{s}$  are in good agreement with values expected for the emergence of collective modes at the respective wavelength [125, 126]. The results are interpreted in terms of a buckling instability as a response to the increased in-plane

fluctuation repulsion for a mechanically quenched system.

A third and (very recent) fourth, synchrotron experiment focused on the interaction of the electro-acoustic field of a SAW with a multilamellar lipid stack, see section 3.3. Preparatory experiments on pure  $LiNbO_3$  substrates revealed a seamless transition between kinematic and dynamical scattering regimes (section 4.2) on the picosecond time scale as result of a coherent acoustic phonon propagating along the surface of the piezoelectric substrate 4.3. For lipid multilayers, ultrafast dynamics on the molecular scale are induced by a standing SAW. By measuring the full x-ray reflectivity curve at different phases between the standing wave and the synchrotron pulses the molecular response by means of the vertical relative electron density profile  $\Delta\rho(z, t)$  could be reconstructed. Relative variations of  $\Delta\rho(z, t)$  are interpreted in terms of the lipid bilayers interacting with the strong electric field accompanying the SAW. Recent experiments however strongly suggest that the observed dynamics are induced by the acoustic component of the SAW rather than the associated electric field.

The timing scheme at Petra III has been strongly influenced by and partly developed in this thesis, see section 1.3. Especially the implementation of the exact 10MHZ reference signal, now being available at every beamline, as well as the exact frequency values distributed by the Petra III bunchclock have been stimulated by the work on SAW excited lipid multilayers, see section 3.3.

In addition to important experimental results related to the out of equilibrium properties of lipid multilayers, major technical achievements arose in the context of this thesis. Most notable a pulse resolved detection scheme was designed and commissioned (section 2.3.2), driven by the lack of x-ray detectors dedicated to time resolved scattering experiments. The presented detector is based on a fast quadrant avalanche photo-diode (QAPD) and high speed digitizers. It enables pulse-by-pulse read-out of the PETRA III 240-bunch mode with single photon detection capability. In contrast to the application of 'photon wasting' pulse selection methods (i.e. high speed choppers or gating of modern pixel detectors) induced dynamics are simultaneously sampled at a high number of time points using each synchrotron bunch, leading to an tremendous increase ( $\frac{f_b}{f_{pp}} \approx 30000$ ) of the effective primary intensity. However, in addition to advantages related to time resolved experiments, the intrinsic linearity and tremendously high dynamic range (up to  $5 \cdot 10^9$  photons per second can be detected and individually time stamped), the presented detector will increase the flexibility and achievable parameter range of synchrotron and especially Free Electron Laser based experiments.

In conclusion, the presented thesis opens up a broad range of experimental capabilities related to the observation of especially non-equilibrium phenomena in soft matter sample systems. Particularly interesting future topics in the field of membrane biophysics are related to membrane fusion, pore formation, protein activity and nerve pulse propagation.



# A Appendix

## A.1 Excitation mechanisms for pump probe experiments on lipid bilayers

As mentioned in the introductory section, apart from shortly pulsed x-ray sources, an elaborated scattering setup and precise timing schemes especially the selective and non destructive excitation of soft matter sample systems poses significant experimental challenges in the context of time resolved diffraction experiments. A short introduction to photo physical processes governing laser excitation of especially biological systems will be given in section A.1.1, being more of a general interest in the context of the presented experiments. General thoughts on the interaction between electric fields as applied by Surface Acoustic Waves (sections 2.1 and 3.3) or high voltage pulses (appendix A.1.3), and lipid bilayers will be discussed in section A.1.2.

### A.1.1 Excitation of lipid membranes by pulsed laser radiation

Depending on the pulse intensity  $P_p$  the primary interaction mechanism between laser radiation and biological tissue (in particular lipid bilayers) is governed by conceptually different interaction mechanisms. For moderate light intensities absorption takes place in a resonant way, i.e. energy can selectively be transferred to certain chromophores (e.g. fluorophores such as Texas-red 5.1.5) and is simply dependent on the linear absorption coefficient of the illuminated material. For strong light intensities  $P_p \geq 10^{11} \frac{\text{W}}{\text{cm}^2}$  complex processes such as non linear photon absorption and optical breakdown occur, being of major importance in the context of opto-poration and laser nano surgery [128, 129]. A short sketch of the main interaction processes for moderate  $P_p \leq 10^{11} \frac{\text{W}}{\text{cm}^2}$  and strong  $P_p \geq 10^{11} \frac{\text{W}}{\text{cm}^2}$  intensities is provided in the following paragraphs, we refer to the extensive literature (especially [128, 129]) for a detailed review on photo absorption processes in biological tissue.

**Photo absorption in biological tissue at moderate light intensities** Resonant absorption processes can at least roughly be further divided into different wavelength regimes.

**UV ( $180\text{nm} \leq \lambda \leq 400\text{nm}$ ):** The absorption of laser light in the ultra violet (UV) region of the electromagnetic spectrum is dominated by the dissociation of covalent bonds and the generation of photo electrons. Dissociation energies of molecular bonds occurring in biological tissue range from  $C = O$  ( $7.5\text{eV} \hat{=} 160\text{nm}$ ) and  $C = C$  ( $6.4\text{eV} \hat{=} 187\text{nm}$ ) to  $C - N$  ( $3.0\text{eV} \hat{=} 414\text{nm}$ ). Chemical effects induced by solvated electrons and free radicals lead to 'lipid-peroxidation' and thus severely

damage lipid bilayers. The general pathway of this chain reaction is e.g. reviewed in [130].

**VIS ( $400\text{nm} \leq \lambda \leq 780\text{nm}$ ):** Generally the absorption of visible (VIS) light is due to electronic transitions in conjugated organic compounds and transition metals (in particular Fe). Except for extinction due to scattering effects, lipid bilayers are transparent in this region. Absorption of light in biological tissue is dominated by hemoglobin ( $\lambda = 433\text{nm}$  and  $\lambda = 414\text{nm}$ ) and melanin ( $400\text{nm} \leq \lambda \leq 780\text{nm}$ ). A variety of proteins is absorbent in this part of the spectrum, for some (i.e. the light driven proton pump *bacteriorhodopsin* [16]) visible light can trigger protein activity.

**IR ( $780\text{nm} \leq \lambda \leq 15\mu\text{m}$ ):** The photon energy of infrared (IR) laser light matches a variety of vibrational stretching and bending modes of molecular bonds. The first absorption maxima of water in the NIR at  $\lambda = 960\text{nm}$ ,  $\lambda = 1.44\mu\text{m}$  and  $\lambda = 1.95\mu\text{m}$  are for example due to high energy stretching modes of the  $O - H$  bond [131]. FTIR spectra of common lipid model systems have e.g. been obtained in [132]. At the extreme long wavelength limit of the IR region of the electromagnetic spectrum terahertz fluctuations of whole molecules start to occur.

**Effects of high intensity laser radiation on biological tissue** For light intensities  $I \geq 10^{11} \frac{\text{W}}{\text{cm}^2}$  even transparent media becomes highly absorbing due to an optical breakdown of the sample. Similar to the processes sketched in section 1.3 multi photon absorption [133], field- and tunneling ionization generate quasi free seed electrons. These seed electrons are further heated by inverse Bremsstrahlung absorption (inelastic scattering of photons) until their energy is sufficient to create another free electron through impact ionization. This chain reaction leads to an avalanche growth of the number of free electrons and therefore the density of the plasma increases. At a critical electron density  $\rho_{crit.} \approx 10^{21} \frac{\text{free electrons}}{\text{cm}^3}$ , the plasma frequency  $\omega_p = \sqrt{\frac{e^2 n_e}{m_e \epsilon_0}}$  will match the frequency of the incoming laser light and huge amounts of energy are absorbed by previously transparent media.

### A.1.2 Lipid bilayers excited by strong electric field pulses

A fundamentally different approach to laser stimulation is to use strong electric fields  $E \approx 10^7 \text{V/m}$  in order to excite lipid membranes. An electric field across a lipid bilayer leads to a variety of forces, resembling physiological and / or experimentally important conditions, see figure A.1. In the following paragraphs a short outline of the most important relations and general orders of magnitude will be presented rather than a detailed theoretical discussion of the underlying physical mechanisms. A more detailed calculation of electric field effects on lipid bilayers can for example be found in [134, 135, 136, 137, 5].

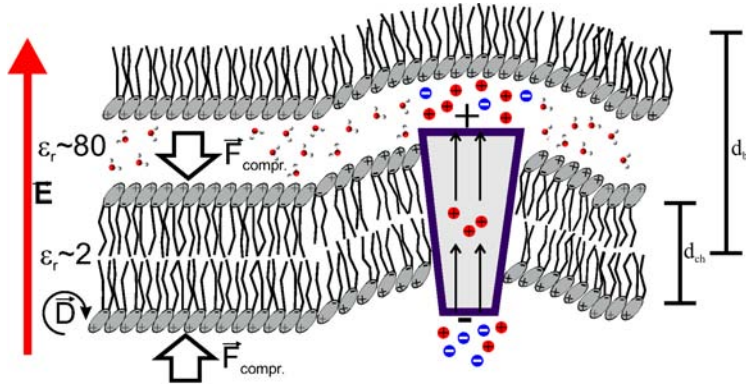


**Figure A.1:** Electric fields acting on a lipid bilayer lead to a variety of compressive  $F_{\text{compr.}}$ , tensile, orientational and rotational forces on the lipid bilayer as described in the text. Additionally electric fields (as well as the photon character of pumping laser light) can trigger the state / activity of e.g. voltage gated ion channels.

Note that the high frequency AC field  $E_l$  in the focus of a high intensity laser beam (intensity  $P_p$ ) can easily reach field strengths of  $10^8 \text{V/m}$ . It is given by

$$E_l = \sqrt{\frac{2P_p}{c\epsilon_0}} \approx 27.4\sqrt{P_p}, \quad (1.29)$$

where  $\epsilon_0$  is the vacuum permittivity,  $c$  is the speed of light,  $P_p$  is given in units of  $[\text{W/m}^2]$  and  $E$  is given in  $[\text{V/m}]$ .

This discussion is however strictly limited to homogeneous DC electric fields. For high frequency AC fields the frequency dependence of the dielectric permittivity  $\epsilon_r$  has to be taken into account and ponderomotive forces become prominent. A qualitative description of especially compressional forces (as detailed in the next paragraph), as the main case of interest during the starting phase of this thesis, is however also valid for AC fields as the predicted effects do only depend on  $\vec{E}_l^2$ .

**Compressive forces acting on the lipid bilayer** The lipid bilayer can be approximated as a capacitor whose plates are separated by an isotropic, elastic and dielectric material of thickness  $d_l$ . This early approach to describe the interaction of a lipid bilayer with an external electric field has been proposed by Crowley et al. [134]. It is assumed that the relation between the applied force  $F_{el.}$ , or the resulting pressure  $p_{el.}$  respectively, and compression  $\Delta d$  of the lipid bilayer follows Hooke's law

$$Y \frac{\Delta d_l}{d_l} = p_{el.}, \quad (1.30)$$

where  $Y$  is Young's modulus of the lipid bilayer. The compressive force due to an electric field  $E_l$  between two plates of a condensator (area  $A$ ), separated by

a medium with a electrical permittivity  $\epsilon_r$ , is  $F_{el.} = \frac{1}{2}\epsilon_0\epsilon_rAE_l^2$ , and hence the thickness  $d_l$  of the bilayer changes according to

$$\Delta d_l = \frac{\epsilon_0\epsilon_r}{2Y} E_l^2 d_l \quad (1.31)$$

Typical values for DOPC are [134]:  $\epsilon_r \approx 2$ ,  $Y = 2.9 \cdot 10^4 \frac{N}{m^2}$  and  $d_l = 3.5 \cdot 10^{-9}m$ . Hence for a trans membrane electric field of  $E = 1 \cdot 10^7 V/m$  (physiological case), a compression of  $\Delta d \approx 1\text{\AA}$  is expected.

Note that a homogeneous compression of a multilamellar stack of lipid bilayers is expected to take place on a time scale of  $t \geq (d * N)/c_{\text{sound}} \approx 5\text{ns}$  where  $N \approx 2000$  is the number of bilayers in the stack and  $c_{\text{sound}} \approx 2000\text{m/s}$  is the speed of sound in water and lipids.

**Fluctuation enhancement due to transverse electric fields** A generalization to mere compressional forces has been proposed by H. Isambert and P. Sens [135, 136]. The proposed estimations emphasize that the special case of a mere compression of a bilayer due to an electric field is only applicable to perfectly flat membranes. For a fluctuating bilayer an additional negative surface tension  $\gamma_{el.} = \epsilon_m \left( \frac{\chi_m}{\chi_1} \right)^2 dE_l^2$  is expected to enhance thermal undulations up to the point of mechanical instability.  $\gamma_{el.}$  is understood as being induced by the interaction of charges with  $E_l$  at the interfaces of the bilayer.  $\chi_m \approx 10^6 \frac{m}{S}$  and  $\chi_1 \approx 10 \frac{m}{S}$  are in this case the electric conductivity of the lipid and water layer,  $\epsilon_m \approx 2\epsilon_0$  is the dielectric permittivity of the lipid layer,  $b \approx 10^8 \text{Pa}\cdot\text{s}\cdot\text{m}$  is the inter monolayer friction coefficient and  $\kappa \approx 10^{-20}\text{J}$  is the bending modulus of a lipid bilayer. Furthermore a preferred growth of undulation modes balanced by an interplay between hydrodynamic and electric forces at a central wavelength  $\Gamma_{el.} = 2\pi \left( \frac{\nu\gamma_{el.}}{bd^2\kappa} \right)^{-1/3}$  is predicted [135], yielding  $\Gamma = 138\text{nm}$  for a hypothetical electric field of  $E_l \approx 4000 \frac{V}{m}$ . This is approximately four orders of magnitude smaller than expected for a physiological situation.

The above estimations are only valid for a freely fluctuating single bilayer, the situation is further complicated in the presence of a rigid wall or a multilamellar lipid stack [18].

**Influence on the orientation of lipid molecules I** The polarized nature of lipid headgroups leads to a strong dipole moment, i.e.  $D \approx 16\text{Debye} = 5.34 \cdot 10^{-29}\text{Cm}$  [138] for the PC-headgroup. Due to the tendency of the lipid headgroup to shield the hydrophobic interior as well as dipole-dipole interactions, the headgroup orientation is tilted by  $\alpha \approx 60^\circ$  with respect to the surface normal [10], without the influence of transverse electric fields. For the physiological case of a DC transverse electric fields of  $E = 1 \cdot 10^7 V/m$  the potential energy  $W_{pot.}$  of each headgroup is

$$W_{pot.} = D \cdot E \approx 2.7 \cdot 10^{-22}\text{J} \approx 0.07k_B T. \quad (1.32)$$

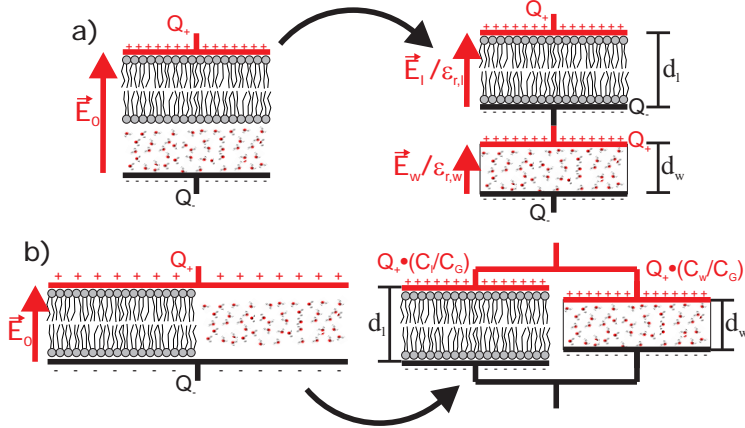


**Figure A.2:** The electric capacity of a lipid membrane (lipid bilayer and water layer) depends strongly on the arrangement of the two dielectric media in a transverse electric field  $E_o$ . The native configuration a) is equivalent to a series connection of two capacities  $C_{lipid}$  and  $C_{water}$ , yielding a total capacity  $C_{\perp} = \frac{C_{lipid}C_{water}}{C_{lipid}+C_{water}}$ . In the (fictional) extreme case of a 'side by side' orientation (b) of lipid and water layer  $C_{\parallel} = C_{lipid} + C_{water}$  corresponds to the capacity of an equivalent parallel connection of  $C_{lipid}$  and  $C_{water}$ .

An energy difference of  $W_{pot.} \approx 0.07k_B T$  will have a negligible effect on the orientation of a single lipid molecule compared to thermal fluctuations (magnitude  $\approx 1k_B T$ ). In an oriented lipid bilayer consisting of several thousand molecules however even small energy differences can outweigh thermal fluctuations because of the oriented nature of the underlying forces.

**Influence on the orientation of lipid molecules II** The former description disregards the contrast in electrical permittivity between water- and lipid layers of multilamellar lipid stacks. Under the influence of a transverse external electric field  $E_o$  the electric potential energy  $W_{el.}$  strongly depends on the relative arrangement of the two dielectric media. The minimization of  $W_{el.}$  leads to collective orientational effects. In a simple model the electric field energy can be estimated by modeling the electric field  $E_o$  across the multilamellar stack as induced by two plates of a condensator with a fixed charge  $Q$ . Keeping  $Q$  rather than the voltage  $U_t$  fixed allows the electric field inside the condensator to change according to thickness and arrangement of the dielectric media. A short estimation of the expected orientational effects will be given, disregarding essentially all mechanical and dynamical properties of lipid bilayers. The proposed model is meant as a thought-provoking impulse rather than an exact theoretical calculation.

In the case of a transverse electric field across a lipid membrane (lipid layer and water layer) the capacity of an equivalent circuit is equal to a series connection of

two capacitors  $C_{\text{lipid}}$  and  $C_{\text{water}}$ , see figure A.2. For a bilayer thickness  $d_l$  and a water layer thickness  $d_w$  the total capacity  $C$  is given by

$$\frac{1}{C} = \frac{1}{C_{\text{lipid}}} + \frac{1}{C_{\text{water}}} = \frac{1}{\epsilon_0 A} \cdot \frac{\epsilon_{r,l} d_w + \epsilon_{r,w} d_l}{\epsilon_{r,l} \epsilon_{r,w}} \quad (1.33)$$

$$C = \epsilon_0 A \cdot \frac{\epsilon_{r,l} \epsilon_{r,w}}{\epsilon_{r,l} d_w + \epsilon_{r,w} d_l}, \quad (1.34)$$

where  $A$  is taken to be the headgroup area of a single lipid molecule,  $\epsilon_{r,l}/\epsilon_{r,w}$  are the dielectric permittivity of lipid and water layer. For a hypothetical 'side-by-side' orientation as an extreme case of e.g. pore formation (see figure A.2) the total capacity  $C$  of water and lipid layer is represented by two capacitors connected in parallel to each other. In this case, the total capacity is just the sum of both capacitors (see figure A.2)

$$C = C_{\text{lipid}} + C_{\text{water}} = \epsilon_0 A \left( \frac{\epsilon_{r,l}}{d_l} + \frac{\epsilon_{r,w}}{d_w} \right). \quad (1.35)$$

The maximum energy difference  $\Delta W$  per lipid molecule under the influence of an electric field of  $E = 1 \cdot 10^7 \text{V/m}$  can thus be roughly estimated to

$$\Delta W = \frac{1}{2} \Delta C \cdot E_0^2 d^2 \quad (1.36)$$

$$\approx 6.2 \cdot 10^{-22} \text{J} = 0.15 \text{k}_B\text{T} \quad (1.37)$$

$d_l = 35 \text{\AA}$ ,  $d_w = 10 \text{\AA}$  and  $A \approx 70 \text{\AA}^2$  has been assumed for the calculation. As argued in the preceding paragraph a potential energy of  $\Delta W = 0.15 \text{k}_B\text{T} \ll 1 \text{k}_B\text{T}$  per lipid will have a measurable effect on the mean orientation of the lipid headgroups in a DC electric field by collective effects. In summary the resulting effects predict a tendency to incorporate water molecules into the lipid bilayer in order to minimize electric field energy.

A similar argumentation predicts relative thickness variations between lipid and water layer for a constant periodicity  $d = d_l + d_w$ . If the orientation of both layers is fixed perpendicular to an external electric field the energy  $W$  of an equivalent condensator will be proportional to

$$W \propto (d\epsilon_{r,l} + d_l(\epsilon_{r,w} - \epsilon_{r,l})). \quad (1.38)$$

In order to minimize electric energy, the relative thickness will change depending on  $\Delta\epsilon_r = \epsilon_{r,w} - \epsilon_{r,l}$ . For  $\Delta\epsilon_r > 1$  as for a DC electric field a thinning of the membrane is expected.

### A.1.3 The high voltage pulser / The thin film diffraction chamber

Given a bilayer thickness of roughly 5nm strong transverse electric fields of  $E \approx 10^7 \text{V/m}$  arise even from minor potential differences  $\Delta U \approx 100 \text{mV}$  in a physiological situation. An experimental realization of electric fields of  $E \approx 10^7 \text{V/m}$  in

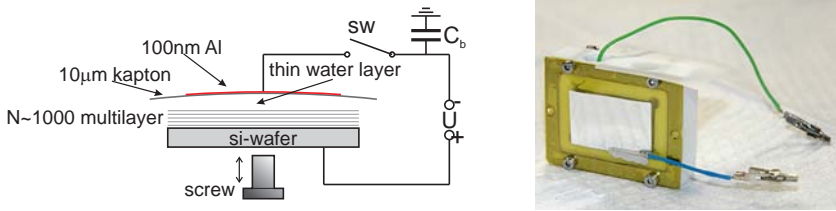


**Figure A.3:** *Left:* Sketch of the thin film electric field chamber allowing for pulsed high voltage (HV) excitation of multi lamellar lipid membranes. A highly arsenide doped Si-wafer supports the multi lamellar lipid stack. The sample is covered by a  $10\mu\text{m}$  thin kapton foil, a  $100\text{nm}$  thin Al layer on top of the kapton foil as well as the arsenide doped Si-wafer are electrically contacted. The sample chamber can be filled with ultra pure water / salt solutions in order to resemble the physiologically relevant situation. **Right:** Photo of the thin film electric field chamber.

combination with a high resolution scattering experiment is however non-trivial, especially in the case of multi lamellar samples. Similar to the situation sketched in section A.1.2 a multi lamellar stack of  $N$  lipid bilayers can be regarded as a series connection of  $2N$  individual capacitors (lipid layer and water layer). The total voltage  $U_t$  across the  $2N$  capacitors needed in order to resemble the physiologically relevant situation for each individual bilayer scales with  $N$ . Hence voltages in the kilo volt (kV) range have to be applied, see e.g. figure A.4. In the context of time resolved x-ray scattering the situation is further complicated by the need for a highly accurate, shortly pulsed excitation mechanism with voltage-rise times in the lower nanosecond range. For this purpose a dedicated electric field chamber has been designed and commissioned as a side project of this thesis, see figure A.3 for a schematic of the experimental realization.

For electric field experiments, multi lamellar lipid bilayers are prepared on highly arsenide doped Si-wafers (thickness  $525\mu\text{m}$ , n-type, specific resistance approximately  $0.005\Omega\cdot\text{cm}$ , Crystec, Berlin). A detailed description of the sample preparation protocol is given in section 2.2. The surface of the resulting highly ordered multi lamellar sample is covered by a  $10\mu\text{m}$  thin Kapton foil (Goodfellow, Huntington, GB), a thin water layer between lipid sample and kapton foil prevents the lipid film from sticking to the cover. A  $100\text{nm}$  thin Al film on top of the Kapton foil and the arsenide doped silicon wafer serve as electric contacts, see figure A.3. Voltages of up to  $U = 4\text{kV}$  have been applied across the chamber without electric discharge and measurable currents across the highly electrically isolating kapton foil.

Voltage rise times on the lower nanosecond timescale can be achieved with a high speed high voltage switch (HTS 41-06-GSM, Behlke, Billerica, USA) in combination with a buffer capacitor  $C_b$  providing high peak currents. In order to properly dimension the electric circuit and especially  $C_b$  an estimation of the total capacity

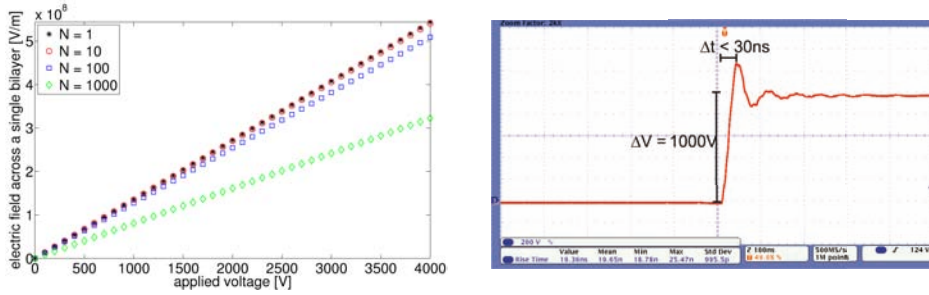


**Figure A.4:** *Left:* The electric field across a single bilayer in a multi lamellar stack of  $N$  bilayers as a function of applied voltage for the electric field chamber. Physiologically relevant field strengths can be reached for  $U \approx 100\text{V}$ , electroporation is expected to occur at  $E \geq 5 \cdot 10^8\text{V/m}$ , corresponding to  $U \geq 3500\text{V}$ . *Right:* Oscilloscope trace as taken during a time resolved diffraction experiment using the high voltage excitation mechanism. A rise time of  $\Delta t < 30\text{ns}$  for a voltage jump of  $\approx 1\text{kV}$  roughly determines the achievable temporal resolution. A slight overshoot indicates a non perfect impedance matching of the high voltage pulser to the sample chamber.

$C_t$  of the sample chamber has been made according to the simple model of a series connection of  $N$  water layer- and  $N$  lipid layer capacitors (capacities  $C_w$  and  $C_l$ ) as well as a capacity  $C_f$  representing the kapton foil yielding

$$C_t = \frac{C_f C_l C_w}{C_l C_w + N(C_f C_w + C_f C_l)} \approx 0.67\text{nF}. \quad (1.39)$$

Typical values of  $\epsilon_l = 2$ ,  $\epsilon_w = 80$ ,  $\epsilon_f = 3.4$ ,  $d_l = 4\text{nm}$ ,  $d_w = 2\text{nm}$ ,  $d_f = 10\mu\text{m}$  have been taken from the literature ([134] and <sup>14</sup>). The buffer capacitor has hence been chosen to  $C_B = 100\text{nF}$  in order to limit the voltage drop  $\Delta U$  at the power supply during the a HV pulse to  $\Delta U \frac{C_t}{C_B} = 0.01 \cdot U$  and therefore provide stable operating conditions. The sample capacity  $C_t$  further limits the minimal achievable rise time to  $\Delta t = \frac{C_g U}{I_{peak}} \leq 40\text{ns}$  because the maximal current is limited to  $I_{peak} \leq 60\text{A}$  (limited by the HV switch, corresponding to a peak power of  $P_{peak} = 240\text{kW}$  at  $U = 6000\text{V}$ ). Stable and reliable operation has been proven for the high voltage pulser as well as the electric field chamber.

It has to be noted that the HV pulser is a highly dangerous piece of equipment, it must only be operated by qualified personnel. When fully charged ( $U = 6\text{kV}$ ) the buffer capacitor carries an electric energy of  $W = C_B U^2 \approx 4\text{J}$ , uncontrolled discharge of the capacitor results in peak powers of  $P_{peak} \gg 1\text{MW}$ .

<sup>14</sup><http://www.goodfellow.com/E/Kapton-HN-Grade.html>



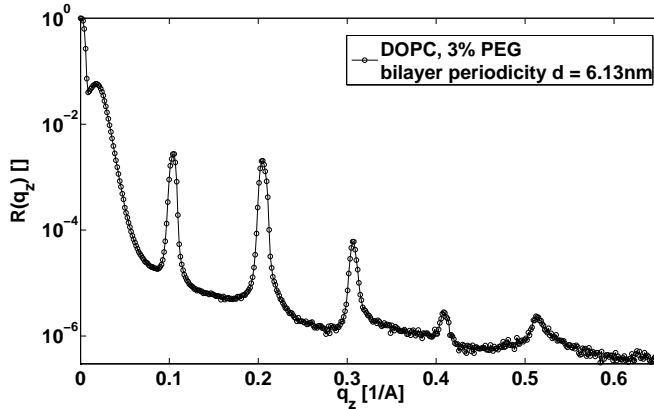


**Figure A.5:** X-ray reflectivity curve of a DOPC multilayer in contact with a 3% wt. PEG solution in the thin film chamber, obtained with  $\text{Cu-K}_\alpha$  x-ray radiation at the in-house diffractometer WENDY. The bilayer periodicity of  $d = 61.3\text{\AA}$  clearly corresponds to a nearly fully swollen state [139].

**The thin film diffraction chamber** In addition to advantages related to the application of strong electric fields, the presented thin film chamber (see figure A.3) allows for diffraction experiments under conditions of full hydration using comparatively low x-ray photon energies, see figure A.5. Strong absorption of x-ray radiation in liquid water otherwise often poses severe restrictions on experimental possibilities, a transmission of only  $\leq 1 \cdot 10^{-3}$  is obtained for an optical path length of 1cm at a photon energy of 8048eV ( $\text{Cu-K}_\alpha$  radiation). The presented approach was inspired by [89].

The optical path length in liquid water is minimized due to the construction of the thin film chamber, a screw below the Si-substrate (see figure A.3 left) is used to apply a gentle pressure between the substrate and the window material. The Al coated kapton window is in this case exchanged by a  $4\mu\text{m}$  thin polypropylene foil, leading to a transmission of approximately 86% at a photon energy of  $E = 8048\text{eV}$  under an angle of incidence of  $\alpha_i = 1^\circ$  (typical position of the first Bragg reflection of a lipid multilayer, optical path length  $458\mu\text{m}$ ). A hypothetical water layer thickness of  $5\mu\text{m}$  still transmits a percentage of approximately 57% under the same experimental conditions (optical path length  $573\mu\text{m}$ ), allowing for standard x-ray reflectivity experiments under conditions of full hydration at a  $\text{Cu-K}_\alpha$  x-ray source as for example the PXS.

## A.2 Ionization chambers as intensity monitors for femtosecond x-ray pulses at 1kHz repetition rate

The primary intensity of the PXS is considered to be rather unstable when compared to standard x-ray tubes or synchrotron sources [120]. Short timescale pulse

to pulse intensity fluctuations are observed as well as long timescale intensity variations due to mechanical instabilities of the copper tape, increasing debris contamination and uncertainties in the positioning of the laser focus. Short timescale fluctuations can in principle be eliminated by averaging over many ( $N \approx 10000$ ) pulses at the laser repetition rate of 1kHz, long time scale intensity fluctuations can only be eliminated from the data by a suitable monitor signal.

The pulsed nature of the PXS poses strict limitations on the detection mechanism of the intensity monitor as well as the primary x-ray detector. Single photon counting techniques are only applicable if the effective intensity is limited to  $\leq 1 \frac{\text{photon}}{\text{pixel-pulse}}$  (see section 2.3.2) and the cw ('un-triggered') readout principle typically applied with standard x-ray photodiodes does not allow for reliable measurements due to the pulsed nature of the PXS. It was discovered that the naturally slow response and time integrating nature of an ionization chamber (JJXray) facilitates the measurement due to a washing out of the pulsed signal, allowing for standard cw current measurements with commercial laboratory equipment. More advanced techniques will be discussed in section 2.3.2.

The easy and reliable operating principle of ionization chambers (see e.g. [110, 140]) is highly used in the context of radiation detection and radiometry. X-ray radiation is partially absorbed in a gas filled closed volume confined by two electrically conducting plates. A voltage  $U$  between these plates separates gas ions and free electrons generated by x-ray absorption and accelerates these towards the plates, leading to a current  $I \propto I_0$  proportional to the time integrated incident x-ray flux  $I_0$ . The drift velocity of a particle under the influence of an electric field  $E_l$  is given by  $v_d = \mu E_l$  [140], where  $\mu$  is the ion mobility and  $p$  the ambient pressure. A typical value of  $\mu = 2.6 \cdot 10^3 \frac{\text{cm}^2}{\text{s}\cdot\text{V}}$  has been determined by [141] for nitrogen  $N^{4+}$ , no significant difference is expected for the case of different ionization states. For the ionization chamber installed at the PXS (width of 1cm) an optimal voltage of  $U = 250\text{V}$  is specified, leading to  $v_d \approx 800\text{m/s}$  and thereby a typical permeation time of  $t_d \approx 1.2\text{ms}$ . As the ion mobility is dependent on the mass of the moving particle permeation times for electrons are expected to be roughly a factor of 1000 shorter, leading to a short electron spike in the observed current signal.

A single fully absorbed  $E = 8048\text{keV}$  Cu- $K_\alpha$  x-ray photon is expected to generate a number of  $N \approx \frac{8048\text{eV}}{36\text{eV}} = 224^{15}$  electron ion pairs in an air (hence mostly nitrogen) filled ionization chamber. Given an absorption of 4.03%<sup>16</sup> in nitrogen for  $E = 8048\text{eV}$  photons on a path length of 1cm, a DC averaged current signal of  $I = \frac{224}{0.0403} \cdot 2e \cdot I_0$  A is generated.

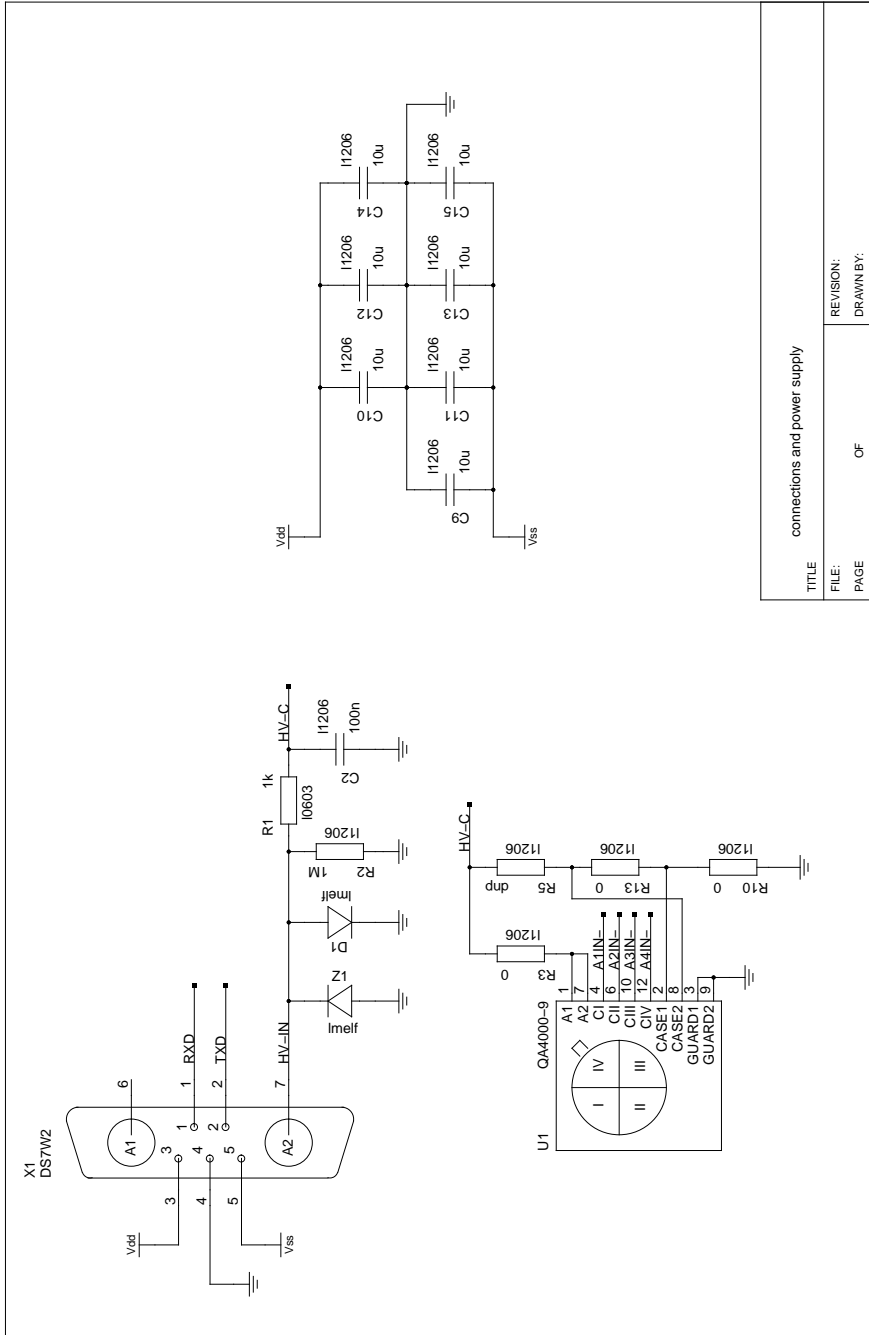
For a x-ray flux of  $I_0 = 1 \cdot 10^7 \text{ph/s}$  as estimated for an ionization chamber (opening  $1 \times 1\text{cm}^2$ ) at a distance of approximately 5cm from the source spot of the PXS this leads to  $I \approx 18\text{nA}$ , being precisely measurable with standard laboratory

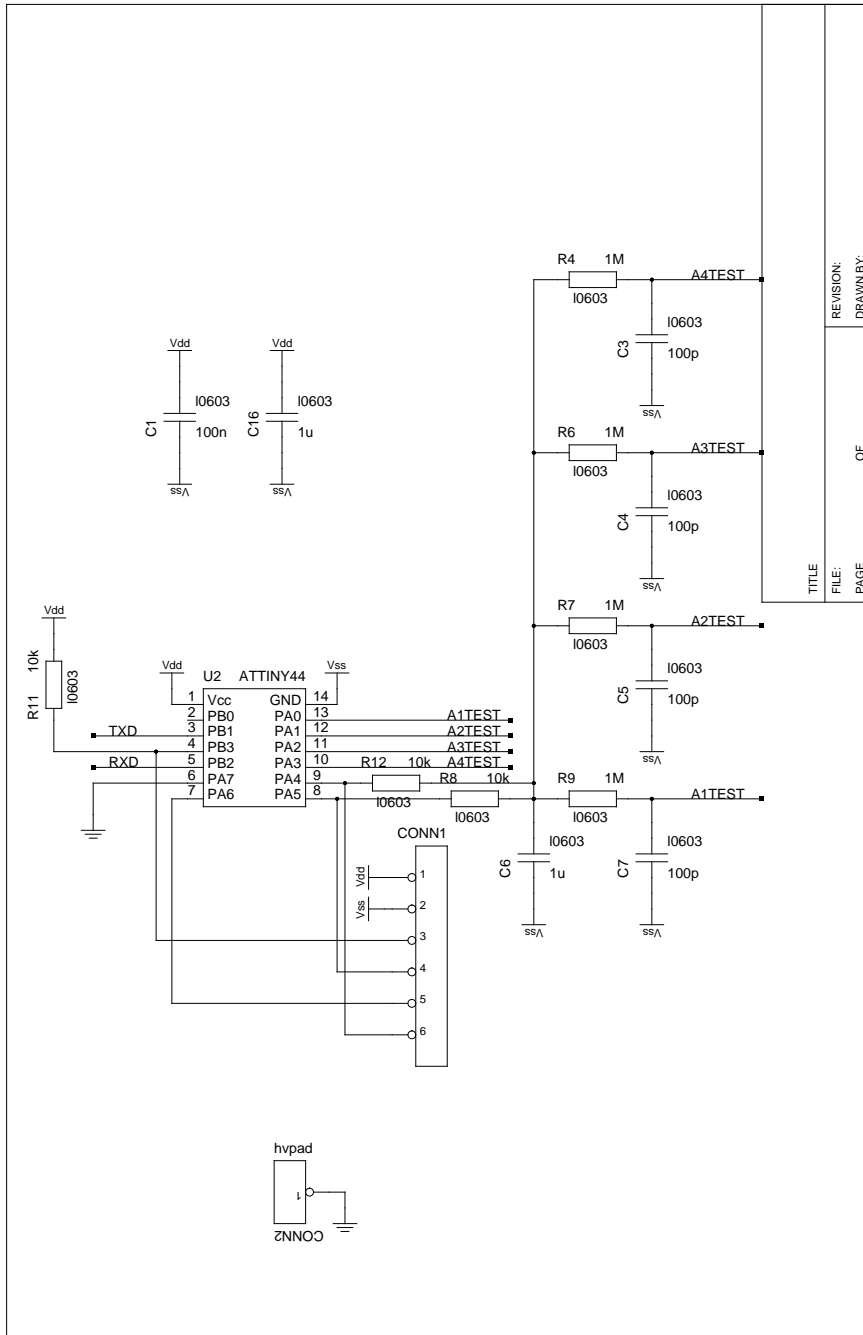
<sup>15</sup>An energy of 36eV is required to produce a single electron ion pair in nitrogen, [http://xdb.lbl.gov/Section4/Sec\\_4-5.pdf](http://xdb.lbl.gov/Section4/Sec_4-5.pdf), requested at the 31.1.2013

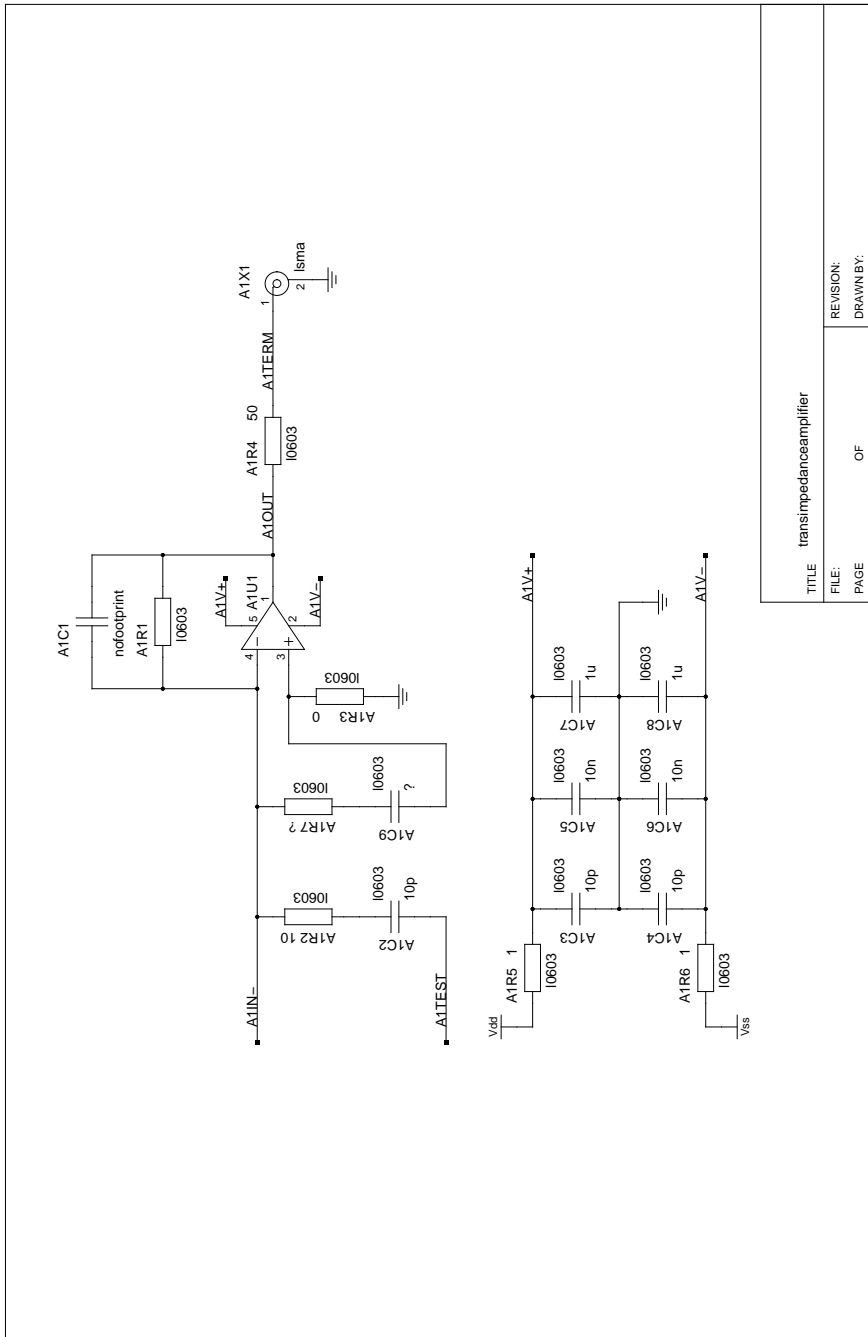
<sup>16</sup>[http://henke.lbl.gov/optical\\_constants/gastrn2.html](http://henke.lbl.gov/optical_constants/gastrn2.html), requested at the 31.1.2013

measurement electronics. An electronic low pass filter hereby flattens the electron spike.

A.3 Electronic schematics of the preamplifier circuit





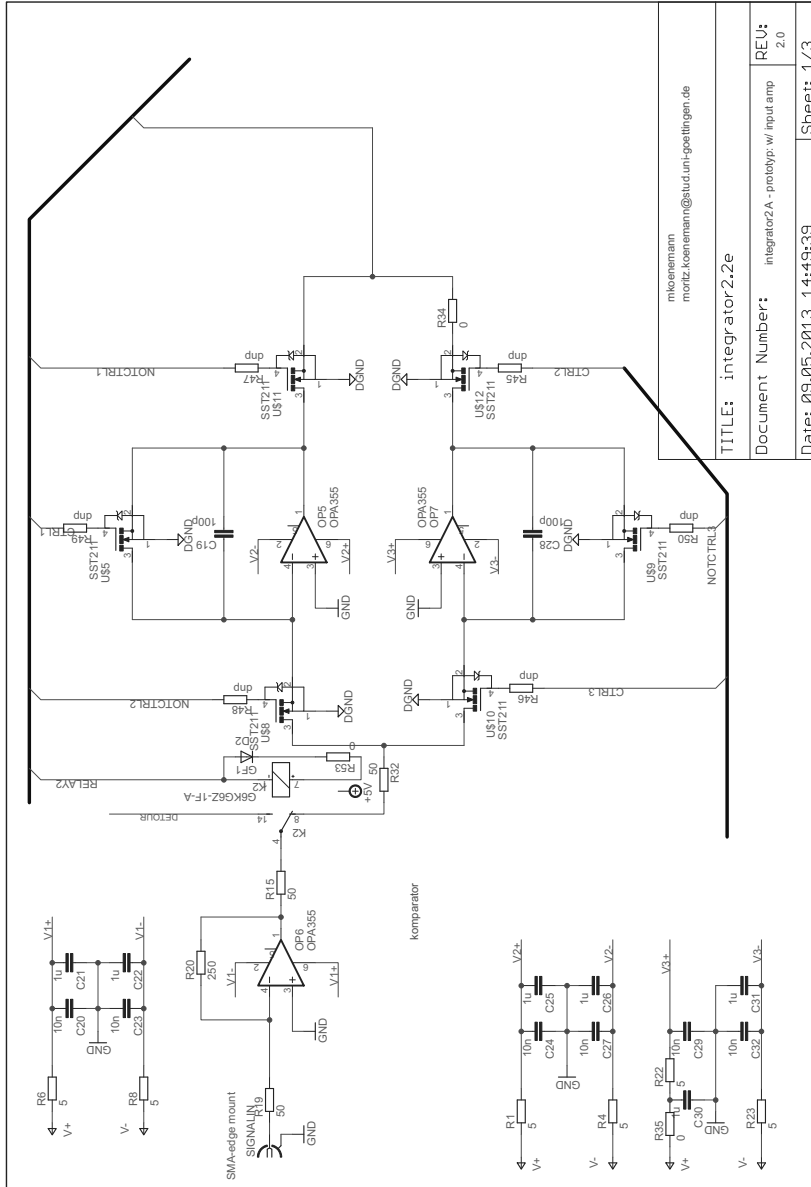


TITLE: transimpedance amplifier

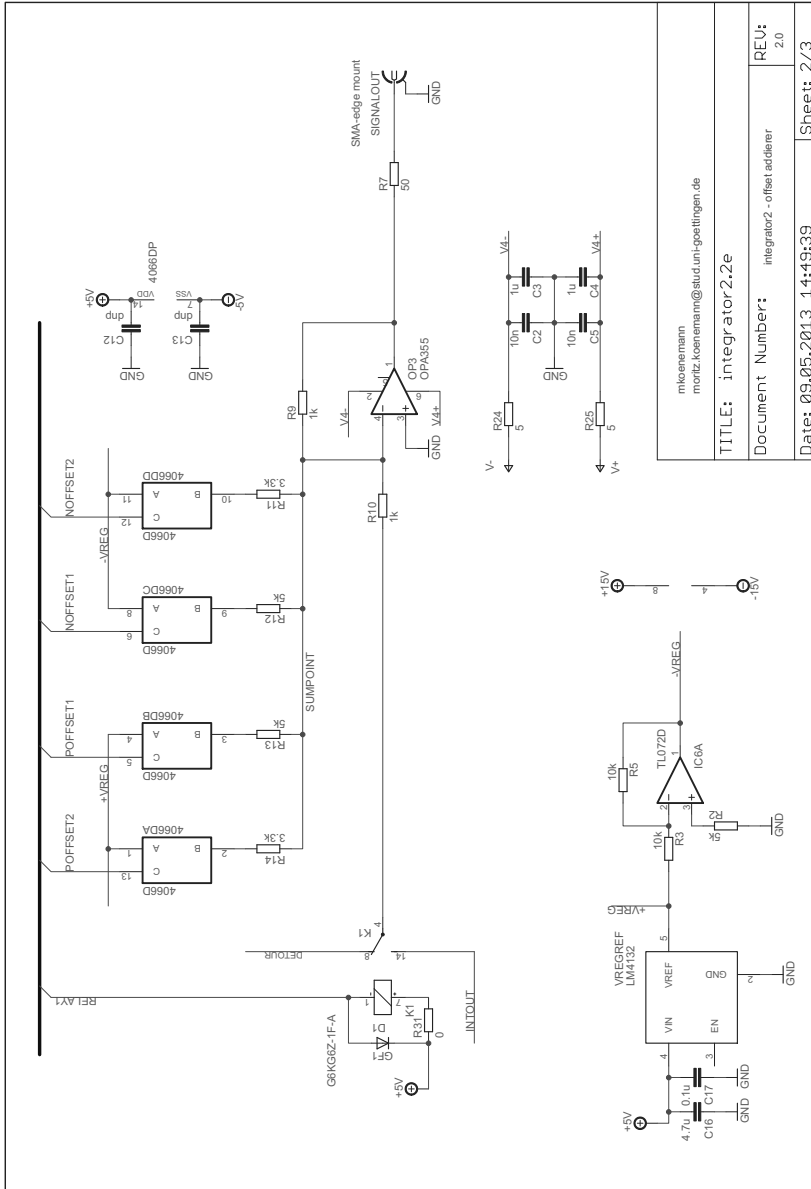
REVISION:  
DRAWN BY:

PAGE: OF:

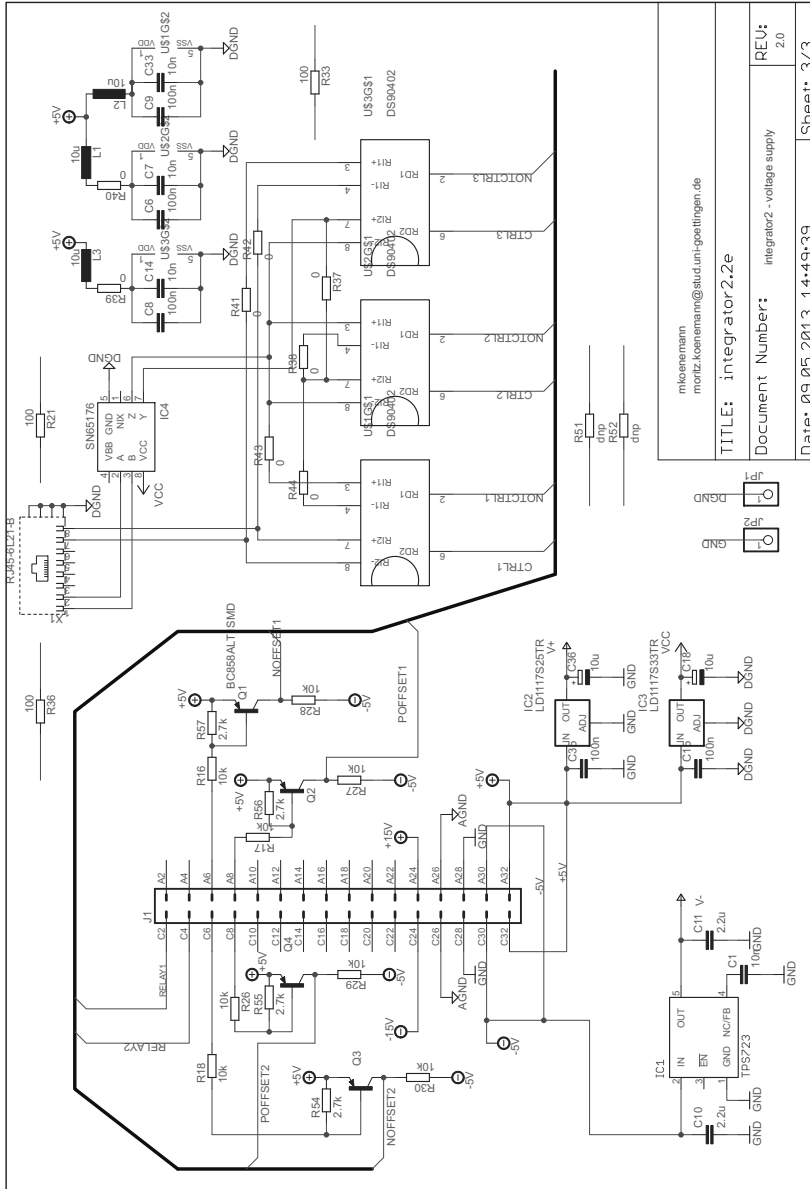
### A.4 Electronic schematics of the gated integrator



mikroemmann moritz.koenemann@stud.uni-goettingen.de	
TITLE: integrator2.2e	REU: 2.0
Document Number: integrator2A - prototyp: w/ input amp	Date: 09.05.2013 14:49:39
Sheet: 1/3	Sheet: 1/3



mikeesemann moritz.koenemann@stud.uni-goettingen.de	
TITLE: integrator2.2.e	
Document Number:	integrator2_offset_addierer
Date: 09.05.2013 14:49:39	Sheet: 2 / 3
REU:	2.0

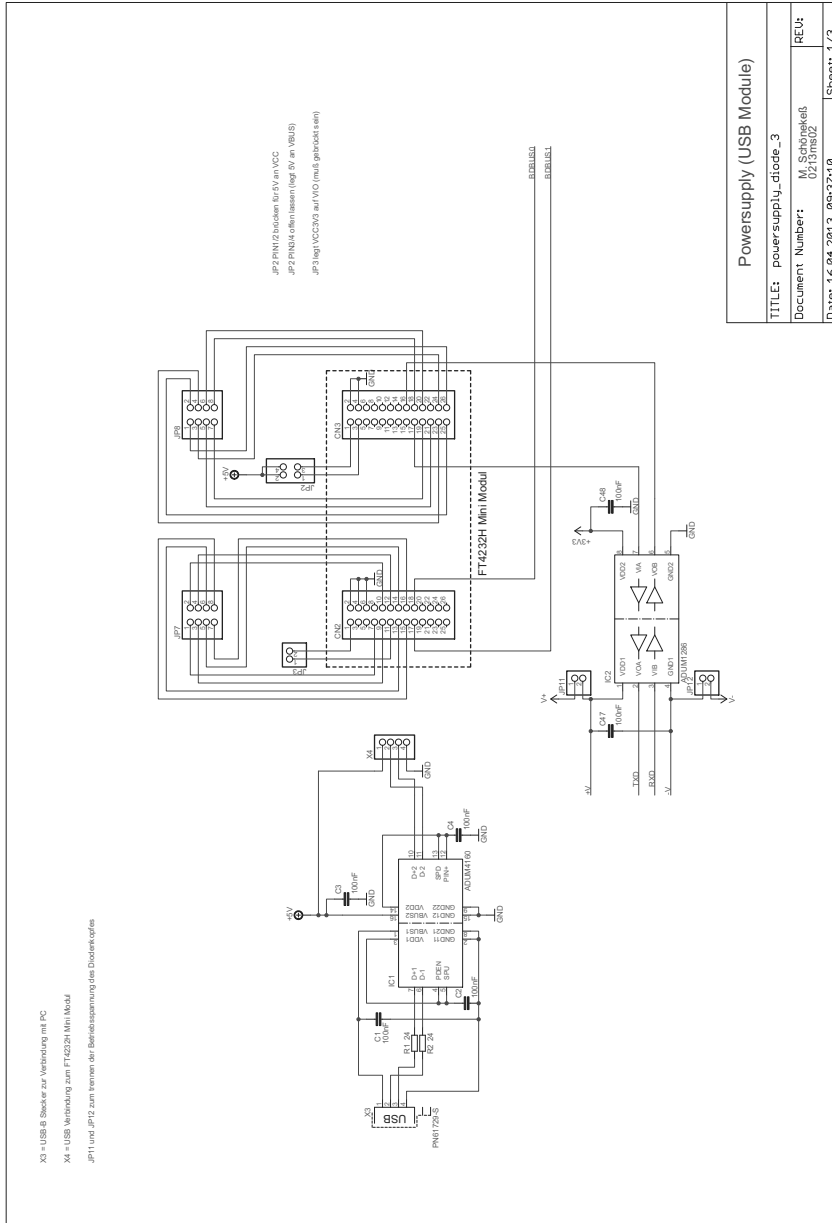


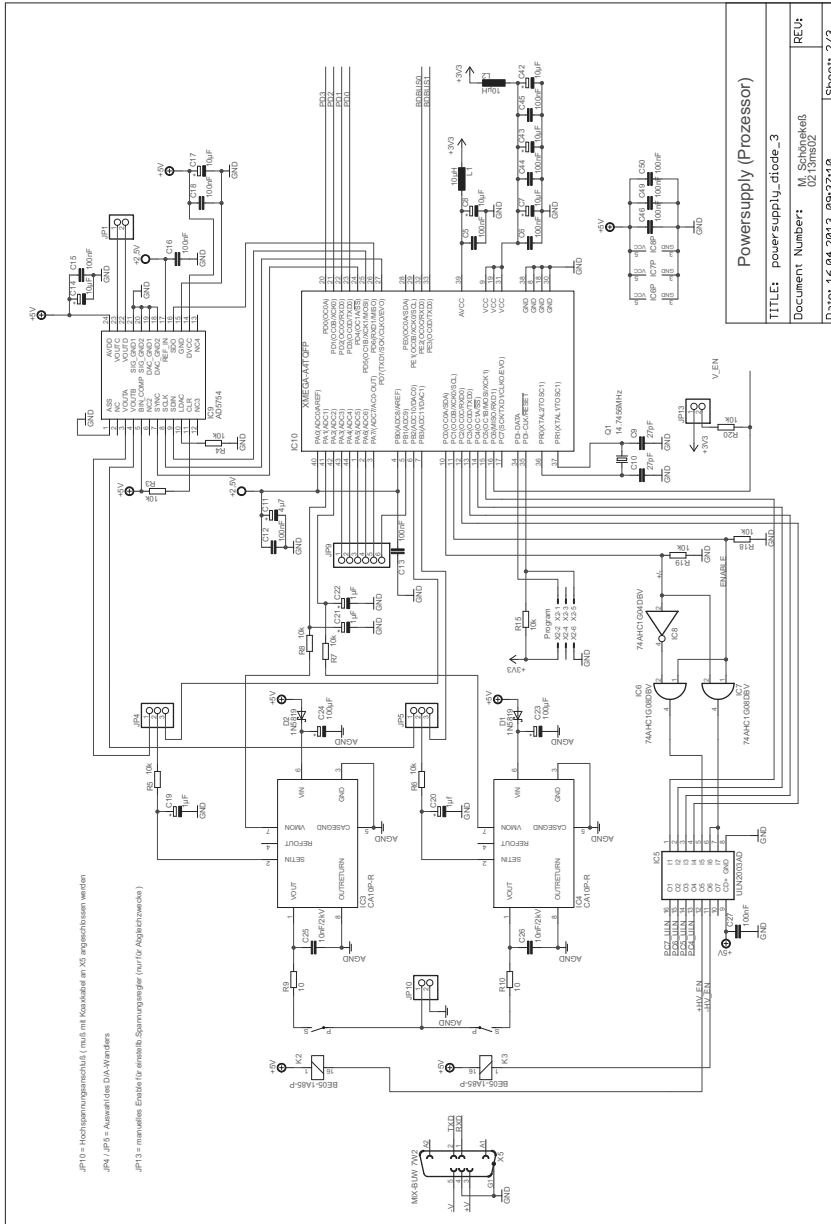
mikroemmann moritz.koenemann@student.uni-goettingen.de	
TITLE: integrator 2.2e	
Document Number:	integrator2 - voltage supply
REU:	2.0
Date: 09.05.2013 14:49:39	Sheet: 3 / 3

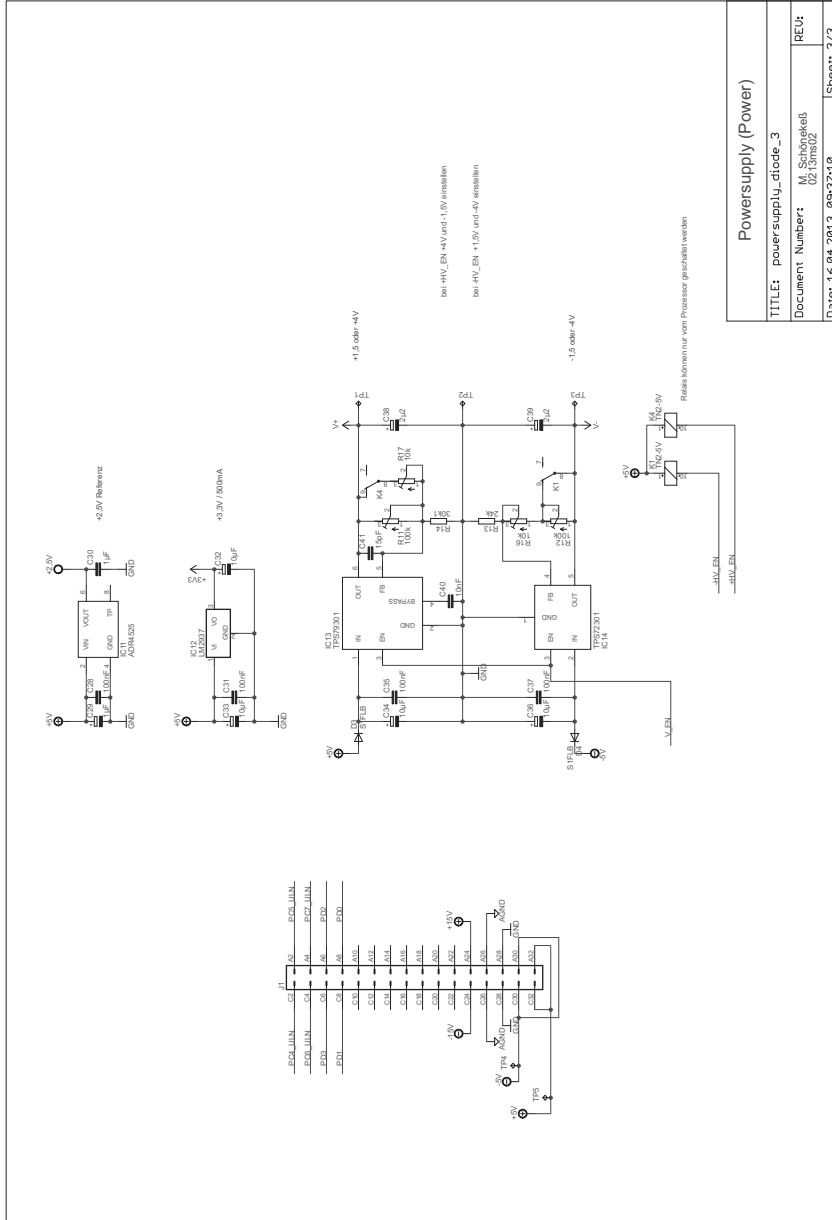




A.5 Electronic schematics of the power supply circuit









## References

- [1] A. L. Hodgkin and A. F. Huxley. Resting and action potentials in single nerve fibres. *J. Physiol.*, 104:176–195, 1945.
- [2] G. Stulen. Electric field effects on lipid membrane structure. *Biochimica et Biophysica Acta*, 640:621, 1981.
- [3] D. Constantin, C. Ollinger, M. Vogel, and T. Salditt. Electric field unbinding of solid-supported lipid multilayers. *The European Physical Journal E: Soft Matter and Biological Physics*, 18(3):273–278, 2005.
- [4] S. Lecuyer, G. Fragneto, and T. Charitat. Effect of an electric field on a floating lipid bilayer: A neutron reflectivity study. *European Physical Journal E*, 21:153–159, 2006.
- [5] C. Chen, S.W. Smye, M.P. Robinson, and J.A. Evans. Membrane electroporation theories: a review. *Medical and Biological Engineering and Computing*, 44(1):5–14, 2006-03-01.
- [6] James C. Weaver and Yu.A. Chizmadzhev. Theory of electroporation: A review. *Bioelectrochemistry and Bioenergetics*, 41(2):135–160, December 1996.
- [7] S. Y. Ho and G. S. Mittal. Electroporation of cell membranes: A review. *Critical Reviews in Biotechnology*, 16(4):349–362, 1996.
- [8] D Peter Tieleman. The molecular basis of electroporation. *BMC Biochemistry*, 5(1):10, 2004.
- [9] Tarek Mounir. Membrane electroporation: A molecular dynamics simulation. *Biophysical Journal*, 88(6):4045–4053, 2005.
- [10] R.A. Boeckmann, B.L. de Groot, S. Kakorin, E. Neumann, and H. Grubmueller. Kinetics, statistics, and energetics of lipid membrane electroporation studied by molecular dynamics simulations. *Biophysical Journal*, 95:1837–1850, 2008.
- [11] K. Weißand J. Enderlein. Lipid diffusion within black lipid membranes measured with dual-focus fluorescence correlation spectroscopy. *ChemPhysChem*, 13(4):990–1000, 2012.
- [12] Robert M. Zucker. Quality assessment of confocal microscopy slide based systems: Performance. *Cytometry Part A*, 69A(7):659–676, 2006.
- [13] Helmut J. Koester, Dagmar Baur, Rainer Uhl, and Stefan W. Hell. Ca<sup>2+</sup> fluorescence imaging with pico- and femtosecond two-photon excitation: Signal and photodamage. *Biophysical Journal*, 77(4):2226 – 2236, 1999.
- [14] Alexander Hopt and Erwin Neher. Highly nonlinear photodamage in two-photon fluorescence microscopy. *Biophysical Journal*, 80(4):2029 – 2036, 2001.
- [15] Stefan W. Hell and Jan Wichmann. Breaking the diffraction resolution limit by stimulated emission: stimulated-emission-depletion fluorescence microscopy. *Opt. Lett.*, 19(11):780–782, Jun 1994.
- [16] RICHARD H Lozier, ROBERTO A Bogomolni, and W Stoeckenius. Bacteriorhodopsin: a light-driven proton pump in halobacterium halobium. *Biophysical journal*, 15(9):955, 1975.

- [17] J. Prost and R. Bruinsma. Shape fluctuations of active membranes. *EPL (Europhysics Letters)*, 33(4):321, 1996.
- [18] J. Prost, J.-B. Manneville, and R. Bruinsma. Fluctuation-magnification of non-equilibrium membranes near a wall. *The European Physical Journal B - Condensed Matter and Complex Systems*, 1:465–480, 1998.
- [19] Sriram Ramaswamy, John Toner, and Jacques Prost. Nonequilibrium noise and instabilities in membranes with active pumps. *Pramana*, 53(1):237–242, 1999.
- [20] Sriram Ramaswamy, John Toner, and Jacques Prost. Nonequilibrium fluctuations, traveling waves, and instabilities in active membranes. *Phys. Rev. Lett.*, 84:3494–3497, Apr 2000.
- [21] Sriram Ramaswamy and Madan Rao. The physics of active membranes. *Comptes Rendus de l'Académie des Sciences-Series IV-Physics*, 2(6):817–839, 2001.
- [22] Hsuan-Yi Chen. Internal states of active inclusions and the dynamics of an active membrane. *Phys. Rev. Lett.*, 92:168101, Apr 2004.
- [23] N Gov. Membrane undulations driven by force fluctuations of active proteins. *Physical review letters*, 93(26):268104, 2004.
- [24] Lawrence C.-L. Lin, Nir Gov, and Frank L. H. Brown. Nonequilibrium membrane fluctuations driven by active proteins. *The Journal of Chemical Physics*, 124(7):074903, 2006.
- [25] Pierre Sens and H. Isambert. Undulation instability of lipid membranes under an electric field. *Phys. Rev. Lett.*, 88:128102, Mar 2002.
- [26] M. C. Rheinstaedter, C. Ollinger, G. Fragneto, F. Demmel, and T. Salditt. Collective dynamics of lipid membranes studied by inelastic neutron scattering. *Phys. Rev. Lett.*, 93(10):108107–, September 2004.
- [27] Maikel C. Rheinstädter, Tilo Seydel, Franz Demmel, and Tim Salditt. Molecular motions in lipid bilayers studied by the neutron backscattering technique. *Phys. Rev. E*, 71(6):061908–, June 2005.
- [28] B. Bruening, M. Rheinstaedter, A. Hiess, B. Weinhausen, T. Reusch, S. Aeffner, and T. Salditt. Influence of cholesterol on the collective dynamics of the phospholipid acyl chains in model membranes. *The European Physical Journal E: Soft Matter and Biological Physics*, 31(4):419–428, 2010.
- [29] M.C Rheinstaedter, C Ollinger, G Fragneto, and T Salditt. Collective dynamics in phospholipid bilayers investigated by inelastic neutron scattering: exploring the dynamics of biological membranes with neutrons. *Physica B: Condensed Matter*, 350(1-3):136–139, July 2004.
- [30] Sebastian Aeffner, Tobias Reusch, Britta Weinhausen, and Tim Salditt. Energetics of stalk intermediates in membrane fusion are controlled by lipid composition. *Proceedings of the National Academy of Sciences*, 109(25):E1609–E1618, 2012.
- [31] S. Aeffner, T. Reusch, B. Weinhausen, , and T. Salditt. Membrane fusion intermediates and the effect of cholesterol: An in-house x-ray scattering study. *European Physical Journal E*, 30:205, 2009.
- [32] Tim Salditt. Thermal fluctuations and stability of solid-supported lipid membranes. *Journal of Physics: Condensed Matter*, 17(6):R287–, 2005.

- [33] A. Giahi, M. El Alaoui Faris, P. Bassereau, and T. Salditt. Active membranes studied by x-ray scattering. *The European Physical Journal E: Soft Matter and Biological Physics*, 23(4):431–437, 2007.
- [34] J R Helliwell. *Time-resolved diffraction*. 1997.
- [35] M. Bargheer, N. Zhavoronkov, Y. Gritsai, J. C. Woo, D. S. Kim, M. Woerner, and T. Elsaesser. Coherent atomic motions in a nanostructure studied by femtosecond x-ray diffraction. *Science*, 306(5702):1771–1773, December 2004.
- [36] M. Bargheer, N. Zhavoronkov, M. Woerner, and T. Elsaesser. Recent progress in ultrafast x-ray diffraction. *Chem. Eur. J. of Chem. Phys.*, 7(4):783–792, 2006.
- [37] S. Techert, F. Schotte, and M. Wulff. Picosecond x-ray diffraction probed transient structural changes in organic solids. *Phys. Rev. Lett.*, 86(10):2030–, March 2001.
- [38] Martin Hennig, Manuel Wolff, Juergen Neumann, Achim Wixforth, Matthias F. Schneider, and Joachim O. Raedler. Dna concentration modulation on supported lipid bilayers switched by surface acoustic waves. *Langmuir*, 27(24):14721–14725, 2011.
- [39] Martin Hennig, Jurgen Neumann, Achim Wixforth, Joachim O. Radler, and Matthias F. Schneider. Dynamic patterns in a supported lipid bilayer driven by standing surface acoustic waves. *Lab Chip*, 9(21):3050–3053, 2009.
- [40] Z. Guttenberg, A. Rathgeber, S. Keller, J. O. Raedler, A. Wixforth, M. Kostur, M. Schindler, and P. Talkner. Flow profiling of a surface-acoustic-wave nanopump. *Phys. Rev. E*, 70(5):056311–, November 2004.
- [41] T Franke. Surface acoustic wave (saw) directed droplet flow in microfluidics for pdms devices. *Lab on a chip*, 9(18):2625–, 2009.
- [42] Kerstin Laenge, Bastian Rapp, and Michael Rapp. Surface acoustic wave biosensors: a review. *Analytical and Bioanalytical Chemistry*, 391(5):1509–1519, 2008-07-01.
- [43] Sajal Ghosh, Bekir Salgin, Diego Pontoni, Tobias Reusch, Patrick Keil, Dirk Vogel, Michael Rohwerder, Harald Reichert, and Tim Salditt. Structure and volta potential of lipid multilayers: Effect of x-ray irradiation. *Langmuir*, 2012.
- [44] D.D. Mai, J. Hallmann, T. Reusch, M. Osterhoff, S. Düsterer, R. Treusch, A. Singer, M. Beckers, T. Gorniak, T. Senkbeil, R. Dronyak, J. Gulden, O.M. Yefanov, A. Al-Shemmary, A. Rosenhahn, A. P. Manusco, I. A. Vartanyants, and T. Salditt. Single pulse coherence measurements in the water window at the free electron laser flash. *Optics Express*, accepted, 2013.
- [45] J. Davaasambuu, P. Durand, and S. Techert. Experimental requirements for light-induced reactions in powders investigated by time-resolved x-ray diffraction. *Journal of Synchrotron Radiation*, 11(6):483–489, Nov 2004.
- [46] Marco Cammarata, Matteo Levantino, Friedrich Schotte, Philip A Anfinrud, Friederike Ewald, Jungkweon Choi, Antonio Cupane, Michael Wulff, and Hyotcherl Ihee. Tracking the structural dynamics of proteins in solution using time-resolved wide-angle x-ray scattering. *Nat Meth*, 5(10):881–886, October 2008.
- [47] J. Als-Nielsen. *Elements of Modern X-Ray Physics*. Wiley, 2001.
- [48] Eric Collet, Marie-Haeene Lemaee-Cailleau, Marylise Buron-Le Cointe, Hervae Cailleau, Michael Wulff, Tadeusz Luty, Shin-Ya Koshihara, Mathias Meyer, Loic

- Toupet, Philippe Rabiller, and Simone Techert. Laser-induced ferroelectric structural order in an organic charge-transfer crystal. *Science*, 300(5619):612–615, April 2003.
- [49] Lin X. Chen, Wighard J. H. Jaeger, Guy Jennings, David J. Gosztola, Anneli Munkholm, and Jan P. Hessler. Capturing a photoexcited molecular structure through time-domain x-ray absorption fine structure. *Science*, 292(5515):262–264, 2001.
- [50] M. Bargheer, N. Zhavoronkov, R. Bruch, H. Legall, H. Stiel, M. Woerner, and T. Elsaesser. Comparison of focusing optics for femtosecond x-ray diffraction. *Applied Physics B*, 80:715–719, 2005.
- [51] Friedrich Schotte, Manho Lim, Timothy A. Jackson, Aleksandr V. Smirnov, Jayashree Soman, John S. Olson, George N. Phillips, Michael Wulff, and Philip A. Anfirud. Watching a protein as it functions with 150-ps time-resolved x-ray crystallography. *Science*, 300(5627):1944–1947, June 2003.
- [52] Sebastian Aeffner. *Stalk structures in lipid bilayer fusion studied by x-ray diffraction*. PhD thesis, Institute for X-ray Physics, Georg-August University Göttingen, 2011.
- [53] Tobias Reusch. Nichtlamellare strukturen in lipidmembranstapeln in abhängigkeit der hydratisierung: Probenumgebung, phasendiagramme und bestimmung der elektronendichte. Master's thesis, Institute for X-ray Physics, Georg-August University Göttingen, 2009.
- [54] D. Constantin, U. Mennicke, C. Li, and T. Salditt. Solid-supported lipid multilayers: Structure factor and fluctuations. *The European Physical Journal E: Soft Matter and Biological Physics*, 12(2):283–290, 2003.
- [55] T. Salditt, C. Münster, J. Lu, M. Vogel, W. Fenzl, and A. Souvorov. Specular and diffuse scattering of highly aligned phospholipid membranes. *Phys. Rev. E*, 60(6):7285–, December 1999.
- [56] M Sivis, M Duwe, B Abel, and C Ropers. Nanostructure-enhanced atomic line emission. *Nature*, 485(7397):E1–E3, 2012.
- [57] P. A. Franken, A. E. Hill, C. W. Peters, and G. Weinreich. Generation of optical harmonics. *Phys. Rev. Lett.*, 7:118–119, Aug 1961.
- [58] Christian Peth, Anton Kalinin, Frank Barkusky, Klaus Mann, J Peter Toennies, and Lev Yu Rusin. Xuv laser-plasma source based on solid ar filament. *Review of Scientific Instruments*, 78(10):103509–103509, 2007.
- [59] F. Zamponi, Z. Ansari, C. Korff Schmising, P. Rothhardt, N. Zhavoronkov, M. Woerner, T. Elsaesser, M. Bargheer, T. Trobitzsch-Ryll, and M. Haschke. Femtosecond hard x-ray plasma sources with a kilohertz repetition rate. *Applied Physics A*, 96:51–58, 2009.
- [60] Masatake Yoshida, Yasushi Fujimoto, Yoichiro Hironaka, Kazutaka G Nakamura, Ken-ichi Kondo, Masayuki Ohtani, and Hiroshi Tsunemi. Generation of picosecond hard x rays by tera watt laser focusing on a copper target. *Applied physics letters*, 73(17):2393–2395, 1998.
- [61] Yan Jiang, Taewoo Lee, and Christoph G Rose-Petruck. Generation of ultrashort hard-x-ray pulses with tabletop laser systems at a 2-khz repetition rate. *JOSA B*, 20(1):229–237, 2003.



- [62] Ch Reich, P Gibbon, I Uschmann, and E Förster. Yield optimization and time structure of femtosecond laser plasma  $k\alpha$  sources. *Physical Review Letters*, 84(21):4846–4849, 2000.
- [63] Georg Korn, Andreas Thoss, Holger Stiel, Ullrich Vogt, Martin Richardson, Manfred Faubel, et al. Ultrashort 1-kHz laser plasma hard x-ray source. *Optics letters*, 27(10):866–868, 2002.
- [64] Heinrich Schwoerer. Generation of x-rays by intense femtosecond lasers. In Friedrich Dausinger, Holger Lubatschowski, and Friedemann Lichtner, editors, *Femtosecond Technology for Technical and Medical Applications*, volume 96 of *Topics in Applied Physics*, pages 235–254. Springer Berlin Heidelberg, 2004.
- [65] WillIaml Kruer. The physics of laser plasma interactions((book)). *Reading, MA, Addison-Wesley Publishing Co.(Frontiers in Physics.*, 73, 1988.
- [66] Wolfgang Demtröder. *Laserspektroskopie: Grundlagen und Techniken*, volume 4. Springer DE, 2004.
- [67] D Von der Linde, K Sokolowski-Tinten, Ch Blome, C Dietrich, P Zhou, A Tarasevitch, A Cavalleri, CW Siders, CPJ Barty, J Squier, et al. Generation and application of ultrashort x-ray pulses. *Laser and Particle Beams*, 19(1):15–22, 2001.
- [68] Christian Reich, Christopher M Laperle, Xiaodi Li, Brian Ahr, Frank Benesch, and Christoph G Rose-Petruck. Ultrafast x-ray pulses emitted from a liquid mercury laser target. *Optics letters*, 32(4):427–429, 2007.
- [69] N. Zhavoronkov, Y. Gritsai, G. Korn, and T. Elsaesser. Ultra-short efficient laser-driven hard x-ray source operated at a kHz repetition rate. *Applied Physics B*, 79:663–667, 2004.
- [70] Mitsuru Uesaka, Toru Ueda, Takahiro Kozawa, and Toshiaki Kobayashi. Precise measurement of a subpicosecond electron single bunch by the femtosecond streak camera. *Nuclear Instruments and Methods in Physics Research Section A: Accelerators, Spectrometers, Detectors and Associated Equipment*, 406(3):371–379, 1998.
- [71] S Düsterer, P Radcliffe, C Bostedt, J Bozek, AL Cavalieri, R Coffee, John T Costello, D Cubaynes, LF DiMauro, Y Ding, et al. Femtosecond x-ray pulse length characterization at the linac coherent light source free-electron laser. *New Journal of Physics*, 13(9):093024, 2011.
- [72] M Beye, O Krupin, G Hays, AH Reid, D Rupp, S de Jong, S Lee, W-S Lee, Y-D Chuang, R Coffee, et al. X-ray pulse preserving single-shot optical cross-correlation method for improved experimental temporal resolution. *Applied Physics Letters*, 100(12):121108–121108, 2012.
- [73] Ulrike Fröhling, Marek Wieland, Michael Gensch, Thomas Gebert, Bernd Schütte, Maria Krikunova, Roland Kalms, Filip Budzyn, Oliver Grimm, Jörg Rossbach, et al. Single-shot terahertz-field-driven x-ray streak camera. *Nature Photonics*, 3(9):523–528, 2009.
- [74] Long-Sheng Ma, Robert K Shelton, Henry C Kapteyn, Margaret M Murnane, and Jun Ye. Sub-10-femtosecond active synchronization of two passively mode-locked ti: sapphire oscillators. *PHYSICAL REVIEW-SERIES A-*, 64(2):021802–R, 2001.
- [75] DE Spence, JM Dudley, K Lamb, WE Sleat, and W Sibbett. Nearly quantum-limited timing jitter in a self-mode-locked ti: sapphire laser. *Optics letters*, 19(7):481–483, 1994.

- [76] T. Ejdrup, H. T. Lemke, K. Haldrup, T. N. Nielsen, D. A. Arms, D. A. Walko, A. Miceli, E. C. Landahl, E. M. Dufresne, and M. M. Nielsen. Picosecond time-resolved laser pump/x-ray probe experiments using a gated single-photon-counting area detector. *Journal of Synchrotron Radiation*, 16(3):387–390, 2009.
- [77] A Miceli. Application of pixel array detectors at x-ray synchrotrons. *Journal of Instrumentation*, 4(03):P03024–, 2009.
- [78] Michael Wulff, Anton Plech, Laurent Eybert, Rudolf Randler, Friedrich Schotte, and Philip Anfinrud. The realization of sub-nanosecond pump and probe experiments at the esrf. *Faraday Discuss.*, 122:13–26, 2003.
- [79] W. Sauer, M. Streibl, T. H. Metzger, A. G. C. Haubrich, S. Manus, A. Wixforth, J. Peisl, A. Mazuelas, J. Hartwig, and J. Baruchel. X-ray imaging and diffraction from surface phonons on gaas. *Applied Physics Letters*, 75(12):1709–1711, sep 1999.
- [80] E Zolotoyabko. Time and phase control of x-rays in stroboscopic diffraction experiments. *Review of scientific instruments*, 73(3):1643–, 2002.
- [81] Lord Rayleigh. On waves propagated along the plane surface of an elastic solid. *Proceedings of the London Mathematical Society*, s1-17(1):4–11, 1885.
- [82] Herbert Matthews. *Surface wave filters design, construction, and use*. Wiley, 1977.
- [83] S.C. Abrahams, J.M. Reddy, and J.L. Bernstein. Ferroelectric lithium niobate. 3. single crystal x-ray diffraction study at 24c. *Journal of Physics and Chemistry of Solids*, 27:997–1012, 1966.
- [84] R. S. Weis and T. K. Gaylord. Lithium niobate: Summary of physical properties and crystal structure. *Applied Physics A: Materials Science & Processing*, 37:191–203, 1985. 10.1007/BF00614817.
- [85] D. Hauden M. Planat. *Nonlinear properties of bulk and surface acoustic waves in piezoelectric crystals*, volume 4. Gordon and Breach Science Publishers, 1985.
- [86] M. Seul and M.J. Sammon. Preparation of surfactant multilayer films on solid substrates by deposition from organic solution. *Thin solid films*, 185:287, 1990.
- [87] Martin A. Green and Mark J. Keevers. Optical properties of intrinsic silicon at 300 k. *Prog. Photovolt: Res. Appl.*, 3(3):189–192, 1995.
- [88] U. Mennicke, D. Constantin, and T. Salditt. Structure and interaction potentials in solid-supported lipid membranes studied by x-ray reflectivity at varied osmotic pressure. *The European Physical Journal E: Soft Matter and Biological Physics*, 20(2):221–230, 2006-06-01.
- [89] T. Koop. Electrochemical cell for in situ x-ray diffraction under ultrapure conditions. *Review of Scientific Instruments*, 69(4):1840–, 1998.
- [90] S.J. Singer and G.L. Nicolson. The fluid mosaic model of the structure of cell membranes. *Science*, 175:720–731, 1972.
- [91] Tim Salditt, Chenghao Li, and Alexander Spaar. Structure of antimicrobial peptides and lipid membranes probed by interface-sensitive x-ray scattering. *Biochimica et Biophysica Acta (BBA)-Biomembranes*, 1758(9):1483–1498, 2006.
- [92] S K Sinha. X-ray diffuse scattering as a probe for thin film and interface structure. *Journal de physique. III*, 4(9):1543–, 1994.

- [93] S. K. Sinha, E. B. Sirota, S. Garoff, and H. B. Stanley. X-ray and neutron scattering from rough surfaces. *Phys. Rev. B*, 38(4):2297–, August 1988.
- [94] A E Blaurock. Evidence of bilayer structure and of membrane interactions from x-ray diffraction analysis. *Biochimica et biophysica acta*, 650(4):167–207, 1982.
- [95] J. Katsaras. X-ray diffraction studies of oriented lipid bilayers. *Biochemistry and Cell Biology*, 73(5-6):209–218, 1995.
- [96] J. Torbet and M.H.F. Wilkins. X-ray diffraction studies of lecithin bilayers. *Journal of Theoretical Biology*, 62(2):447 – 458, 1976.
- [97] Britta Weinhausen. Strukturanalyse von phospholipidmembranen in abhängigkeit von der hydratisierung und dem cholesteringehalt: Elektronendichteprofile und ordnung der acylketten. Master's thesis, Institute for X-ray Physics, Georg-August University Göttingen, 2010.
- [98] Lin Yang and Huey W. Huang. A rhombohedral phase of lipid containing a membrane fusion intermediate structure. *Biophysical Journal*, 84(3):1808–1817, March 2003.
- [99] Lin Yang and Huey W. Huang. Observation of a membrane fusion intermediate structure. *Science*, 297(5588):1877–1879, September 2002.
- [100] A Caille. Remarques sur la diffusion des rayons x dans les smectiques. *CR Acad. Sci. Serie B*, 274:891–893, 1972.
- [101] W. Helfrich. Elastic properties of lipid bilayers: Theory and possible experiments. *Z. f. Naturforschung*, 28c:693–703, 1973.
- [102] P. Girard, J. Prost, and P. Bassereau. Passive or active fluctuations in membranes containing proteins. *Phys. Rev. Lett.*, 94:088102, Mar 2005.
- [103] T. Salditt, T. H. Metzger, J. Peisl, B. Reinker, M. Moske, and K. Samwer. Determination of the height-height correlation function of rough surfaces from diffuse x-ray scattering. *EPL (Europhysics Letters)*, 32(4):331, 1995.
- [104] T. Salditt, T. H. Metzger, and J. Peisl. Kinetic roughness of amorphous multilayers studied by diffuse x-ray scattering. *Phys. Rev. Lett.*, 73:2228–2231, Oct 1994.
- [105] T. Salditt, T. H. Metzger, Ch. Brandt, U. Klemradt, and J. Peisl. Determination of the static scaling exponent of self-affine interfaces by nonspecular x-ray scattering. *Phys. Rev. B*, 51:5617–5627, Mar 1995.
- [106] T. Salditt, M. Vogel, and W. Fenzl. Thermal fluctuations and positional correlations in oriented lipid membranes. *Phys. Rev. Lett.*, 90(17):178101–, April 2003.
- [107] Horia I. Petrache, Nikolai Gouliarov, Stephanie Tristram-Nagle, Ruitian Zhang, Robert M. Suter, and John F. Nagle. Interbilayer interactions from high-resolution x-ray scattering. *Phys. Rev. E*, 57(6):7014–, June 1998.
- [108] B Henrich, J Becker, R Dinapoli, P Goettlicher, H Graafsma, H Hirsemann, R Klanner, H Krueger, R Mazzocco, A Mozzanica, et al. The adaptive gain integrating pixel detector agipd a detector for the european xfel. *Nuclear Instruments and Methods in Physics Research Section A: Accelerators, Spectrometers, Detectors and Associated Equipment*, 633:S11–S14, 2011.
- [109] Sven Herrmann, Sébastien Boutet, Brian Duda, David Fritz, Gunther Haller, Philip Hart, Ryan Herbst, Christopher Kenney, Henrik Lemke, Marc Messerschmidt, et al.

- Cspad-140k-a versatile detector for lcls experiments. *Nuclear Instruments and Methods in Physics Research Section A: Accelerators, Spectrometers, Detectors and Associated Equipment*, 2013.
- [110] Glenn F Knoll. *Radiation detection and measurement*. Wiley, 2010.
- [111] Ekbert Hering, Klaus Bressler, and Jürgen Gutekunst. *Elektronik für Ingenieure und Naturwissenschaftler*. Springer, 2005.
- [112] Paul Horowitz, Winfield Hill, and Thomas C Hayes. *The art of electronics*, volume 2. Cambridge university press Cambridge, 1989.
- [113] C Olandrowitz, M Bartels, M Krenkel, A Beerlink, R Mokso, M Sprung, and T Salditt. Phase-contrast x-ray imaging and tomography of the nematode *caenorhabditis elegans*. *Physics in Medicine and Biology*, 57(16):5309, 2012.
- [114] O. H. Seeck, C. Deiter, K. Pflaum, F. Bertam, A. Beerlink, H. Franz, J. Horbach, H. Schulte-Schrepping, B. M. Murphy, M. Greve, and O. Magnussen. The high-resolution diffraction beamline p08 at petra iii. *Journal of Synchrotron Radiation*, 19(1):30–38, 2012.
- [115] R. Tucoulou and Dimitry Roshchupkin F. de Bergevin, O. Mathon. X-ray bragg diffraction of  $linbo_3$  crystals excited by surface acoustic waves. *Phys. Rev. B*, 64(13):134108–, September 2001.
- [116] W. Sauer, T.H. Metzger, J. Peisl, Y. Avrahami, and E. Zolotoyabko. X-ray diffraction under surface acoustic wave excitation. *Physica B: Condensed Matter*, 248(1-4):358–365, June 1998.
- [117] Igor A. Schelokov, Dmitry V. Roshchupkin, Dmitry V. Irzhak, and Remi Tucoulou. Dynamical theory for calculations of x-ray spectra from crystals modulated by surface acoustic waves. *Journal of Applied Crystallography*, 37(1):52–61, 2004.
- [118] R. Tucoulou, R. Pascal, M. Brunel, O. Mathon, D. V. Roshchupkin, I. A. Schelokov, E. Cattan, and D. Remiens. X-ray diffraction from perfect silicon crystals distorted by surface acoustic waves. *Journal of Applied Crystallography*, 33(4):1019–1022, 2000.
- [119] Julie A. Titus, Richard Haugland, Susan O. Sharrow, and David M. Segal. Texas red, a hydrophilic, red-emitting frouophore for use with frouescen in dual parameter flow microfluorometric and frouescence microscopic studies. *Journal of Immunological Methods*, 50(2):193 – 204, 1982.
- [120] D Schick, A Bojahr, M Herzog, C Schmising, R Shayduk, W Leitenberger, P Gaal, and M Bargheer. Normalization schemes for ultrafast x-ray diffraction using a tabletop laser-driven plasma source. *Review of Scientific Instruments*, 83(2):025104–025104, 2012.
- [121] Jianjun Pan, Stephanie Tristram-Nagle, Norbert Kucerka, and John F. Nagle. Temperature dependence of structure, bending rigidity, and bilayer interactions of dioleoylphosphatidylcholine bilayers. *Biophysical Journal*, 94(1):117–124, 2008.
- [122] M. Delaye, R. Ribotta, and G. Durand. Buckling instability of the layers in a smectic-a liquid crystal. *Physics Letters A*, 44(2):139 – 140, 1973.
- [123] J. Prost P.-G. de Gennes. *The Physics of Liquid Crystals*. Clarendon Press, Oxford, 2nd edition, 1993.

- [124] Zhen-Gang Wang. Response and instabilities of the lamellar phase of diblock copolymers under uniaxial stress. *Journal of Chemical Physics*, 100(3):2298–2309, 1994.
- [125] AG Zilman and R Granek. Undulations and dynamic structure factor of membranes. *Physical review letters*, 77(23):4788–4791, 1996.
- [126] Takayoshi Takeda, Y Kawabata, H Seto, S Komura, SK Ghosh, M Nagao, and D Okuhara. Neutron spin-echo investigations of membrane undulations in complex fluids involving amphiphiles. *Journal of Physics and Chemistry of Solids*, 60(8):1375–1377, 1999.
- [127] Maikel C Rheinstädter, Wolfgang Häußler, and Tim Salditt. Dispersion relation of lipid membrane shape fluctuations by neutron spin-echo spectrometry. *Physical review letters*, 97(4):48103, 2006.
- [128] Alfred Vogel, Joachim Noack, G Hüttman, and G Paltauf. Mechanisms of femtosecond laser nanosurgery of cells and tissues. *Applied Physics B: Lasers and Optics*, 81(8):1015–1047, 2005.
- [129] Alfred Vogel, Vasana Venugopalan, et al. Mechanisms of pulsed laser ablation of biological tissues. *Chemical Reviews*, 103(2):577–644, 2003.
- [130] Barry Halliwell and Susanna Chirico. Lipid peroxidation: Its mechanism, measurement, and significance. *The American journal of clinical nutrition*, 57(5):715S–724S, 1993.
- [131] Harry D. Downing and Dudley Williams. Optical constants of water in the infrared. *Journal of Geophysical Research*, 80(12):1656–1661, 1975.
- [132] Eva Novakova. *Structure of charged two-component lipid membranes and their interaction with colloids studied by different X-ray and microscopy techniques*. PhD thesis, Georg-August Universität Göttingen, Institut fuer Roentgenphysik, 2008.
- [133] Maria Göppert-Mayer. Über elementarakte mit zwei quantensprüngen. *Annalen der Physik*, 401(3):273–294, 1931.
- [134] J.M. Crowley. Electrical breakdown of bimolecular lipid membranes as an electromechanical instability. *Biophysical Journal*, 13:711–724, 1973.
- [135] Herve Isambert. Understanding the electroporation of cells and artificial bilayer membranes. *Phys. Rev. Lett.*, 80(15):3404, 1998.
- [136] P. Sens and H. Isambert. Undulation instability of lipid membranes under an electric field. *Physical Review Letters*, 88:128102, 2002.
- [137] D. S. Dimitrov. Electric field-induced breakdown of lipid bilayers and cell membranes: A thin viscoelastic film model. *Journal of Membrane Biology*, 78(1):53–60, 1984-02-01.
- [138] Heinz Beitinger, Viola Vogel, Dietmar Möbius, and Hinrich Rahmann. Surface potentials and electric dipole moments of ganglioside and phospholipid monolayers: contribution of the polar headgroup at the water/lipid interface. *Biochimica et Biophysica Acta (BBA)-Biomembranes*, 984(3):293–300, 1989.
- [139] Stephanie Tristram-Nagle, Horia I Petrache, and John F Nagle. Structure and interactions of fully hydrated dioleoylphosphatidylcholine bilayers. *Biophysical journal*, 75(2):917, 1998.

- [140] Sukhbir Singh Kapoor and V Ramamurthy. *Nuclear radiation detectors*, volume 1. New Age International, 1993.
- [141] James A. R. Samson and G. L. Weessler. Mobilities of oxygen and nitrogen ions. *Phys. Rev.*, 137:A381–A383, Jan 1965.

## Danksagung

Die erfolgreiche Durchführung der in der vorliegenden Arbeit vorgestellten Projekte wäre ohne die starke Unterstützung und das Vertrauen sehr vieler Personen nicht möglich gewesen. An dieser Stelle möchte ich gerne allen Beteiligten meinen Dank aussprechen.

Professor Dr. Tim Salditt danke ich für die Möglichkeit zur Anfertigung dieser Arbeit unter seiner Leitung. Die stets sehr engagierte, kompetente und enthusiastische Zusammenarbeit haben mich auch in schwierigen Phasen dieses Projektes sehr motiviert. Ich weiß sein mir entgegengebrachtes Vertrauen sehr zu schätzen. Ich bedanke mich herzlich bei Professor Dr. Simone Techert für ihre Bereitschaft, das Amt der Koreferentin für diese Dissertation zu übernehmen, sowie für die Begleitung und die vielen guten Ratschläge insbesondere in der Startphase dieser Arbeit.

Dr. Markus Osterhoff, Dr. Dong-Du Mai, Dr. Jörg Hallmann, Christina Bömer, Jan-David Nicolas und Christian Holme danke ich für die aufopferungsvolle Begleitung mehrerer Messreisen und die stets schnelle Unterstützung bei diversen Problemen. Insbesondere Christinas Begeisterungsfähigkeit und technisches Verständnis halfen sehr bei unserer Eroberung der SAW Technologie für zeitaufgelöste Streuexperimente. Dr. Jörg Hallmann danke ich besonders für die Unterstützung in der Frühphase der Arbeit und bei dem Aufbau der Röntgenplasmaquelle.

Johannes Agricola, Dr. Markus Osterhoff und Moritz Könemann danke ich von ganzem Herzen für die Unterstützung und die Expertise bei der Entwicklung der QAPD. Ohne Euer Engagement und besonders Johannes' Unterstützung in der Frühphase der Detektorentwicklung wäre ein zügiger Erfolg unmöglich zustande gekommen.

Ein spontaner Anruf von Dr. André Beerlink löste eine regelrechte Lawine aus deren Folgen den Fortgang dieser Arbeit maßgeblich beeinflusst haben. Vor und während der hierauf folgenden Messzeiten bekamen wir weiterhin ausnahmslos freundliche und ausgesprochen kompetente Hilfestellungen von Dr. Oliver Seeck und Kathrin Pflaum.

Ich danke Florian Schüle in und Professor Dr. Achim Wixforth für die spontane Bereitschaft zur Zusammenarbeit und die Produktion der auf unsere speziellen Anforderungen zugeschnittenen SAW Chips. Auch die anschließende Zusammenarbeit bei der Veröffentlichung der Ergebnisse war sehr produktiv und von interessanten Diskussionen geprägt.

Während der Experimente an dem Strahlrohr ID09B an der ESRF erfuhren wir sehr intensive Unterstützung durch Dr. Dmitry Khakulin und Dr. Michael Wulff. Auch sie haben sich von von anfänglichen Rückschlägen nicht entmutigen lassen und zusammen mit uns die ein- oder andere Nacht in der Messkabine zugebracht. Ohne die stets gut gelaunte und kompetente technische Unterstützung von Jan Goeman, Peter Nieschalk, Jochen Herbst und Thorsten Gronemann hätte die Entwicklung der Messtechnik nicht in der notwendigen Qualität und Geschwindigkeit voranschreiten können. Desweiteren bedanke ich mich herzlich bei Dr. Karl

Lautscham, Markus Schönekeß und Malte Bürsing für die Produktive Zusammenarbeit im Rahmen der Elektronikentwicklung.

Bei Sabine Balder, Kerstin Reinecke und Kerstin Pluschke möchte ich mich ganz herzlich für die Unterstützung bei organisatorischen Fragen aller Art bedanken.

Schließlich gilt mein großer Dank allen Mitarbeitern des Instituts für Röntgenphysik für die ausgesprochen freundschaftliche und hilfsbereite Atmosphäre, die das Arbeiten hier sehr angenehm macht.

Dem Sonderforschungsbereich 937 *Kollektives Verhalten weicher und biologischer Materie*, dem Courant Research Centre *Nano-Spectroscopy and x-ray Imaging* und damit verbunden der Deutschen Forschungsgemeinschaft danke ich für die finanzielle Unterstützung des Projektes.

Abschließend möchte ich meiner Familie und Friederike von ganzem Herzen für Ihre Unterstützung und Ihr Vertrauen in allen Lebenslagen danken.



## Personal data

name	Tobias Reusch
date of birth	September 23, 1983
place of birth	Aachen
citizenship	German

## Education and professional experience

since 08/2009	PhD student and scientific employee, Institute for X-ray Physics Georg-August-Universität Göttingen
04/2009	Diploma in physics (Dipl.-Phys.), thesis title: “Nichtlamellare Strukturen in Lipidmembranstapeln in Abhängigkeit der Hydratisation: Probenumgebung, Phasendiagramme und Bestimmung der Elektronendichte”
08/2007–12/2007	Internship at the Institut Laue Langevin, Grenoble, France
10/2004–04/2009	Studies of physics, Georg-August-Universität Göttingen
08/2003–04/2004	Military Service, Panzerlehrbataillon 9, Munster
06/2003	Abitur
08/1996–06/2003	Gymnasium Oedeme, Lüneburg
08/1994–07/1996	Orientierungsstufe Oedeme, Lüneburg
08/1990–07/1994	Grundschule Reppenstedt

The main goal of this thesis was to extend and apply time resolved x-ray scattering experiments at in-house, synchrotron and free electron laser sources to soft matter sample systems, in particular aligned lipid multilayers on solid support. A special emphasis was placed on a characterization of the non-equilibrium fast time response of the multilamellar stack to shortly pulsed optical excitation as well as the acousto-electric field accompanying a surface acoustic wave (SAW). In addition to fundamental questions associated with non-equilibrium dynamics of soft matter films such as driven membrane undulations, this thesis addresses technological challenges of time resolved x-ray diffraction, in particular concerning the timing scheme that has been implemented at the synchrotron storage ring Petra III, DESY, Hamburg. Importantly, a conceptually new pulse resolved x-ray detection scheme, well exceeding the performance of present detector concepts, has been developed and is described in detail.



ISBN 978-3-86395-127-6  
ISSN 2191-9860

Universitätsverlag Göttingen